Cover Page

Universiteit Leiden

The handle http://hdl.handle.net/1887/138677 holds various files of this Leiden University dissertation.

Author: Egorova, E.A.
Title: Gold nanoparticle-peptide conjugates for biomedical applications
Issue Date: 2020-12-15

Gold nanoparticle-peptide conjugates for biomedical applications

Proefschrift

ter verkrijging van
de graad van Doctor aan de Universiteit Leiden,
op gezag van Rector Magnificus prof. mr. C.J.J.M. Stolker
volgens het besluit van het College voor Promoties
te verdedigen op dinsdag 15 december 2020
klokke 13:45 uur

door

Elena A. Egorova
geboren op 28 mei 1989 te Serpoechov, Rusland

Promotiecommissie

Promotor: Prof. dr. A. Kros

Copromotor: Dr. A.L. Boyle

Overige leden

Prof. dr. H.S. Overkleeft (voorzitter)

Prof. dr. S.A. Bonnet (secretaris)

Prof. dr. P.Y.W. Dankers

Prof. dr. B.J. Ravoo

Dr. S.I. van Kasteren

Doctoral Thesis, Leiden University, 2020

Cover design: Elena Egorova

Table of Contents

Chapter 1

Introduction

Chapter 2

Peptide amphiphiles: a comparison of the self-assembly behavior exhibited by conventional and thiolated analogues

Chapter 3

Peptidic stabilization of gold nanoparticles

Chapter 4

Peptidic stabilization of gold nanorods

Chapter 5

Gold nanoparticles decorated with ovalbumin-derived epitopes: effect of shape and size on T-cell immune responses

Chapter 6

Summary and Perspectives

Chapter 7

Nederlandse Samenvatting en Perspectieven

Curriculum Vitae

List of Publications

CHAPTER 1

Introduction

Since the first synthesis of colloidal gold was reported in 1951,[1] researchers worldwide have been exploring the potential of gold nanoparticles (GNPs) in multiple fields of materials science. The appeal of GNPs arises from their distinct features, such as their facile synthesis, programmable shape and size, unique optical properties, and ease of surface functionalization, in combination with their large surface area. In more recent years, synthesis protocols for different GNPs have been developed, including for: spherical GNPs from 1 to 200 nm diameter,[2] gold nanorods (GNRs) with programmable dimensions,[3] and unconventional shapes including nanourchins, nanostars, nanodogbones, nanodumbbells, nanocubes, and nanotriangles.[4] With this shape and size diversity comes a wide range of optical properties. GNPs are plasmonic: the electrons on the surface form an electron cloud that oscillates in a manner that is dependent on particle shape and size.[5] Thus, every GNP shape has a characteristic positioning of the absorbance band that defines their localized surface plasmon resonance (LSPR). Spherical GNPs exhibit LSPRs located between 500-600 nm, while LSPRs of more complex shapes are shifted to the near infra-red region (NIR).

GNPs have found applications in a multitude of different fields. They are attractive for applications including drug delivery and vaccine development due to their high relative surface area that can be functionalized with targeting ligands or therapeutic molecules.[6-9] [10] In materials science, GNPs are commonly used in detection assays where the readout is based on optical property changes triggered by GNPs agglomeration.[11, 12] Non-spherical gold nanoparticles have been applied in biomacromolecule sensing,[13, 14] nanophotonics,[15] and in the enhancement of Raman scattering.[16] Differently shaped GNPs are also used in plasmonic photothermal therapy (PPTT).[17-19] GNPs are also widely employed as contrast agents in imaging,[20-22] labeling,[23] and tracking[24] of cellular processes *in vitro* and *in vivo*. GNPs of a size (or shape) range covering the nanometer-

to-submicrometer scale can be used to study size (or shape) effects on cellular uptake,[25-27] clearance from the bloodstream,[28] evoked immune response,[8, 9] or nanoparticle-associated impairment of native cellular function.[29-32] In addition, several groups have investigated the formation of a protein corona around GNPs and GNRs as a function of the applied surface coating and tried to unravel the effects it imposes on the particles' biological fate.[33-36]

One drawback of using GNPs for *in vitro* and *in vivo* applications is that 'as-synthesized' GNPs are not stable in saline, leading to GNP aggregation.[37, 38] Moreover, this aggregation behavior is believed to be the reason these particles are cytotoxic.[31, 35] In order to minimize cytotoxicity and to make GNPs biocompatible, the GNP surface has to be stabilized with alternative ligands. Silica or polymer coatings are commonly used to efficiently prevent GNP aggregation and abolish cytotoxicity,[31, 35, 39, 40] but they have disadvantages. The control over the silica coating thickness is poor, and the coating thickness commonly exceeds 10 nm.[41, 42] Moreover, silica coatings are porous which can lead to accumulation of undesired molecules within the shell. Polyethyleneglycols (PEGs) have been shown to induce immune responses upon persistent exposure, thus the use of thiolated PEGs as GNP stabilizers can have adverse effects.[43] Additionally, it is often desirable for these coatings to be further functionalized, with targeting ligands for example, and functionalization of long PEG molecules is not a trivial task.

In 2004, Levy *et al.* proposed the use of cysteine-containing oligopeptides to stabilize spherical GNPs: these peptides displace citrate from the gold surface and form a protective coating.[44] The study evaluated 58 different peptides and devised rules for the design of GNP-stabilizing peptides. Firstly, the presence of cysteine at the N-terminus is essential for establishing Au-S bonds. Only free thiols (HS-groups) of cysteine side chains participate in

binding, while disulfide-bound cysteines do not form Au-S bonds. The presence of a free amine at the N-terminus was found to aid coordination of the thiols to the gold surface. Secondly, charged residues (lysine or aspartate, for example) should not be placed in the middle of the peptide, as they induce repulsion within the peptide shell leading to GNP aggregation. Moreover, it is crucial to have a C-terminal carboxyl moiety but not a C-terminal amide. This facilitates electrostatic repulsion between individual GNPs and helps to maintain their colloidal stability. Thirdly, the rest of the peptide sequence should consist of non-polar residues. It is beneficial if they are capable of self-assembling into β-structures both in solution and on the gold surface. These β-structures, or β-sheets as they are often referred to in literature, are a distinct peptide secondary structure that exhibit intermolecular hydrogen bonding between neighboring peptide backbones. Due to these tight interactions, water molecules are depleted from the gold surface, thus a high colloidal stability is maintained. The peptide sequences that have been reported to efficiently stabilize GNPs are presented in **Table 1.1**. Such peptide include CALNN, CCVVVTT,[44] and the amyloid-inspired CFGAILSS.[45] These provide 'protein-like' surface chemistry implying that GNPs coated with these peptides exhibit long term-stability under biologically relevant conditions and are resistant towards freeze-drying, repetitive centrifugation, and can be purified *via* size-exclusion chromatography. Interestingly, α-helical peptides were also used coat GNPs, but they exhibited a much lower coverage density:[46] 0.72 peptide/nm^2 versus 2.55 peptide/nm^2 reported for CFGAILSS.[45] This difference indicates that peptides capable of self-assembly into β-structures provide higher coverage densities and potentially better colloidal stabilities. Although these peptides were widely used for stabilizing GNPs and imparting acquired functionalities (**Table 1.2**), use of these peptides for stabilization of GNPs larger than 30 nm, or for non-spherical GNPs has not been reported.

Another widely used approach utilizes short PEG molecules (≥ tetraethyleneglycol) conjugated to a thiolated alkyl chain (≥ C8).[47-50] These molecules possess a terminal thiol enabling binding to a gold surface (**Table 1.1**). GNPs stabilized with these molecules and equipped with an active moiety, such as an enzyme substrate, have been reported.[47] These molecules were shown to stabilize small GNPs (up to 25 nm in diameter) with comparable efficiency to peptides, but they also failed to efficiently stabilize larger GNPs (35 nm in diameter).[48] Interestingly, Schulz *et al.* reported the use of PEG_{2000} conjugated to 11-mercaptoundecanoic acid as a surface stabilizer for GNRs.[51] This amphiphilic stabilizer provided a ~3x higher coverage density, and hence higher colloidal stability, than non-functionalized thiolated PEG_{2000}. It was suggested that the amphiphilic PEG penetrates the hydrophobic CTAB bilayer at the GNR surface more readily than regular, hydrophilic PEG.

Table 1.1. Commonly used peptide sequences and PEG-based compounds for stabilization of GNPs and GNRs.

Peptide sequence	**GNP size, nm**	**Reference**
CALNN NNLACCALNN CCVVVT	12.3	44
CFGAILSS	5; 8; 10; 25	45, 47
CLPFFD-amine*	25	52
Chemical structure		
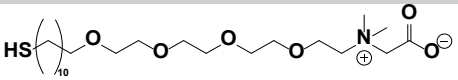	15; 25; 35	48
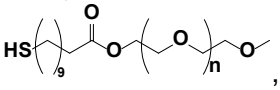 , n = ~45	12; 30 ~85 by 25 (GNRs)	50 51

*- this peptide had an amide group at the C-terminus.[52]

Table 1.2. Additional functionalities appended to CALNN-stabilized GNPs.

Functionality	Comments	Reference
Biotin	Streptavidin docking proved availability of biotin displayed on the GNP surface	44, 54
Oligonucleotides	Interactions between GNPs decorated with complementary strands led to controllable GNP assembly proving that the proposed derivatization route was successful	53
TAT peptide*	These GNPs permeated the cellular membrane and can be used as transporters	54
Epitopes**	Upon contact with specific antibodies, GNPs agglomerate and their optical properties change, which provided the readout in the immunoassay	10, 55
Enzyme substrates***	Caspase-3 cascade was triggered by these GNPs though the cleavage of the substrate	56

*- The human immunodeficiency virus (HIV)-derived trans-activator of transcription peptide (TAT) is a cell-penetrating peptide with the following peptide sequence: GRKKRRQRRRPPQ.[54] **- epitopes were derived from *haemophilus influenzae* hemeagglutinin, *herpes simplex* virus glycoprotein D, and c-Myc protein,[10] or abscisic acid glucose ester was used.[55] ***- the following substrates were used: PFFDVED and KYDDVED.[56]

Although several stabilizers have been developed for GNPs and GNRs, a new approach is needed for larger GNPs (> 30 nm in diameter). We propose to expand the peptidic stabilizer approach by using peptide amphiphiles (**Scheme 1.1**). Peptide amphiphiles are composed of a β-sheet forming peptide sequence coupled to an alkyl chain.[57] They are capable of self-assembling to form a range of structures including 1D cylindrical fibers and well-defined 2D antiparallel β-sheet ribbons.[58] Moreover, peptide amphiphiles can form hydrogels upon the addition of salts;[59, 60] and serve as templates for the mineralization of various inorganic compounds, *e.g.* hydroxyapatite and $CaCO_3$.[61, 62] These applications are possible due to the robustness of the peptide amphiphile self-assembly, which is beneficial for

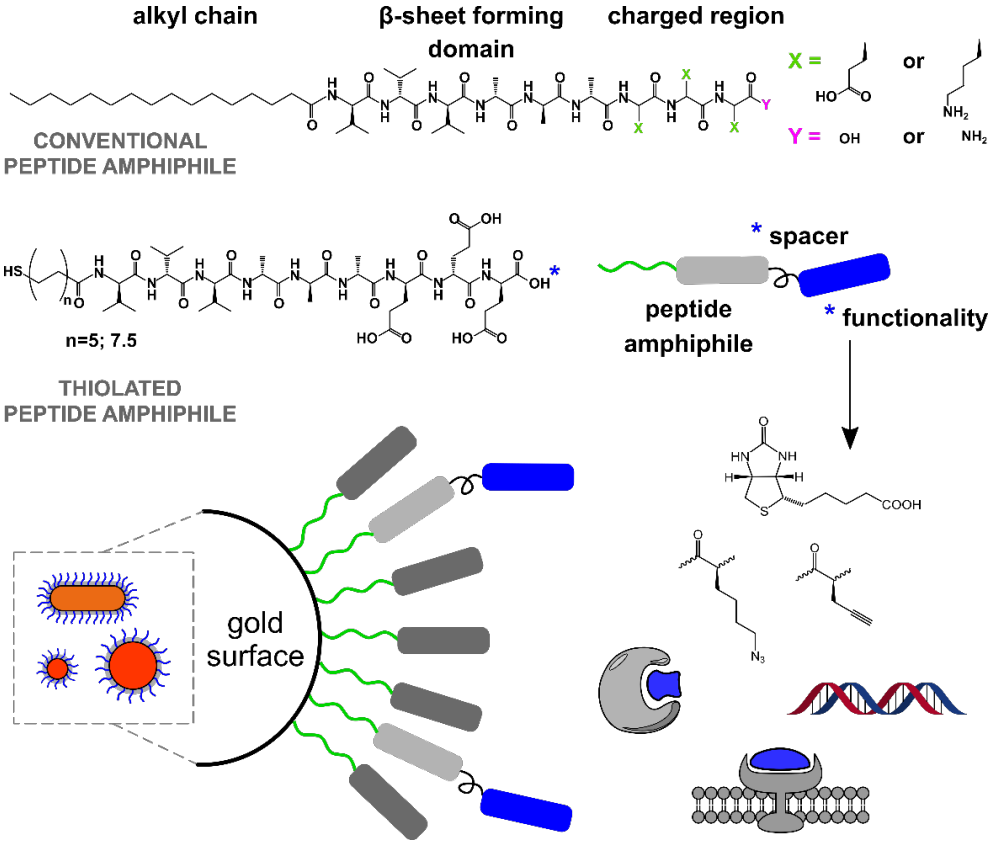

Scheme 1.1. The structure of a typical conventional peptide amphiphile comprises an alkyl chain, β-sheet forming peptide domain, and charged region. Lysine residues provide positive net charge, while glutamate residues provide a negative charge. The design of thiolated peptide amphiphiles is based on a similar structure: a thiol group (HS-) is introduce at the alkyl chain terminus, and a functionality is coupled to the N-terminus of the peptide segment. The thiol groups enable binding to a gold surface in such a way that alkyl chains are located close to the gold surface and the peptide segments are exposed to the aqueous environment. Examples of functionalities include biotin, “click”-handles, oligonucleotides, enzyme substrates, and receptor-specific ligands including B- or T-cell epitopes, *etc*.

their use as a GNP stabilizer. In addition to their other benefits, peptide chemistry offers easy chemical routes to extend the peptide sequences with various ligands thus functionalization of peptide amphiphile-coated GNPs and GNRs with active moieties is possible. We have designed peptide amphiphiles to contain a terminal thiol group that binds to the gold surface.

The alkyl chains subsequently undergo hydrophobic collapse and are sequestered from the aqueous environment. The middle segment of the peptide amphiphile, formed by a β-sheet forming motif, enables intermolecular hydrogen bonding resulting in dense peptide packing. Additionally, we designed the peptide amphiphiles to exhibit a high net charge. These charged residues, which can be either positive or negative, are located at the C-terminus and are therefore exposed to the aqueous environment and promote electrostatic repulsion, thereby aiding colloidal stability.

The experimental work presented in this thesis focuses on the design of peptide-amphiphile ligands capable of stabilizing GNPs of differing sizes and shapes. A large part of this thesis is devoted to determining the optimal conditions for coating GNPs with peptide amphiphiles and evaluating the stabilizing effects that these thiolated peptide amphiphiles afford. Peptide amphiphile-coated GNPs are also demonstrated to be suitable for use in *in vitro* experiments, which facilitates the study of how the physico-chemical properties of GNPs influences T-cell immune responses.

In **Chapter 2** the design and synthesis of thiolated peptide amphiphiles is described. The changes of peptide amphiphile self-assembly behavior in response to variations in the alkyl chain length and composition of the β-sheet forming domain is studied. A comprehensive analysis of data obtained using circular dichroism (CD) spectroscopy, transmission electron microscopy (TEM), and Fourier-transform infrared (FT-IR) spectroscopy is presented.

Chapter 3 describes the coating procedure used to prepare peptide amphiphile-coated spherical GNPs with a size range of 20 to 100 nm. Using dynamic light scattering (DLS), ultraviolet–visible spectroscopy (UV-Vis), and

TEM it was shown that thiolated peptide amphiphiles stabilize all GNP sizes tested. CD and FT-IR were used to assess the self-assembly of these amphiphiles on the gold surface into a self-assembled monolayer (SAM). Two assays: an NaCl-induced aggregation assay and a thiol displacement-induced aggregation assay, were employed to obtain insight into the colloidal stability of the peptide amphiphile-coated GNPs.

In **Chapter 4** thiolated peptide amphiphiles were used for GNR stabilization. UV-Vis spectroscopy, TEM analysis, and zeta-potential measurements were performed to demonstrate the successful displacement of CTAB from the GNR surface and to evaluate the colloidal stability of the resulting particles. Determination of coverage densities of the peptide amphiphiles on the GNR surface, combined with FT-IR data revealed that densely-packed SAMs similar to those formed on the surface of spherical GNPs were also formed on GNRs.

In **Chapter 5** peptide amphiphile-coated GNPs and GNRs were equipped with chicken ovalbumin-derived epitopes in order to study the effect of GNP size and shape on immune response. DLS, UV-Vis spectroscopy, TEM, and inductively coupled plasma mass spectrometry (ICP-MS) were used to characterize epitope-decorated GNPs and GNRs. The cytotoxicity of the particles in bone marrow-derived dendritic cells (BMDCs) was probed with a lactate dehydrogenase (LDH) release assay. Cellular uptake was visualized with TEM and quantified with ICP-MS. Activation of BMDCs through upregulation in cellular receptors, clusters of differentiation CD80 and CD86 was monitored using flow cytometry, while activation through IL-12 and IL-1β cytokine secretion was evaluated with an enzyme-linked immunosorbent assay (ELISA). Efficacy of antigen presentation mediated by the corresponding major histocompatibility complex class I (MHC-I) was assessed using flow cytometry. GNP- and GNR-triggered T-cell immune

responses were studied *in vitro* using cells derived from ovalbumin transgenic mice. The immune responses elicited by different GNPs and GNRs were compared on the basis of T-cell proliferation rates, which were derived from a $CD25^{+}CFSE^{low}$ T-cell subset using flow cytometry.

References

1. Turkevich, J.; Stevenson, P. C.; Hillier, J., A Study of the Nucleation and Growth Processes in the Synthesis of Colloidal Gold. *Discuss Faraday Soc* **1951,** (11), 55-75.

2. Bastus, N. G.; Comenge, J.; Puntes, V., Kinetically Controlled Seeded Growth Synthesis of Citrate-Stabilized Gold Nanoparticles of up to 200 nm: Size Focusing versus Ostwald Ripening. *Langmuir* **2011,** *27* (17), 11098-11105.

3. Gonzalez-Rubio, G.; Kumar, V.; Llombart, P.; Diaz-Nunez, P.; Bladt, E.; Altantzis, T.; Bals, S.; Pena-Rodriguez, O.; Noya, E. G.; MacDowell, L. G.; Guerrero-Martinez, A.; Liz-Marzan, L. M., Disconnecting Symmetry Breaking from Seeded Growth for the Reproducible Synthesis of High Quality Gold Nanorods. *ACS Nano* **2019,** *13* (4), 4424-4435.

4. Dreaden, E. C.; Alkilany, A. M.; Huang, X. H.; Murphy, C. J.; El-Sayed, M. A., The golden age: gold nanoparticles for biomedicine. *Chem Soc Rev* **2012,** *41* (7), 2740-2779.

5. Huang, X. H.; El-Sayed, M. A., Gold nanoparticles: Optical properties and implementations in cancer diagnosis and photothermal therapy. *J Adv Res* **2010,** *1* (1), 13-28.

6. Versiani, A. F.; Andrade, L. M.; Martins, E. M. N.; Scalzo, S.; Geraldo, J. M.; Chaves, C. R.; Ferreira, D. C.; Ladeira, M.; Guatimosim, S.; Ladeira, L. O.; da Fonseca, F. G., Gold nanoparticles and their applications in biomedicine. *Future Virol* **2016,** *11* (4), 293-309.

7. Han, G.; Ghosh, P.; Rotello, V. M., Functionalized gold nanoparticles for drug delivery. *Nanomedicine (Lond)* **2007,** *2* (1), 113-123.

8. Kang, S.; Ahn, S.; Lee, J.; Kim, J. Y.; Choi, M.; Gujrati, V.; Kim, H.; Kim, J.; Shin, E. C.; Jon, S., Effects of gold nanoparticle-based vaccine size on lymph node delivery and cytotoxic T-lymphocyte responses. *J Control Release* **2017,** *256*, 56-67.

9. Niikura, K.; Matsunaga, T.; Suzuki, T.; Kobayashi, S.; Yamaguchi, H.; Orba, Y.; Kawaguchi, A.; Hasegawa, H.; Kajino, K.; Ninomiya, T.; Ijiro, K.; Sawa, H., Gold Nanoparticles as a Vaccine Platform: Influence of Size and Shape on Immunological Responses in Vitro and in Vivo. *ACS Nano* **2013,** *7* (5), 3926-3938.

10. Yeste, A.; Nadeau, M.; Burns, E. J.; Weiner, H. L.; Quintana, F. J., Nanoparticle-mediated codelivery of myelin antigen and a tolerogenic small molecule suppresses experimental autoimmune encephalomyelitis. *P Natl Acad Sci USA* **2012,** *109* (28), 11270-11275.

11. Andresen, H.; Mager, M.; Griessner, M.; Charchar, P.; Todorova, N.; Bell, N.; Theocharidis, G.; Bertazzo, S.; Yarovsky, I.; Stevens, M. M., Single-Step Homogeneous Immunoassays Utilizing Epitope-Tagged Gold Nanoparticles: On the Mechanism, Feasibility, and Limitations. *Chem Mater* **2014,** *26* (16), 4696-4704.

12. Kim, D. S.; Kim, Y. T.; Hong, S. B.; Kim, J.; Heo, N. S.; Lee, M. K.; Lee, S. J.; Kim, B. I.; Kim, I. S.; Huh, Y. S.; Choi, B. G., Development of Lateral Flow Assay Based on Size-Controlled Gold Nanoparticles for Detection of Hepatitis B Surface Antigen. *Sensors-Basel* **2016,** *16* (12): e2154.

13. Cao, J.; Sun, T.; Grattan, K. T. V., Gold nanorod-based localized surface plasmon resonance biosensors: A review. *Sensor Actuat B-Chem* **2014,** *195*, 332-351.

14. Paulo, P. M. R.; Zijlstra, P.; Orrit, M.; Garcia-Fernandez, E.; Pace, T. C. S.; Viana, A. S.; Costa, S. M. B., Tip-Specific Functionalization of Gold Nanorods for Plasmonic Biosensing: Effect of Linker Chain Length. *Langmuir* **2017,** *33* (26), 6503-6510.

15. Sonnichsen, C.; Alivisatos, A. P., Gold nanorods as novel nonbleaching plasmon-based orientation sensors for polarized single-particle microscopy. *Nano Letters* **2005,** *5* (2), 301-304.

16. Bhamidipati, M.; Fabris, L., Multiparametric Assessment of Gold Nanoparticle Cytotoxicity in Cancerous and Healthy Cells: The Role of Size, Shape, and Surface Chemistry. *Bioconjugate Chem* **2017,** *28* (2), 449-460.

17. Wu, Y.; Ali, M. R. K.; Dong, B.; Han, T. G.; Chen, K. C.; Chen, J.; Tang, Y.; Fang, N.; Wang, F. J.; El-Sayed, M. A., Gold Nanorod Photothermal Therapy Alters Cell Junctions and Actin Network in Inhibiting Cancer Cell Collective Migration. *ACS Nano* **2018,** *12* (9), 9279-9290.

18. Riley, R. S.; Day, E. S., Gold nanoparticle-mediated photothermal therapy: applications and opportunities for multimodal cancer treatment. *Wiley Interdiscip Rev Nanomed Nanobiotechnol* **2017,** *9* (4): e1449.

19. Kennedy, L. C.; Bickford, L. R.; Lewinski, N. A.; Coughlin, A. J.; Hu, Y.; Day, E. S.; West, J. L.; Drezek, R. A., A new era for cancer treatment: gold-nanoparticle-mediated thermal therapies. *Small* **2011,** *7* (2), 169-183.

20. Xu, K. Y.; Shi, J. W.; Pourmand, A.; Udayakumar, T. S.; Dogan, N.; Zhao, W. Z.; Pollack, A.; Yang, Y. D., Plasmonic Optical Imaging of Gold Nanorods Localization in Small Animals. *Sci Rep-Uk* **2018,** *8*: e9342.

21. Wang, H. F.; Huff, T. B.; Zweifel, D. A.; He, W.; Low, P. S.; Wei, A.; Cheng, J. X., In vitro and in vivo two-photon luminescence imaging of single gold nanorods. *P Natl Acad Sci USA* **2005,** *102* (44), 15752-15756.

22. Tong, L.; Wei, Q. S.; Wei, A.; Cheng, J. X., Gold Nanorods as Contrast Agents for Biological Imaging: Optical Properties, Surface Conjugation and Photothermal Effects. *Photochem Photobiol* **2009,** *85* (1), 21-32.

23. Durr, N. J.; Larson, T.; Smith, D. K.; Korgel, B. A.; Sokolov, K.; Ben-Yakar, A., Two-photon luminescence imaging of cancer cells using molecularly targeted gold nanorods. *Nano Letters* **2007,** *7* (4), 941-945.

24. van den Broek, B.; Ashcroft, B.; Oosterkamp, T. H.; van Noort, J., Parallel Nanometric 3D Tracking of Intracellular Gold Nanorods Using Multifocal Two-Photon Microscopy. *Nano Letters* **2013,** *13* (3), 980-986.

25. Chithrani, B. D.; Ghazani, A. A.; Chan, W. C. W., Determining the size and shape dependence of gold nanoparticle uptake into mammalian cells. *Nano Letters* **2006,** *6* (4), 662-668.

26. Xie, X. P.; Liao, J. F.; Shao, X. R.; Li, Q. S.; Lin, Y. F., The Effect of shape on Cellular Uptake of Gold Nanoparticles in the forms of Stars, Rods, and Triangles. *Sci Rep-Uk* **2017,** *7*: e3827.

27. Monikh, F. A.; Fryer, B.; Arenas-Lago, D.; Vijver, M. G.; Darbha, G. K.; Valsami-Jones, E.; Peijnenburg, W. J. G. M., A Dose Metrics Perspective on the Association of Gold Nanomaterials with Algal Cellsy. *Environ Sci Tech Let* **2019,** *6* (12), 732-738.

28. Campbell, F.; Bos, F. L.; Sieber, S.; Arias-Alpizar, G.; Koch, B. E.; Huwyler, J.; Kros, A.; Bussmann, J., Directing Nanoparticle Biodistribution through Evasion and Exploitation of Stab2-Dependent Nanoparticle Uptake. *ACS Nano* **2018,** *12* (3), 2138-2150.

29. Hocevar, S.; Milosevic, A.; Rodriguez-Lorenzo, L.; Ackermann-Hirschi, L.; Mottas, I.; Petri-Fink, A.; Rothen-Rutishauser, B.; Bourquin, C.; Clift, M. J. D., Polymer-Coated Gold Nanospheres Do Not Impair the Innate Immune Function of Human B Lymphocytes in Vitro. *ACS Nano* **2019,** *13* (6), 6790-6800.

30. Fytianos, K.; Rodriguez-Lorenzo, L.; Clift, M. J. D.; Blank, F.; Vanhecke, D.; von Garnier, C.; Petri-Fink, A.; Rothen-Rutishauser, B., Uptake efficiency of surface modified gold nanoparticles does not correlate

with functional changes and cytokine secretion in human dendritic cells in vitro. *Nanomed-Nanotechnol* **2015,** *11* (3), 633-644.

31. Grabinski, C.; Schaeublin, N.; Wijaya, A.; D'Couto, H.; Baxamusa, S. H.; Hamad-Schifferli, K.; Hussain, S. M., Effect of Gold Nanorod Surface Chemistry on Cellular Response. *ACS Nano* **2011,** *5* (4), 2870-2879.

32. Villiers, C. L.; Freitas, H.; Couderc, R.; Villiers, M. B.; Marche, P. N., Analysis of the toxicity of gold nano particles on the immune system: effect on dendritic cell functions. *J Nanopart Res* **2010,** *12* (1), 55-60.

33. Garcia-Alvarez, R.; Hadjidemetriou, M.; Sanchez-Iglesias, A.; Liz-Marzan, L. M.; Kostarelos, K., In vivo formation of protein corona on gold nanoparticles. The effect of their size and shape. *Nanoscale* **2018,** *10* (3), 1256-1264.

34. Mosquera, J.; Garcia, I.; Henriksen-Lacey, M.; Gonzalez-Rubio, G.; Liz-Marzan, L. M., Reducing Protein Corona Formation and Enhancing Colloidal Stability of Gold Nanoparticles by Capping with Silica Monolayers. *Chem Mater* **2019,** *31* (1), 57-61.

35. Ding, L.; Yao, C. J.; Yin, X. F.; Li, C. C.; Huang, Y. A.; Wu, M.; Wang, B.; Guo, X. Y.; Wang, Y. L.; Wu, M. H., Size, Shape, and Protein Corona Determine Cellular Uptake and Removal Mechanisms of Gold Nanoparticles. *Small* **2018,** *14* (42): e1801451.

36. Walkey, C. D.; Olsen, J. B.; Song, F. Y.; Liu, R.; Guo, H. B.; Olsen, D. W. H.; Cohen, Y.; Emili, A.; Chan, W. C. W., Protein Corona Fingerprinting Predicts the Cellular Interaction of Gold and Silver Nanoparticles. *ACS Nano* **2014,** *8* (3), 2439-2455.

37. Zhang, Q.; Hitchins, V. M.; Schrand, A. M.; Hussain, S. M.; Goering, P. L., Uptake of gold nanoparticles in murine macrophage cells without cytotoxicity or production of pro-inflammatory mediators. *Nanotoxicology* **2011,** *5* (3), 284-295.

38. De Jong, W. H.; Hagens, W. I.; Krystek, P.; Burger, M. C.; Sips, A. J. A. M.; Geertsma, R. E., Particle size-dependent organ distribution of gold nanoparticles after intravenous administration. *Biomaterials* **2008,** *29* (12), 1912-1919.

39. Naha, P. C.; Chhour, P.; Cormode, D. P., Systematic in vitro toxicological screening of gold nanoparticles designed for nanomedicine applications. *Toxicol in Vitro* **2015,** *29* (7), 1445-1453.

40. Mallick, S.; Sun, I. C.; Kim, K.; Yi, D. K., Silica Coated Gold Nanorods for Imaging and Photo-Thermal Therapy of Cancer Cells. *J Nanosci Nanotechno* **2013,** *13* (5), 3223-3229.

41. Knowles, B. R.; Yang, D.; Wagner, P.; Maclaughlin, S.; Higgins, M. J.; Molino, P. J., Zwitterion Functionalized Silica Nanoparticle Coatings: The Effect of Particle Size on Protein, Bacteria, and Fungal Spore Adhesion. *Langmuir* **2019,** *35* (5), 1335-1345.

42. Comenge, J.; Fragueiro, O.; Sharkey, J.; Taylor, A.; Held, M.; Burton, N. C.; Park, B. K.; Wilm, B.; Murray, P.; Brust, M.; Levy, R., Preventing Plasmon Coupling between Gold Nanorods Improves the Sensitivity of Photoacoustic Detection of Labeled Stem Cells in Vivo. *ACS Nano* **2016,** *10* (7), 7106-7116.

43. Shiraishi, K.; Yokoyama, M., Toxicity and immunogenicity concerns related to PEGylated-micelle carrier systems: a review. *Sci Technol Adv Mat* **2019,** *20* (1), 324-336.

44. Levy, R.; Thanh, N. T. K.; Doty, R. C.; Hussain, I.; Nichols, R. J.; Schiffrin, D. J.; Brust, M.; Fernig, D. G., Rational and combinatorial design of peptide capping Ligands for gold nanoparticles. *J Am Chem Soc* **2004,** *126* (32), 10076-10084.

45. Shaw, C. P.; Middleton, D. A.; Volk, M.; Levy, R., Amyloid-derived peptide forms self-assembled monolayers on gold nanoparticle with a curvature-dependent beta-sheet structure. *ACS Nano* **2012,** *6* (2), 1416-1426.

46. Mikolajczak, D. J.; Heier, J. L.; Schade, B.; Koksch, B., Catalytic Activity of Peptide-Nanoparticle Conjugates Regulated by a Conformational Change. *Biomacromolecules* **2017,** *18* (11), 3557-3562.

47. Pengo, P.; Baltzer, L.; Pasquato, L.; Scrimin, P., Substrate modulation of the activity of an artificial nanoesterase made of peptide-functionalized gold nanoparticles. *Angew Chem Int Ed Engl* **2007,** *46* (3), 400-404.

48. Gupta, A.; Moyano, D. F.; Parnsubsakul, A.; Papadopoulos, A.; Wang, L. S.; Landis, R. F.; Das, R.; Rotello, V. M., Ultrastable and Biofunctionalizable Gold Nanoparticles. *ACS Appl Mater Inter* **2016,** *8* (22), 14096-14101.

49. Marson, D.; Guida, F.; Sologan, M.; Boccardo, S.; Pengo, P.; Perissinotto, F.; Iacuzzi, V.; Pellizzoni, E.; Polizzi, S.; Casalis, L.; Pasquato, L.; Pacor, S.; Tossi, A.; Posocco, P., Mixed Fluorinated/Hydrogenated Self-Assembled Monolayer-Protected Gold Nanoparticles: In Silico and In Vitro Behavior. *Small* **2019,** *15* (17): e1900323.

50. Schulz, F.; Vossmeyer, T.; Bastus, N. G.; Weller, H., Effect of the Spacer Structure on the Stability of Gold Nanoparticles Functionalized with

Monodentate Thiolated Poly(ethylene glycol) Ligands. *Langmuir* **2013,** *29* (31), 9897-9908.

51. Schulz, F.; Friedrich, W.; Hoppe, K.; Vossmeyer, T.; Weller, H.; Lange, H., Effective PEGylation of gold nanorods. *Nanoscale* **2016,** *8* (13), 7296-7308.

52. Olmedo, I.; Araya, E.; Sanz, F.; Medina, E.; Arbiol, J.; Toledo, P.; Alvarez-Lueje, A.; Giralt, E.; Kogan, M. J., How changes in the sequence of the peptide CLPFFD-NH2 can modify the conjugation and stability of gold nanoparticles and their affinity for beta-amyloid fibrils. *Bioconjugate Chem* **2008,** *19* (6), 1154-1163.

53. Wang, Z.; Levy, R.; Fernig, D. G.; Brust, M., The peptide route to multifunctional gold nanoparticles. *Bioconjugate Chem* **2005,** *16* (3), 497-500.

54. Todorova, N.; Chiappini, C.; Mager, M.; Simona, B.; Patel, I. I.; Stevens, M. M.; Yarovsky, I., Surface Presentation of Functional Peptides in Solution Determines Cell Internalization Efficiency of TAT Conjugated Nanoparticles. *Nano Letters* **2014,** *14* (9), 5229-5237.

55. Zhou, G. H.; Liu, Y. Z.; Luo, M.; Xu, Q. F.; Ji, X. H.; He, Z. K., Peptide-Capped Gold Nanoparticle for Colorimetric Immunoassay of Conjugated Abscisic Acid. *ACS Appl Mater Inter* **2012,** *4* (9), 5010-5015.

56. Zhao, C. L.; Qiu, L. H.; Lv, P.; Han, A. L.; Fang, G. Z.; Liu, J. F.; Wang, S., AuNP-peptide probe for caspase-3 detection in living cells by SERS. *Analyst* **2019,** *144* (4), 1275-1281.

57. Hendricks, M. P.; Sato, K.; Palmer, L. C.; Stupp, S. I., Supramolecular Assembly of Peptide Amphiphiles. *Acc Chem Res* **2017,** *50* (10), 2440-2448.

58. Cavalli, S.; Handgraaf, J. W.; Tellers, E. E.; Popescu, D. C.; Overhand, M.; Kjaer, K.; Vaiser, V.; Sommerdijk, N. A. J. M.; Rapaport, H.; Kros, A., Two-dimensional ordered beta-sheet lipopeptide monolayers. *J Am Chem Soc* **2006,** *128* (42), 13959-13966.

59. Pashuck, E. T.; Cui, H. G.; Stupp, S. I., Tuning Supramolecular Rigidity of Peptide Fibers through Molecular Structure. *J Am Chem Soc* **2010,** *132* (17), 6041-6046.

60. Greenfield, M. A.; Hoffman, J. R.; de la Cruz, M. O.; Stupp, S. I., Tunable Mechanics of Peptide Nanofiber Gels. *Langmuir* **2010,** *26* (5), 3641-3647.

61. Newcomb, C. J.; Bitton, R.; Velichko, Y. S.; Snead, M. L.; Stupp, S. I., The Role of Nanoscale Architecture in Supramolecular Templating of Biomimetic Hydroxyapatite Mineralization. *Small* **2012,** *8* (14), 2195-2202.

62. Cavalli, S.; Popescu, D. C.; Tellers, E. E.; Vos, M. R. J.; Pichon, B. P.; Overhand, M.; Rapaport, H.; Sommerdijk, N. A. J. M.; Kros, A., Self-organizing beta-sheet lipopeptide monolayers as template for the mineralization of $CaCO_3$. *Angew Chem Int Edit* **2006,** *45* (5), 739-744.

CHAPTER 2

Peptide amphiphiles: a comparison of the self-assembly behavior exhibited by conventional and thiolated analogues

2.1 Abstract

Peptide amphiphiles self-assemble in solution into an array of three-dimensional structures, while at interfaces two-dimensional structures are formed. This makes peptide amphiphiles a potentially attractive stabilizing coating for gold nanoparticles enabling future applications in biomedical fields like imaging and theranostics. For this, peptide amphiphiles must be functionalized with a thiol group to covalent facilitate attachment to the gold surface. Peptide amphiphiles usually comprise a peptidic headgroup conjugated to an alkyl chain. Small changes in their structure, for example alterations in peptide composition or modifications to the alkyl chain, including changes in length or the introduction of a thiol group, can lead to significant changes in the morphology of the resulting self-assembled structures. In this chapter, a range of amphiphiles with different peptide sequences, alkyl chain lengths, and with or without a terminal thiol are designed, synthesized and characterized to determine which amphiphiles demonstrate self-assembly behavior appropriate to stabilize gold nanoparticles.

2.2 Introduction

To date there is still a need to develop colloidally stable gold nanoparticles (GNPs) that are easy-to-functionalize, biocompatible, and suitable for biological applications. GNPs are typically synthesized with a citrate coating as a stabilizer, which is unstable under physiological conditions and a different coating is therefore required.[1, 2] Polymers[3-5] or silica[6-8] coatings are commonly used for this purpose.[5] However, the size of the GNPs is often significantly increased due to the thickness of these coatings.[8] Therefore, low molecular weight molecules are also studied as a GNP stabilizer. Among others,[9, 10] oligopeptides are able to stabilize small spherical GNPs (≤30 nm). These peptides tether to a gold surface *via* the cysteine side chain resulting in covalent binding through Au-S bond formation.[11, 12] The stabilizing effect of these peptides was partially attributed to their propensity to self-assemble into β-structures both in solution and when attached to a gold surface.[13, 14] Peptide backbones arrange perpendicularly to the gold surface and are held in place by intermolecular hydrogen bonding and hydrophobic interactions resulting in self-assembled monolayers (SAMs). However, these peptides also have limitations: their use for coating larger GNPs or GNPs of other shapes than spherical has not been reported.

To overcome the limitations of cysteine-containing peptides as GNP stabilizers, a new design based on peptide amphiphiles is suggested in this thesis. Peptide amphiphiles are a class of self-assembling materials and composed of a (polar) peptide segment conjugated to an aliphatic chain.[15] This molecule type differs from amphiphilic peptides, which are also capable of forming self-assembled structures either due to the presence of

hydrophobic and hydrophilic peptide blocks,[16] or due to the alternating order of hydrophobic and hydrophilic amino acid residues.[17]

Peptide amphiphiles are designed to form well-defined supramolecular structures in aqueous conditions. The driving force is hydrophobic collapse by sequestering the alkyl chains from the solvent to form the core of the supramolecular structure, and ordered secondary structure formation as a result of intermolecular hydrogen bonding by the peptide segment.[18] Additionally, these amphiphiles usually are (partially) charged thereby increasing solubility and the electrostatic repulsion at the periphery of the assembly prevents aggregation.[15] Peptide amphiphiles can be designed *de novo*, or inspired by example from Nature (e.g. toll-like receptor motifs with multiple alkyl chains attached to a single peptide domain).[19]

If a thiol group is introduced at the terminus of the amphiphile's alkyl chain, it is possible to tether these molecules on a gold surface *via* an Au-S bond. In this arrangement the gold core is surrounded with a hydrophobic environment created by the alkyl chains, therefore shielding the gold surface from undesired interactions with the biological medium. Also, the charged surface of peptide amphiphile-based supramolecular structures, increases the colloidal stability of coated GNPs due to the increased repulsive forces.[11] Additionally, a high propensity to form β-sheets, typical for peptide amphiphiles, is an advantage for a GNP stabilizer. There are three variables affecting peptide amphiphiles self-assembly in aqueous media or on a surface: the alkyl chain (*e.g.* length, degree of unsaturation, and functional groups like thiol), the amino acid sequence within the peptide domain, and the net charge. Previously it was shown that altering one of these components can already have a significant effect on the self-assembly behavior.[18, 20-22] Typically, peptide amphiphiles in solution assemble into

micelles and fibers. However, other morphologies including nanoribbons and nanobelts, or 1D fibers that align into more complex structures are also observed (**Scheme 2.1**).[15]

Alkyl chains spanning a length range from 6-24 carbon atoms have been used to control peptide amphiphile assembly. The results of these collective studies were presented in an elaborate review by Hamley.[23] The minimum alkyl chain length required to induce formation of a supramolecular structure has been discussed in several studies.[24] Alterations made to the alkyl chain define the stability of the supramolecular structures formed though the molecule's geometry. In some cases, it is favourable to use shorter alkyl chains as they do not interfere with the peptide self-assembly behavior, therefore maintaining the peptide-driven mode of self-assembly.[25]

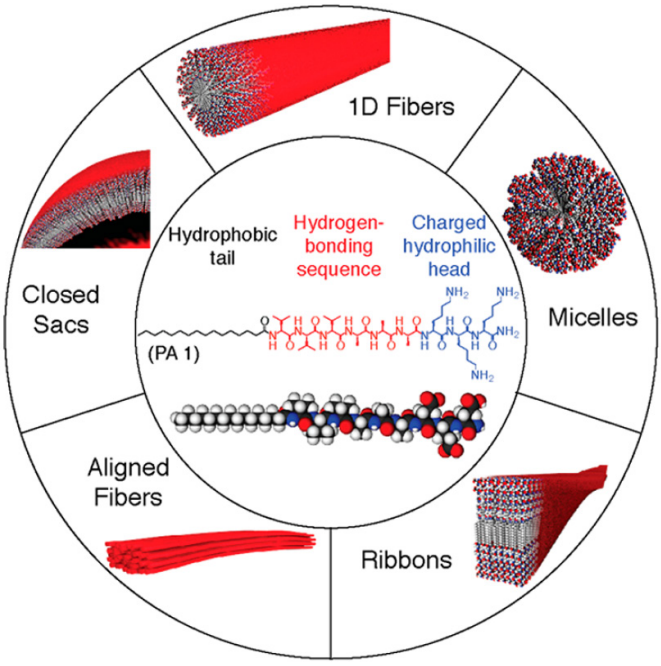

Scheme 2.1. Schematic explanation of different morphologies that can be formed by peptide amphiphiles (a generic amphiphile structure is shown in the middle). Image adapted from reference 15.

The primary amino acid sequence of peptide amphiphiles is always a combination of non-polar residues such as alanine (Ala, A), valine (Val, V), leucine (Leu, L), isoleucine (Ile, I), or phenylalanine (Phe, F), and charged residues including lysine (Lys, K), arginine (Arg, R), glutamic acid (Glu, E), or aspartic acid (Asp, D).[15, 23, 26]. The steric bulk of the side chains is important for both non-polar and charged residues, since it defines the molecule's geometry and self-assembly propensity. Numerous studies have reported how the amino acid sequence influences the self-assembly of peptide amphiphiles.[23, 26]. Stupp and coworkers observed that, for higher-order self-assembly into supramolecular fibers, it is beneficial to have longer peptide domains comprising more non-polar residues in comparison to charged residues, with bulky non-polar residues directly conjugated to a palmitoyl (C16) alkyl chain. This is due to hydrogen bond alignment being more effective when bulky residues are located next to the hydrophobic core.[18] In this study, the sequence palmitoyl-$V_4A_2E_3$ was the best-performing sequence as it demonstrated the highest β-sheet propensity. The composition of the peptide domain also influences the dynamic exchange of monomers between the supramolecular fibers as was revealed by Stochastic optical reconstruction microscopy (STORM).[27] Palmitoyl-$A_3G_3K_3$ assemblies showed to be more dynamic and flexible compared to palmitoyl-$V_3A_3K_3$ affecting the viability of cells cultured on these materials.[28] It was shown that flexible peptide amphiphiles cause cell death. Furthermore, reducing the amino acid residue number has also an impact on the resulting assemblies: palmitoyl-$V_3A_3E_3$ assembled into cylindrical fibers, while palmitoyl-$V_2A_2E_3$ yielded twisted nanoribbons.[29]

Peptide amphiphile assemblies are responsive to both the pH and ionic strength of the solution. For example, lowering the pH led to protonation of Glu residues in palmitoyl-I-A_3E_4-NH_2 resulting in a decrease in electrostatic

repulsion and a concomitant morphology change from spherical micelles to fibers with a predominantly β-sheet structure.[30] In another example, increasing the pH of a palmitoyl-VEVE solution led to a rearrangement of supramolecular sheets into nanobelts.[31, 32] Interestingly, the same peptide amphiphile showed three distinctly different arrangements at different concentrations: twisted nanoribbons at 0.01 wt%, a “broom”-like morphology at 0.05 wt%, and nanobelts at 0.1 wt%.[31]

The ionic strength has also a pronounced effect on peptide amphiphile assembly. Repulsion between positively charged Lys residues in palmitoyl-$V_3A_3K_3$ decreases when the ionic strength increases leading to charge screening and enhanced β-sheet formation.[33] Addition of divalent salts (*e.g.* $CaCl_2$) led to a transformation of the palmitoyl-$V_3A_3E_3$ peptide amphiphile solution into a gel.[34, 35] In a different approach, combining two peptide amphiphiles with opposite charge, leads to the formation of a mixed fiber exhibiting decreased thermal stability.[20]

In summary, these examples prove that many factors influence the self-assembly behavior of peptide amphiphiles, including the peptide amphiphile chemical composition, and external factors such as changes in the peptide amphiphile environment.

The extraordinary propensities of such peptide amphiphiles to form morphologies with tunable features has been utilized in the development of novel materials. Examples are tunable hydrogels, the development of delivery platforms, and as peptide amphiphiles scaffolds for regenerative medicine.[26, 36] Also, electrospinning of peptide amphiphiles as a protective layer for metal surfaces was reported to produce biocompatible coatings for medical devices.[37]

To obtain colloidally stable GNPs for a variety of (biomedical) applications, a protective coating is required. The present work aims to design peptide amphiphiles suitable for functionalization of GNPs and preventing their aggregation in a biological environment. For this, a thiol-group was introduced at the alkyl chain terminus to yield functional peptide amphiphiles generally described as mercaptoacyl-$[VA]_3K_3$, where either a mercaptohexadecanoyl or mercaptoundecanoyl chain is conjugated to a $[VA]_3$ peptide segment, representing four different peptide sequences: VVVAAA, AAAVVV, VAVAVA, and AVAVAV. In addition, thiolated peptide amphiphiles were oxidized to form dimerized peptide amphiphiles with two alkyl chains and two identical peptide domains coupled through an S-S bridge. Altering the hydrophobic segment in a peptide amphiphile may induce changes to its self-assembly behavior. Therefore, the effect of alkyl chain thiolation on the peptide amphiphile secondary structure was investigated in detail. The propensities of both thiolated and conventional amphiphiles to form ordered secondary structures and to self-assemble into supramolecular fibers were evaluated with circular dichroism (CD) and attenuated total reflection infrared spectroscopy (ATR-IR), as well as transmission electron microscopy (TEM). This approach allowed for identification of peptide amphiphiles that exhibit peptide-driven self-assembly which should be able to stabilize GNPs.

2.3 Results and Discussion

2.3.1 Peptide amphiphile design

The composition of the peptide and alkyl chain segments of the peptide amphiphiles were altered in order to tune the physical and chemical properties as well as the self-assembly behavior. For this, five different peptide domains and five alkyl chains (including two dimerized variants) were investigated (**Scheme 2.2**). The peptide amphiphiles were synthesized using solid-phase peptide synthesis according to standard Fmoc-chemistry protocols. Alkyl chains were coupled directly to the N-terminus of the peptide segment. After cleavage, the peptide amphiphiles were purified using high performance liquid chromatography (HPLC) and purity was determined by mass-spectrometry (MS, see **Figures S2.1-S2.15**). Dimerization of the thiolated peptide amphiphiles was achieved through oxidation with I_2 (**Figures S2.16-2.25**).

Peptide sequences investigated in this study contained the non-polar residues valine (Val, V) and alanine (Ala, A) in combination with the positively-charged residue lysine (Lys, K). All peptide sequences had a C-terminal amide followed by three Lys residues. Three Val and three Ala residues were either put in blocks ($\mathbf{V_3A_3}$ and $\mathbf{A_3V_3}$ in **Scheme 2.2**) or in an alternating sequence ($\mathbf{(VA)_3}$ and $\mathbf{(AV)_3}$). Also, a peptide comprising six Ala residues was synthesized ($\mathbf{A_6}$) for comparison. These sequences had either Val or Ala at the N-terminus, which was previously shown to have an effect on self-assembly propensities, as the hydrogen bond alignment is determined by the residues next to the hydrophobic core.[18]

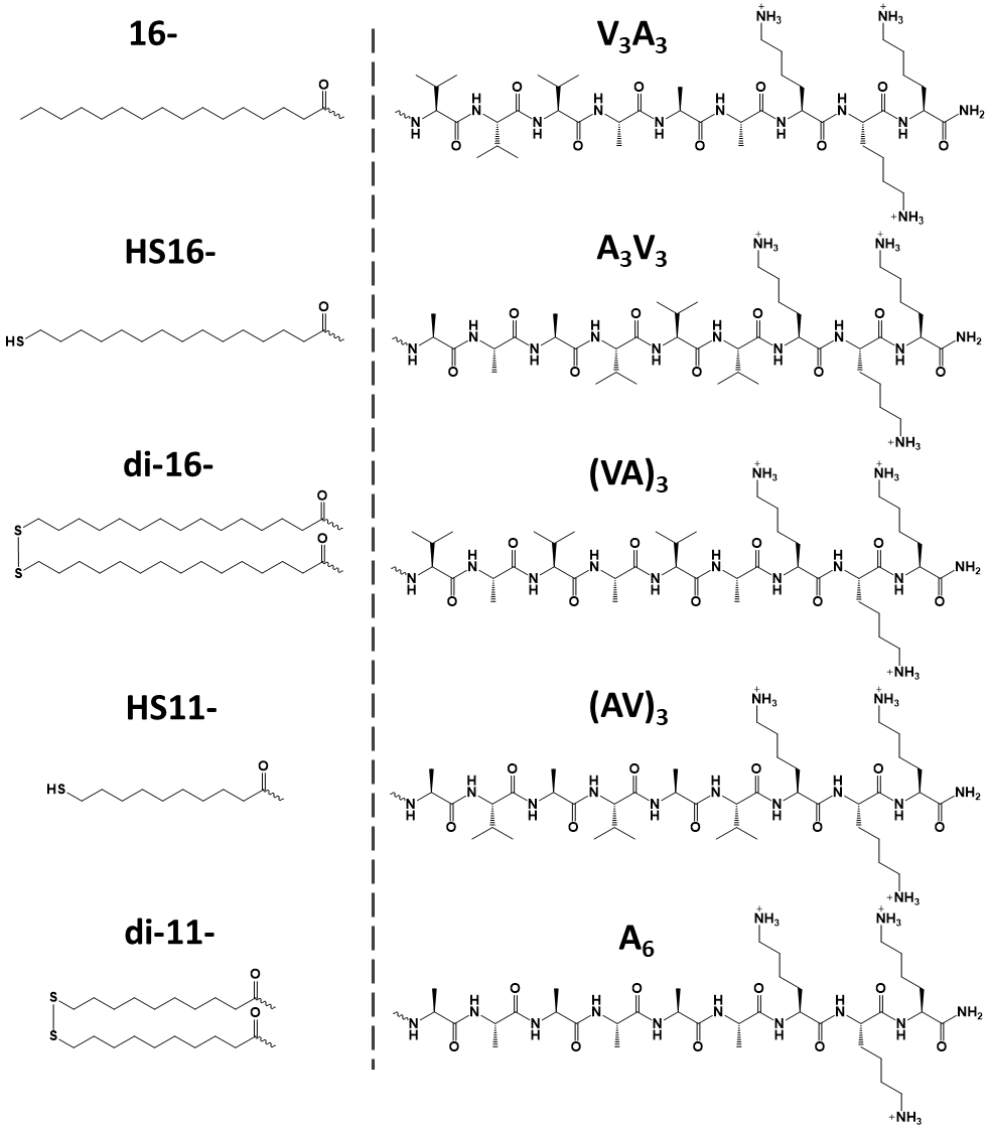

Scheme 2.2. Peptide amphiphiles were generated as a combination of one of the acyl chain options and one of the peptide sequences resulting in 25 different peptide amphiphiles. **Di-16-** and **di-11-** peptide amphiphiles comprised two identical molecules dimerized *via* the thiols to form a disulfide.

We also varied the alkyl chain length between 11 and 16 carbons. The C16 (palmitoyl) chain is typically used in peptide amphiphile designs as it was

presumed to result in more stable assemblies in comparison to shorter alkyl chains.[15, 38] Also, the resulting assembly shape may vary: cylindrical fibers were observed in the case of longer alkyl chains and micelles with shorter alkyl chains. Introduction of a thiol at the alkyl chain terminus may not only influence molecules-surface interactions but also the peptide amphiphile self-assembly process *via* dimerization. To probe the nature of the self-assembly (peptide-driven or alkyl chain-driven), peptide amphiphiles with a thiolated C11 (undecanoyl) chain were also studied, since this chain is at the lower limit of reported peptide amphiphile assemblies due to the reduced hydrophobicity.[23, 39] Palmitoylated amphiphiles were denoted as **16-** and thiolated amphiphiles were denoted as **HS16-** and **HS11-** (**Scheme 2.2**).

Oxidation of the terminal thiols was observed during storage of the peptide amphiphiles; both lyophilized and in solution (**Figure S2.26**). Close proximity of the thiols inside the fiber core most likely enabled dimer formation. It was speculated that this could change the mutual orientation of two neighboring peptide amphiphiles, giving rise to self-assembled structures with morphologies different to those formed by the monomeric species. Therefore, disulfide-bonded molecules were synthesized and evaluated as well (**di-16-** and **di-11-** in **Scheme 2.2**).

A total of 25 peptide amphiphiles were studied in this chapter. Pure peptide amphiphiles were first investigated for their propensities to form ordered peptide secondary structures using circular dichroism (CD) spectroscopy. The peptide conformation was also probed by Fourier-transform infrared spectroscopy (FT-IR) and the resulting assemblies were visualized with transmission electron microscopy (TEM).

2.3.2 Self-assembly of thiolated peptide amphiphiles

Formation of supramolecular structures can be affected by several factors, including the concentration of the self-assembling molecules and the composition of the solvent.[31, 32, 35] Circular dichroism (CD) spectroscopy is well-suited to screen peptide amphiphiles secondary structure of proteins and peptides in solution.[18, 40, 41]

The optimal concentration of peptide amphiphiles for reliable CD measurements was determined by recording spectra of **16-V_3A_3** and **HS11-V_3A_3** at different concentrations (**Figure 2.1A,B**). The spectra are typical for β-structured peptides. These peptides typically possess a minimum at 216 nm, and a maximum at 195 nm,[18, 42] but for peptide amphiphiles the minimum can be significantly red-shifted (up to 10 nm) due to a change in the mutual orientation of the peptide backbones.[18] Both peptide amphiphiles showed a minimum between 220 and 224 nm. **16-V_3A_3** showed highly comparable CD spectra in the range of 100 to 25 µM with a significant decrease in the quality of the signal at 10 µM (**Figure 2.1A**). Thus, a concentration of 50 µM was chosen for all peptide amphiphiles coupled with **16-**, and **HS16-** alkyl chains, and 25 µM for **di-16-** peptide amphiphiles. A higher optimal concentration was expected for the shorter C11 chain. **HS11-V_3A_3** at 1 mM concentration showed a significant difference in the normalized CD intensity compared to lower concentrations, suggesting that in this concentration range the linear dependence is lost (**Figure 2.1B**).[15] At 100 µM, a very low intensity was recorded, therefore, a concentration of 250 µM was chosen for all **HS11-** peptide amphiphiles, and 125 µM for **di-11-** peptide amphiphiles.

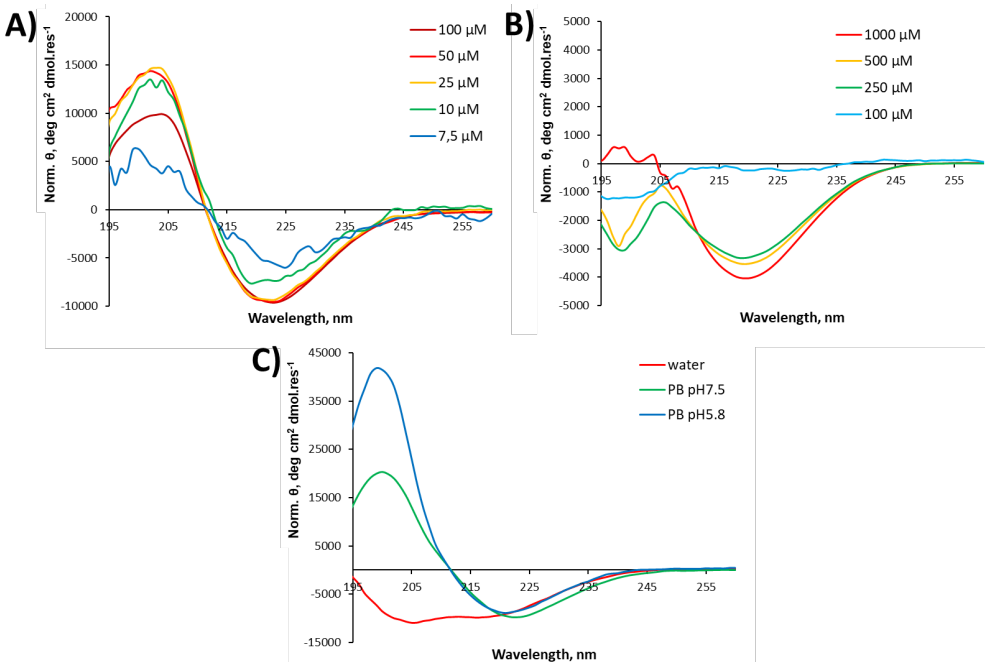

Figure 2.1. Optimization of different conditions for self-assembly monitored with CD spectroscopy: (A) **16-V$_3$A$_3$** in the concentration range of 7.5 to 100 µM (aq.); (B) **HS11-V$_3$A$_3$** in the concentration range of 100 to 1000 µM (aq.); (C) **16-(AV)$_3$** prepared in different buffers at a concentration of 100 µM. Ellipticity (θ, deg) was normalized for concentration and number of amino acid residues.

The effect of ionic strength on the secondary structure was subsequently investigated. **16-(AV)$_3$** was dissolved in water or in 10 mM phosphate buffer (PB) at two different pHs: 5.8 and 7.5 (**Figure 2.1C**). In all cases the peptide amphiphiles had protonated lysine side chains. Significant differences were observed: **16-(AV)$_3$** prepared in water showed a noticeable presence of α-helical structures (minima at 206 nm and 220 nm), at pH 7.5 the minimum at 223 nm was attributed to β-structures, also a small shoulder at 210 nm was observed. In PB at pH 5.8 the peptide amphiphile was predominantly β-structured, indicated by a single minimum at 221 nm. Interestingly, at pH 7.5 the maximum was red-shifted and broad, indicating less-ordered structures when compared to the peptide amphiphile at pH 5.8. In the remaining

chapter, samples were therefore analyzed in PB at pH 5.8, although published reports on **16-V_3A_3** utilized neutral pH conditions for assessment of the self-assembly properties.[43]

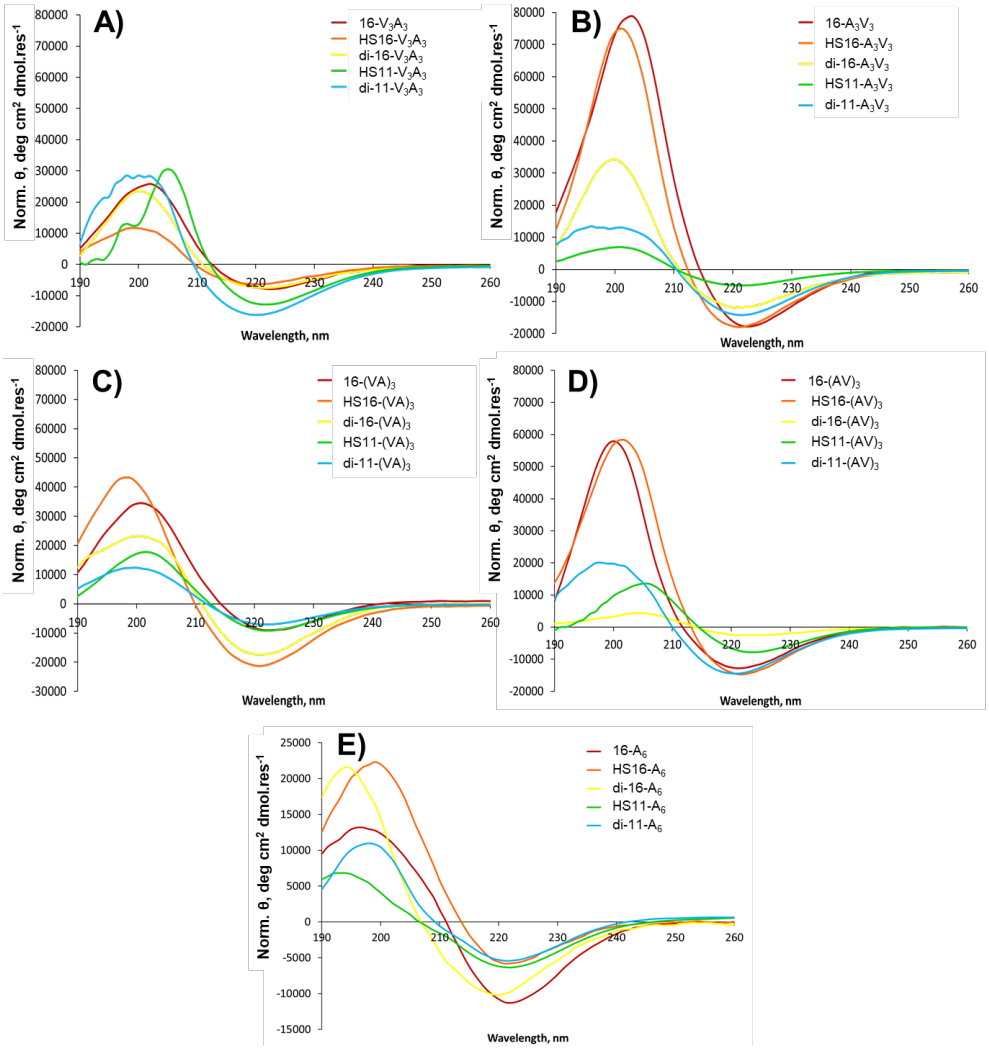

Figure 2.2. CD spectra for peptide amphiphiles: (A) **V_3A_3**; (B) **A_3V_3**; (C) **$(VA)_3$;** (D) **$(AV)_3$**; (E) **A_6**. Samples were prepared in 10 mM PB (pH 5.8).

Next, the self-assembly of all 25 synthesized peptide amphiphiles was probed with CD spectroscopy (**Figure 2.2**). Only peptide amphiphiles with the $\mathbf{A_6}$ domain deviated from the typical β-structure (**Figure 2.2**). The minimum position and peak intensity of **HS16-** peptide amphiphiles were compared to their **C16-** counterparts to obtain insight in the hydrogen bond alignment and β-structure-forming ability.[18]

The $\mathbf{V_3A_3}$ domain did not undergo a significant rearrangement when the **16-** chain was replaced by **di-16-**, only a slight blue-shift (-2 nm) in the minimum position was observed for **HS16-$\mathbf{V_3A_3}$** (**Figure 2.2A**). Shortening the alkyl chain to **HS11-** caused a higher molar ellipticity, while dimerization resulted in peak broadening. The reversed block sequence, $\mathbf{A_3V_3}$, responded to the alkyl chain alteration differently (**Figure 2.2B**): thiolation of the C16 chain resulted in a blue-shift and dimerization to **di-16-$\mathbf{A_3V_3}$** significantly reduced the peak minimum intensity. Shortening the alkyl chain reduced the peak intensity by almost 25%, but dimerization of **HS11-$\mathbf{A_3V_3}$** restored the signal to the level of **di-16-$\mathbf{A_3V_3}$**.

Interestingly, thiolation of **16-$\mathbf{(VA)_3}$** significantly enhanced the CD signal, and the dimerized **di-16-$\mathbf{(VA)_3}$** showed almost the same minimum intensity (**Figure 2.2C**). Almost no difference in the minimum intensity was detected between **16-$\mathbf{(VA)_3}$**, **HS11-$\mathbf{(VA)_3}$**, and **di-11-$\mathbf{(VA)_3}$**, yet peak broadening was apparent for the two thiolated amphiphiles. The second alternating peptide domain **$\mathbf{(AV)_3}$** (**Figure 2.2D**) responded to thiolation in a similar fashion as $\mathbf{A_3V_3}$: **16-** and **HS16-** variants showed minimal differences, while **di-16-** was again less structured. In summary, $\mathbf{A_3V_3}$ and **$\mathbf{(AV)_3}$** behaved quite comparable. Interestingly, the similarities between the two peptide domains were maintained for the **HS11-** and **di-11-** coupled molecules: the intensity of the **HS11-$\mathbf{(AV)_3}$** spectrum was significantly lower compared to **di-11-$\mathbf{(AV)_3}$**.

Also, **HS11-$(AV)_3$** showed the highest red-shift (+3 nm) relative to its **16-** variant. These differences imply a significant rearrangement within the assemblies.

A_6 peptide amphiphiles revealed the lowest overall ellipticity signal for all five variants (**Figure 2.2E**). Thiolation of the C16 chain led to a significant reduction of the signal for **HS16-A_6**. Shortening the thiolated chain to **HS11-A_6** resulted in a CD spectrum that could not belong to a predominantly β-structured peptide amphiphile. A shoulder at 208 nm could either be explained by a blue-shift of the minimum position or a contribution from an α-helical structure.[41] Similar small shoulders were evident for the dimerized molecules **di-16-A_6** and **di-11-A_6**.

In summary, while some similarities and trends between peptide domains could be observed, especially for the **A_3V_3** and **$(AV)_3$** domains, it was clear that both the peptide and alkyl chain domains affected the peptide amphiphile self-assembly behavior.

Thiols are prone to oxidation, as after prolonged storage (>3 months, RT, both solid state and in solution) the formation of dimers was observed with LC-MS (**Figure S2.26**). Two reducing agents, tris(2-carboxyethyl)phosphine (TCEP) or dithiothreitol (DTT), were therefore tested for their ability to prevent oxidation. TCEP or DTT (2 eq.) was added to the solvent (water) prior to dissolution of a peptide amphiphile and the peptide amphiphile self-assembly was monitored with CD spectroscopy (**Figure 2.3**). Surprisingly, TCEP disturbed the self-assembly of both **16-V_3A_3** and **HS16-V_3A_3** amphiphiles. With respect to an aqueous or buffered solution, TCEP addition to **16-V_3A_3** resulted in a significant increase of molar ellipticity indicative of more intense polarized light scattering by the assemblies and hence a

different mode of self-assembly (**Figure 2.3A**).[18] However, TCEP addition to a **HS16-V_3A_3** solution prompted formation of significantly less ordered assemblies (**Figure 2.3B**). DTT seemed to have a milder effect on the thiolated peptide amphiphiles as CD spectra of **HS16-V_3A_3** prepared in the presence and absence of DTT were identical. However, that was not the case for all thiolated peptide amphiphiles. Therefore, it was decided not to use any reducing agents in the remainder of this study.

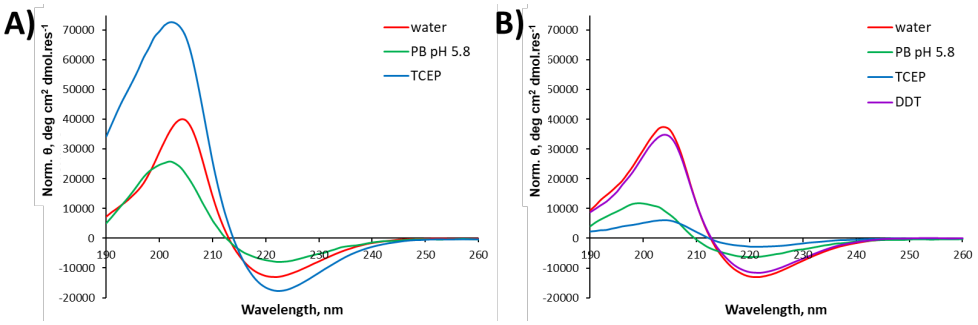

Figure 2.3. The effect of reducing agents on peptide amphiphile self-assembly monitored with CD spectroscopy: (A) **16-V_3A_3** prepared at a concentration of 100 μM with and without reducing agents; and (B) **HS16-V_3A_3** prepared at a concentration of 100 μM with and without reducing agents.

To obtain insight into the β-content within the assemblies, attenuated total reflection Fourier-transform infra-red spectroscopy (ATR-FTIR) spectra of lyophilized peptide amphiphiles were recorded (**Figure 2.4** and **Figure S2.27-S2.31**). The Amide I peak is typically centered between 1575-1725 cm^{-1} and represents a superposition of signals deriving from different conformations of the peptide backbone: 1627-1640 cm^{-1} is attributed to β-structures; 1647-1654 cm^{-1} to α-structures; and 1650-1670 cm^{-1} to random and other structures.[44, 45]

The Amide I peak overlaps with peaks corresponding to the C-terminal amide (around 1615 cm^{-1}) and the Lys side chain amine (1629 cm^{-1}). Therefore, the

Amide I peak was fitted to three peaks with maxima at 1615 cm^{-1}, 1630 cm^{-1}, and 1667 cm^{-1} (**Figure 2.4A**). These positions were present in all spectra, although small shifts occurred for some of the samples (**Figure S2.27-S2.31**). If a peak at 1654 cm^{-1}, indicative of α-structure, could be resolved, it was added to the fitting procedure. IR spectra of lysine-containing peptides are known to be sensitive to the pH of the solution they are lyophilized from, resulting in a peak shift and peak broadening.[46, 47] The two bands centered at 1615 cm^{-1} and 1630 cm^{-1} overlap in a way that does not allow for good-resolution fitting. Therefore, the joint contribution of β-structures and primary amines of lysine side chains was compared. This value was considered to reflect the content of β-structures in the samples, while the rest of the Amide I peak was attributed to other structures. The β-associated content for all 25 peptide amphiphiles is summarized in a heatmap (**Figure 2.4B**).

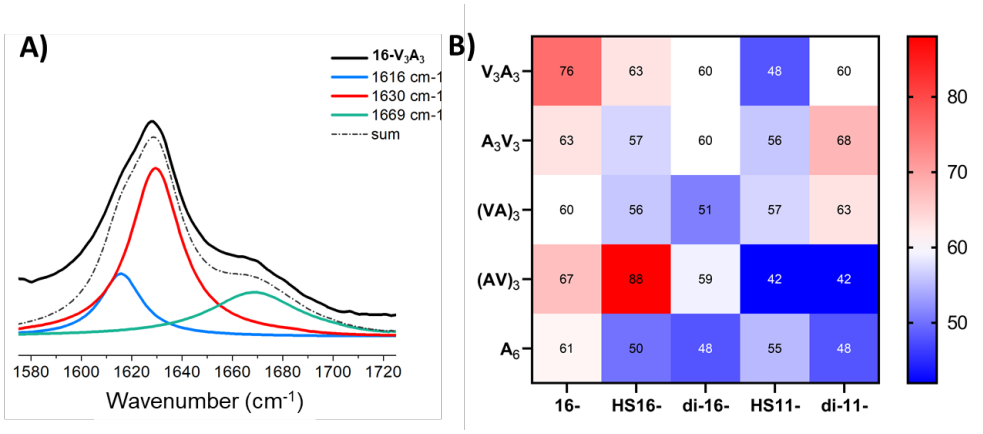

Figure 2.4. Characterization of self-assembly behavior by means of ATR-IR spectroscopy: (A) Amide I peak fitting for **16-V_3A_3** and (B) a heatmap illustrating the β-associated content derived from the Amide I peak fitting, blue shades represent low amounts of β-structure whereas red shades indicate a high percentage of β-structure. Near-white shades indicate an average level of β-structure for these systems.

Interestingly, it was only possible to resolve a peak at 1654 cm^{-1} for some of the thiolated peptide amphiphiles, and it was absent in all palmitoylated peptide amphiphiles (**Figure S2.27-S2.31**). Relatively low levels of self-assembly (β-associated content < 60% and high α-content – between 10 and 25%) were observed for the $\mathbf{A_6}$ amphiphiles, which is in good agreement with the CD data (**Figure 2.2E**, **Figure S2.31**). For the $\mathbf{V_3A_3}$ peptide domain (**Figure S2.27**) thiolation of the C16 alkyl chain had a negative effect: the β-content dropped from 76% to 63%. Dimerization of the latter molecule did not significantly change the structure of the peptide domain, consistent with the CD spectra. **HS11-$\mathbf{V_3A_3}$** showed 48% β-content, but its dimer **di-11-$\mathbf{V_3A_3}$** was comparable to more structured C16 peptide amphiphiles. The $\mathbf{A_3V_3}$ peptide domain showed a smaller change when the alkyl chain composition was altered: the β-associated content ranged between 56 and 68% (**Figure S2.27**) with **di-11-$\mathbf{A_3V_3}$** being the most β-structured. On the other hand, alternating sequences $\mathbf{(VA)_3}$ and $\mathbf{(AV)_3}$ showed more deviant behavior. In general, **16-$\mathbf{(VA)_3}$** showed the lowest β-associated content (60%) among all palmitoylated peptide amphiphiles (**Figure S2.29**). Although thiolation or shortening the alkyl chain to yield **HS16-** and **HS11-** variants did not significantly change the β-associated content, dimerization of these molecules showed an opposite effect. One particular feature was observed for the $\mathbf{(AV)_3}$ peptide domain: it was the only example where thiolation of the C16 chain gave rise to a more β-structured assembly (67 *versus* 88%, **Figure S2.30**). All other variants (**di-16-**, **HS11-**, **di-11-**) showed a β-associated content below 60%. **HS11-$\mathbf{(AV)_3}$** and **di-11-$\mathbf{(AV)_3}$** also contained α-structures. In some instances, results of the CD analysis would signify a certain value for the β-associated content, but these trends were not necessarily observed with FTIR analysis. For example, the CD spectra of **16-$\mathbf{(VA)_3}$** and **HS16-$\mathbf{(VA)_3}$** would suggest a higher level of self-assembly for the

latter, but according to the FTIR data, the β-associated content did not significantly differ between the two (**Figure 2.2C** and **Figure 2.4B**). In contrast, the **16-$(AV)_3$** and **HS16-$(AV)_3$** had similar CD spectra, however FTIR showed the latter was significantly more β-structured (**Figure 2.2D** and **Figure 2.4B**).

In summary, the combined CD and FT-IR study on the secondary structure of each peptide domain revealed that finding common self-assembly trends is not trivial. In general, thiolated peptide amphiphiles were less structured than their C16 counterparts. Dimerization and substitution of the C16 alkyl chain for C11 had different impacts depending on the peptide sequence. The discrepancies between the CD and IR spectra observed for some samples, could be attributed to the differences in preparation method, and also to the concentration of the samples, which has already been established to affect the amphiphile self-assembly (see **Figure 2.1**).

To obtain more insight on the effect of thiolation and dimerization of peptide amphiphiles on self-assembly in solution, transmission electron microscopy (TEM) imaging was performed.

2.3.3 Evaluation of peptide amphiphile fibers in TEM

For TEM analysis, samples were prepared in 10 mM PB (pH 5.8) and aged for 14 days, deposited on carbon TEM grids and negatively stained with 0.5% uranyl acetate (**Figure 2.5**). All peptide amphiphiles assembled into cylindrical fibers as was previously reported for palmitoyl (C16) peptide amphiphiles.[28] This indicated that thiolation did not disrupt self-assembly, or affect fiber morphology, thus maintaining the fiber core sequestered from the aqueous environment due to effective hydrophobic collapse. Since images were acquired relatively close to focus with a certain defocus needed, and

most of the samples were represented as fiber bundles, quantitative information based on the TEM images, such as true fiber thickness, could not be obtained. Nonetheless, all observed fibers had a diameter of ~9 nm, corresponding to the length of two peptide amphiphiles, irrespective of the peptide domain composition.[33]

Fibers composed of palmitoyl peptide amphiphiles were very long (typically >500 nm) and aligned into sheets (top panels in **Figure 2.5)**. Also, some sort of fracturing of these stacks appeared to be present in some images, *e.g.* see **16-(AV)$_3$**. Sample preparation could have caused these effects, since the samples were blotted and dried on the TEM grid, but it was not possible to determine the exact reason for fracturing.[48] It was obvious that thiol introduction reduced the average fiber length irrespective of peptide domain composition. Furthermore, all five dimeric (**di-16-**) peptide amphiphiles formed very short fibers (<200 nm). In contrast, no general trend was observed for **HS11-** peptide amphiphiles: **HS11-V$_3$A$_3$**, **HS11-A$_3$V$_3$**, or **HS11-(VA)$_3$** showed a similar length distribution as their **HS16-** counterparts, while intense bundling was observed for **HS11-(AV)$_3$** or no fiber interaction at all (**HS11-A$_6$**). No clear tendency was observed that would unify the effect of thiolation on fiber formation. Dimerization of C11 peptide amphiphiles changed the appearance of the fibers (except for **di-11-V$_3$A$_3$**): it either made the assemblies more defined and long, similar to their **16-** counterparts (**di-11-A$_6$**); reduced the interaction between individual fibers (**di-11-(VA)$_3$**); or on the contrary, induced more fiber bundling (**di-11-A$_3$V$_3$** and **di-11-(AV)$_3$**). Due to the variety of formed assemblies, it appeared that the self-assembly of C11 peptide amphiphiles was more sensitive towards the peptide sequence as compared to their C16 variants. Most of the **HS11-** peptide amphiphiles showed less β-associated content and/or significant contributions of α- and other structures. Moreover, dimers of thiolated peptide amphiphiles like **di-**

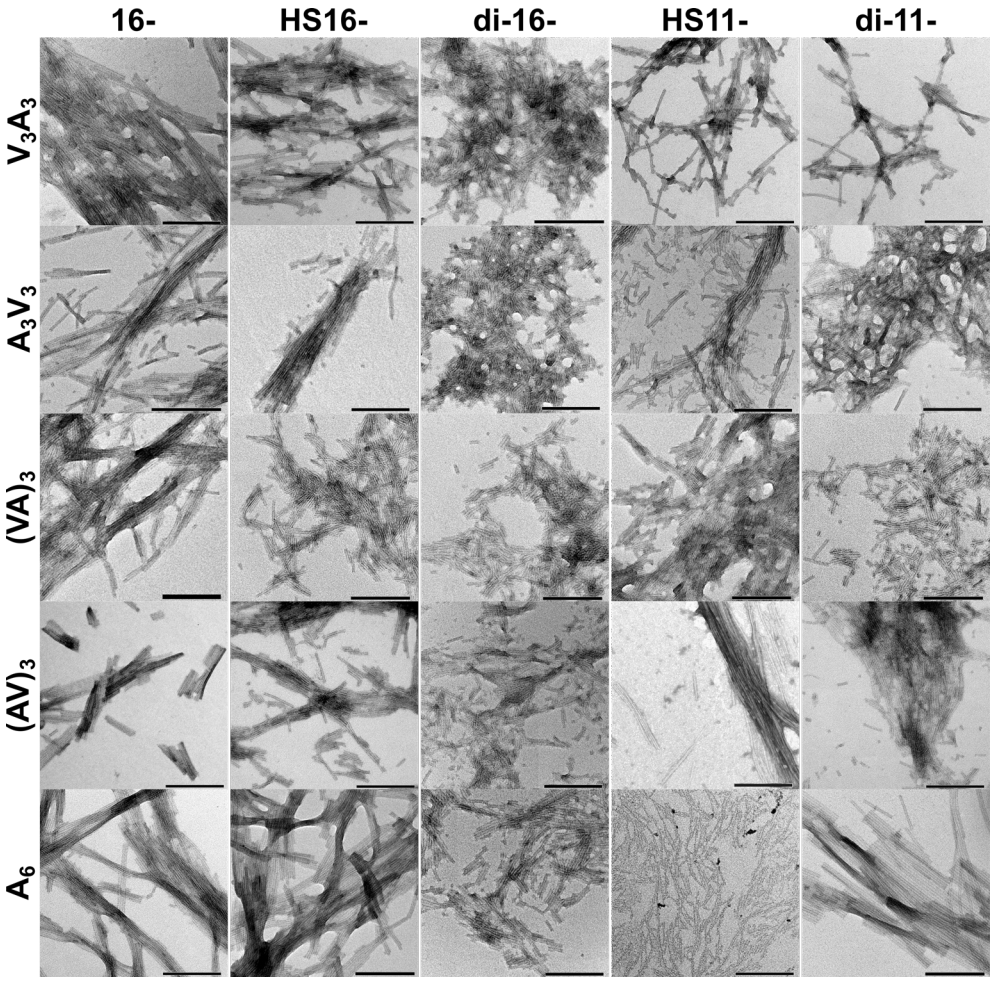

Figure 2.5. Representative TEM images of peptide amphiphiles (uranyl acetate stained). Columns show evolution of the same peptide domain conjugated to different alkyl chains, while rows show evolution of the same alkyl chain conjugated to different peptide portions. Samples were prepared in 10 mM PB (pH 5.8) at peptide amphiphile concentrations of: 50 μM for **16-** and **HS16-** samples; 25 μM for **di-16-**; 250 μM for **HS11-**; and 125 μM for **di-11-**. Scale bar is 200 nm.

16-A_3V_3 and **di-11-A_3V_3** formed almost 3D-like morphologies with pore-like patterns formed by fiber bundling. Notably, dimers showed better length distributions and intensive bundling. A clear difference between **V_3A_3**, or **$(VA)_3$**, and **A_3V_3**, **$(AV)_3$**, or **A_6** was observed: the latter amphiphiles tended to

form rope-like fiber bundles, stacks covering vast areas, while the former amphiphiles yielded smaller-scale structures. Thiolated variants of **A_6** peptide amphiphiles distinctly differed from the rest of the samples, which was attributed to the low β-content and high α-content (**Figure 2.4B**).

In summary, TEM imaging revealed large differences in fiber appearance between palmitoyl and thiolated peptide amphiphiles. Additionally, the difference between fibers formed by highly β-structured molecules (such as all **16-** samples) and molecules with high α-content (for example, **HS11-A_6** – 25% α-structures) was observed. Peptide amphiphiles coupled to the **V_3A_3** peptide headgroup were arguably the only tested group that exhibited relatively similar fiber appearance for all five alkyl chain variants.

2.3.4 Analysis of fiber formation

Through the combined use of CD, FTIR, and TEM, the secondary structure and self-assembly properties of 25 different peptide amphiphiles was assessed. The data obtained supports the hypothesis that the geometry of the molecule, in addition to its composition, defines its self-assembly behavior.

A more in-depth CD analysis can unravel how peptide amphiphile molecules are orientated within the fibers.[18] The minimum position characterizes the internal orientation of peptide chains. If peptide backbones form flat stacks that propagate along the fiber axis (**Scheme 2.3**, upper panel), the peptide amphiphile will have a CD minimum at ~216 nm.[18] But if the aligned peptide backbones propagate in twisted spirals (**Scheme 2.3**, lower panel), then the minimum will be red-shifted proportional to the amount of twisting. It was shown that the internal twisting was affected by the number of valine and alanine residues, as well as their position in the peptide segment. In

comparison to palmitoyl-$V_4A_2E_3$, palmitoyl-$A_3V_3E_3$ showed more intense internal twisting within the fibers associated with concomitant changes in hydrogen bond alignment and assemblies stability.[18, 28] It was therefore anticipated that by varying the alkyl chain composition, the propensities to form intermolecular hydrogen bonds, and hence β-structures, could be affected too.

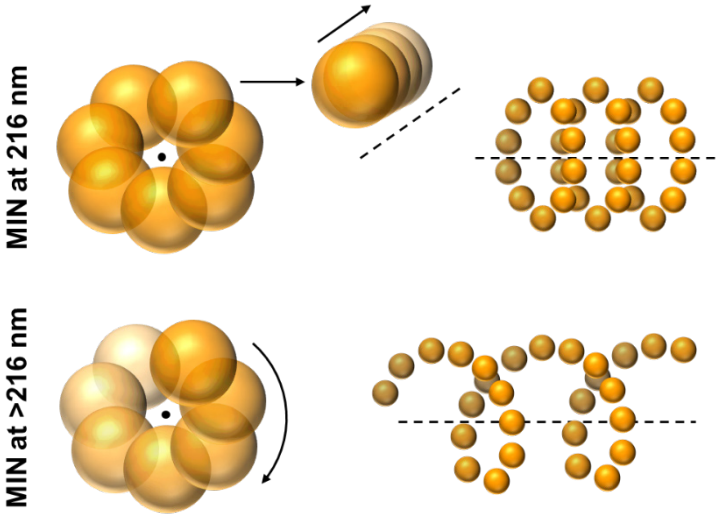

Scheme 2.3. CD minimum position defines the propagation mode of molecules within a supramolecular fiber. Spheres represent individual peptide amphiphiles. Peptide amphiphile backbones are perpendicular to the fiber propagation axis (dashed line). When molecules propagate as flat stacks along the fiber axis, then the ellipticity minimum is typically located at 216 nm. When molecules propagate along the fiber axis with a twist, a red-shift of the ellipticity minimum is observed.[18]

To investigate the internal organization of the fibers, the ellipticity minima (θ_{min}) were compared (**Figure 2.6B**, top graph). The average value for the minimum position amongst the 25 studied peptide amphiphiles was at 221 nm. The intensity of the peak centered around 221 nm is dependent on the order within the assemblies (**Figure 2.6B**, bottom graph). Peptide amphiphile assemblies scatter circularly polarized light.[18] For example, intense fiber bundling causes more light scattering, and hence, an increase

in the θ_{min} intensity. However, since the CD signal is a superposition of different secondary structures, contributions of which can also affect the θ_{min} intensity in the predominantly β-structured assemblies. Thus, the θ intensity at 221 nm (θ_{221}) is a measure of β-structures contribution. Furthermore, assemblies with more internal twisting would have larger hydrogen-bonding distances, which potentially introduce packing defects such as the presence of unordered structures and cause the θ_{min} intensity to change.

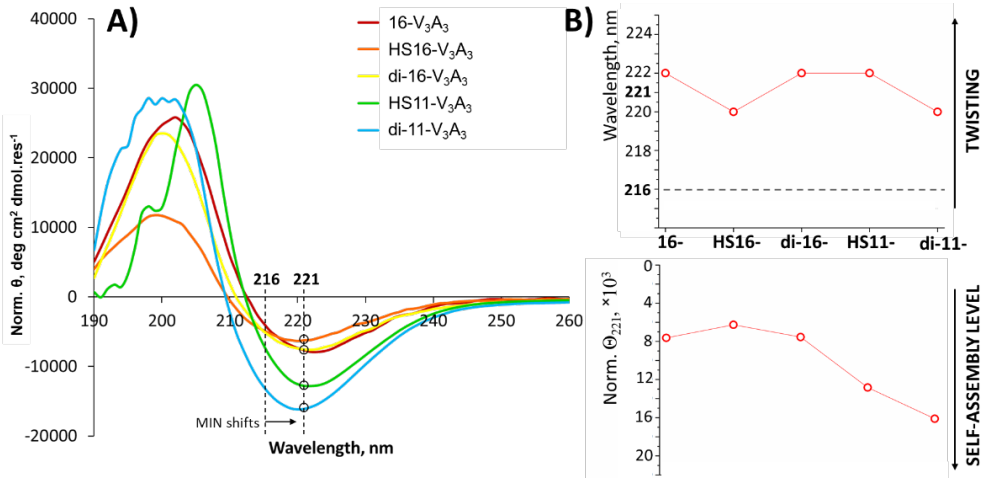

Figure 2.6. Characterization of self-assembly behavior using CD spectroscopy: (A) CD spectra for all **V_3A_3** peptide amphiphiles; (B) minimum positions (top panel) and normalized ellipticity minimum (bottom panel). Samples were prepared in 10 mM PB (pH 5.8).

The same approach was applied to the other peptide amphiphiles (**Figure 2.7**). With respect to their C16 variants, the θ_{min} did not significantly shift for thiolated peptide amphiphiles with a **A_3V_3** and **$(VA)_3$** domain. **$(AV)_3$** and **A_6** peptide amphiphiles showed ±1-3 nm θ_{min} shifts indicative of notable hydrogen bond rearrangement within the fibers. In terms of θ_{min} position and internal twisting, with respect to the average, only **HS11-$(AV)_3$** showed more

internal twisting, while **HS16-A_3V_3** and **HS11-A_6** showed less, but the β-content decreased for all three peptide amphiphiles. Interestingly, more intense internal twisting was associated with a stronger impact on the β-content than less internal twisting: - 25% for **HS11-$(AV)_3$** *versus* -13% for **HS16-A_3V_3** and **HS11-A_6**. As **HS11-$(AV)_3$** showed a significant increase in α-content, it seems as if more internal twisting weakened intramolecular hydrogen bonding, but allowed for more effective intermolecular hydrogen bonding. Interestingly, a common trend was observed for **16-** variants compared to **HS16-** variants for all peptide domains except **$(AV)_3$**: the θ_{min} position was less shifted from 216 nm, hence, less internal twisting was expected, but the β-associated content decreased. Notably, **HS16-** fibers were shorter than their **16-** analogues (**Figure 2.5**). **HS16-$(VA)_3$** showed the most intense CD spectrum when compared to **16-$(VA)_3$**, suggestive of a more-ordered structure.

Dimerization of **HS16-** peptide amphiphiles did not significantly affect the β-associated content (from -5 to +3%), except for the **$(AV)_3$** domain (**Figure 2.4**). Importantly, the β-associated content for all **di-16-** peptide amphiphiles was within the 48-60% range. Also, the least β-structured **A_6** domain was not dramatically affected by dimerization. Unlike the **HS16-** peptide amphiphiles, all **di-16-** fibers showed similar fiber bundling (**Figure 2.5**).

Furthermore, **HS11-** peptide amphiphiles were compared to their **16-** counterparts. All **HS11-** peptide amphiphiles were less β-structured and assembled into shorter fibers (**Figure 2.5** and **Figure 2.7**). When compared to the **HS16-** analogues, **HS11-** demonstrates moderate β-associated content values: 42-57% *versus* 50-88%. Also, broadening of the FT-IR

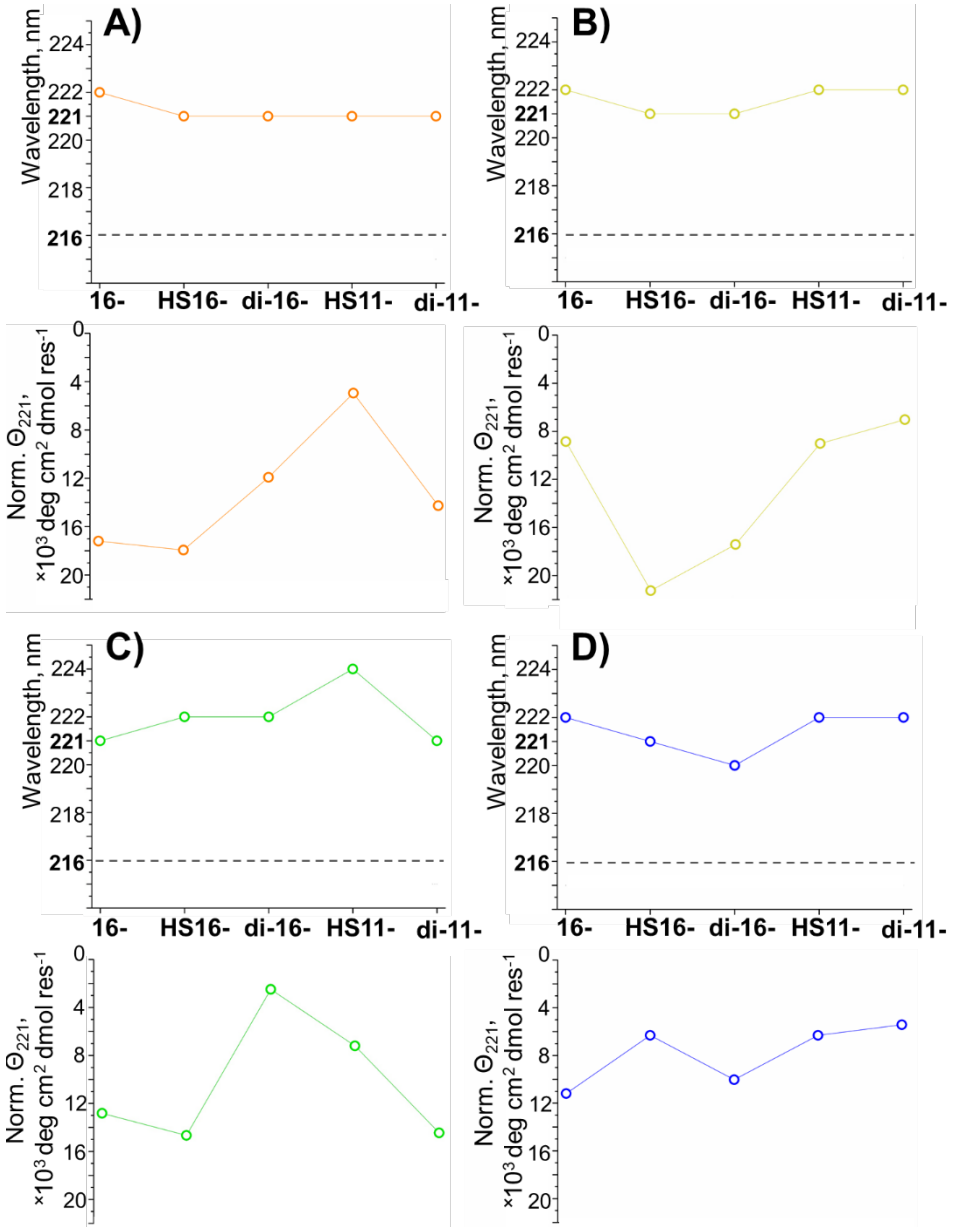

Figure 2.7. Characterization of self-assembly behavior using CD spectroscopy for different peptide amphiphiles: (A) **A_3V_3**; (B) **$(VA)_3$**; (C) **$(AV)_3$**; and (D) **A_6**. Samples were prepared in 10 mM PB (pH 5.8).

absorption band centered around 1630 cm^{-1} typical for **HS11-** peptide amphiphiles indicated an increased contribution of α-structures in comparison to the C16 variants (especially, $\mathbf{V_3A_3}$ and $\mathbf{(AV)_3}$). However, it was not possible to link a change in the θ_{min} position with a one-directional change in the level of self-assembly when **HS16-** analogues were compared to their **HS11-** variants.

The dimers **di-11-$\mathbf{A_3V_3}$** and **di-11-$\mathbf{(VA)_3}$** have the same degree of internal twisting as their monomeric counterparts, but a higher level of self-assembly and β-associated content, as well as θ_{min} intensity. Also, fiber formation in the case of **di11-$\mathbf{V_3A_3}$** and **di11-$\mathbf{A_3V_3}$** was similar to their monomeric species. This was not the case for **di11-$\mathbf{(VA)_3}$**, **di11-$\mathbf{(AV)_3}$**, and **di11-$_6$**. **Di-11-$\mathbf{A_6}$**: while the mutual orientation of peptide amphiphiles within the fibers did not change with respect to **HS11-$\mathbf{A_6}$**, the β-associated content decreased due to an increase in contributions coming from other secondary structures (1672 cm^{-1}). Interestingly, fibers formed by **di-11-$\mathbf{A_6}$** appeared to be more defined and formed one-layer stacks, while **HS11-$\mathbf{A_6}$** fibers showed a deviant thickness and no integration into a network (**Figure 2.5**), probably due to the presence of α-helices (**Figure S2.31**). This behavior was also observed for **HS11-$\mathbf{(AV)_3}$** versus **di11-$\mathbf{(AV)_3}$.** Interestingly, peptide amphiphiles with $\mathbf{V_3A_3}$ and $\mathbf{(VA)_3}$ domains showed less variations in terms of their β-associated content than $\mathbf{A_6}$-, $\mathbf{A_3V_3}$-, and $\mathbf{(AV)_3}$-based peptide amphiphiles. This suggests that the first Val residue next to the hydrophobic core, is important in terms of hydrogen bond alignment. No clear common trends for $\mathbf{V_3A_3}$ and $\mathbf{(VA)_3}$ or $\mathbf{A_6}$, $\mathbf{A_3V_3}$, and $\mathbf{(AV)_3}$ could be established however. Nevertheless, it shows that the molecule geometry plays an important role: block sequences $\mathbf{V_3A_3}$ and $\mathbf{A_3V_3}$ were more structured and less responsive to alterations in the alkyl chain composition, as compared to alternating sequences $\mathbf{(VA)_3}$ or $\mathbf{(AV)_3}$. No hydrogen bond rearrangements occurred upon changing the alkyl chain

length for the **A_3V_3** peptide amphiphiles (**Figure 2.2B,D**). Hydrogen bond alignment within **$(AV)_3$** peptide amphiphile assemblies was the most susceptible to every change in the alkyl chain. As expected, **A_6**-based amphiphiles possessed the lowest β-structure propensity among all peptide amphiphiles tested regardless of the alkyl chain properties (**Figure 2.7D**). Finally, the presence of an α-helical component was observed for all **HS11-** variants (**Figure S2.27-S2.31**).

Presumably, due to the higher hydrophobicity of Val compared to Ala and a small increase in steric bulk of the side chain, a tighter packing with less monomer freedom is possible within the supramolecular fiber. From the obtained data it is clear that the first amino acid residues (two or potentially even three) next to the alkyl chain are crucial for the resulting assembly's rigidity, which is in line with literature.[18]

Within this study it was not possible to distinguish a single parameter that would define the "best" self-assembly behavior: the θ_{min} position, determination of internal twisting within the fibers and hydrogen bond alignment, did not always directly follow the change in the β-associated content. Self-assembly is a complex process and one change in chemical composition of the monomer can induce simultaneous changes of several parameters as has been shown in this study. From the obtained data, the **V_3A_3** peptide domain appears to be the most suited for functionalization of metal surfaces. This peptide domain is robust in terms of preserving the β-content upon modifications of the alkyl chain. These findings open up the possibility of using thiolated peptide amphiphiles to form a highly ordered self-assembled monolayer (SAM) on the curved surface of gold nanoparticles.

2.4 Conclusions

The self-assembly of peptide amphiphiles is dependent on both the peptide domain and the alkyl chain used. From the structural analysis based on CD and FT-IR spectroscopy data, peptide amphiphiles could be divided into two groups based on the mode of self-assembly: peptide-driven or driven by alkyl chain characteristics. This study shows that a peptide sequence with amino acid residues arranged in blocks of three is beneficial, as the block $\mathbf{V_3A_3}$ and $\mathbf{A_3V_3}$ sequences were less responsive to changes in alkyl chain length and composition. They consistently demonstrated more-ordered self-assemblies and possessed the ability to adopt a β-strand conformation when coupled to different alkyl chains, while alternating sequences $\mathbf{(VA)_3}$ and $\mathbf{(AV)_3}$ rearranged the hydrogen bond alignment in response to every change in the alkyl chain composition. In contrast, peptide amphiphiles with alternating peptide domains ($\mathbf{(VA)_3}$ and $\mathbf{(AV)_3}$) were more sensitive to changes to the alkyl chain composition. These sequences showed dramatically different self-assembly behavior for palmitoyl and thiolated variants, as well as for monomeric and dimeric species.

Ultimately, this study provides design rules and synthetic procedures for thiolated peptide amphiphiles with a high level of self-assembly and high β-content. Depending on the composition, thiolated peptide amphiphiles can be as structured as conventional palmitoyl peptide amphiphiles, and they offer new approaches in surface modification and systems where redox reactions are of value. In the system where rigid assemblies on a surface are required, as for example, surface stabilization of GNPs, thiolated peptide amphiphiles can be used. From this perspective, the $\mathbf{V_3A_3}$ peptide domain was chosen for the further work on coating gold nanoparticles of different shape and size. **Chapters 3** and **4** of this thesis demonstrate performance of $\mathbf{V_3A_3}$-based peptide amphiphiles on the surface of gold nanoparticles of different size and shape.

2.5 Experimental section

2.5.1 Materials

All chemicals were purchased from Sigma-Aldrich except where stated otherwise. TFA, piperidine, DMF, DCM, methanol, and acetonitrile were purchased from Biosolve. Oxyma pure was supplied by Carl Roth GmbH. Formvar Carbon/Copper (200 mesh) TEM grids were purchased from Electron Microscopy Sciences.

2.5.2 Peptide amphiphile synthesis

All peptide amphiphile sequences were synthesized by solid-phase peptide synthesis using standard Fmoc-chemistry protocols (9-fluorenylmethyloxycarbonyl-protected amino acids were used to propagate the peptide chain). The synthesis was performed on an automated microwave peptide synthesizer Liberty Blue (CEM) using standard settings. 5 equivalents (relative to the resin loading) of Fmoc-protected amino acids were used to propagate the peptide chain. 20% piperidine in DMF was used as the deprotection agent (90 °C, 60 secs) and DIC/Oxyma were employed as activator/activator base (5 equivalents relative to the resin loading, 95 °C, 4 mins). All sequences were synthesized on a high-loading Rink Amide resin, which yields a C-terminal amide. The alkyl chains were introduced *via* an on-resin coupling of the corresponding chain to the terminal amine of the corresponding peptide (the same protocol as for amino acid coupling). The list of peptides and alkyl chains is shown in **Scheme 2.2.** All the molecules were cleaved from the resin using a trifluoroacetic acid (TFA) cocktail with 1.5% deionized water, 2.5% triisopropylsilane (TIS), and 2.5% 3,4-

ethylenedioxythiophene (EDOT) for thiolated peptide amphiphiles only (2 hours, RT). The crude amphiphiles were precipitated into cold diethyl ether, pelleted by centrifugation, redissolved in water, and lyophilized prior to purification.

2.5.3 Peptide amphiphile purification

HPLC purification was performed on a Shimadzu system equipped with two LC-20AR pumps, an SPD-20A UV-Vis detector and a Phenomenex Kinetex EVO C18 column. The mobile phases were water and acetonitrile, containing 0.1% TFA. The purity of the compounds was assessed using LC-MS (**Figures S2.1-S2.15**). All purified molecules were lyophilized and stored at -20 °C until required. VariPure IPE (PL3540-D603VP, 100 mg, Agilent) columns were used to capture and remove TFA traces from the sample after purification and drying if needed.

2.5.4 Peptide amphiphile dimerization

Dimerization was conducted *via* oxidation of terminal thiols with iodine to form a disulfide bridge. A peptide amphiphile was dissolved in 80% methanol at a concentration of 2 mg/mL and 0.5 M iodine solution was added dropwise to the stirred solution. The addition of iodine was stopped as soon as the color became persistently yellow. Stirring was continued for another 15 min and excess iodine was quenched with 1 M ascorbic acid. Methanol was evaporated and the presence of the dimers was confirmed with LC-MS. Dimerized amphiphiles were purified and lyophilized in the same way as described above. The purity of the compounds was assessed using LC-MS (**Figures S2.16-S2.25**).

2.5.5 Circular dichroism measurements

Circular dichroism (CD) spectra of the amphiphiles were recorded using a JASCO J-815 spectropolarimeter, fitted with a Peltier temperature controller. All measurements were performed at 20 °C. Lyophilized powders of peptide amphiphiles were dissolved in 10 mM PB (pH 5.8) at the following concentrations: 50 μM for peptide amphiphiles terminated with **16-** and **HS16-** alkyl chains; 25 μM for peptide amphiphiles terminated with **di16-** chains; 250 μM for peptide amphiphiles terminated with **HS11-** alkyl chains; and 125 μM for peptide amphiphiles terminated with **di11-** alkyl chains. Samples were left in the dark in sealed vials for 14 days to age. Samples were measured in quartz cuvettes with a 12 mm path length, and spectra were recorded from 260 to 190 nm at 1 nm intervals with a 1 nm bandwidth. All spectra were converted to mean residue ellipticity (deg cm^2 $dmol\ res^{-1}$) using equation 1:

$$[\theta] = \frac{100 * [\theta]obs}{c * n * l} \quad (1)$$

where $[\theta]_{obs}$ is the observed ellipticity in mdeg, c is the concentration of the sample in mM, n is the number of amino acids in the peptide or amphiphile and l is the path length of the cuvette in cm.

2.5.6 Infra-red spectroscopy measurements

Attenuated total reflection-infrared (ATR-IR) spectra were recorded on an Excalibur FTS 4000 setup equipped with a “golden gate”. A lyophilized powder of a peptide amphiphile was placed on top of the crystal and a spectrum was recorded (512 scans at 2 cm^{-1} aperture). Deconvolution and

fitting of the Amide I peaks to the Lorenz function were performed using Origin Pro.

2.5.7 Transmission electron microscopy

For transmission electron microscopy (TEM) measurements, a 10 µL droplet of the sample was placed on a continuous carbon grid on a copper support (200 mesh) and left for 20 secs. The excess liquid was removed by manually blotting with filter paper. The grid was washed with deionized water once and blotted again. Uranyl acetate staining (0.5% w/v) was applied, followed immediately by blotting. Images were collected on a JEM1400 Plus (JEOL) transmission electron microscope operated at 80 kV and equipped with a CCD camera.

2.6 References

1. Goodman, C. M.; McCusker, C. D.; Yilmaz, T.; Rotello, V. M., Toxicity of gold nanoparticles functionalized with cationic and anionic side chains. *Bioconjugate Chem* **2004,** *15* (4), 897-900.

2. Bhamidipati, M.; Fabris, L., Multiparametric Assessment of Gold Nanoparticle Cytotoxicity in Cancerous and Healthy Cells: The Role of Size, Shape, and Surface Chemistry. *Bioconjugate Chem* **2017,** *28* (2), 449-460.

3. Bogliotti, N.; Oberleitner, B.; Di-Cicco, A.; Schmidt, F.; Florent, J. C.; Semetey, V., Optimizing the formation of biocompatible gold nanorods for cancer research: Functionalization, stabilization and purification. *J Colloid Interf Sci* **2011,** *357* (1), 75-81.

4. Schulz, F.; Friedrich, W.; Hoppe, K.; Vossmeyer, T.; Weller, H.; Lange, H., Effective PEGylation of gold nanorods. *Nanoscale* **2016,** *8* (13), 7296-7308.

5. Fytianos, K.; Rodriguez-Lorenzo, L.; Clift, M. J. D.; Blank, F.; Vanhecke, D.; von Garnier, C.; Petri-Fink, A.; Rothen-Rutishauser, B., Uptake efficiency of surface modified gold nanoparticles does not correlate with functional changes and cytokine secretion in human dendritic cells in vitro. *Nanomed-Nanotechnol* **2015,** *11* (3), 633-644.

6. Liu, S. H.; Han, M. Y., Silica-Coated Metal Nanoparticles. *Chem-Asian J* **2010,** *5* (1), 36-45.

7. Hanske, C.; Sanz-Ortiz, M. N.; Liz-Marzan, L. M., Silica-Coated Plasmonic Metal Nanoparticles in Action. *Adv Mater* **2018,** *30* (27): e1707003.

8. Knowles, B. R.; Yang, D.; Wagner, P.; Maclaughlin, S.; Higgins, M. J.; Molino, P. J., Zwitterion Functionalized Silica Nanoparticle Coatings: The Effect of Particle Size on Protein, Bacteria, and Fungal Spore Adhesion. *Langmuir* **2019,** *35* (5), 1335-1345.

9. Sakellari, G. I.; Hondow, N.; Gardiner, P. H. E., Factors influencing the surface functionalization of citrate stabilizaed gold nanoparticles with cysteamine, 3-mercaptopropionic acid or L-selenocysteine for sensor applications. *Chemosensors* **2020,** *8* (3): e80.

10. Gupta, A.; Moyano, D. F.; Parnsubsakul, A.; Papadopoulos, A.; Wang, L. S.; Landis, R. F.; Das, R.; Rotello, V. M., Ultrastable and Biofunctionalizable Gold Nanoparticles. *Acs Appl Mater Inter* **2016,** *8* (22), 14096-14101.

11. Levy, R.; Thanh, N. T. K.; Doty, R. C.; Hussain, I.; Nichols, R. J.; Schiffrin, D. J.; Brust, M.; Fernig, D. G., Rational and combinatorial design of peptide capping Ligands for gold nanoparticles. *J Am Chem Soc* **2004,** *126* (32), 10076-10084.

12. Mei, B. C.; Oh, E.; Susumu, K.; Farrell, D.; Mountziaris, T. J.; Mattoussi, H., Effects of Ligand Coordination Number and Surface Curvature on the Stability of Gold Nanoparticles in Aqueous Solutions. *Langmuir* **2009,** *25* (18), 10604-10611.

13. Shaw, C. P.; Middleton, D. A.; Volk, M.; Levy, R., Amyloid-derived peptide forms self-assembled monolayers on gold nanoparticle with a curvature-dependent beta-sheet structure. *ACS Nano* **2012,** *6* (2), 1416-26.

14. Colangelo, E.; Chen, Q.; Davidson, A. M.; Paramelle, D.; Sullivan, M. B.; Volk, M.; Levy, R., Computational and Experimental Investigation of the Structure of Peptide Monolayers on Gold Nanoparticles. *Langmuir* **2017,** *33* (1), 438-449.

15. Hendricks, M. P.; Sato, K.; Palmer, L. C.; Stupp, S. I., Supramolecular Assembly of Peptide Amphiphiles. *Acc Chem Res* **2017,** *50* (10), 2440-2448.

16. Dreher, M. R.; Simnick, A. J.; Fischer, K.; Smith, R. J.; Patel, A.; Schmidt, M.; Chilkoti, A., Temperature triggered self-assembly of polypeptides into multivalent spherical micelles. *J Am Chem Soc* **2008,** *130* (2), 687-694.

17. Boyle, A. L.; Rabe, M.; Crone, N. S. A.; Rhys, G. G.; Soler, N.; Voskamp, P.; Pannu, N. S.; Kros, A., Selective coordination of three transition metal ions within a coiled-coil peptide scaffold. *Chem Sci* **2019,** *10* (31), 7456-7465.

18. Pashuck, E. T.; Cui, H.; Stupp, S. I., Tuning supramolecular rigidity of peptide fibers through molecular structure. *J Am Chem Soc* **2010,** *132* (17), 6041-6046.

19. Hamley, I. W.; Kirkham, S.; Dehsorkhi, A.; Castelletto, V.; Reza, M.; Ruokolainen, J., Toll-like receptor agonist lipopeptides self-assemble into distinct nanostructures. *Chem Commun (Camb)* **2014,** *50* (100), 15948-15951.

20. Behanna, H. A.; Donners, J. J. J. M.; Gordon, A. C.; Stupp, S. I., Coassembly of amphiphiles with opposite peptide polarities into nanofibers. *J Am Chem Soc* **2005,** *127* (4), 1193-1200.

21. Paramonov, S. E.; Jun, H. W.; Hartgerink, J. D., Self-assembly of peptide-amphiphile nanofibers: the roles of hydrogen bonding and amphiphilic packing. *J Am Chem Soc* **2006,** *128* (22), 7291-7298.

22. Malkar, N. B.; Lauer-Fields, J. L.; Juska, D.; Fields, G. B., Characterization of peptide-amphiphiles possessing cellular activation sequences. *Biomacromolecules* **2003,** *4* (3), 518-528.

23. Hamley, I. W., Self-assembly of amphiphilic peptides. *Soft Matter* **2011,** *7* (9), 4122-4138.

24. Booth, R.; Insua, I.; Bhak, G.; Montenegro, J., Self-assembled micro-fibres by oxime connection of linear peptide amphiphiles. *Org Biomol Chem* **2019,** *17* (7), 1984-1991.

25. Elgersma, R. C.; Meijneke, T.; de Jong, R.; Brouwer, A. J.; Posthuma, G.; Rijkers, D. T.; Liskamp, R. M., Synthesis and structural investigations of N-alkylated beta-peptidosulfonamide-peptide hybrids of the amyloidogenic amylin(20-29) sequence: Implications of supramolecular folding for the design of peptide-based bionanomaterials. *Org Biomol Chem* **2006,** *4* (19), 3587-3597.

26. Dasgupta, A.; Das, D., Designer Peptide Amphiphiles: Self-Assembly to Applications. *Langmuir* **2019,** *35* (33), 10704-10724.

27. da Silva, R. M. P.; van der Zwaag, D.; Albertazzi, L.; Lee, S. S.; Meijer, E. W.; Stupp, S. I., Super-resolution microscopy reveals structural diversity in molecular exchange among peptide amphiphile nanofibres. *Nat Commun* **2016,** *7*: e11561.

28. Newcomb, C. J.; Sur, S.; Ortony, J. H.; Lee, O. S.; Matson, J. B.; Boekhoven, J.; Yu, J. M.; Schatz, G. C.; Stupp, S. I., Cell death versus cell survival instructed by supramolecular cohesion of nanostructuresl. *Nat Commun* **2014,** *5*: e3321.

29. Newcomb, C. J.; Bitton, R.; Velichko, Y. S.; Snead, M. L.; Stupp, S. I., The Role of Nanoscale Architecture in Supramolecular Templating of Biomimetic Hydroxyapatite Mineralization. *Small* **2012,** *8* (14), 2195-2202.

30. Cote, Y.; Fu, I. W.; Dobson, E. T.; Goldberger, J. E.; Nguyen, H. D.; Shen, J. K., Mechanism of the pH-Controlled Self-Assembly of Nanofibers from Peptide Amphiphiles. *J Phys Chem C Nanomater Interfaces* **2014,** *118* (29), 16272-16278.

31. Cui, H.; Muraoka, T.; Cheetham, A. G.; Stupp, S. I., Self-assembly of giant peptide nanobelts. *Nano Lett* **2009,** *9* (3), 945-51.

32. Cui, H. G.; Cheetham, A. G.; Pashuck, E. T.; Stupp, S. I., Amino Acid Sequence in Constitutionally Isomeric Tetrapeptide Amphiphiles Dictates Architecture of One-Dimensional Nanostructures. *J Am Chem Soc* **2014,** *136* (35), 12461-12468.

33. Tantakitti, F.; Boekhoven, J.; Wang, X.; Kazantsev, R. V.; Yu, T.; Li, J. H.; Zhuang, E.; Zandi, R.; Ortony, J. H.; Newcomb, C. J.; Palmer, L. C.; Shekhawat, G. S.; de la Cruz, M. O.; Schatz, G. C.; Stupp, S. I., Energy landscapes and functions of supramolecular systems. *Nat Mater* **2016,** *15* (4), 469-476.

34. Greenfield, M. A.; Hoffman, J. R.; de la Cruz, M. O.; Stupp, S. I., Tunable Mechanics of Peptide Nanofiber Gels. *Langmuir* **2010,** *26* (5), 3641-3647.

35. Preslar, A. T.; Lilley, L. M.; Sato, K.; Zhang, S. R.; Chia, Z. K.; Stupp, S. I.; Meade, T. J., Calcium-Induced Morphological Transitions in Peptide Amphiphiles Detected by F-19-Magnetic Resonance Imaging. *ACS Appl Mater Inter* **2017,** *9* (46), 39890-39894.

36. Edwards-Gayle, C. J. C.; Hamley, I. W., Self-assembly of bioactive peptides, peptide conjugates, and peptide mimetic materials. *Org Biomol Chem* **2017,** *15* (28), 5867-5876.

37. Tayi, A. S.; Pashuck, E. T.; Newcomb, C. J.; McClendon, M. T.; Stupp, S. I., Electrospinning Bioactive Supramolecular Polymers from Water. *Biomacromolecules* **2014,** *15* (4), 1323-1327.

38. Moyer, T. J.; Finbloom, J. A.; Chen, F.; Toft, D. J.; Cryns, V. L.; Stupp, S. I., pH and Amphiphilic Structure Direct Supramolecular Behavior in Biofunctional Assemblies. *J Am Chem Soc* **2014,** *136* (42), 14746-14752.

39. Xu, X. D.; Jin, Y.; Liu, Y.; Zhang, X. Z.; Zhuo, R. X., Self-assembly behavior of peptide amphiphiles (PAs) with different length of hydrophobic alkyl tails. *Colloid Surface B* **2010,** *81* (1), 329-335.

40. Kelly, S. M.; Price, N. C., The application of circular dichroism to studies of protein folding and unfolding. *Biochim Biophys Acta* **1997,** *1338* (2), 161-185.

41. Greenfield, N. J., Using circular dichroism spectra to estimate protein secondary structure. *Nat Protoc* **2006,** *1* (6), 2876-2890.

42. Berova N., N. K., Woody R., *Circular Dichroism: Principles and Applications*. Wiley-VCH: New York, 2000.

43. Ferreira, D. S.; Marques, A. P.; Reis, R. L.; Azevedo, H. S., Hyaluronan and self-assembling peptides as building blocks to reconstruct the extracellular environment in skin tissue. *Biomater Sci-Uk* **2013,** *1* (9), 952-964.

44. Chirgadze, Y. N.; Nevskaya, N. A., Infrared-Spectra and Resonance Interaction of Amide-One Vibration of Parallel-Chain Pleated Sheet. *Biopolymers* **1976,** *15* (4), 627-636.

45. Susi, H.; Byler, D. M., Resolution-Enhanced Fourier-Transform Infrared-Spectroscopy of Enzymes. *Method Enzymol* **1986,** *130*, 290-311.

46. Venyaminov, S. Y.; Kalnin, N. N., Quantitative Ir Spectrophotometry of Peptide Compounds in Water (H2o) Solutions .1. Spectral Parameters of Amino-Acid Residue Absorption-Bands. *Biopolymers* **1990,** *30* (13-14), 1243-1257.

47. Rozenberg, M.; Shoham, G., FTIR spectra of solid poly-l-lysine in the stretching NH mode range. *Biophys Chem* **2007,** *125* (1), 166-171.

48. Newcomb, C. J.; Moyer, T. J.; Lee, S. S.; Stupp, S. I., Advances in cryogenic transmission electron microscopy for the characterization of dynamic self-assembling nanostructures. *Curr Opin Colloid In* **2012,** *17* (6), 350-359.

2.7 Supporting Information

Purity and identity of all 25 molecules used in this study was determined using LC-MS:

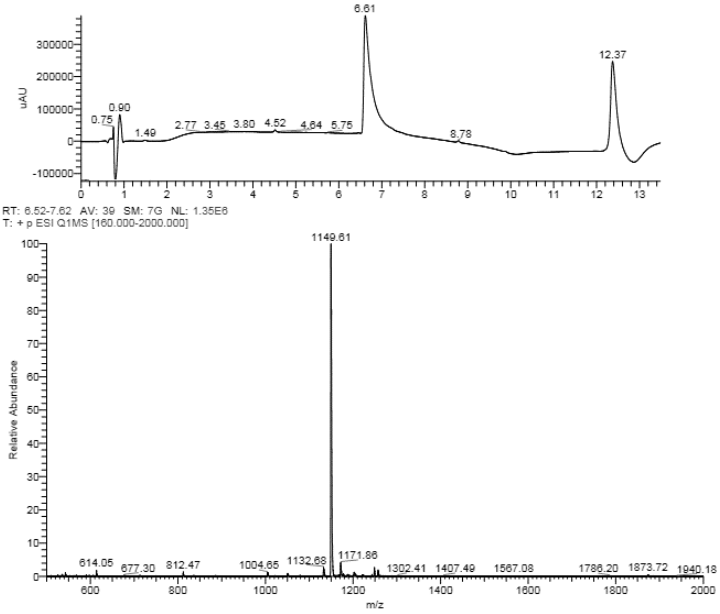

Figure S2.1. LC-MS spectrum of **16-V_3A_3**. $[M+H]^{1+}_{theor}$ = 1149.86.

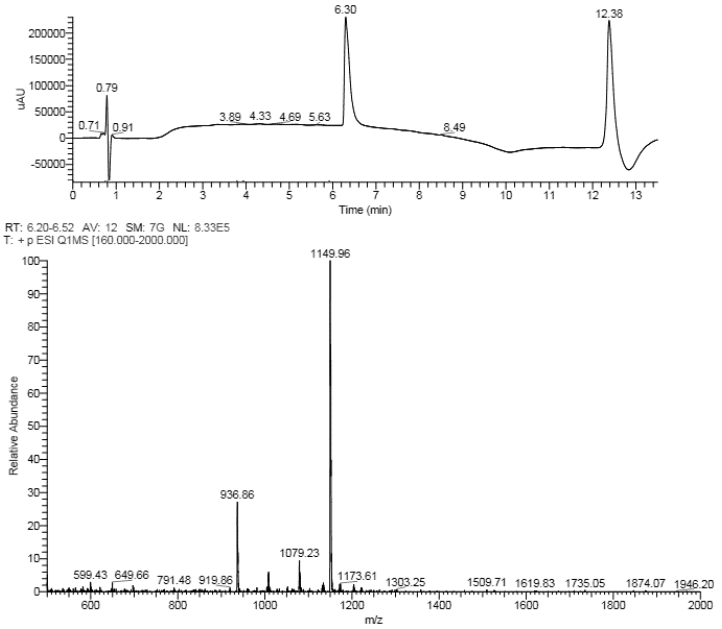

Figure S2.2. LC-MS spectrum of **16-A_3V_3**. $[M+H]^{1+}_{theor}$ = 1149.86.

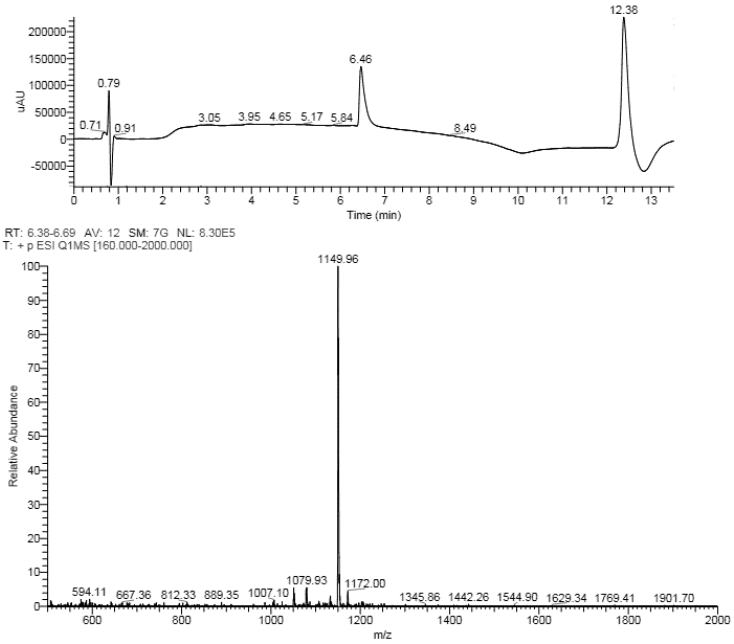

Figure S2.3. LC-MS spectrum of **16-$(VA)_3$**. $[M+H]^{1+}_{theor}$ = 1149.86.

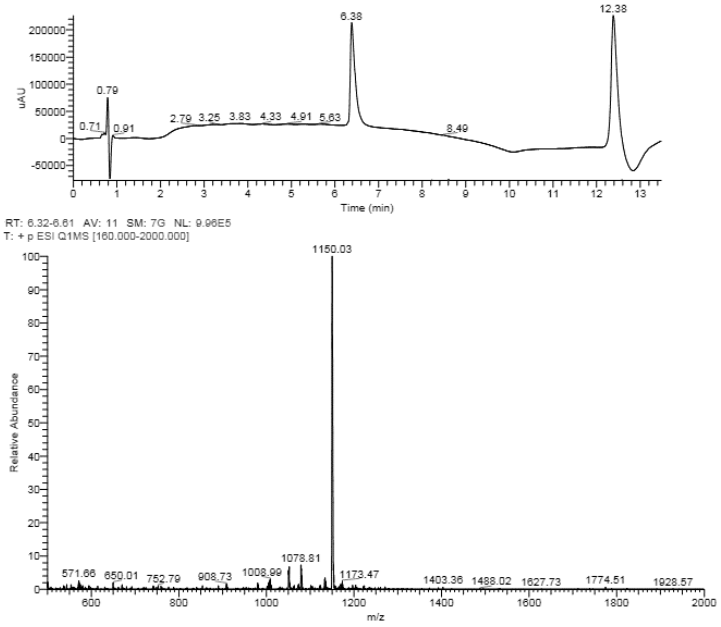

Figure S2.4. LC-MS spectrum of **16-(AV)$_3$**. $[M+H]^{1+}_{theor}$ = 1149.86.

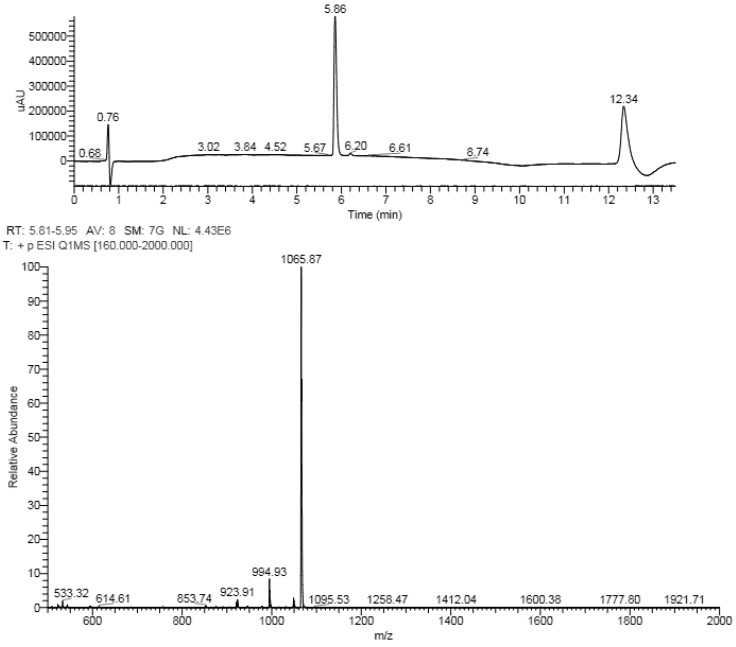

Figure S2.5. LC-MS spectrum of **16-A$_6$**. $[M+H]^{1+}_{theor}$ = 1065.76.

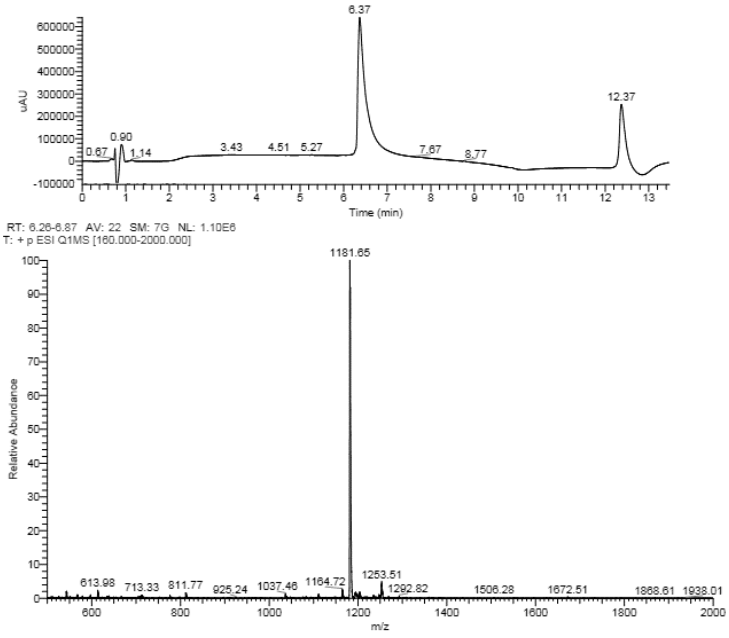

Figure S2.6. LC-MS spectrum of **HS16-V$_3$A$_3$**. $[M+H]^{1+}_{theor}$ = 1181.83.

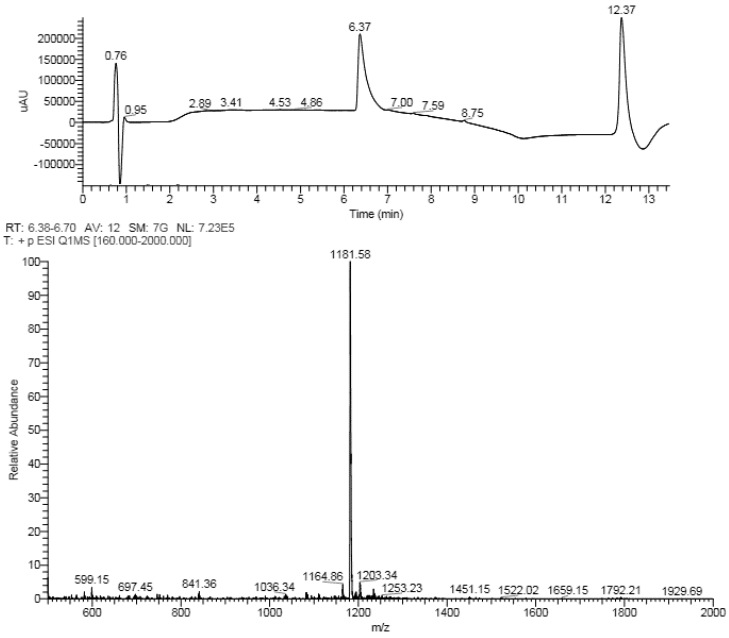

Figure S2.7. LC-MS spectrum of **HS16-A$_3$V$_3$**. $[M+H]^{1+}_{theor}$ = 1181.83.

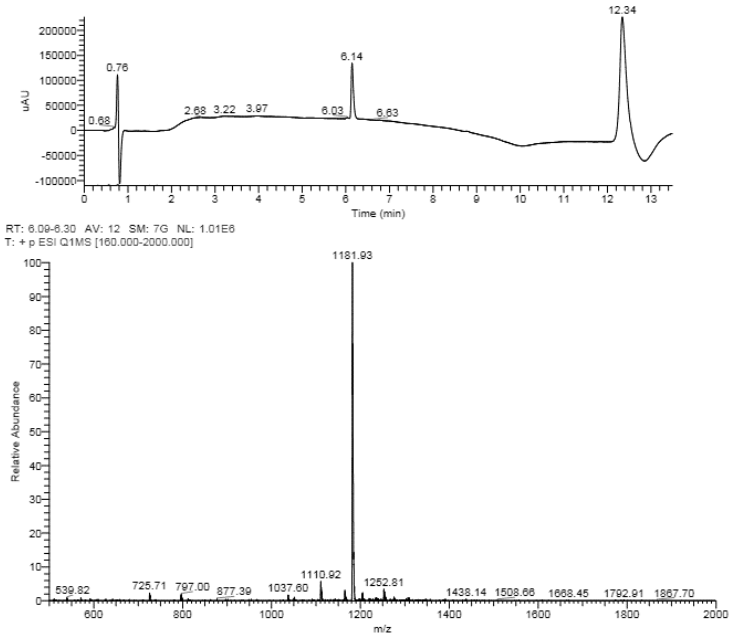

Figure S2.8. LC-MS spectrum of **HS16-(VA)$_3$**. $[M+H]^{1+}_{theor}$ = 1181.83.

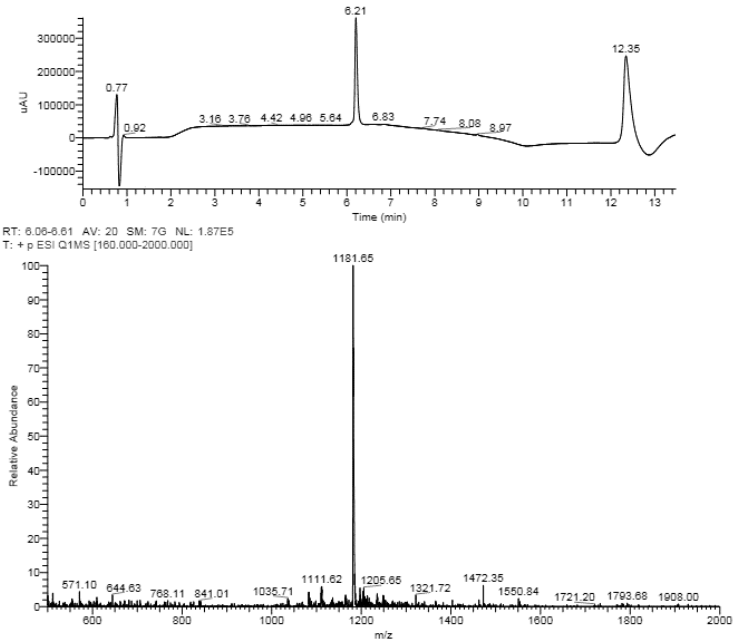

Figure S2.9. LC-MS spectrum of **HS16-(AV)$_3$**. $[M+H]^{1+}_{theor}$ = 1181.83.

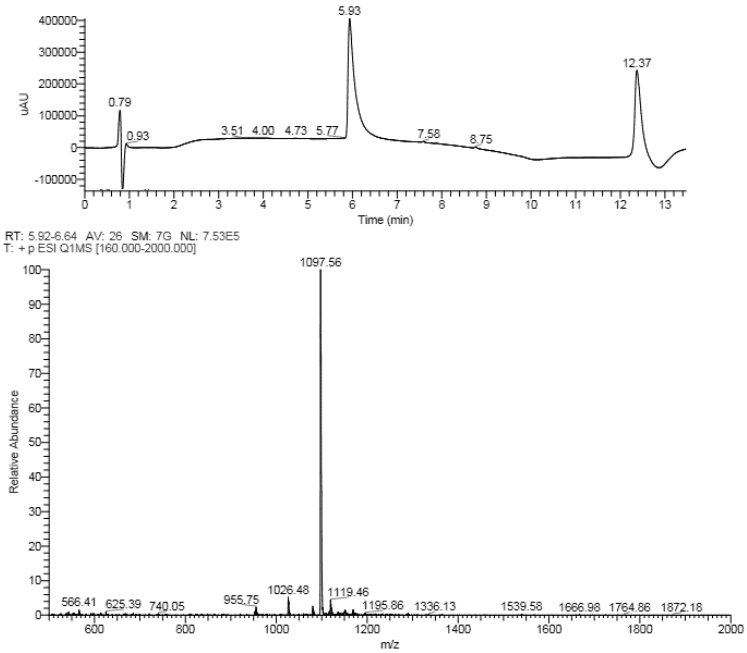

Figure S2.10. LC-MS spectrum of **HS16-A$_6$**. $[M+H]^{1+}_{theor}$ = 1097.74.

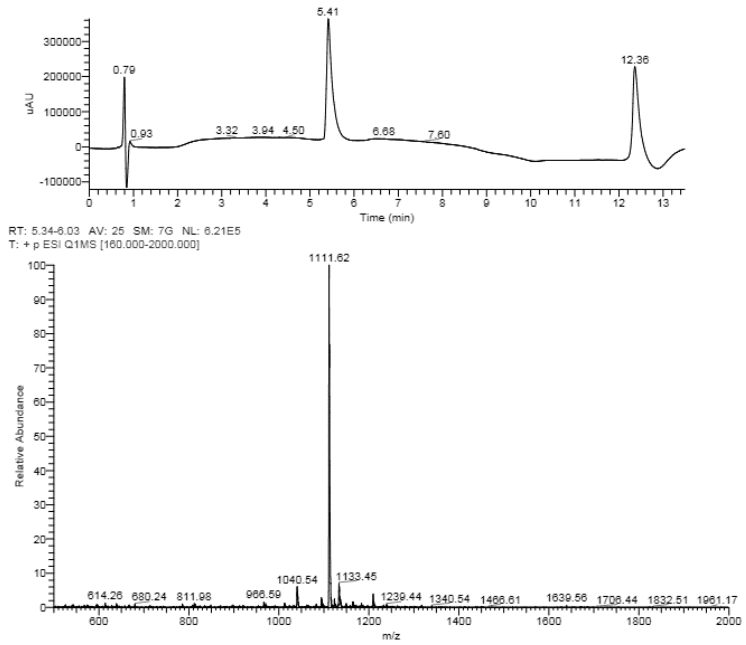

Figure S2.11. LC-MS spectrum of **HS11-V$_3$A$_3$**. $[M+H]^{1+}_{theor}$ = 1111.75.

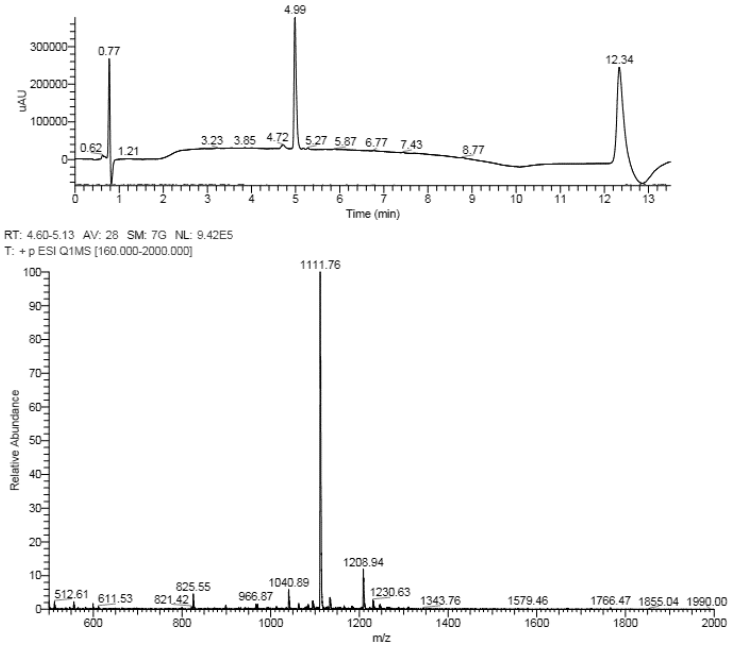

Figure S2.12. LC-MS spectrum of **HS11-A_3V_3**. $[M+H]^{1+}_{theor}$ = 1111.75.

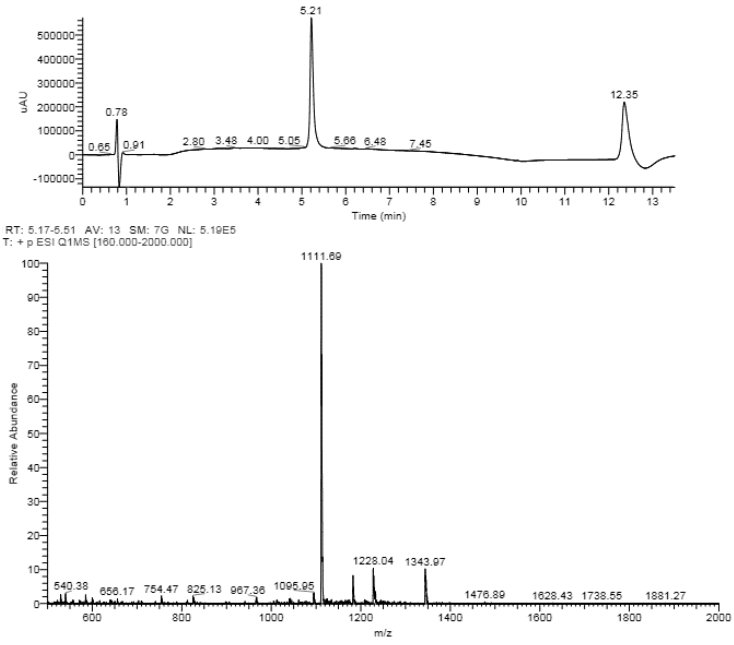

Figure S2.13. LC-MS spectrum of **HS11-$(VA)_3$**. $[M+H]^{1+}_{theor}$ = 1111.75.

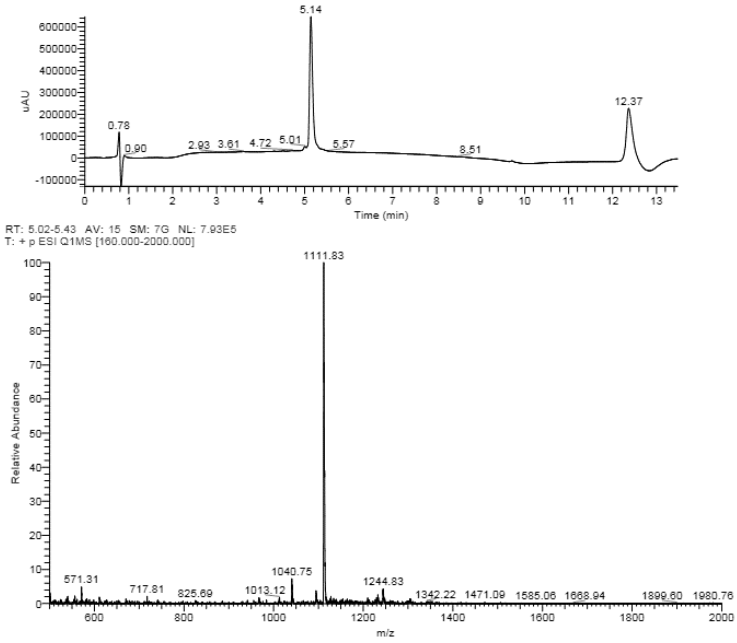

Figure S2.14. LC-MS spectrum of **HS11-(AV)$_3$**. $[M+H]^{1+}_{theor}$ = 1111.75.

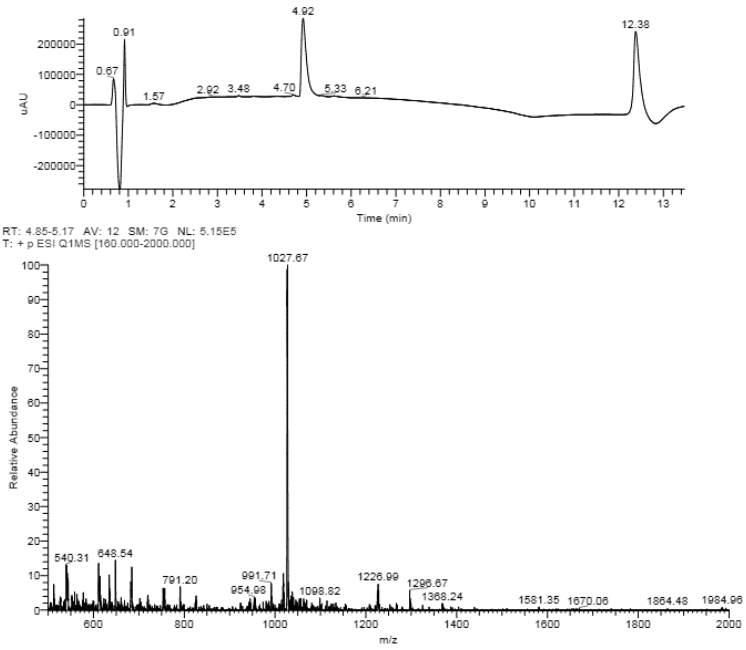

Figure S2.15. LC-MS spectrum of **HS11-A$_6$**. $[M+H]^{1+}_{theor}$ = 1027.66.

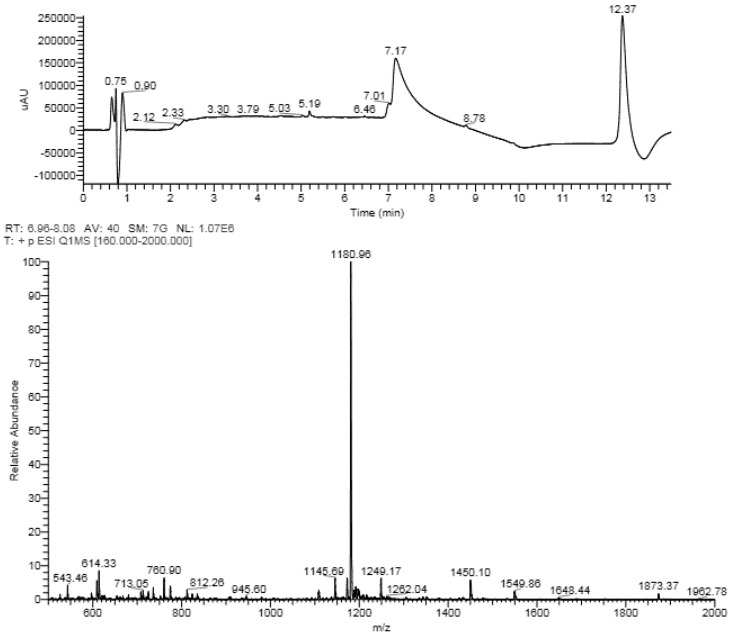

Figure S2.16. LC-MS spectrum of **di-16-V_3A_3**. $[M+2H]^{2+}_{theor}$ = 1181.33.

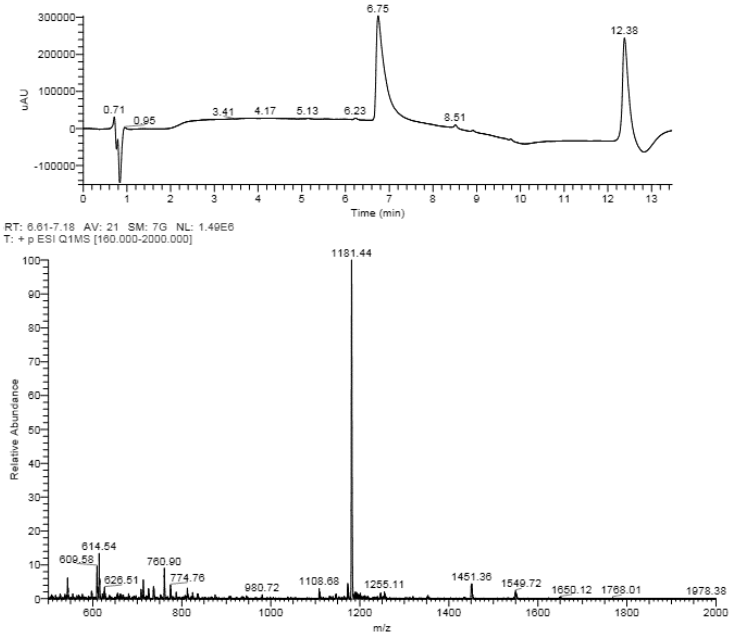

Figure S2.17. LC-MS spectrum of **di-16-A_3V_3**. $[M+2H]^{2+}_{theor}$ = 1181.33.

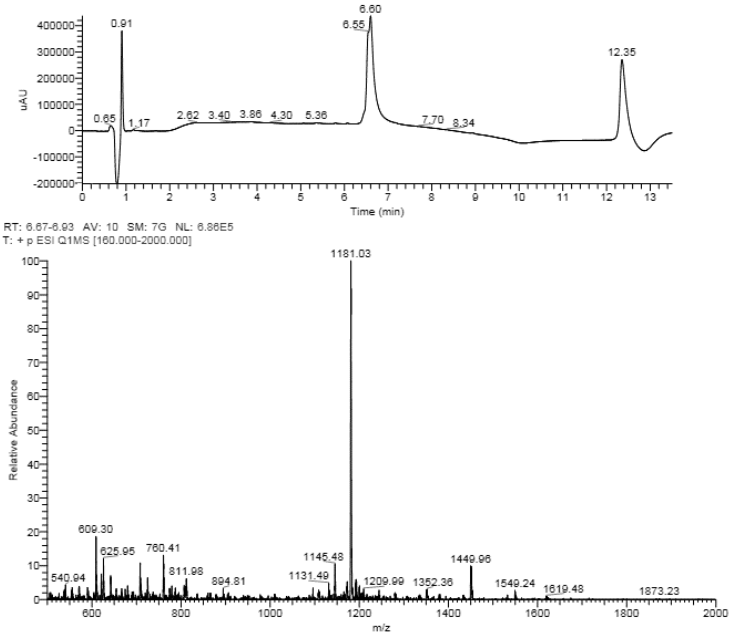

Figure S2.18. LC-MS spectrum of **di-16-(VA)$_3$**. $[M+2H]^{2+}_{theor}$ = 1181.33.

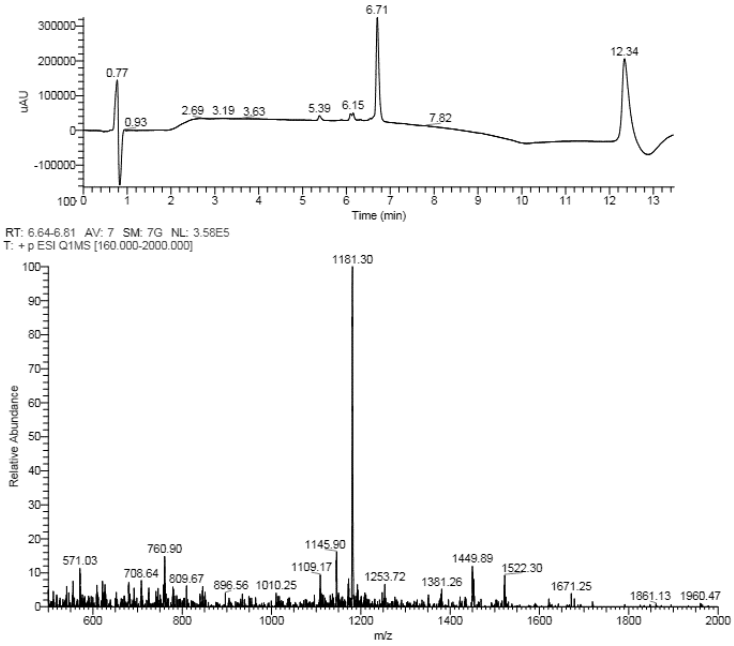

Figure S2.19. LC-MS spectrum of **di-16-(AV)$_3$**. $[M+2H]^{2+}_{theor}$ = 1181.33.

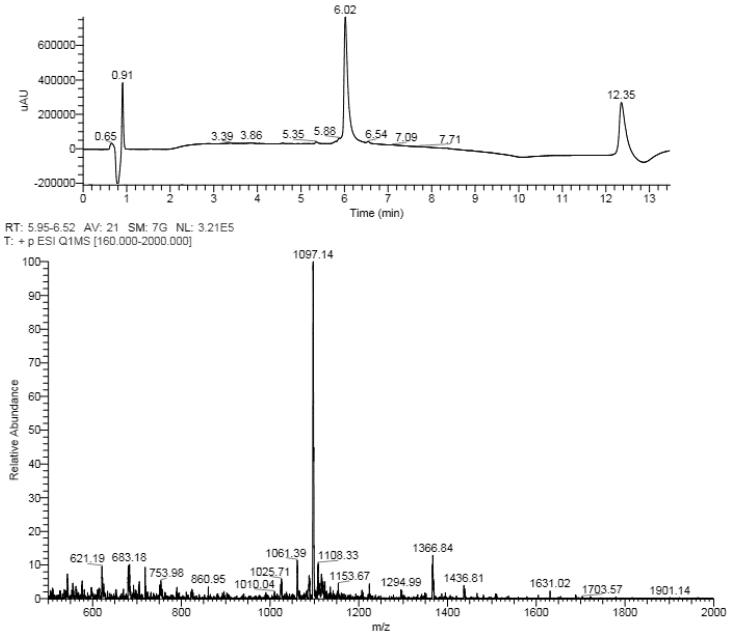

Figure S2.20. LC-MS spectrum of **di-16-A$_6$**. $[M+2H]^{2+}_{theor}$ = 1097.23.

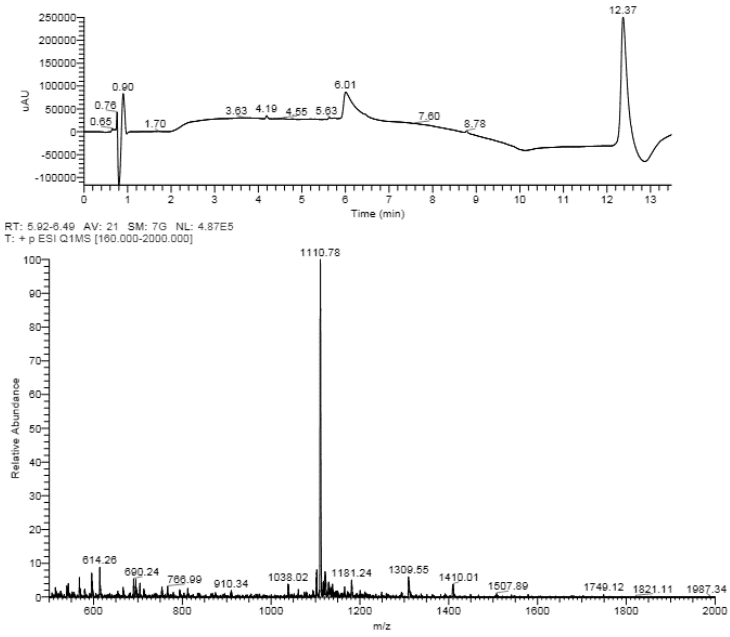

Figure S2.21. LC-MS spectrum of **di-11-V$_3$A$_3$**. $[M+2H]^{2+}_{theor}$ = 1181.33.

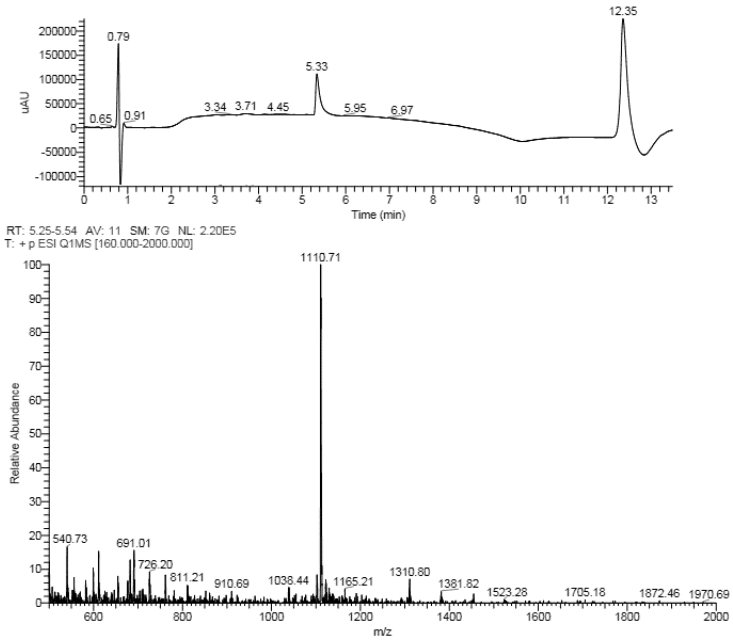

Figure S2.22. LC-MS spectrum of **di-11-A_3V_3**. $[M+2H]^{2+}_{theor}$ = 1111.25.

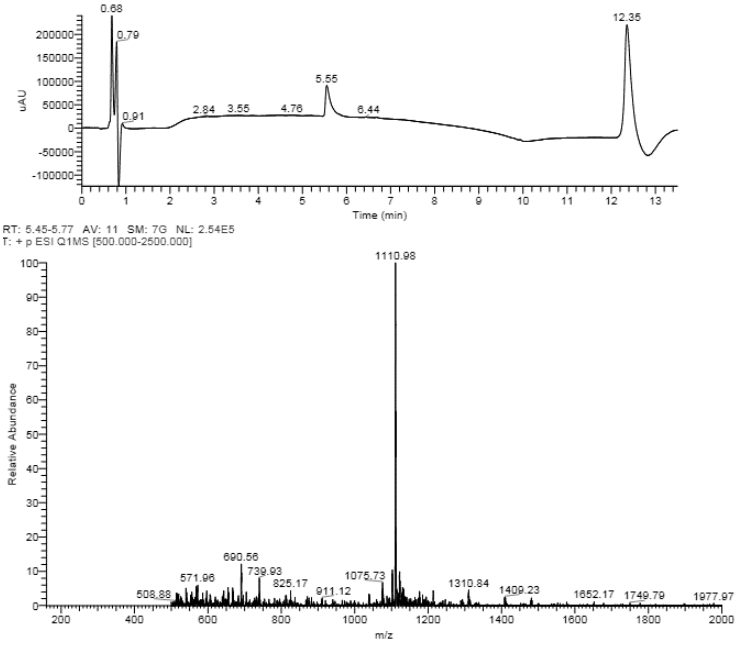

Figure S2.23. LC-MS spectrum of **di-11-$(VA)_3$**. $[M+2H]^{2+}_{theor}$ = 1111.25.

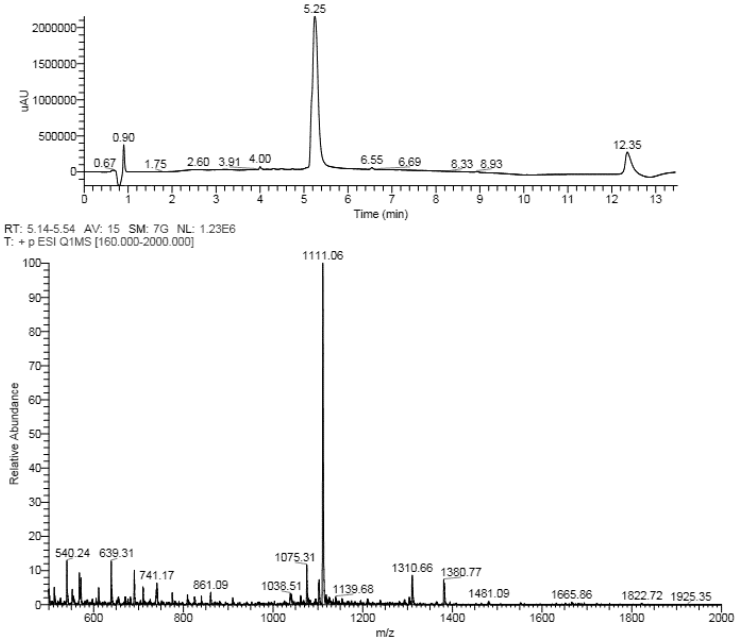

Figure S2.24. LC-MS spectrum of **di-11-(AV)$_3$**. $[M+2H]^{2+}_{theor}$ = 1111.25.

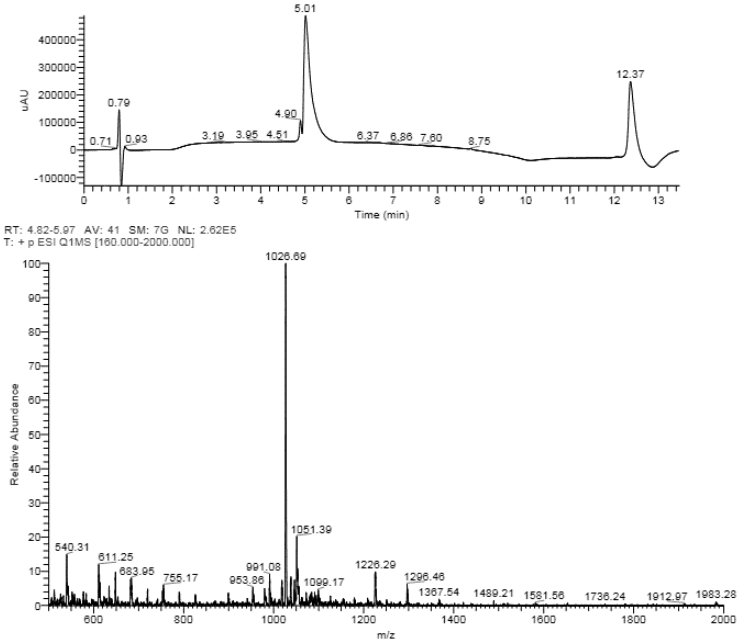

Figure S2.25. LC-MS spectrum of **di-11-A$_6$**. $[M+2H]^{2+}_{theor}$ = 1027.15.

Spontaneous oxidation of peptide amphiphile thiol groups:

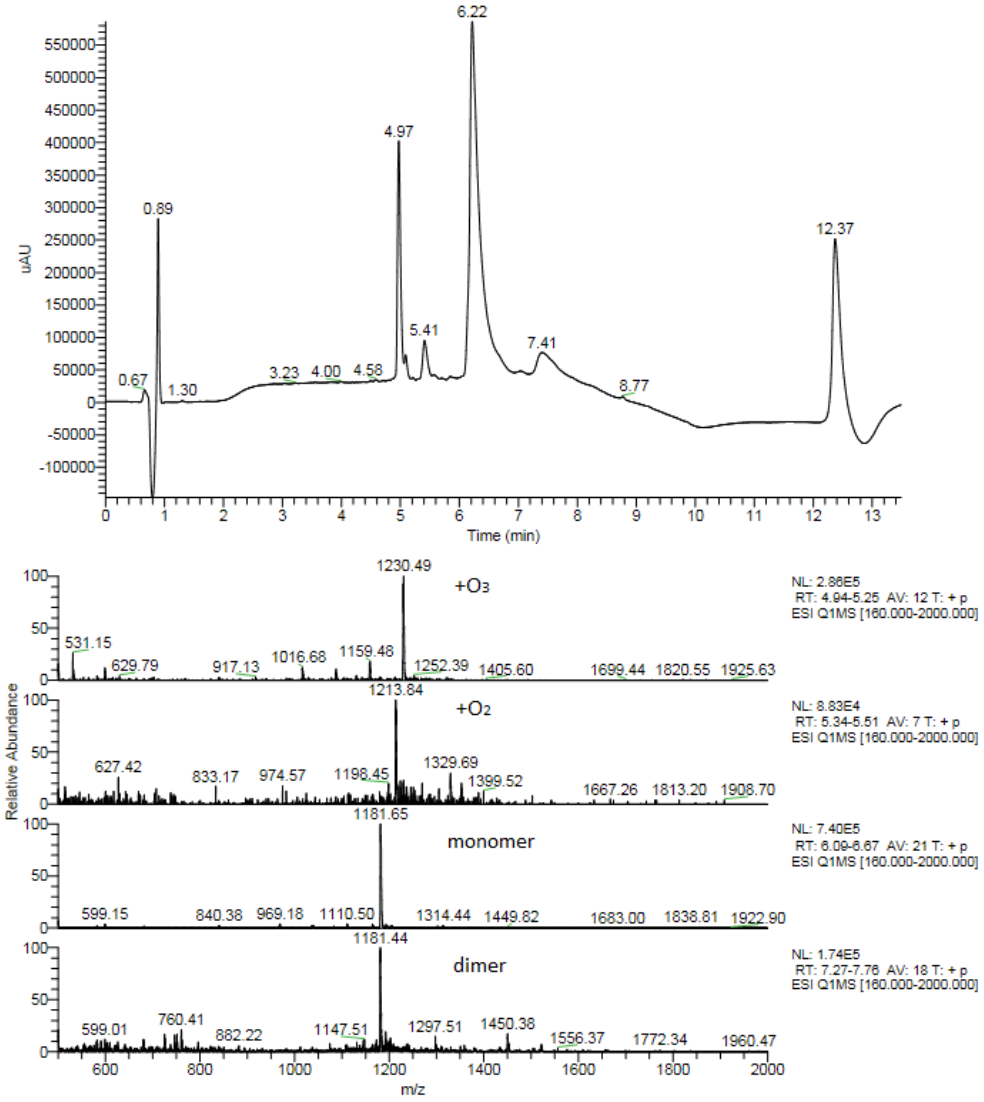

Figure S2.26. LC-MS spectra of **HS16-A$_3$V$_3$** after long-term storage in the lyophilized state at +4 ºC (~1 year). Oxidation of the terminal thiol gave rise to a dimeric species, as well as +O_2 and +O_3.

Secondary structure profiling based on Amide I fitting:

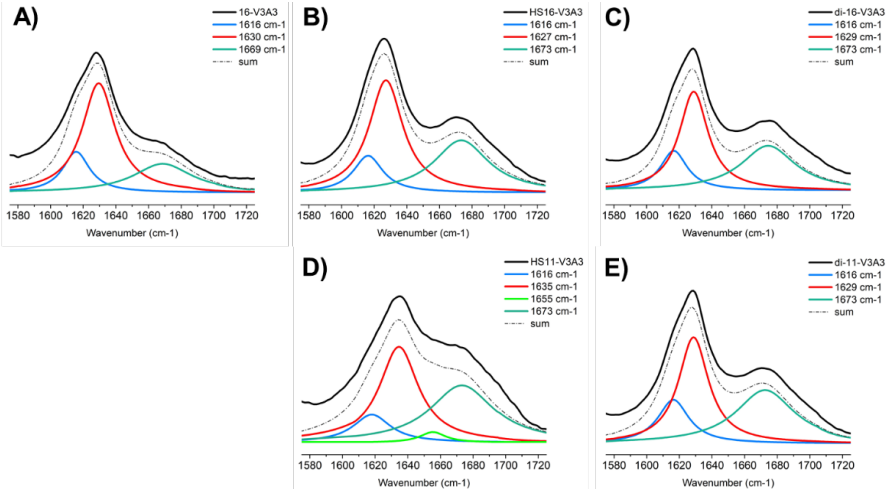

Figure S2.27. Fitting of the Amide I peak for peptide amphiphiles bearing the **V_3A_3** peptide domain: blue line represents the terminal amide; red line - the joint contribution of β-structures and amino groups of Lys residues; green line – α-helices; cyan line – other structures. Each figure shows the same peptide domain coupled to different alkyl chains: (A) **16-**, (B) **HS16-**, (C) **di-16-**, (D) **HS11-**, (E) and **di-11-**.

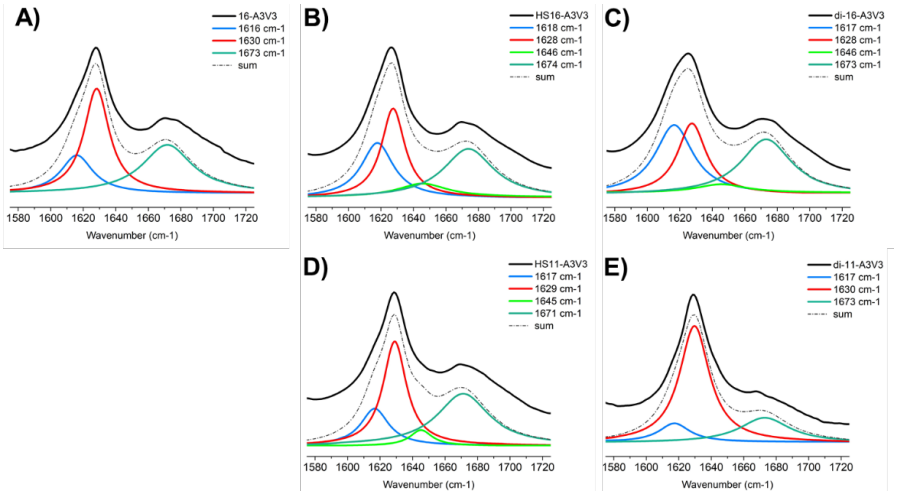

Figure S2.28. Fitting of the Amide I peak for peptide amphiphiles bearing the **A_3V_3** peptide domain: blue line represents the terminal amide; red line - the joint contribution of β-structures and amino groups of Lys residues; green line – α-helices; cyan line – other structures. Each figure shows the same peptide domain coupled to different alkyl chains: (A) **16-**, (B) **HS16-**, (C) **di-16-**, (D) **HS11-**, (E) and **di-11-**.

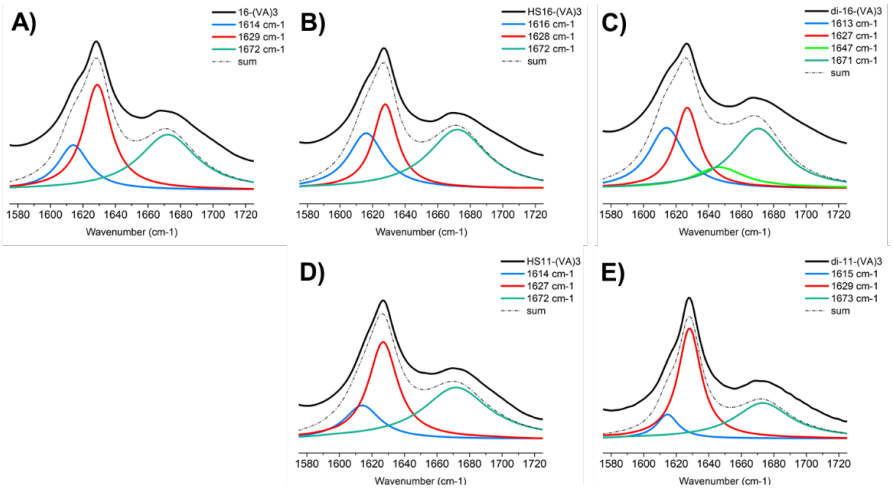

Figure S2.29. Fitting of the Amide I peak for peptide amphiphiles bearing the **$(VA)_3$** peptide domain: blue line represents the terminal amide; red line - the joint contribution of β-structures and amino groups of Lys residues; green line – α-helices; cyan line – other structures. Each figure shows the same peptide domain coupled to different alkyl chains: (A) **16-**, (B) **HS16-**, (C) **di-16-**, (D) **HS11-**, (E) and **di-11-**.

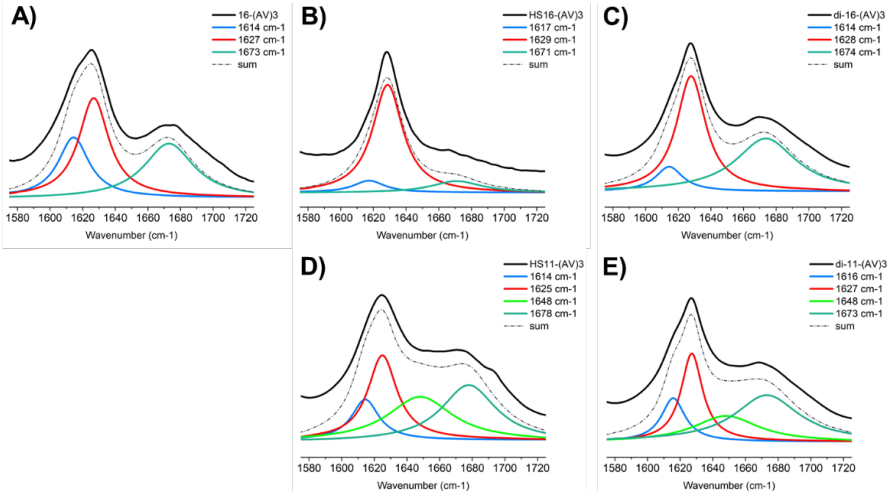

Figure S2.30. Fitting of the Amide I peak for peptide amphiphiles bearing the **$(AV)_3$** peptide domain: blue line represents the terminal amide; red line - the joint contribution of β-structures and amino groups of Lys residues; green line – α-helices; cyan line – other structures. Each figure shows the same peptide domain coupled to different alkyl chains: (A) **16-**, (B) **HS16-**, (C) **di-16-**, (D) **HS11-**, (E) and **di-11-**.

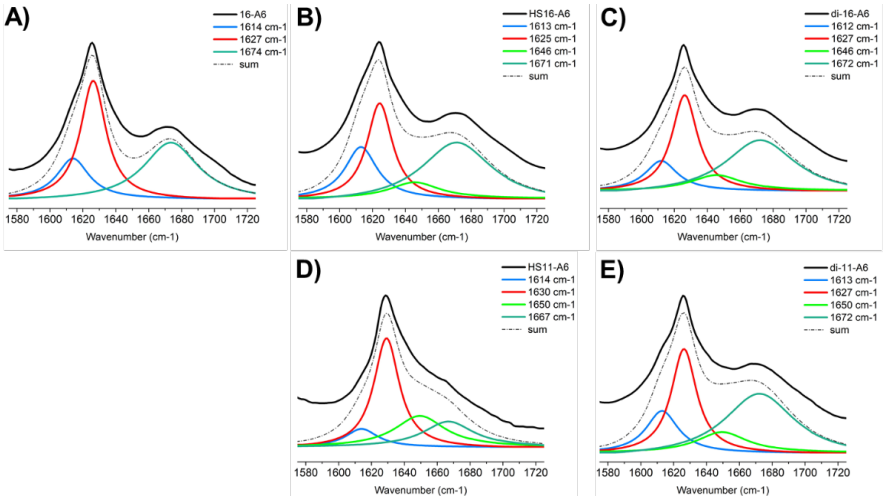

Figure S2.31. Fitting of the Amide I peak for peptide amphiphiles bearing the $\mathbf{A_6}$ peptide domain: blue line represents the terminal amide; red line - the joint contribution of β-structures and amino groups of Lys residues; green line – α-helices; cyan line – other structures. Each figure shows the same peptide domain coupled to different alkyl chains: (A) **16-**, (B) **HS16-**, (C) **di-16-**, (D) **HS11-**, (E) and **di-11-**.

CHAPTER 3

Peptidic stabilization of gold nanoparticles

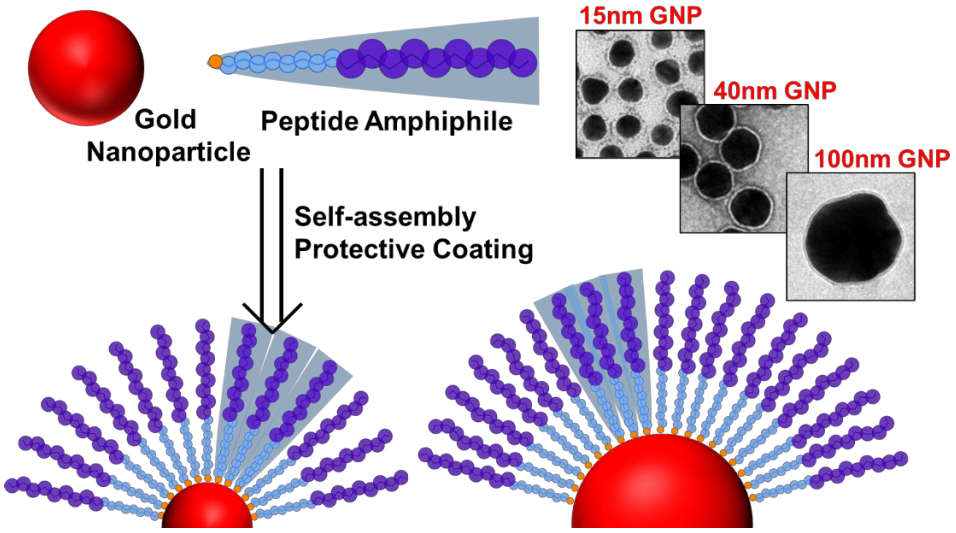

This chapter was published as an Original Research paper: E. Egorova, M.J.M. van Rijt, N. Sommerdijk, G.S. Gooris, J.A. Bouwstra, A.L. Boyle, A. Kros, ACS Nano **2020**, *14* (5), 5874-5886 (https://dx.doi.org/10.1021/acsnano.0c01021)

3.1 Abstract

The functionalization of gold nanoparticles (GNPs) with peptidic moieties can prevent their aggregation and facilitate their use for applications both *in vitro* and *in vivo*. To date, no peptide-based coating has been shown to stabilize GNPs larger than 30 nm in diameter; such particles are of interest for applications including vaccine development, drug delivery, and sensing. Here, GNPs with diameters of 20, 40, and 100 nm are functionalized with peptide amphiphiles. Using a combination of transmission electron microscopy, UV−vis spectroscopy, and dynamic light scattering, we show that GNPs up to 100 nm in size can be stabilized by these molecules. Moreover, we demonstrate that these peptide amphiphiles form curvature-dependent, ordered structures on the surface of the GNPs and that the GNPs remain disperse at high-salt concentrations and in the presence of competing thiol-containing molecules. These results represent the development of a peptide amphiphile-based coating system for GNPs which has the potential to be beneficial for a wide range of biological applications, in addition to image enhancement and catalysis.

3.2 Introduction

Gold nanoparticles (GNPs) have been extensively studied in recent years and have found wide-ranging applications in areas including: photothermal therapy;[1, 2] drug delivery;[3, 4] catalysis;[5-7] biosensing;[8, 9] and vaccine development.[10-12] GNPs are suited to such purposes due to their unique optical properties,[13] ease of functionalization,[14] facile synthesis, and programmable shape and size.[15-17]

One major disadvantage of GNPs is that they are toxic both *in vitro* and *in vivo*.[18-20] GNPs also have a tendency to aggregate, resulting in limited mobility which restricts the possibility of targeted delivery and prevents a uniform size distribution of GNPs, properties which are crucial requirements for drug delivery and photothermal therapy, for example.

To circumvent these issues, GNPs can be coated with a moiety that prevents aggregation. Examples of GNP coatings include: silica,[21] PEG,[22, 23] low molecular weight alkanethiols,[24, 25] and thiolated fatty acids.[26, 27] Whilst these coatings reduce the toxicity of GNPs they have inherent limitations, for example silica coatings are porous, and often heterogeneous,[28, 29] meaning they are reactive to components of cell culture media. Many polymers are large in size, therefore the diameters of polymer-coated GNPs are greatly increased, which limits cellular penetration. Additionally, polymers often exhibit packing defects that leave the gold surface exposed and cause aggregation.[30] Alkane thiols and fatty acids are inherently hydrophobic, therefore they have poor solubility and can interact strongly with cellular membranes.[31]

A solution to many of these issues is to employ peptides: they are inherently biocompatible; can be programmed to possess well-defined folds; and can be facilely modified with targeting ligands, or therapeutic molecules. Several peptide sequences have been developed, the most notable of which is CALNN, a five-amino acid peptide developed by the Levy group.[32] When this peptide is attached to small (<30 nm) GNPs, the resulting conjugates have been shown to be stable at high salt concentrations (>500 mM), and resistant to physical manipulations including size-exclusion chromatography (SEC), centrifugation, and lyophilization. Functional moieties have been appended to the peptide and have been demonstrated to remain active, for example: biotin-functionalized peptides bind streptavidin or avidin and act as a platform for bio-sensing;[32, 33] ligands such as abscisic acid are recognized by specific antibodies;[34] and peptidic substrates are cleaved by their corresponding enzymes.[35] There is no information available regarding the stability of larger GNPs (>30 nm) coated with CALNN.[34, 36] Similarly, other peptide sequences including CLPFFD,[37] and CFGAILSS,[38] have only been employed to stabilize small (*i.e.* <30 nm) GNPs.

A second effective approach to GNP stabilization is to employ a short, thiolated, alkyl chain coupled to either a PEG molecule or a peptide.[39-41] This method results in a thin GNP coating and the packing of the alkyl chains is uniform. It is theorized that the success of this coating approach is due, in addition to the tight packing, to the hydrophobic nature of the alkyl chain meaning water molecules are depleted at the GNP surface, which helps stabilize the particles. GNPs with such coatings have been equipped with targeting peptides and proven to fulfil the designed function.[42] As with the peptide-coated GNPs, particles >35 nm in diameter were not stabilized effectively.[39]

Peptide amphiphiles are a class of molecules which possess both a hydrophilic peptidic portion and a hydrophobic alkyl tail.[43, 44] These molecules combine the favorable properties of alkyl chains and peptides, namely hydrophobicity, tight, ordered packing, and the formation of defined structures; therefore we hypothesize that peptide amphiphiles could be used to effectively coat and stabilize GNPs.

We have developed a series of peptide amphiphiles, using peptide sequences developed by the Stupp group.[45] These have a sequence of $(Val)_v(Ala)_a(Xxx)_x$ where, usually, v=3, a=3, $(Xxx)_x$ = Glu_3 or Lys_3, although other combinations have been published.[46] Alkyl chains of 11- or 16-carbons in length were attached to the peptide N-terminus. These amphiphiles adopt a β-sheet conformation and form long cylindrical fibers in aqueous environments. Although peptide conformations have been shown to differ when in solution or when confined to a flat or curved surface,[38, 47] it has been hypothesized that the ability of peptides to self-assemble and adopt a defined conformation is important for GNP stabilization.[38]

To elucidate the impact of both domains, peptides were evaluated with and without alkyl chains attached, and the alkyl chain length was varied. In addition, our designed constructs were compared to state-of-the-art peptides. Initially, the structures and self-assembly properties of the peptides and amphiphiles were probed in solution. A coating protocol was subsequently devised, and the resulting GNP-peptide/amphiphile conjugates were assessed using UV-Vis spectroscopy, dynamic light scattering (DLS), and transmission electron microscopy (TEM) to determine the aggregation degree, which provided insights as to how effectively the GNPs were stabilized. The secondary structure of the coatings on the surface of GNPs of different sizes was evaluated using Fourier transform-infrared (FT-IR)

spectroscopy to determine if secondary structure affected stabilization. This technique also allowed us to probe whether confining the peptides and amphiphiles to surfaces of differing curvatures altered their secondary structure. In addition, the effects of high salt concentrations and the presence of dithiothreitol (DTT), a competitive thiol-containing ligand, were also evaluated to determine the feasibility of employing such gold bioconjugates for applications *in vitro* and *in vivo*.

3.3 Results and Discussion

3.3.1 Peptide and peptide amphiphile design

Peptide amphiphiles comprising a thiolated alkyl tail of either 11 or 16 carbons in length and a peptide domain with the sequence $V_3A_3E_3$ were designed and synthesized. A third construct with two C-11 alkyl chains was generated to investigate the effect of increased steric bulk within the hydrophobic domain and to probe the presence of a bidentate gold binding motif. The sequences and structures of these three peptide amphiphiles, dubbed molecules **1-3**, are shown in **Scheme 3.1**. For amphiphile **3,** a fourth glutamic acid residue (Glu, E) was incorporated into the sequence to aid solubility.

These designs are envisaged to stabilize GNPs for multiple reasons: similar amphiphilic constructs adopt well-defined β-sheet structures,[45] and the formation of an ordered structure is thought to be important for effective GNP coating.[36] The strong negative charge of the amphiphiles aids GNP stability under physiological conditions, and there is evidence that negatively charged GNPs are less toxic than positively charged particles.[20] The alkyl chain provides a dense, hydrophobic shell around the GNP thereby aiding stability.[30]

In addition to molecules **1-3**, a peptide without an alkyl chain but with a cysteine (Cys, C) residue was also designed, (molecule **4**, **Scheme 3.1**), to determine whether the peptide sequence alone was capable of stabilizing GNPs. State-of-the-art peptides CALNN, CVALNN and CVVVT were synthesized and compared to molecules **1-4**. **5** is the most commonly used sequence for the peptidic stabilization of GNPs, and its derivative, **6**, was

developed as there is evidence that additional steric bulk and hydrophobicity, provided by the valine (Val, V) residue, may provide additional stability.[32] Peptide **7** has been demonstrated to be highly efficient at stabilizing small GNPs,[32] and was included to probe its stabilizing effects on larger GNPs.

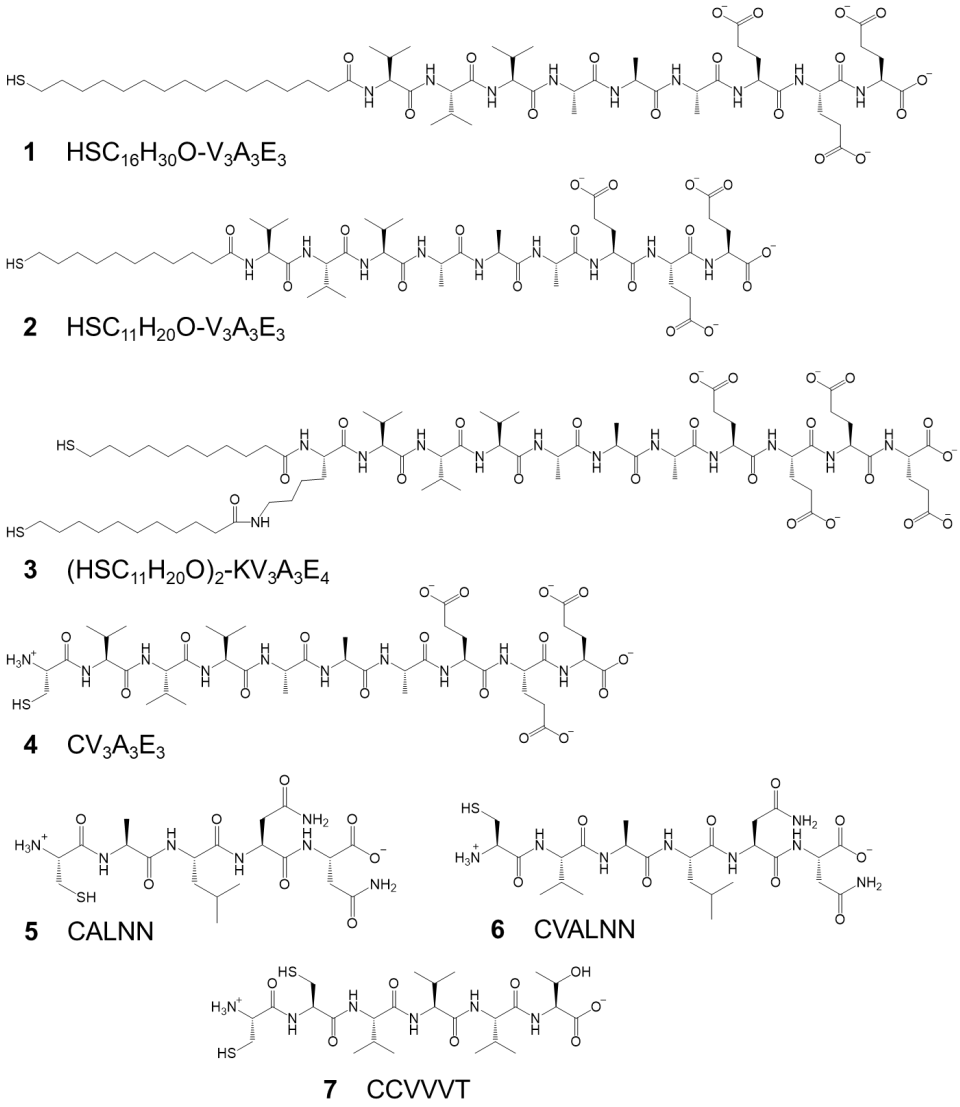

Scheme 3.1. Sequences and structures of peptides and amphiphiles generated for this study. Liquid chromatography-mass spectrometry (LC-MS) was employed to assess compound purity (**Figures S3.1-3.11**).

All peptides were synthesized by solid-phase peptide synthesis, (see **3.5.2** for full details). Briefly, after automated synthesis of the peptidic portion, both **1** and **2** were completed with an automated coupling of either 16-mercaptohexadecanoic acid (**1**) or 11-mercaptoundecanoic acid (**2**). For **3**, Fmoc-Lys(Fmoc)-OH was coupled at the N-terminus of the $V_3A_3E_4$ peptide, and upon Fmoc deprotection with 20% piperidine, 11-mercaptoundecanoic acid was coupled to both the N-terminus and the amine side-chain of the Lys moiety to yield a double chain peptide amphiphile.

3.3.2 Assembly in solution

The peptide amphiphiles developed by the Stupp group self-assembled into β-structured fibers in aqueous solution.[45] To determine whether thiolation and alterations to the alkyl chain length affected the secondary structure of the peptide amphiphiles, their circular dichroism (CD) spectra were recorded, **Figure 3.1**, and compared to $C_{16}H_{31}O\text{-}V_3A_3E_3$.[45]

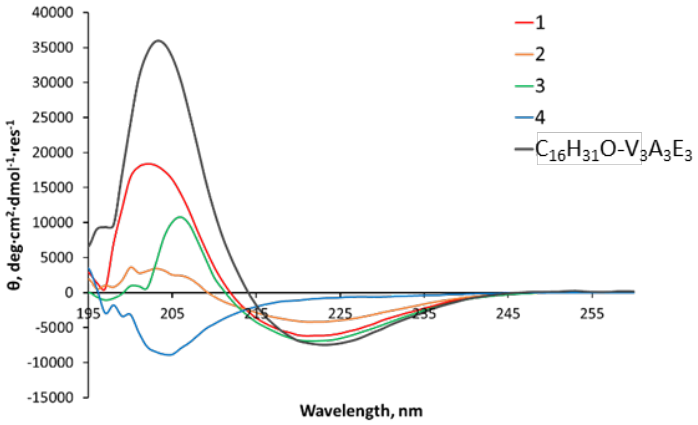

Figure 3.1. CD spectra of amphiphiles **1-3**, the peptidic analogue **4**, and $C_{16}H_{31}O\text{-}V_3A_3E_3$, a peptide amphiphile developed by the Stupp group. All samples were prepared in PBS, pH 7.2, at a concentration of 100 μM for **1** and $C_{16}H_{31}O\text{-}V_3A_3E_3$, and 250 μM for **2-4**. The CD signal was converted to mean residue ellipticity which normalizes for peptide length and concentration (see **3.5.10** for details).

The spectra revealed that the introduction of a thiol, to generate amphiphile **1**, did not significantly alter the secondary structure as a spectrum corresponding to a β-structured species was observed. The magnitude of the CD signal was less intense than for $C_{16}H_{31}O$-$V_3A_3E_3$, we postulate that this could be due to intermolecular disulfide bond formation, or thiol oxidation, since both were observed by liquid chromatography-mass spectrometry (LC-MS), see **Figure S3.12**. Shortening the alkyl chain to produce **2** led to a reduction in the intensity of the CD signal, although a β-structure was still adopted. Interestingly, incorporation of two mercaptoundecanoyl chains, to form **3**, produced a signal which was comparable in intensity to **1** and to $C_{16}H_{31}O$-$V_3A_3E_3$. It should be noted that **1-3** exhibited a small shift in the position of the peak minimum when compared to $C_{16}H_{31}O$-$V_3A_3E_3$. This could be due to a difference in the twist of the β-sheets,[48] possibly as a result of disulfide bond formation. The peptide analogue **4** did not adopt an ordered structure, indicating the alkyl chain is important for self-assembly and the resultant formation of a defined secondary structure.

$C_{16}H_{31}O$-$V_3A_3E_3$ forms β-sheets in aqueous media, and these β-sheets propagate into long, cylindrical fibers.[45] The self-assembly properties of **1-4** were therefore investigated further with TEM (**Figure 3.2)**. The TEM images show that **1-3** form fibers although the fiber morphologies vary, which is likely to be due to the differences in the number or length of the alkyl chains. No defined assemblies were observed for **4**, which is in agreement with the absence of a defined secondary structure, as determined by CD spectroscopy.

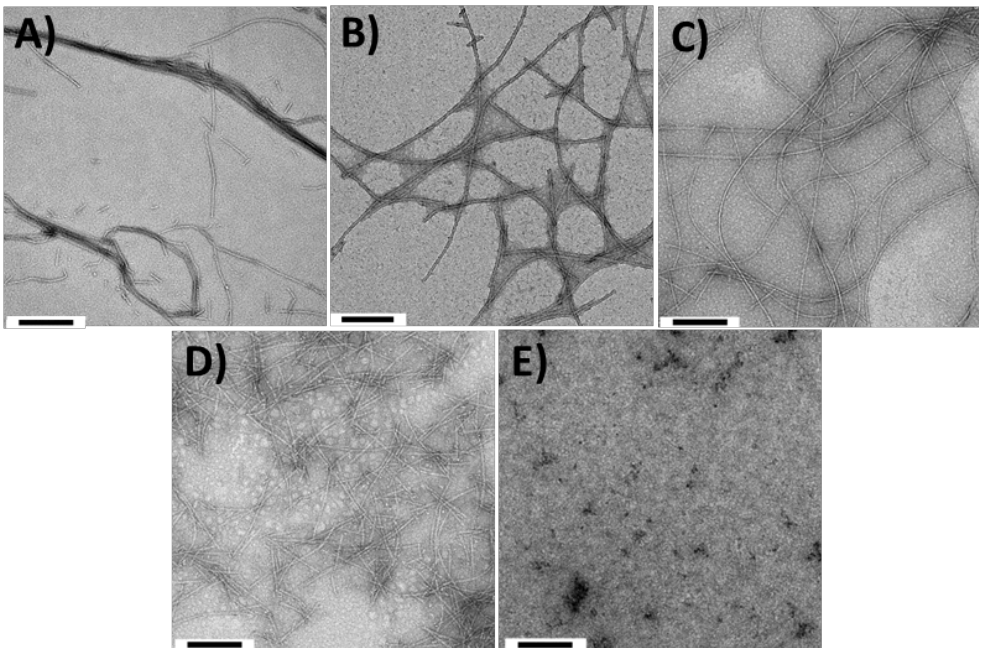

Figure 3.2. Representative TEM images for (A) $C_{16}H_{31}O$-$V_3A_3E_3$; (B) **1**; (C) **2**; (D) **3**; (E) **4**. Samples were prepared in PBS, pH 7.2, and stained with 0.5% uranyl acetate. Scale bar is 200 nm for all images.

These studies confirm that peptide amphiphiles **1-3** self-assemble to form β-structured fibers in aqueous solution. Whilst small differences in the secondary structures of the amphiphiles were observed, and the dimensions of the resulting fibers vary, it could be concluded that changing the alkyl chain length and adding a thiol to the N-terminus of these amphiphiles does not prevent their self-assembly.

3.3.3 Coating of GNPs

GNPs with diameters of 20, 40, or 100 nm were synthesized *via* sodium citrate reduction of chloroauric acid according to literature protocols,[15, 49, 50] (see **3.5.4** and **Figure S3.13** for further information). 20 nm particles were evaluated as this size lies within the 10-30 nm range, which is commonly

employed by other researchers when probing coating efficiency.[26, 29, 30, 32, 37-39, 47, 51] 40 and 100 nm GNPs were chosen as 'large' GNPs (>35 nm), and have not previously been successfully coated with peptides or amphiphiles.

Ligand exchange is a technique commonly employed to generate covalently-attached coatings on GNP surfaces *via* the displacement of citrate ions utilized in GNP synthesis.[52] This strategy was employed to coat GNPs with our peptide amphiphiles. To circumvent undesired fiber formation during GNP coating, the thiolated peptide amphiphiles were dissolved in dimethylsulfoxide (DMSO). This solution was mixed with an aqueous GNP suspension, yielding an initial GNP:peptide ratio of 1:100,000 and a final DMSO concentration of 25% (v/v). After 1 hour of incubation, the samples were centrifuged to remove any unbound peptide before the pellet was resuspended in 5% DMSO (v/v). To eliminate any remaining unbound peptide or amphiphile, and to exchange buffers, size exclusion chromatography (SEC) was performed using PBS as the eluent.

The colloidal stability of the GNPs was initially studied using dynamic light scattering (DLS)**. Table 3.1** summarizes the average hydrodynamic diameters of the peptide- or peptide amphiphile-coated particles compared to the citrate-coated GNPs. **1** preserves the original size distribution for all three sizes of GNPs evaluated and no aggregation was observed; although the hydrodynamic diameter increased for all particle sizes due to the presence of the peptide amphiphile on the GNP surface (**Table 3.1** and **Figure S3.14)**. Amphiphile **2** successfully stabilized 20 and 40 nm GNPs but 100 nm particles aggregated. Interestingly, **3**, with two mercaptoundecanoyl alkyl chains, was capable of stabilizing all GNP sizes. To determine whether the enhanced stabilizing effect of **3**, in comparison to **2**, was due to the presence of two alkyl chains or to the additional Glu residue and the resulting

increased negative charge, analogous amphiphiles with only one mercaptoundecanoyl chain were synthesized (for structures see **Figure 3.3A**). These peptide amphiphiles could not stabilize larger particles, (**Figure 3.3B**), indicating that either the increased hydrophobicity, or the bidentate nature of **3** was the reason for the improved GNP stability. Collectively, the behavior of **1-3** indicate that increased hydrophobicity of the amphiphile is critical for the stabilization of larger nanoparticles.

Table 3.1. Average hydrodynamic diameters of citrate and peptide/amphiphile-capped GNPs.

coating identity	hydrodynamic diameter ± SD*, nm		
citrate	**22.0 ± 0.7**	**43.5 ± 0.3**	**101 ± 2**
1	35.1 ± 0.7	51.3 ± 0.6	115 ± 1
2	30.1 ± 0.1	51.3 ± 0.4	172 ± 6
3	33.6 ± 0.3	54.6 ± 0.4	113 ± 2
4	28.8 ± 0.1	48.3 ± 0.5	234 ±37
5	21.0 ± 0.1	225 ± 23	x
6	23.3 ± 0.2	110 ± 4	x
7	23.4 ± 1.4	155 ± 10	x

'x' indicates that the coating experiments were not conducted as aggregation occurred for a smaller GNP size. Three independent measurements were recorded, and an average hydrodynamic diameter was calculated. *- SD = standard deviation. For representative size distribution profiles, see **Figure S3.14**.

Molecule **4** was analyzed to investigate the stabilizing effect of the peptide domain alone. **4** could successfully stabilize 20 and 40 nm GNPs but not 100 nm particles, **Table 3.1**. The successful stabilization of the smaller particles is likely due to electrostatic repulsion induced by the highly negatively charged peptide sequence. Neither **5**, **6**, nor **7** were able to

stabilize particles larger than 20 nm, which is in line with previous reports.[34, 36, 38] It has been suggested that adding a bulky hydrophobic residue to **5**, to generate **6**, would enhance the stabilizing ability of the peptide. However, no evidence was found for this here, as 40 and 100 nm particles still aggregated. Equally, substituting Val for Ile, Leu or Phe did not improve stability of larger GNPs (**Figure 3.3C**). These results indicate that, to stabilize larger GNPs, either a significant increase in hydrophobicity or net charge of the stabilizing peptide is required, or that the geometry of the peptide packing is not optimal for the stabilization of larger particles.

In addition to size distributions of the GNPs, their zeta potential was measured. Due to the peptide design, the surface charge of all samples was negative (**Figure 3.4** and **Table S3.1**). The citrate-stabilized GNPs exhibited a tendency for the surface charge to increase with size: a zeta potential of -31 mV was measured for 20 nm GNPs, whilst values of -35 mV and -40 mV were recorded for 40 nm and 100 nm GNPs respectively. Similar values have been reported by Piella *et.al*.[53] After coating, the zeta potential of the particles ranged between -15 and -25 mV for 20 nm GNPs; for all 40 nm GNPs the zeta potential was approximately -25 mV; and for 100 nm GNPs values between -34 and -40 mV were obtained. It is anticipated that this net negative charge will cause electrostatic repulsion between the particles, helping to prevent aggregation.

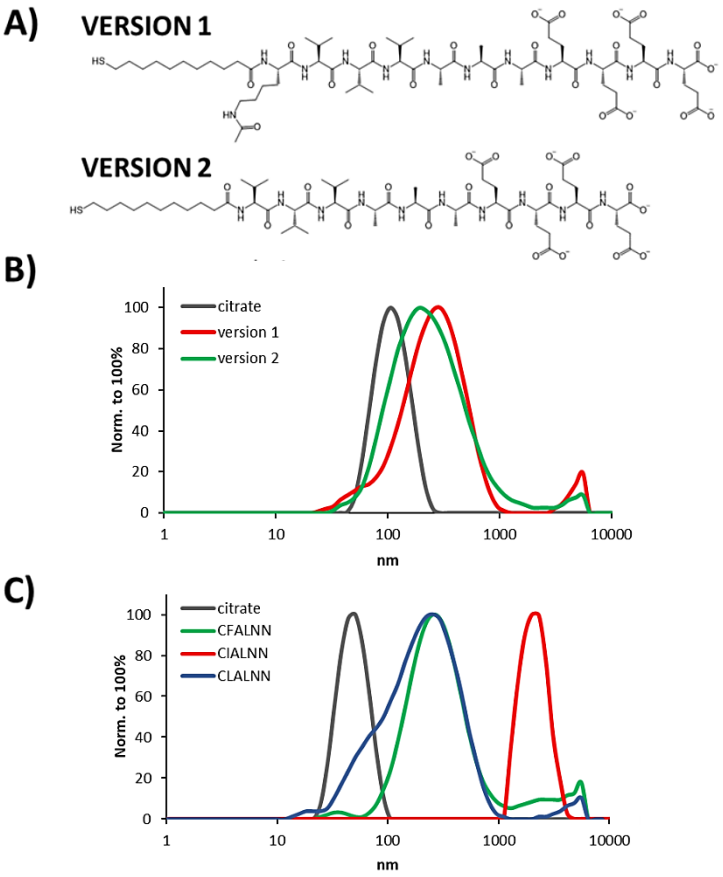

Figure 3.3. (A) Chemical structures of single-chain analogues of molecule **3**: version 1 contains an acetylated Lys residue (to neutralize the charged side-chain as would occur if an alkyl chain was attached in this position): and in version 2 the Lys residue is omitted. (B) Intensity size distributions by DLS for 100 nm GNPs coated with the two versions of amphiphile **3**. Neither of these molecules stabilize the GNPs, demonstrating the stabilizing effect of **3** is due to the presence of two mercaptoundecanoyl chains. (C) Variants of CVALNN with Phe, Ile, and Leu in place of Val fail to stabilize 40 nm GNPs. Measurements performed in PBS, pH 7.2. Intensities are normalized to 100%.

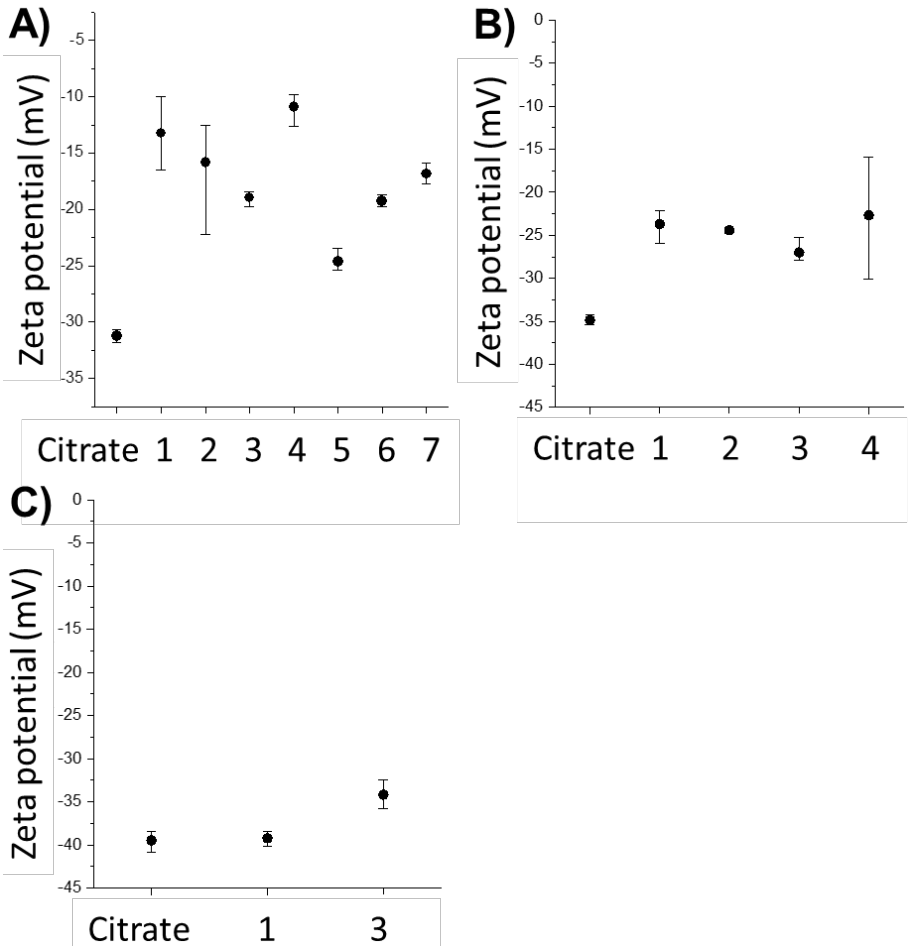

Figure 3.4. Zeta-potential values for: (A) 20 nm; (B) 40 nm; (C) 100 nm GNPs with citrate and peptide/amphiphile coatings. Coated GNPs were prepared in PBS (pH 7.2) and diluted 10 times with water prior the measurement. An average of three measurements is shown here. Error bars indicate max and min values.

UV-Vis spectroscopy and TEM were utilized to further probe the properties of the coated GNPs. Citrate-capped GNPs exhibit characteristic surface plasmon resonance (SPR) peaks: for our 20, 40, and 100 nm GNPs peak maxima occur at 521, 530, and 577 nm, respectively (**Figure 3.5**). Coated GNPs that exhibited no aggregation by DLS showed no peak broadening or any significant red-shift, (**Figure 3.5**); both features would be indicative of

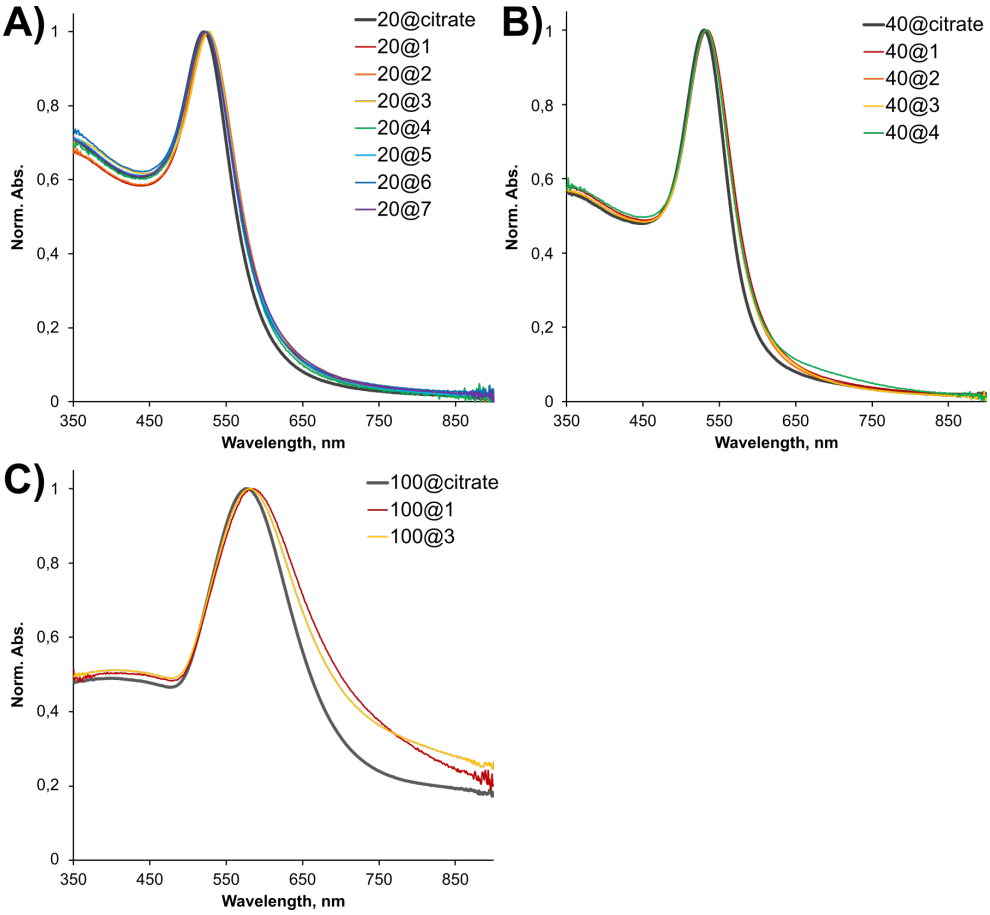

Figure 3.5. Normalized UV-Vis spectra of coated GNPs: A) 20 nm GNPs coated with **1**-**7**; B) 40 nm GNPs with molecules **1**-**4**, and; C) 100 nm GNPs coated with molecules **1** and **3**. Conditions: PBS, pH 7.2.

aggregation. Small red-shifts, between 1-7 nm, were observed and were attributed to an alteration in the dielectric constant at the GNP surface due to substitution of citrate by the peptides and amphiphiles. Some peak broadening was observed for 100 nm GNPs; this is likely a result of the natural sedimentation of these larger nanoparticles: the DLS data showed the samples were monodisperse and this was confirmed by TEM analysis (*vide infra)*, in which no GNP aggregates were observed (**Figure 3.6**). These

UV-Vis spectra confirm the results of the DLS experiments: molecules **1**-**7** are capable of stabilizing 20 nm particles, **1-4** can stabilize 40 nm particles, but only **1** and **3** provide a stabilizing coating for 100 nm GNPs.

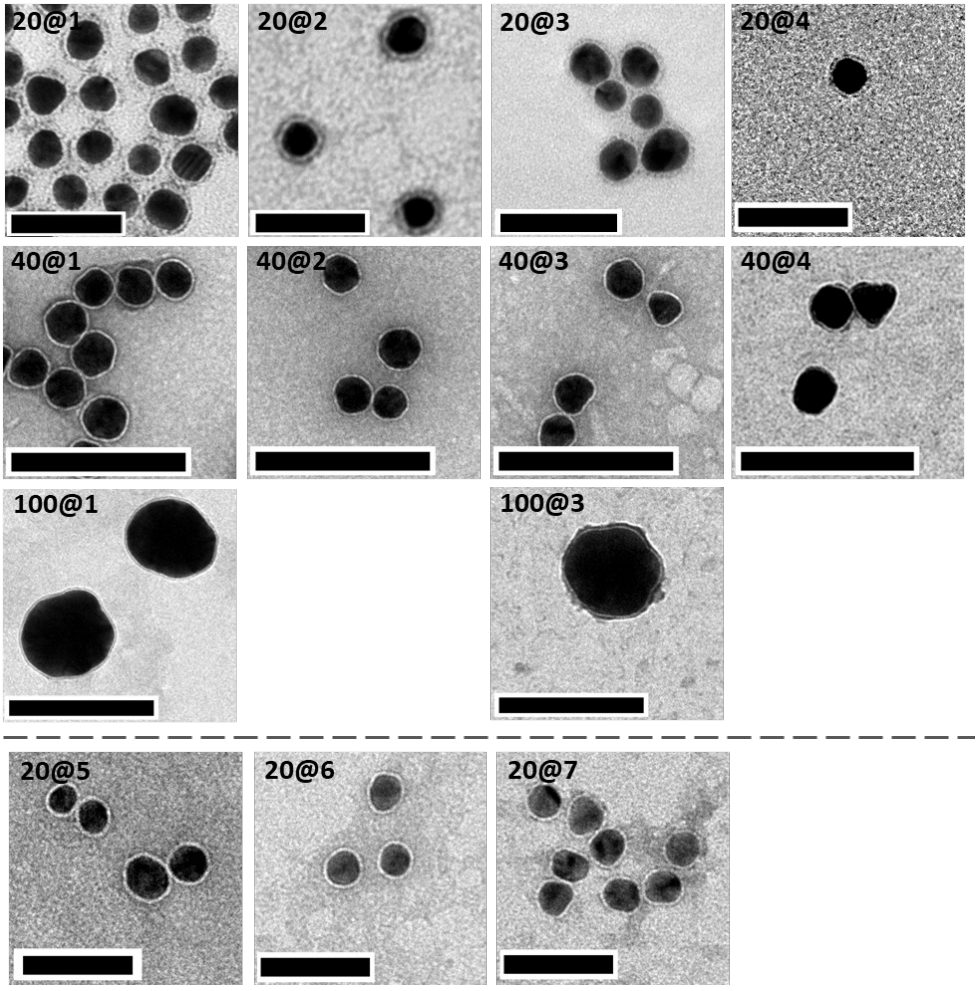

Figure 3.6. TEM micrographs of peptide-capped GNPs. Top row: 20 nm GNPs coated with molecules **1**-**4**; second row: 40 nm GNPs coated with **1**-**4**, and; third row: 100 nm GNPs coated with molecules **1** and **3**. Images for 20 nm GNPs coated with molecules **5**-**7** are shown on the bottom row and are separated from the rest with a dashed line**.** No TEM images were recorded for 100 nm GNPs coated with molecules **2** and **4** as DLS indicated these samples aggregated. Low magnification images can be found in **Figures S3.15-S3.18**. Scale bars: 20 nm GNPs = 50 nm; 40 and 100 nm GNPs = 200 nm.

All GNPs that had been demonstrated to have stable coatings were subsequently analyzed by TEM (**Figure 3.6**). The samples were negatively stained with uranyl acetate to determine whether the coating around the particles could be observed and also to ensure our coating method was effective at preventing fiber formation.

Gratifyingly, a thin uniform shell around each particle was clearly visible indicating the presence of an ordered coating.[38] It should be noted that the observation of this surface layer around the 100 nm GNPs is in part hampered by the Fresnel fringes that arise from the underfocus imaging that is needed for their visualization in TEM.[54]

For all the samples analyzed no GNP aggregation or fibers were observed, (**Figure 3.6** and **Figures S3.15-S3.18**), confirming the devised coating method was effective.

3.3.4 Coverage density of GNP coatings

As the TEM images appeared to indicate dense monolayers were formed on the surface of the GNPs, coverage densities were determined. High coverage densities indicate a tightly-packed ligand shell is formed around the GNP, leading to increased particle stability.[36, 38] Through incorporation of a tyrosine (Tyr, Y) residue, coverage densities were determined using UV-Vis spectroscopy; a similar method has been employed previously.[6] Amphiphile **1** was therefore synthesized with a terminal Tyr residue (see **Scheme S3.1** for the structure), and the GNPs were coated in the manner described in the previous section. The UV-Vis absorbance of the supernatant, containing the unbound amphiphile, was measured after two cycles of centrifugation. As the initial concentration of peptide was known, it was possible to establish the amount of peptide attached to the GNPs. Combining this information with

knowledge of the concentration and surface area of the GNPs allowed coverage densities to be calculated (for full details, see **3.5.12**). Using this method, the following coverage densities were determined: 3.72 peptides/nm^2 for 20 nm GNPs, 2.47 peptides/nm^2 for 40 nm GNPs, and for 100 nm GNPs the density was determined to be 2.17 peptides/nm^2. These densities are high: comparable densities determined by Shaw *et al.* for their 25 nm GNPs were 2.55 or 2.4 peptides/nm^2 depending on the peptide sequence used;[38] and a density of 0.72 peptides/nm^2 for 5.4 nm GNPs was determined for samples prepared by Mikolajczak *et al*.[6] It is likely that these high coverage densities are one of the reasons why the GNPs are so effectively stabilized.

3.3.5 Peptide and amphiphile assembly on GNP surfaces

Several studies have highlighted that the surface curvature of nanoparticles can affect the secondary structure of covalently attached peptides.[38, 47, 55] We have demonstrated that peptide amphiphiles **1-3** adopt defined β-sheet secondary structures in solution, therefore their structures on the surface of GNPs were studied to determine whether they retain this structure when confined to a surface. Initially, the amphiphiles were probed using CD spectroscopy, **Figure S3.19**. A signal with a minimum at 215 nm, corresponding to the presence of β-structure, was detected on 20 nm GNPs coated with **1** even at GNP concentrations as low as 6 nM. Peptide amphiphile **2** behaved similarly but exhibited a minimum at 212 nm. The structure formed by **3** was more difficult to interpret as the signal was very noisy due to both the low concentration of amphiphile and the scattering of the GNPs.

Analysis of secondary structure formation on larger GNPs using CD spectroscopy was problematic due to the strong scattering of the particles. Therefore, to probe the structures of **1-3** on the GNPs, and to obtain quantitative data, Fourier-transform infra-red (FTIR) spectra were obtained.

The data collected, **Figure 3.7,** and **Figure S3.20**, confirm that **1-3** do indeed form β-sheet structures, both in isolation and on GNP surfaces. The position of the peak maximum of the Amide I region is suggestive of the predominant secondary structure type.[6, 47, 56] Thus, an Amide I peak located between 1629-1640 cm^{-1} is indicative of β-structure; and 1649-1656 cm^{-1} is a typical position for α-structured peptides. Usually, the Amide I peak is a superposition of different backbone conformations and can be deconvoluted to quantify the amount of different types of secondary structure present.

Deconvolution and fitting of the Amide I region showed that, in isolation, **1** and **3** almost exclusively adopted a β-sheet structure (**Figure 3.7A&E** and **Table 3.2**), whilst **2** exhibited 85% β-sheet content, (**Figure 3.7I**, and **Table 3.2**). This high propensity to form β-structures in solution was translated to the surface of 20 nm GNPs for all three molecules; they all self-assembled to form structures with >70% β-content, (**Figure 3.7B,F&J**). For 40 and 100 nm particles, the data was more challenging to interpret. The large sizes of the particles meant that surface selection rules, which state that vibrations whose dipole moment are parallel to the nanoparticle surface will be suppressed,[57] strongly influenced the spectra obtained. The general trend however, appeared to be that the amphiphiles displayed a lower amount of β-structure on these larger particles, (**Figure 3.7C-H** and **Table 3.2**). This decrease in the amount of β-structure observed is in contrast to other studies. It should be noted however that previous studies have examined particles between 5 – 25 nm in diameter,[36, 38] where this study looks at GNP sizes of

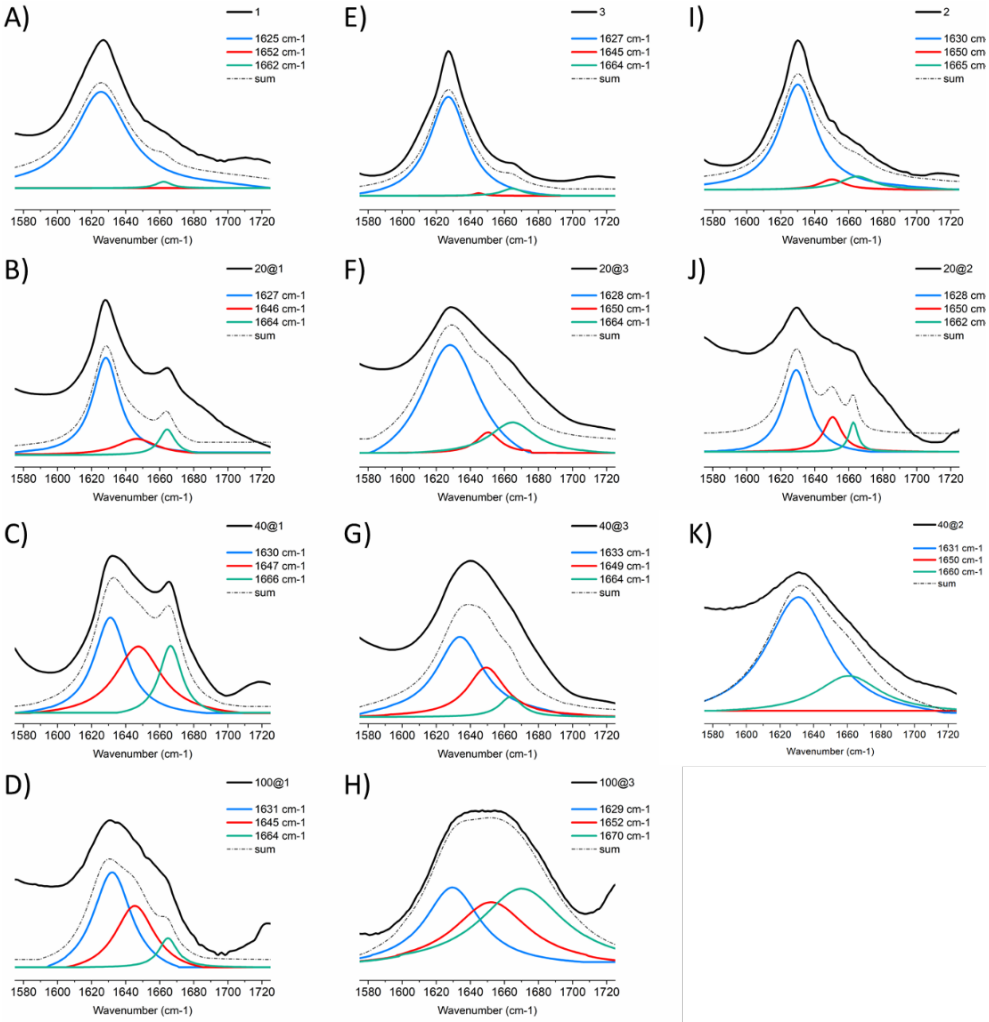

Figure 3.7. Deconvoluted Amide I peaks for **1-3** in powder form, and on GNP surfaces. (A) **1**, and as a coating on: (B) 20 nm; (C) 40 nm; and (D) 100 nm GNPs. (E) **3**, and as a coating on: (F) 20 nm; (G) 40 nm, and; (H) 100 nm GNPs. (I) **2**, and as a coating on: (J) 20 nm; and (K) 40 nm GNPs. Measurements were performed on lyophilized powders of peptide amphiphiles and on hydrated films for GNPs conjugates.

Table 3.2. Secondary structure percentages for amphiphiles in isolation and when bound to the surface of 20, 40, and 100 nm GNPs.

Sample	β, %	α, %	others, %
1	97.7	0	2.3
20@1	73.8	13.1	13.1
40@1	41.8	38.6	19.6
100@1	54.0	35.7	10.3
3	94.8	0.8	4.4
20@3	72.5	7.7	19.8
40@3	60.9	31.4	7.7
100@3	29.0	29.9	41.1
2	85.2	5.4	9.4
20@2	70.4	19.4	10.2
40@2	76.9	23.1	

≥20 nm, therefore there is no precedent for structure formation on particles of this size. We hypothesize that, along with the detrimental effect of the surface selection rules, the decrease in propensity to form ordered structures observed may be related to several different factors. Firstly, the coverage densities decrease with increasing particle size, therefore the spacing between the amphiphiles is increased making it more difficult for intermolecular hydrogen bonds, and therefore extended β-sheets, to form. Secondly, the amphiphiles are longer than the peptide sequences previously studied meaning they have more conformational freedom which can affect self-assembly. This is supported by the fact that **2**, which has a shorter alkyl chain than **1**, is more ordered on both 20 and 40 nm GNPs. Finally, the low curvature of 100 nm GNPs means **1** is likely to be more tightly packed than **3** as it only has a single alkyl chain meaning more amphiphiles can be attached to the surface, therefore the level of self-assembly is increased.

This is reflected in the relative percentages of β-structure observed. While it can be concluded that the peptide amphiphiles do self-assemble to form defined β-structures on 20 nm particles, and appear to do so on 40 and 100 nm GNPs, more detailed studies will be required to fully account for the effects of nanoparticle size and the surface selection rules.

In addition to analyzing the amide I band, analysis of the region between 2700-3500 cm^{-1} provides information about the packing of alkyl chains, (for spectra, see **Figures S3.20-S3.21**). The band centered around 2850 cm^{-1} is attributed to the CH_2 symmetric stretching mode and can be used to infer information regarding the alkyl chain packing.[58, 59] The well-defined and sharp bands observed for our molecules indicate they possess tightly packed alkyl chains when not conjugated to GNPs. Upon conjugation, a shift to higher wavenumbers and a broadening of the band is observed. This indicates the packing of the alkyl chains is less ordered, with the shift being more pronounced with larger GNP sizes. This is consistent with the observation that coverage density decreases with increasing particle size, meaning the molecules are further apart and therefore not optimally spaced to pack regularly.

3.3.6 Stability of capped GNPs to electrolytes

DLS, TEM, and UV-Vis data have demonstrated that both **1** and **3** can stabilize a range of GNP sizes in PBS. Particle stability at elevated salt concentrations provides information about the type of stabilizing interactions present, for example: if GNP stability is based solely upon repulsive electrostatic interactions, as with citrate-coated nanoparticles, then as the electrolyte concentration is increased the magnitude of electrostatic repulsion is diminished as the surface charge of the GNPs is screened by

the salt. As the stabilization of GNPs by both **1** and **3** is presumed to be largely due to hydrophobic effects, the GNPs should be resistant to high salt concentrations.

Five different salt concentrations were tested: 0 mM; 150 mM; 500 mM; 1.5 M; and 3.0 M. The GNPs were incubated with these salt solutions and their aggregation was monitored by UV-Vis, **Figure 3.8A-C** and **Figure S3.22**. To compare aggregation tendencies, the optical density (OD) at each salt concentration was normalized to the intensity of the LSPR peak maximum at 0 mM NaCl, (see **3.5.13** for full details).

Whilst **1** was able to stabilize 20 nm GNPs at moderate salt concentrations, at concentrations >1.5 M aggregation was evident. The same molecule could only stabilize 40 and 100 nm particles at low salt concentrations. In contrast, **2** stabilized both 20 and 40 nm particles, even at high salt concentrations (**2** was not tested with 100 nm particles as aggregation is observed in PBS). Finally, amphiphilic molecule, **3**, proved highly effective at stabilizing the 20 nm particles, but some aggregation was present for 40 nm particles, and for 100 nm particles severe aggregation occurred at salt concentrations >1.5 M. Our peptide molecule, **4**, outperformed peptides **5-7** on 20 nm particles and it was demonstrated to stabilize these particles even at high salt concentrations (**Figure 3.8A**). **4** was not effective at stabilizing 40 nm particles however. What is particularly interesting is that **1** is less effective at high salt concentrations in comparison to **2** and **3**. It is assumed this is due to the longer alkyl chain length of **1**, meaning the peptides have increased conformational freedom which may allow salt molecules to penetrate the coating, leading to destabilization.

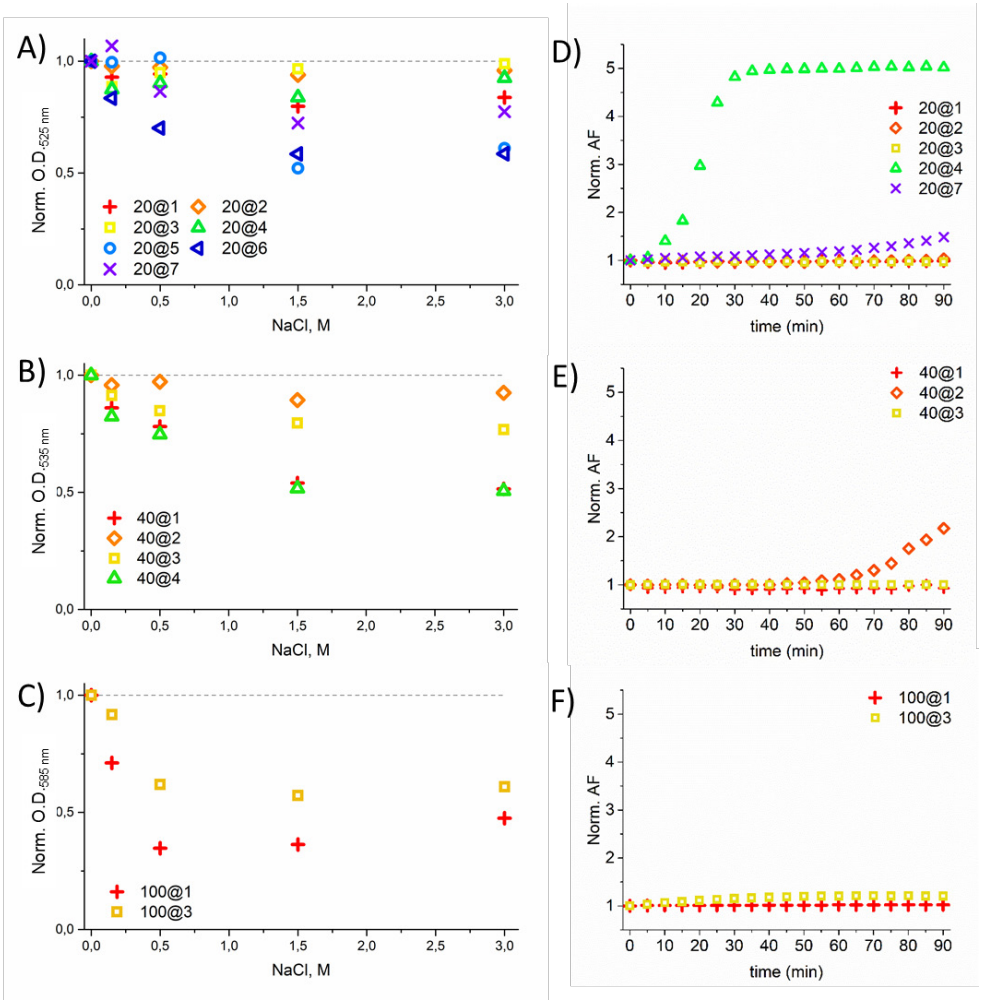

Figure 3.8. GNP stability to electrolytes and DTT. Aggregation tendencies in 0−3 M NaCl are shown for: (A) 20 nm, (B) 40 nm, and (C) 100 nm GNPs. The Y-axis represents OD at the LSPR peak maximum, the wavelength of which varies with GNP size and is as follows: (A) 525 nm, (B) 535 nm, and (C) 585 nm. The OD is normalized to the value for 0 mM NaCl in each case. A decrease in normalized OD indicates aggregation. Aggregation after exposure to 1 M DTT is expressed by the normalized aggregation factor (AF) for: (D) 20 nm, (E) 40 nm, and (F) 100 nm GNPs. Exposure to DTT was conducted in the presence of NaCl at the following concentrations: (D, E) 400 mM and (F) 150 mM.

3.3.7 Stability against DTT-induced aggregation

GNP stability to dithiothreitol (DTT) was also probed, as DTT is a small molecule that is known to be capable of displacing thiol ligands from gold surfaces, leading to GNP aggregation.[30, 51] Resistance to thiol displacement indicates the gold surface is shielded from the surrounding solvent environment. Stability in the presence of DTT is important for GNPs with intended *in vitro* and *in vivo* functions, as intracellular thiol-containing molecules, such as glutathione, could displace the coating from the surface. In these experiments, DTT acts as a model for such molecules.

The experimental protocol was adapted from one devised by Mei *et al.*[51] The GNP samples were incubated with 1 M DTT, and their UV-Vis spectra were recorded over a period of 90 mins, **Figure S3.23**. NaCl was added as its presence leads to additional screening effects, speeding up the aggregation process. 400 mM NaCl was added to 20 nm and 40 nm GNP samples, but as this concentration led to aggregation of 100 nm GNPs, a lower NaCl concentration of 150 mM was employed. To quantify the amount of aggregation as a result of ligand displacement, we used the normalized aggregation factor (AF) parameter.[51] To calculate this parameter, two absorbance peaks were compared: the original plasmon band and an emerging peak found at higher wavelengths (615 nm for 20 and 40 nm GNPs; and 700 nm for 100 nm GNPs), the emergence of this second peak is indicative of aggregation. The latter was divided by the former to yield the AF, which in turn was normalized to the absorbance at 0 minutes (**Figure 3.8D-F**). If the normalized AF is higher than 1, it indicates aggregation is occurring.

The amphiphilic molecules **1-3** effectively insulated the surface of 20 nm GNPs from DTT, though particles coated with **2** showed a slight tendency to aggregate after 80 mins (**Figure 3.8D**). This effect was more prominent when 40 nm GNPs were studied: aggregation of these particles with **2** was evident after 50 mins and aggregation was more pronounced after 90 mins when compared to the 20 nm particles (**Figure 3.8E**). 100 nm particles were coated with amphiphiles **1** and **3** and both appear to stabilize the particles over the time range tested, although **3** does show a small increase in AF after 15 mins; this does not increase significantly for the remainder of the experiment however (**Figure 3.8F**).

When **4** was examined on 20 nm GNPs, aggregation in the presence of DTT was observed almost immediately with severe aggregation being observed after 15 mins (**Figure 3.8D**). In comparison, peptide **7**, the best performing reference peptide from the electrolyte-induced aggregation experiments, showed significantly less aggregation than **4**, although an AF of 1.5 was recorded after 90 mins (**Figure 3.8D**).

The results of this DTT competition experiment highlight the importance of the alkyl chains and demonstrate that they can effectively shield the GNP surface from small molecules. This further reinforces the idea that these peptide amphiphiles form dense, well-ordered monolayers on the GNP surface.

3.4 Conclusions

We have developed four molecules: three peptide amphiphiles and one peptide, and evaluated their ability to act as coatings for different sizes of GNPs. The DLS, UV−vis, and TEM data indicate that amphiphiles **1** and **3** are capable of stabilizing all three sizes of GNPs under biologically relevant conditions (**Scheme 3.2**), while 2 can stabilize 20 and 40 nm particles. FTIR analysis revealed that the amphiphiles retain their abilities to self-assemble on the surfaces of the GNPs, leading to the creation of dense, ordered monolayers.

The stabilizing effect of **1** is likely due to its long alkyl chain which provides increased hydrophobicity. For **3**, stability is provided by a combination of hydrophobicity and the bidentate nature of the ligand, meaning that it has a stronger interaction with the GNPs and therefore an increased stabilizing effect. Both **1** and **3** proved to be resistant to DTT over 90 min, and **3** outperformed **1** at high-salt concentrations. We hypothesize that this is to do with the packing of the peptides because the longer chain of **1** provides more conformational flexibility, meaning the peptides are not as ordered and the protective “shell” created by the amphiphile is more permeable. his is supported by the fact that **3** is more structured on 40 nm particles, suggesting it is better self-assembled than **1**.

While **1** and **3** are universal sequences and stabilize all three GNP sizes tested, it should be noted that amphiphile **2** and our peptide, **4**, could stabilize both 20 and 40 nm GNPs (**Scheme 3.2**). Therefore, in addition to creating two universal stabilizing sequences, we have added other designs to the “toolkit” of peptide-based stabilizing sequences for GNPs, and we have demonstrated that 4 outperforms the current “state-of-the-art” peptide

sequences. Future work will focus on derivatizing these molecules with targeting and/or therapeutic moieties to probe their activities *in vitro* and *in vivo*.

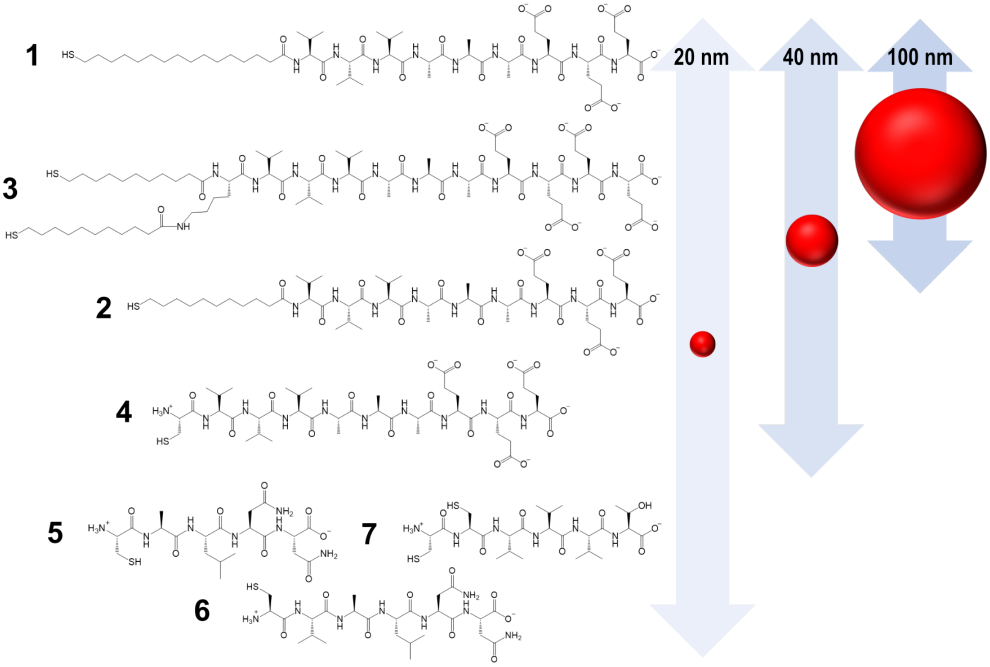

Scheme 3.2. GNPs (to scale) and the molecules capable of stabilizing each size. Arrows represent the span of molecules that are capable of stabilizing each GNP size, that is, all molecules can act as coatings for 20 nm GNPs, **1**–**4** stabilize 40 nm GNPs, and **1** and **3** are effective coatings for the 100 nm GNPs.

3.5 Experimental section

3.5.1 Materials

All chemicals were purchased from Sigma-Aldrich except where stated. TFA, piperidine, DMF, DCM, and acetonitrile were purchased from Biosolve. Oxyma pure was supplied by Carl Roth GmbH. TEM grids (Formvar Carbon/Copper, 200 mesh) were purchased from Electron Microscopy Sciences.

3.5.2 Peptide and peptide amphiphile synthesis

All peptide and peptide amphiphile sequences were synthesized by solid-phase peptide synthesis using standard Fmoc-chemistry protocols. 20% piperidine in DMF was used as the deprotection agent, and DIC/Oxyma were employed as activator/activator base. All sequences were synthesized on Wang resin preloaded with the corresponding C-terminal residue. All the molecules were cleaved from the resin using 1.5% deionized water, 2.5% triisopropylsilane (TIS), 2.5% phenol, and 2.5% 3,4-ethylenedioxythiophene (EDOT) in trifluoroacetic acid (TFA). The crude peptides and amphiphiles were precipitated into cold diethyl ether, pelleted by centrifugation, redissolved in water, and lyophilized prior to purification.

3.5.3 Peptide and peptide amphiphile purification

HPLC purification was performed on a Shimadzu system equipped with two LC-20AR pumps, an SPD-20A UV−vis detector, and a Phenomenex Kinetex EVO C18 column. The mobile phases were water and acetonitrile, containing either 0.1% TFA, for peptides, or 0.1% NH_3, for amphiphiles. The purity of

the compounds was assessed using LCMS (**Figures S3.1−S3.11**). All purified molecules were lyophilized and stored at −20 °C until required.

3.5.4 Gold nanoparticle synthesis

The 20 nm particles were prepared according to a combination of the Turkevich and Frens' methods.[49, 50] In short, 25 mL of a 1 mM chloroauric acid ($HAuCl_4$) solution was brought to a gentle boil while stirring. 5 mL of a 1% trisodium citrate dehydrate solution was added to the boiling solution, and a condenser was attached to the flask. The mixture was boiled for 10 min before the sample was cooled to room temperature. The size of the particles was confirmed using DLS.

A seed-mediated growth was used to obtain particles of 40 and 100 nm diameter.[15] Seeds were prepared by heating 15 mL of a 2.2 mM sodium citrate solution to boiling. 50 µL of 50 mM $HAuCl_4$ was added, and the mixture boiled for 10 min, before the temperature of the solution was maintained at 90 °C. To perform controlled overgrowth of the seeds, the sequential addition of small amounts (1−3 mL) of 10 mM citrate solution was alternated with that of a 1 mM $HAuCl_4$ solution (0.35−1 mL). It is critical to keep the molar ratio of citrate:$HAuCl_4$ at 10:1. This manipulation was repeated as many times as required to obtain particles of the desired size, which was monitored by DLS. The sizes of the GNPs were confirmed by TEM and DLS (**Figure S3.13**).

3.5.5 Preparation of peptide-capped GNPs

Coating of the GNPs was performed via a ligand exchange strategy. The desired coating molecule was dissolved in DMSO and added to a stirred GNP suspension. The volumes of coatings and GNPs were such that the final concentration of DMSO in the solution was 20−25% (v/v). After 1 h, the

sample was centrifuged, (14,000 rpm, 45 min for 20 nm GNPs; 10 min for 40 nm GNPs; 5 min for 100 nm GNPs), and the supernatant removed and replaced with 5% DMSO. Size exclusion chromatography was performed to remove any remaining free ligand, and the elution buffer was phosphate buffered saline (PBS).

3.5.6 Dynamic light scattering measurements

Size distributions of all particles in this study were obtained by dynamic light scattering (DLS) using a Zetasizer Nano-7 S (Malvern Instruments) with a 633 nm laser wavelength and a 173° fixed scattering angle. The temperature was maintained at 25 °C during the measurements. An aliquot of 500 µL for each sample was placed into a disposable plastic cuvette, and three separate measurements were recorded from which a mean hydrodynamic diameter was calculated.

3.5.7 Zeta potential measurements

All ζ potential measurements were performed on a Zetasizer Nano-7 S (Malvern Instruments) equipped with the same laser as described above. Samples in PBS were diluted 10 times with deionized water to reduce the salt concentration to <20 mM. Sample aliquots of 1 mL were placed in a universal dip cuvette, and the ζ potential was calculated from an average of three measurements.

3.5.8 UV−Vis spectroscopy

Spectra were recorded using a Cary 300 UV−vis spectrophotometer (Agilent). Samples were placed in 1 mm quartz cuvettes, and spectra were recorded between 900 and 350 nm unless otherwise stated. Samples were

diluted with either MQ water or PBS as appropriate to provide an OD in the range of 0.6−1.0. All spectra were normalized to provide an OD = 1 to aid comparison, except for the spectra recorded for the electrolyte-induced aggregation experiments which were calculated as described below.

3.5.9 Transmission electron microscopy

For transmission electron microscopy (TEM) measurements, a 10 µL droplet of the sample of interest was placed on a continuous carbon grid on a copper support (200 mesh) and left for 20 min. The excess liquid was removed by manually blotting with filter paper. The grid was washed with deionized water once and blotted again. Uranyl acetate staining (0.5% for fiber samples and 1% for GNP samples) was applied, followed immediately by blotting. Images were collected on a JEM1400 Plus (JEOL) transmission electron microscope operated at 80 kV and equipped with a CCD camera or on the TU/e Sphera (TFS, www.cryotem.nl) operated at 200 kV, equipped with a 4096 × 4096 CDD camera.

3.5.10 Circular dichroism spectroscopy

Circular dichroism (CD) spectra of the amphiphiles and peptides were recorded using a JASCO J-815 spectropolarimeter, fitted with a Peltier temperature controller. All measurements were performed at 20 °C. Samples were measured in quartz cuvettes with a 2 mm path length, and spectra were recorded from 260 to 190 nm at 2 nm intervals with a 1 nm bandwidth. All spectra were converted to mean residue ellipticity (deg cm^2 $dmol \cdot res^{-1}$) using equation 1:

$$[\theta] = \frac{100 * [\theta]obs}{c * n * l} \quad (1),$$

where $[\theta]_{obs}$ is the observed ellipticity in mdeg, *c* is the concentration of the sample in mM, *n* is the number of amino acids in the peptide or amphiphile, and *l* is the path length of the cuvette in cm.

3.5.11 Attenuated total reflection-infrared spectroscopy

Attenuated total reflection-infrared (ATR-IR) spectra were recorded on an Excalibur FTS 4000 setup equipped with a “golden gate”. For peptide-capped GNPs, the sample preparation was as follows: a 5 µL drop of a highly concentrated sample in D_2O was placed on top of the crystal and dried under a stream of air. After a uniform film was formed, a spectrum was recorded. For peptides, a lyophilized powder was used. Deconvolution and fitting of the Amide I peaks to the Lorenz function were performed using Origin Pro.

3.5.12 Coverage density measurements

Coverage densities were determined for all three sizes of the GNPs used in this study. Peptide amphiphile **1** was modified with a Tyr residue and was used to prepare coated GNPs. The supernatant of the first centrifugation cycle was collected and combined with the supernatant of the following washes. As the concentration of Tyr-modified **1** added to the GNP solution was known, the concentration of peptide in the combined supernatants was determined using UV−vis. The average size and number concentration of the GNPs was also calculated,[60] and coverage densities were determined from this information.

3.5.13 Stability to electrolyte-induced aggregation

An aqueous GNP suspension was mixed with a 4.5 M NaCl solution to yield samples with the following final concentrations of salt: 150 mM, 500 mM,

1.5 M, and 3.0 M. The final volume of each sample and the GNP concentration remained constant for all samples tested. The optical densities of each sample at their maximum absorption wavelength were recorded using an Infinite M1000 plate-reader (Tecan). A spectrum from 650−400 nm was also recorded. This is because when GNPs aggregate, they exhibit a red-shift and often a broadening of the plasmon band. The OD values at the maximum absorption wavelength (OD_{LSPR}) corresponded to the control sample (0 M NaCl), and this was taken as the value of a pristine, nonaggregated sample. The OD of the samples with increasing amounts of NaCl were compared to this sample, and a decrease in the value of the OD indicated aggregation. The LSPR peak maxima for GNPs of different sizes were as follows: 525 nm for 20 nm GNPs, 535 nm for 40 nm GNPs, and 585 nm for 100 nm GNPs.

3.5.14 Stability study by means of DTT-induced aggregation

The protocol adopted was adapted from that published by the Mattoussi group.[51] 4 M DTT, 2 M NaCl, deionized water, and coated GNPs were mixed to yield a solution with final concentrations of 1 M DTT and 400 mM NaCl, (150 mM for 100 nm GNPs). Addition of NaCl accelerates aggregation due to Debye screening effects. The OD of the final mixture was adjusted to a value of 0.35. Aggregation was monitored by UV−vis using a BioDrop Duo UV−vis spectrophotometer (Harvard Bioscience) for 90 min with a 5 min interval between the data points. The aggregation factor (AF) was expressed as a ratio between the OD at the peak maximum of the LSPR and the OD at 615 nm for 20 and 40 nm GNPs and the OD at 700 nm for 100 nm GNPs.

3.6 References

1. Kennedy, L. C.; Bickford, L. R.; Lewinski, N. A.; Coughlin, A. J.; Hu, Y.; Day, E. S.; West, J. L.; Drezek, R. A., A new era for cancer treatment: gold-nanoparticle-mediated thermal therapies. *Small* **2011,** *7* (2), 169-183.

2. Riley, R. S.; Day, E. S., Gold nanoparticle-mediated photothermal therapy: applications and opportunities for multimodal cancer treatment. *Wiley Interdiscip Rev Nanomed Nanobiotechnol* **2017,** *9* (4):e1449.

3. Dreaden, E. C.; Austin, L. A.; Mackey, M. A.; El-Sayed, M. A., Size matters: gold nanoparticles in targeted cancer drug delivery. *Ther Deliv* **2012,** *3* (4), 457-478.

4. Han, G.; Ghosh, P.; Rotello, V. M., Functionalized gold nanoparticles for drug delivery. *Nanomedicine (Lond)* **2007,** *2* (1), 113-123.

5. Corma, A.; Garcia, H., Supported gold nanoparticles as catalysts for organic reactions. *Chem Soc Rev* **2008,** *37* (9), 2096-2126.

6. Mikolajczak, D. J.; Heier, J. L.; Schade, B.; Koksch, B., Catalytic Activity of Peptide-Nanoparticle Conjugates Regulated by a Conformational Change. *Biomacromolecules* **2017,** *18* (11), 3557-3562.

7. Pengo, P.; Baltzer, L.; Pasquato, L.; Scrimin, P., Substrate modulation of the activity of an artificial nanoesterase made of peptide-functionalized gold nanoparticles. *Angew Chem Int Ed Engl* **2007,** *46* (3), 400-404.

8. Gao, J.; Liu, D.; Wang, Z., Microarray-based study of carbohydrate-protein binding by gold nanoparticle probes. *Anal Chem* **2008,** *80* (22), 8822-8827.

9. Jena, B. K.; Raj, C. R., Electrochemical biosensor based on integrated assembly of dehydrogenase enzymes and gold nanoparticles. *Anal Chem* **2006,** *78* (18), 6332-6339.

10. Almeida, J. P. M.; Lin, A. Y.; Figueroa, E. R.; Foster, A. E.; Drezek, R. A., In vivo gold nanoparticle delivery of peptide vaccine induces anti-tumor immune response in prophylactic and therapeutic tumor models. *Small* **2015,** *11* (12), 1453-1459.

11. Kang, S.; Ahn, S.; Lee, J.; Kim, J. Y.; Choi, M.; Gujrati, V.; Kim, H.; Kim, J.; Shin, E. C.; Jon, S., Effects of gold nanoparticle-based vaccine size on lymph node delivery and cytotoxic T-lymphocyte responses. *J Control Release* **2017,** *256*, 56-67.

12. Niikura, K.; Matsunaga, T.; Suzuki, T.; Kobayashi, S.; Yamaguchi, H.; Orba, Y.; Kawaguchi, A.; Hasegawa, H.; Kajino, K.; Ninomiya, T.; Ijiro, K.; Sawa, H., Gold nanoparticles as a vaccine platform: influence of size and shape on immunological responses in vitro and in vivo. *ACS Nano* **2013,** *7* (5), 3926-3938.

13. Link, S.; El-Sayed, M. A., Size and temperature dependence of the plasmon absorption of colloidal gold nanoparticles. *J Phys Chem B* **1999,** *103* (21), 4212-4217.

14. Hakkinen, H., The gold-sulfur interface at the nanoscale. *Nat Chem* **2012,** *4* (6), 443-455.

15. Bastus, N. G.; Comenge, J.; Puntes, V., Kinetically Controlled Seeded Growth Synthesis of Citrate-Stabilized Gold Nanoparticles of up to 200 nm: Size Focusing versus Ostwald Ripening. *Langmuir* **2011,** *27* (17), 11098-11105.

16. Grzelczak, M.; Perez-Juste, J.; Mulvaney, P.; Liz-Marzan, L. M., Shape control in gold nanoparticle synthesis. *Chem Soc Rev* **2008,** *37* (9), 1783-1791.

17. Piella, J.; Bastus, N. G.; Puntes, V., Size-Controlled Synthesis of Sub-10-nanometer Citrate-Stabilized Gold Nanoparticles and Related Optical Properties. *Chemistry of Materials* **2016,** *28* (4), 1066-1075.

18. Bhamidipati, M.; Fabris, L., Multiparametric Assessment of Gold Nanoparticle Cytotoxicity in Cancerous and Healthy Cells: The Role of Size, Shape, and Surface Chemistry. *Bioconjug Chem* **2017,** *28* (2), 449-460.

19. Fraga, S.; Brandao, A.; Soares, M. E.; Morais, T.; Duarte, J. A.; Pereira, L.; Soares, L.; Neves, C.; Pereira, E.; Bastos Mde, L.; Carmo, H., Short- and long-term distribution and toxicity of gold nanoparticles in the rat after a single-dose intravenous administration. *Nanomed J* **2014,** *10* (8), 1757-1766.

20. Goodman, C. M.; McCusker, C. D.; Yilmaz, T.; Rotello, V. M., Toxicity of gold nanoparticles functionalized with cationic and anionic side chains. *Bioconjug Chem* **2004,** *15* (4), 897-900.

21. Liu, S. H.; Han, M. Y., Silica-Coated Metal Nanoparticles. *Chem-Asian J* **2010,** *5* (1), 36-45.

22. Jokerst, J. V.; Lobovkina, T.; Zare, R. N.; Gambhir, S. S., Nanoparticle PEGylation for imaging and therapy. *Nanomedicine (Lond)* **2011,** *6* (4), 715-728.

23. Wuelfing, W. P.; Gross, S. M.; Miles, D. T.;Murray, R. W., Nanometer gold clusters protected by surface-bound monolayers of thiolated poly(ethylene glycol) polymer electrolyte. *J Am Chem Soc* **1998,** *120* (48), 12696-12697.

24. Boal, A. K.; Rotello, V. M., Intra- and intermonolayer hydrogen bonding in amide-functionalized alkanethiol self-assembled monolayers on gold nanoparticles. *Langmuir* **2000,** *16* (24), 9527-9532.

25. Templeton, A. C.; Hostetler, M. J.; Warmoth, E. K.; Chen, S. W.; Hartshorn, C. M.; Krishnamurthy, V. M.; Forbes, M. D. E.; Murray, R. W., Gateway reactions to diverse, polyfunctional monolayer-protected gold clusters. *J Am Chem Soc* **1998,** *120* (19), 4845-4849.

26. Ansar, S. M.; Chakraborty, S.; Kitchens, C. L., pH-Responsive Mercaptoundecanoic Acid Functionalized Gold Nanoparticles and Applications in Catalysis. *Nanomaterials* **2018,** *8* (5): e339.

27. Laaksonen, T.; Ahonen, P.; Johans, C.; Kontturi, K., Stability and electrostatics of mercaptoundecanoic acid-capped gold nanoparticles with varying counterion size. *Chemphyschem* **2006,** *7* (10), 2143-2149.

28. Hanske, C.; Sanz-Ortiz, M. N.; Liz-Marzan, L. M., Silica-Coated Plasmonic Metal Nanoparticles in Action. *Adv Mater* **2018,** *30* (27): e1707003.

29. Knowles, B. R.; Yang, D.; Wagner, P.; Maclaughlin, S.; Higgins, M. J.; Molino, P. J., Zwitterion Functionalized Silica Nanoparticle Coatings: The Effect of Particle Size on Protein, Bacteria, and Fungal Spore Adhesion. *Langmuir* **2019,** *35* (5), 1335-1345.

30. Schulz, F.; Vossmeyer, T.; Bastus, N. G.; Weller, H., Effect of the Spacer Structure on the Stability of Gold Nanoparticles Functionalized with Monodentate Thiolated Poly(ethylene glycol) Ligands. *Langmuir* **2013,** *29* (31), 9897-9908.

31. Atukorale, P. U.; Guven, Z. P.; Bekdemir, A.; Carney, R. P.; Van Lehn, R. C.; Yun, D. S.; Silva, P. H. J.; Demurtas, D.; Yang, Y. S.; Alexander-Katz, A.; Stellacci, F.; Irvine, D. J., Structure-Property Relationships of Amphiphilic Nanoparticles That Penetrate or Fuse Lipid Membranes. *Bioconjugate Chem* **2018,** *29* (4), 1131-1140.

32. Levy, R.; Thanh, N. T. K.; Doty, R. C.; Hussain, I.; Nichols, R. J.; Schiffrin, D. J.; Brust, M.; Fernig, D. G., Rational and combinatorial design of peptide capping Ligands for gold nanoparticles. *J Am Chem Soc* **2004,** *126* (32), 10076-10084.

33. Wang, Z.; Levy, R.; Fernig, D. G.; Brust, M., The peptide route to multifunctional gold nanoparticles. *Bioconjugate Chem* **2005,** *16* (3), 497-500.

34. Zhou, G. H.; Liu, Y. Z.; Luo, M.; Li, X. H.; Xu, Q. F.; Ji, X. H.; He, Z. K., Controlled Assembly of Gold Nanoparticles through Antibody Recognition: Study and Utilizing the Effect of Particle Size on Interparticle Distance. *Langmuir* **2013,** *29* (15), 4697-4702.

35. Zhao, C. L.; Qiu, L. H.; Lv, P.; Han, A. L.; Fang, G. Z.; Liu, J. F.; Wang, S., AuNP-peptide probe for caspase-3 detection in living cells by SERS. *Analyst* **2019,** *144* (4), 1275-1281.

36. Colangelo, E.; Chen, Q. B.; Davidson, A. M.; Paramelle, D.; Sullivan, M. B.; Volk, M.; Levy, R., Computational and Experimental Investigation of the Structure of Peptide Monolayers on Gold Nanoparticles. *Langmuir* **2017,** *33* (1), 438-449.

37. Olmedo, I.; Araya, E.; Sanz, F.; Medina, E.; Arbiol, J.; Toledo, P.; Alvarez-Lueje, A.; Giralt, E.; Kogan, M. J., How changes in the sequence of the peptide CLPFFD-NH2 can modify the conjugation and stability of gold nanoparticles and their affinity for beta-amyloid fibrils. *Bioconjugate Chem* **2008,** *19* (6), 1154-1163.

38. Shaw, C. P.; Middleton, D. A.; Volk, M.; Levy, R., Amyloid-derived peptide forms self-assembled monolayers on gold nanoparticle with a curvature-dependent beta-sheet structure. *ACS Nano* **2012,** *6* (2), 1416-1426.

39. Gupta, A.; Moyano, D. F.; Parnsubsakul, A.; Papadopoulos, A.; Wang, L. S.; Landis, R. F.; Das, R.; Rotello, V. M., Ultrastable and Biofunctionalizable Gold Nanoparticles. *Acs Applied Materials & Interfaces* **2016,** *8* (22), 14096-14101.

40. Marson, D.; Guida, F.; Sologan, M.; Boccardo, S.; Pengo, P.; Perissinotto, F.; Iacuzzi, V.; Pellizzoni, E.; Polizzi, S.; Casalis, L.; Pasquato, L.; Pacor, S.; Tossi, A.; Posocco, P., Mixed Fluorinated/Hydrogenated Self-Assembled Monolayer-Protected Gold Nanoparticles: In Silico and In Vitro Behavior. *Small* **2019,** *15* (17): e1900323.

41. Wilder, L. M.; Fies, W. A.; Rabin, C.; Webb, L. J.; Crooke, R. M., Conjugation of an alpha-Helical Peptide to the Surface of Gold Nanoparticles. *Langmuir* **2019,** *35* (9), 3363-3371.

42. Jha, S.; Ramadori, F.; Quarta, S.; Biasiolo, A.; Fabris, E.; Baldan, P.; Guarino, G.; Ruvoletto, M.; Villano, G.; Turato, C.; Gotta, A.; Mancin, F.; Pontisso, P.; Scrimin, P., Binding and Uptake into Human Hepatocellular

Carcinoma Cells of Peptide-Functionalized Gold Nanoparticles. *Bioconjugate Chem* **2017,** *28* (1), 222-229.

43. Cui, H. G.; Webber, M. J.; Stupp, S. I., Self-Assembly of Peptide Amphiphiles: From Molecules to Nanostructures to Biomaterials. *Biopolymers* **2010,** *94* (1), 1-18.

44. Hamley, I. W., Self-assembly of amphiphilic peptides. *Soft Matter* **2011,** *7* (9), 4122-4138.

45. Pashuck, E. T.; Cui, H. G.; Stupp, S. I., Tuning Supramolecular Rigidity of Peptide Fibers through Molecular Structure. *J Am Chem Soc* **2010,** *132* (17), 6041-6046.

46. Hendricks, M. P.; Sato, K.; Palmer, L. C.; Stupp, S. I., Supramolecular Assembly of Peptide Amphiphiles. *Acc Chem Res* **2017,** *50* (10), 2440-2448.

47. Mandal, H. S.; Kraatz, H. B., Effect of the surface curvature on the secondary structure of peptides adsorbed on nanoparticles. *J Am Chem Soc* **2007,** *129* (20), 6356-6357.

48. Micsonai, A.; Wien, F.; Kernya, L.; Lee, Y. H.; Goto, Y.; Refregiers, M.; Kardos, J., Accurate secondary structure prediction and fold recognition for circular dichroism spectroscopy. *Proceedings of the National Academy of Sciences of the United States of America* **2015,** *112* (24), E3095-E3103.

49. Frens, G., Controlled Nucleation for Regulation of Particle-Size in Monodisperse Gold Suspensions. *Nature-Phys Sci* **1973,** *241* (105), 20-22.

50. Turkevich, J.; Stevenson, P. C.; Hillier, J., A Study of the Nucleation and Growth Processes in the Synthesis of Colloidal Gold. *Discuss Faraday Soc* **1951,** (11), 55-75.

51. Mei, B. C.; Oh, E.; Susumu, K.; Farrell, D.; Mountziaris, T. J.; Mattoussi, H., Effects of Ligand Coordination Number and Surface Curvature on the Stability of Gold Nanoparticles in Aqueous Solutions. *Langmuir* **2009,** *25* (18), 10604-10611.

52. Spicer, C. D.; Jumeaux, C.; Gupta, B.; Stevens, M. M., Peptide and protein nanoparticle conjugates: versatile platforms for biomedical applications. *Chem Soc Rev* **2018,** *47* (10), 3574-3620.

53. Piella, J.; Bastus, N. G.; Puntes, V., Size-Dependent Protein-Nanoparticle Interactions in Citrate-Stabilized Gold Nanoparticles: The Emergence of the Protein Corona. *Bioconjugate Chem* **2017,** *28* (1), 88-97.

54. Friedrich, H.; Frederik, P. M.; de With, G.; Sommerdijk, N., Imaging of Self-Assembled Structures: Interpretation of TEM and Cryo-TEM Images. *Angew Chemie-International Edition* **2010,** *49* (43), 7850-7858.

55. White, S. J.; Johnson, S. D.; Sellick, M. A.; Bronowska, A.; Stockley, P. G.; Walti, C., The Influence of Two-Dimensional Organization on Peptide Conformation. *Angewandte Chem Int* **2015,** *54* (3), 974-978.

56. Goormaghtigh, E.; Cabiaux, V.; Ruysschaert, J. M., Secondary structure and dosage of soluble and membrane proteins by attenuated total reflection Fourier-transform infrared spectroscopy on hydrated films. *Eur J Biochem* **1990,** *193* (2), 409-420.

57. Lee, S. J.; Han, S. W.; Kim, K., Perfluorocarbon-stabilized silver nanoparticles manufactured from layered silver carboxylates. *Chem Comm* **2002,** (5), 442-443.

58. Beddoes, C. M.; Gooris, G. S.; Bouwstra, J. A., Preferential arrangement of lipids in the long-periodicity phase of a stratum corneum matrix model. *J Lipid Res* **2018,** *59* (12), 2329-2338.

59. Lewis, R.; McElhaney, R. N., Membrane lipid phase transitions and phase organization studied by Fourier transform infrared spectroscopy. *Biochim Biophys Acta Biomembr* **2013,** *1828* (10), 2347-2358.

60. Haiss, W.; Thanh, N. T. K.; Aveyard, J.; Fernig, D. G., Determination of size and concentration of gold nanoparticles from UV-Vis spectra. *Anal Chem* **2007,** *79* (11), 4215-4221.

3.7 Supporting Information

Characterization of the synthesized peptides and peptide amphiphiles by means of LC-MS:

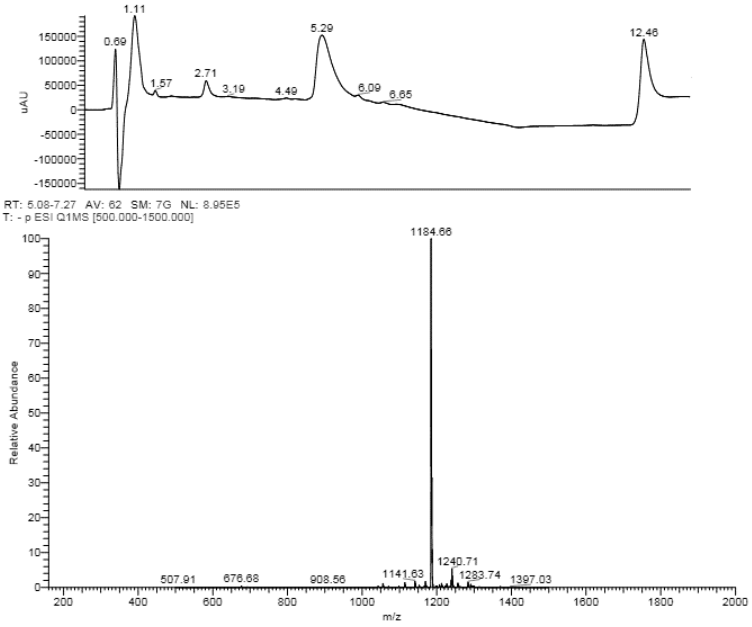

Figure S3.1. LC-MS spectrum for **1**: HS-$C_{16}H_{30}O$-$V_3A_3E_3$-OH. $[M-H]^{1-}_{theor}$ =1184.65.

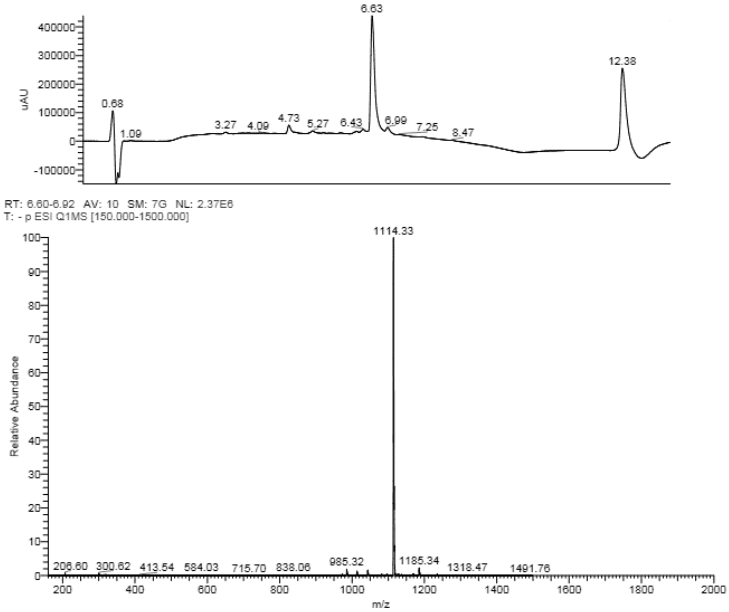

Figure S3.2. LC-MS spectrum for **2**: HS-$C_{11}H_{20}O$-$V_3A_3E_3$-OH. $[M-H]^{1-}_{theor}$ =1114.57.

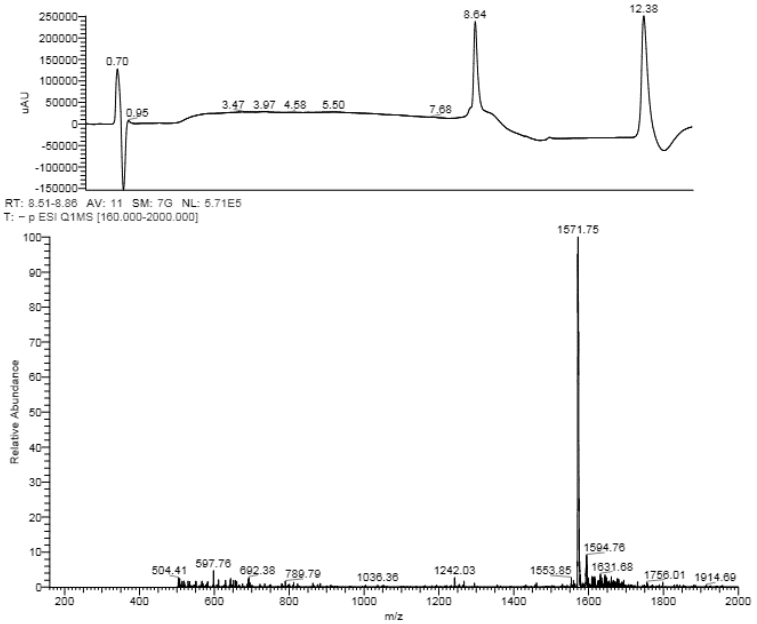

Figure S2.3. LC-MS spectrum for **3**: $(HS-C_{11}H_{20}O)_2$-$KV_3A_3E_4$-OH. $[M-H]^{1-}_{theor}$ =1571.83.

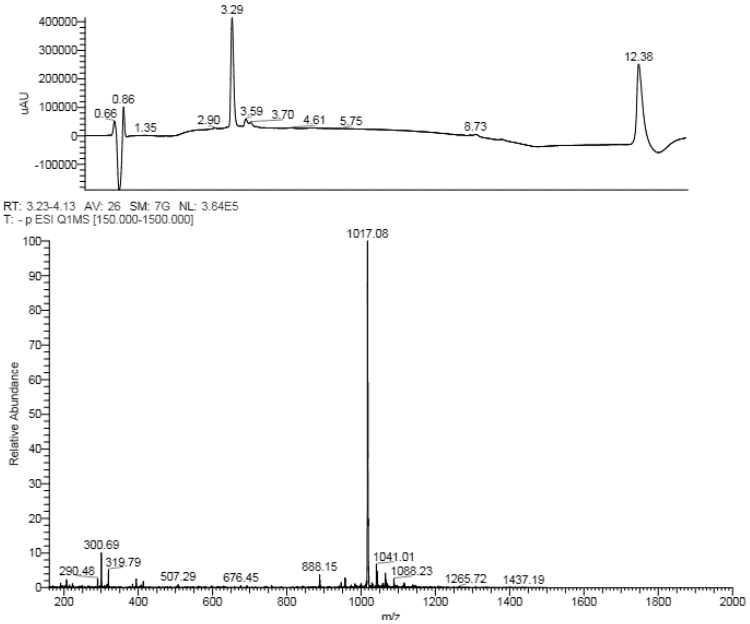

Figure S3.4. LC-MS spectrum for **4**: H_2N-$CV_3A_3E_3$-OH. $[M-H]^{1-}_{theor}$ =1017.45.

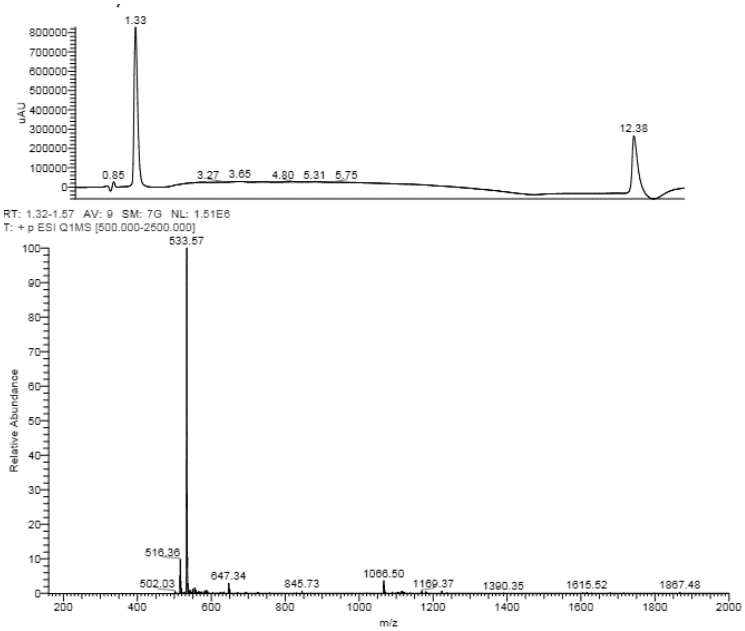

Figure S3.5. LC-MS spectrum for **5**: H_2N-CALNN-OH. $[M-H]^{1-}_{theor}$ =533.23.

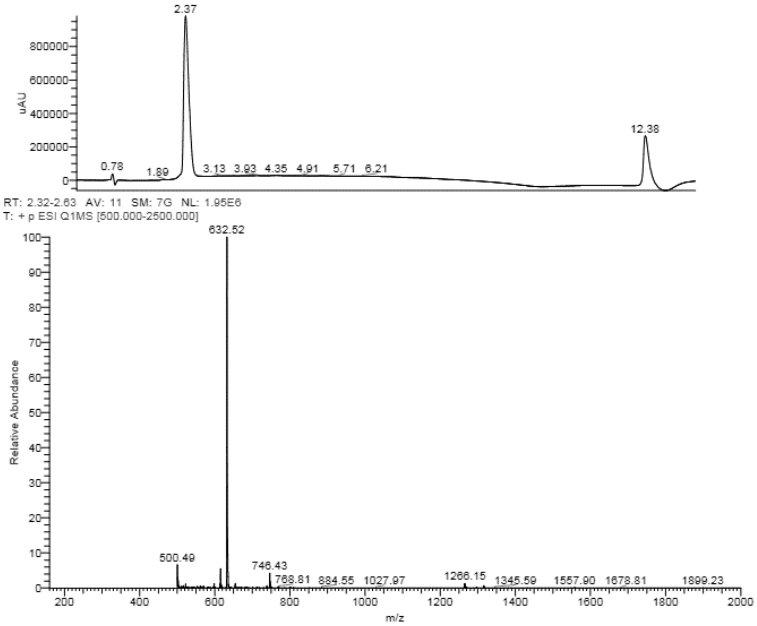

Figure S3.6. LC-MS spectrum for **6**: H_2N-CVALNN-OH. $[M-H]^{1-}_{theor}$ =632.41.

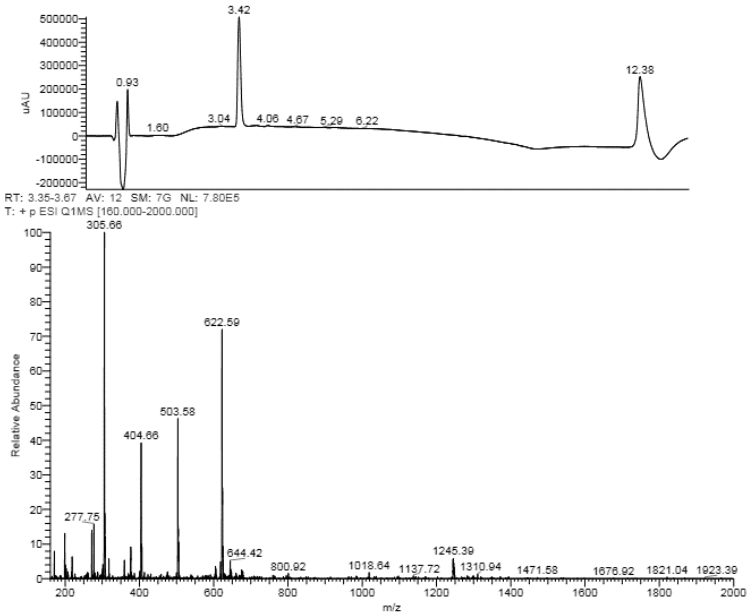

Figure S3.7. LC-MS spectrum for **7**: H_2N-CCVVVT-OH. $[M+H]^{1+}_{theor}$ =622.28.

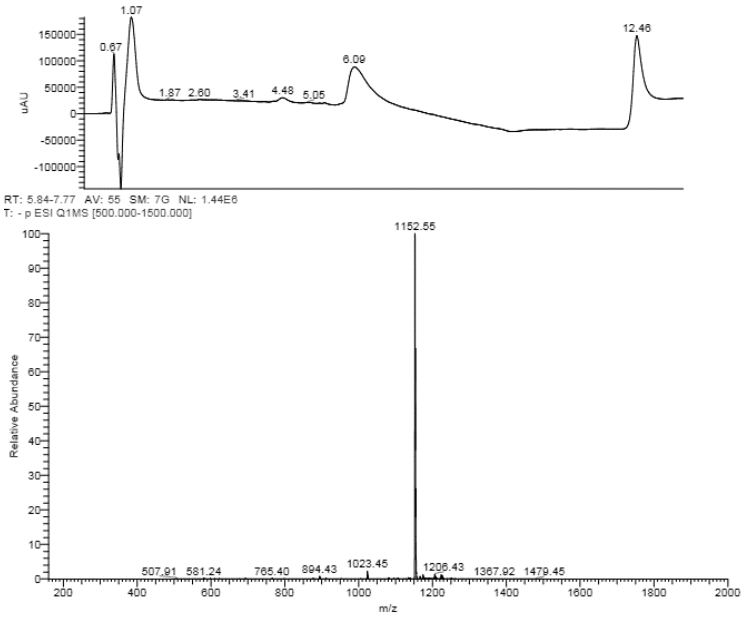

Figure S3.8. LC-MS spectrum for $C_{16}H_{31}O$-$V_3A_3E_3$-OH. $[M\text{-}H]^{1-}_{theor}$ =1152.67.

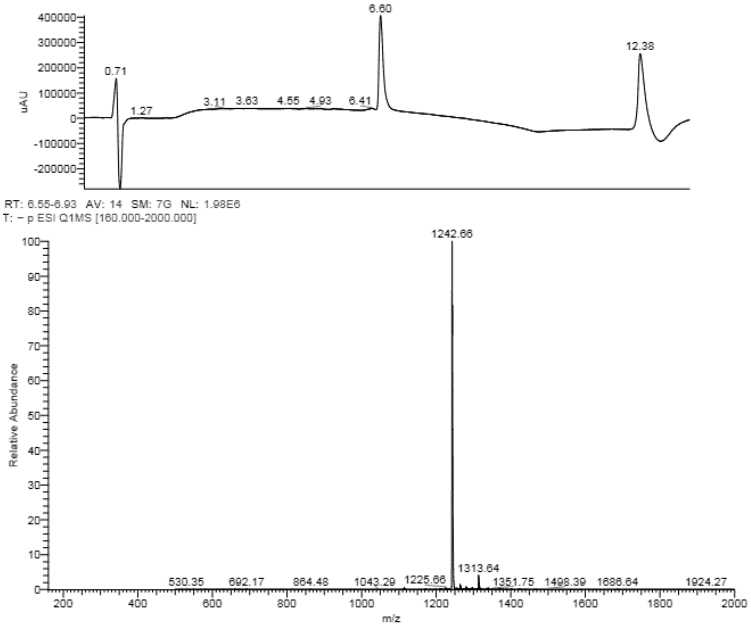

Figure S3.9. LC-MS spectrum for HS-$C_{11}H_{20}O$-$V_3A_3E_4$-OH. $[M\text{-}H]^{1-}_{theor}$ =1242.60.

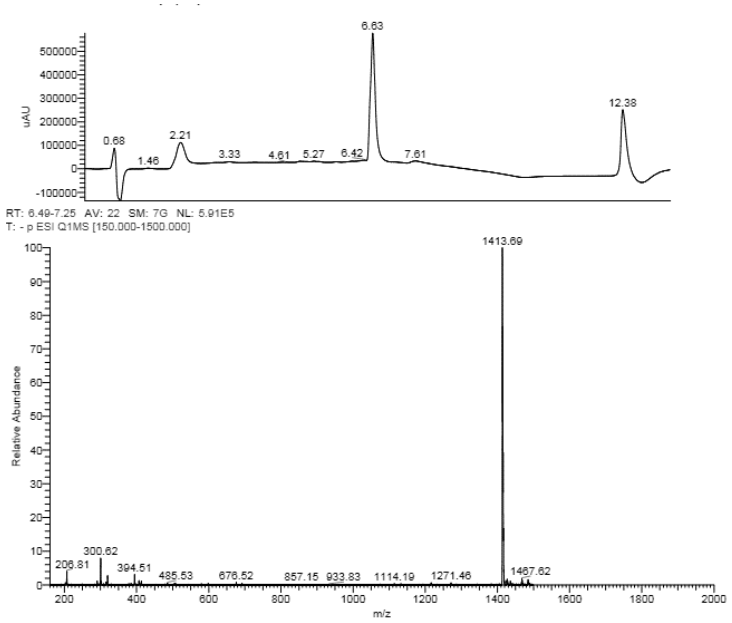

Figure S3.10. LC-MS spectrum for: HS-$C_{11}H_{20}O$-$K^{Ac}V_3A_3E_4$-OH. $[M-H]^{1-}_{theor}$ =1413.72.

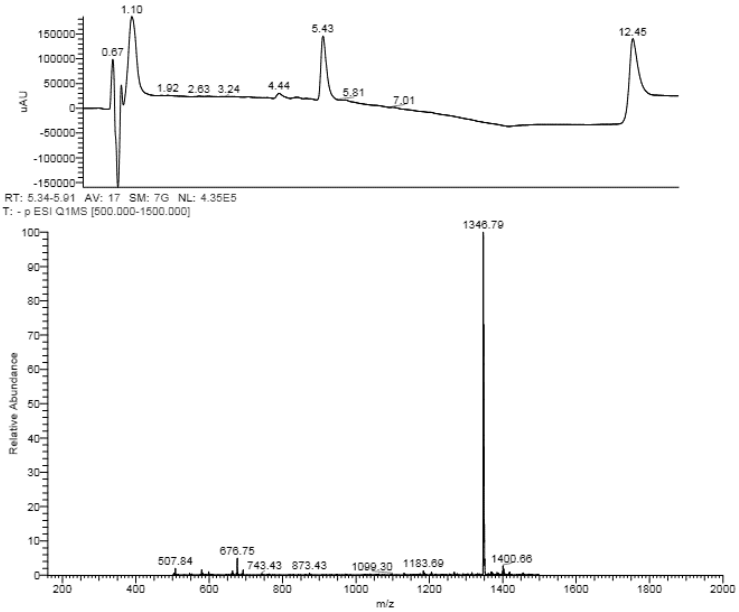

Figure S3.11. LC-MS spectrum for: HS-$C_{16}H_{30}O$-$V_3A_3E_3Y$-OH. $[M-H]^{1-}_{theor}$ =1346.53.

Spontaneous oxidation of peptide amphiphile thiol groups:

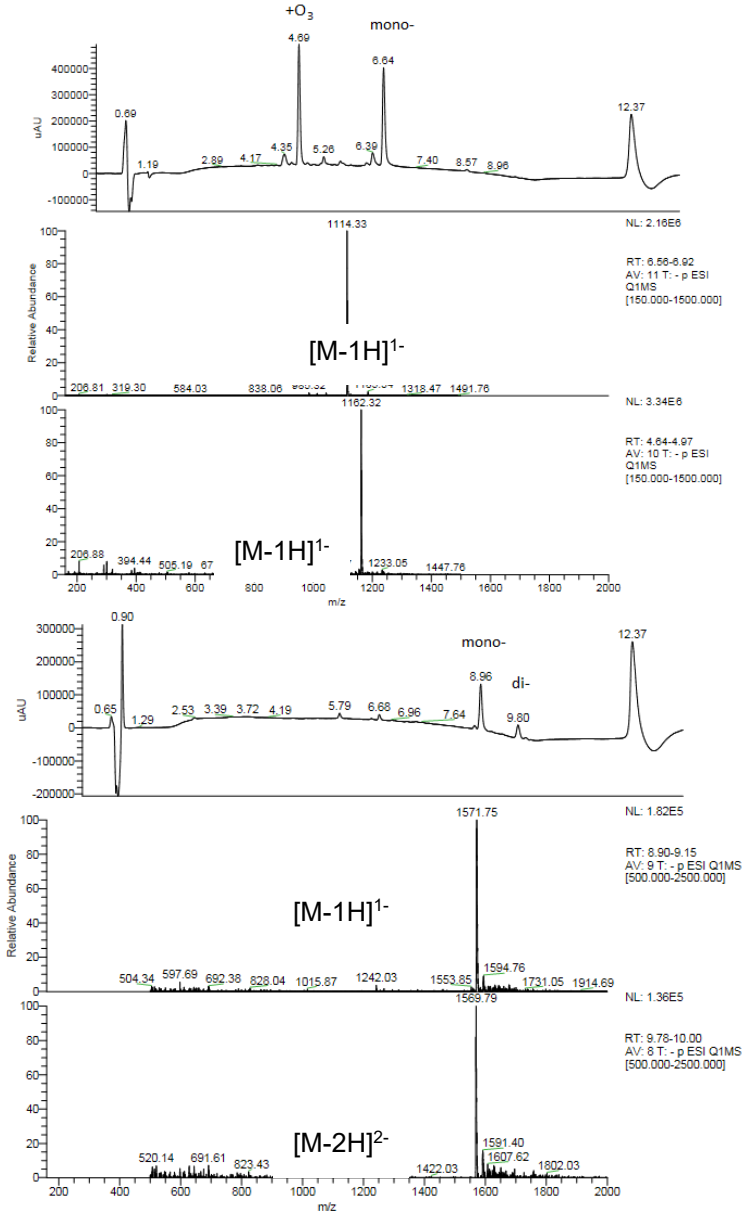

Figure S3.12. LC-MS data showing dimer formation and oxidation of (A) **2**, and (B) **3** after dissolution in PBS. The samples were stored for >3 months. Dimerization resulted in a decrease in mass of 1 or 2 Da, for single- and double-chain amphiphiles respectively. Oxidation of the terminal thiol was characterized by the appearance of a new peak with a shorter retention time and an increase in mass of 48 Da.

Characterization of citrate-capped GNPs of different sizes:

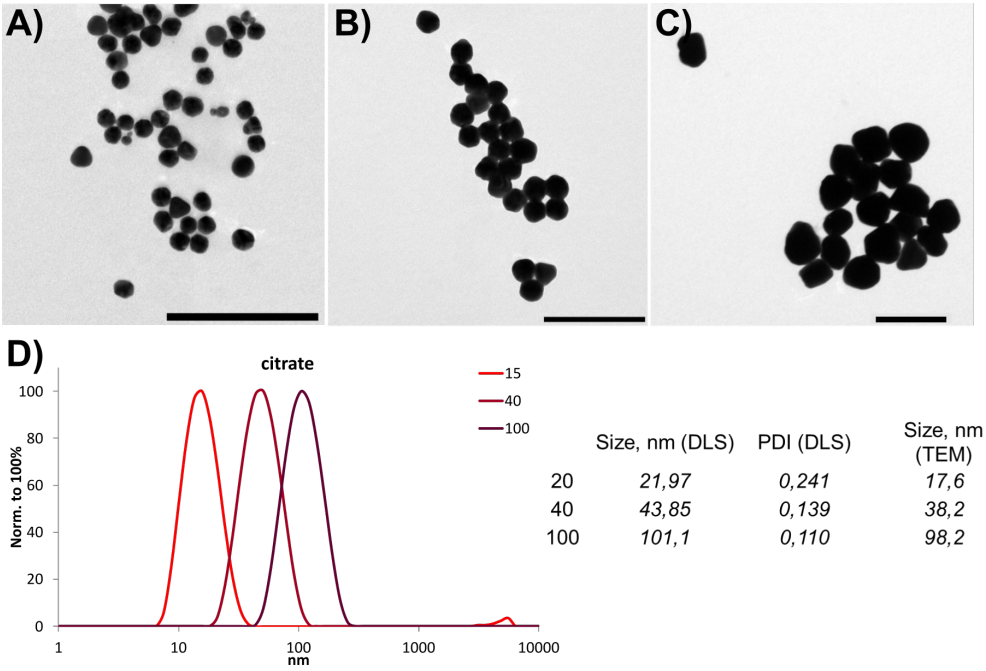

	Size, nm (DLS)	PDI (DLS)	Size, nm (TEM)
20	*21,97*	*0,241*	*17,6*
40	*43,85*	*0,139*	*38,2*
100	*101,1*	*0,110*	*98,2*

Figure S3.13. Size data for citrate-capped GNPs. TEM micrographs for (A) 20 nm GNPS, (B) 40 nm GNPs, and (C) 100 nm GNPs. (D) DLS data showing the size distributions for citrate-capped GNPs. The average sizes of the GNPs as determined by both DLS and TEM are shown in the table. Scale bar: 200 nm.

Table S3.1. Average Zeta potential values for citrate- and peptide-/amphiphile-coated GNPs. For conditions, see **3.6.7**.

Sample	ζ, mV (average)		
	20 nm GNPs	**40 nm GNPs**	**100 nm GNPs**
citrate	-31.25	-34,87	-39.47
1	-13.25	-23,70	-39.20
2	-15.83	-24,40	
3	-18.97	-27.00	-34.17
4	-10.93	-22.67	
5	-24.63		
6	-19.27		
7	-16.87		

Characterization of GNPs after modification with peptides and peptide amphiphiles:

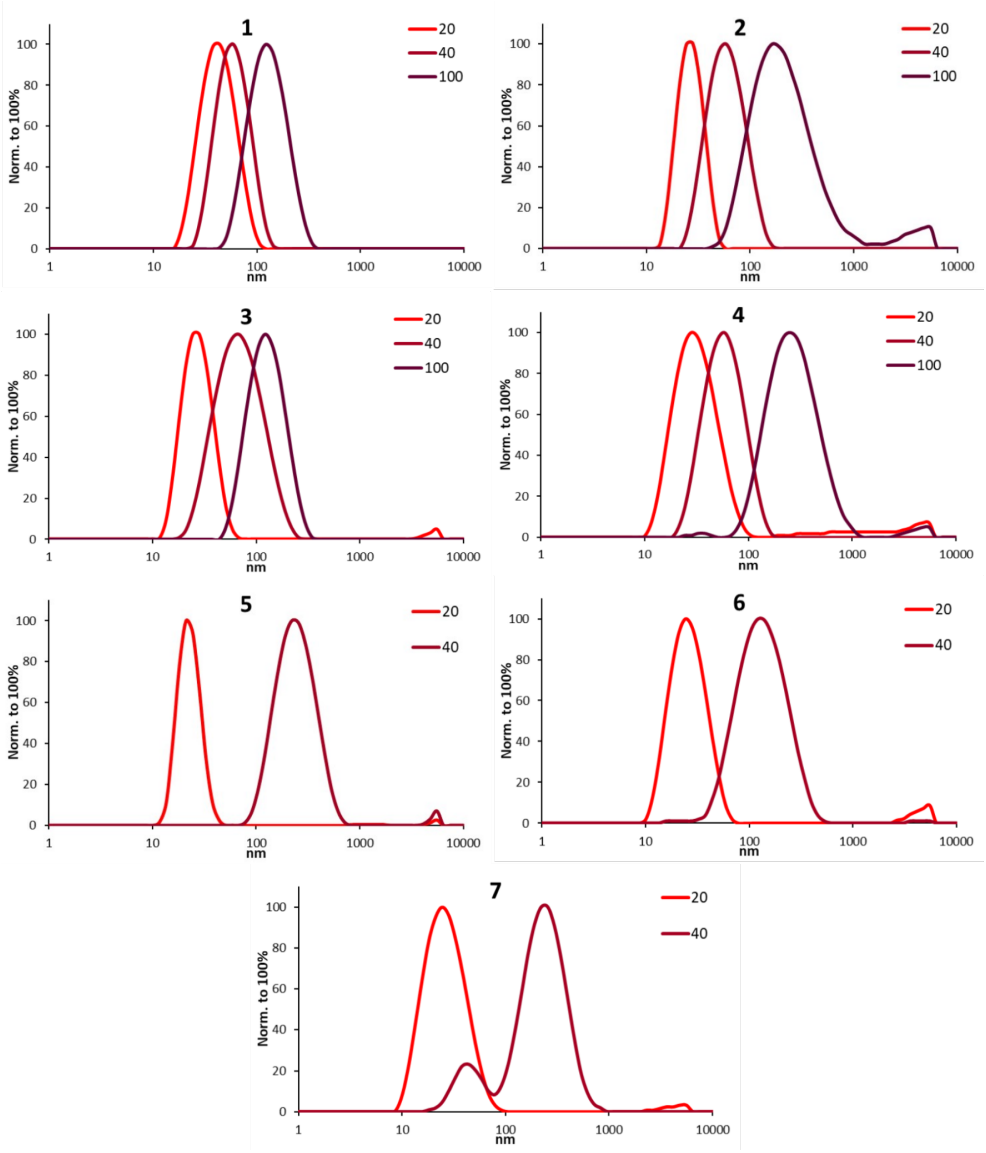

Figure S3.14. Intensity size distributions by DLS for GNPs functionalized with **1-7**. All distributions are normalized to 100%. Measurement conditions: PBS, pH 7.2.

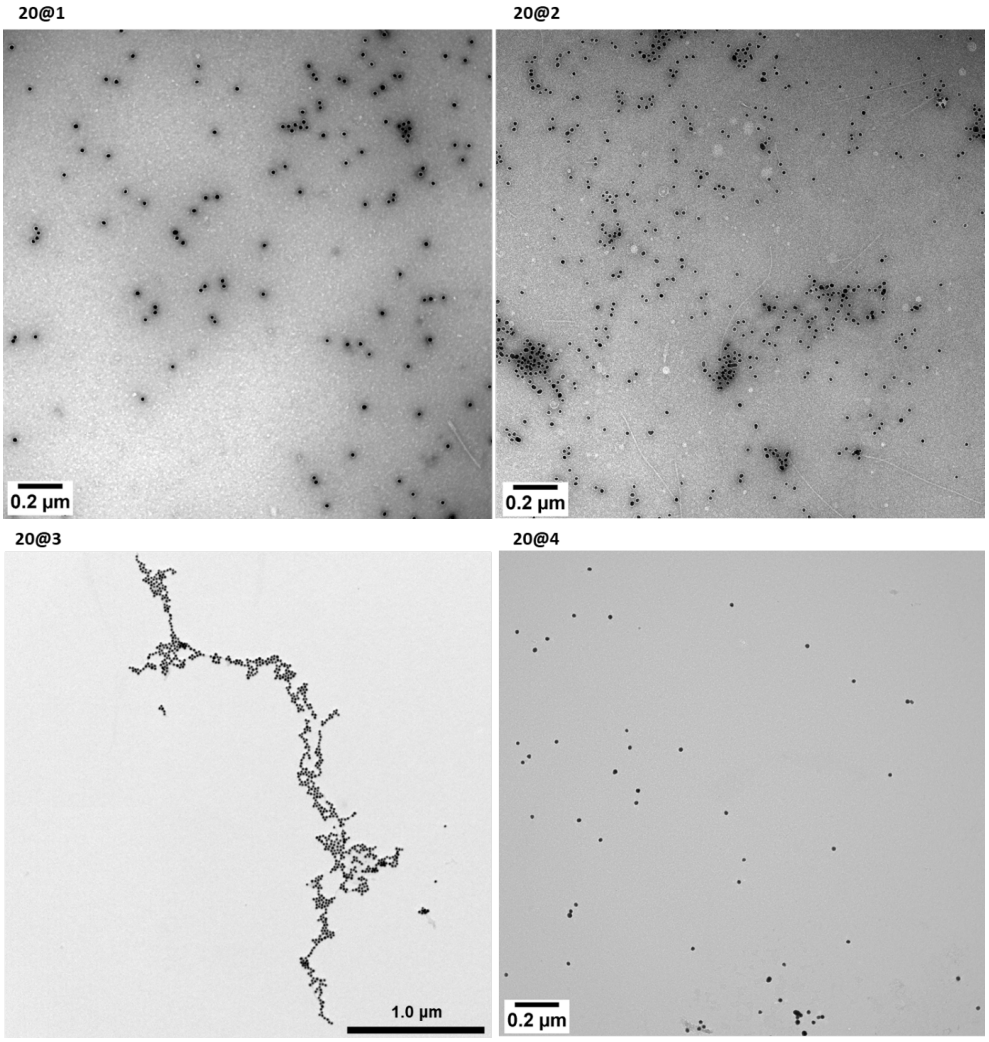

Figure S3.15. Representative low magnification images of 20 nm GNPs coated with molecules **1**-**4**.

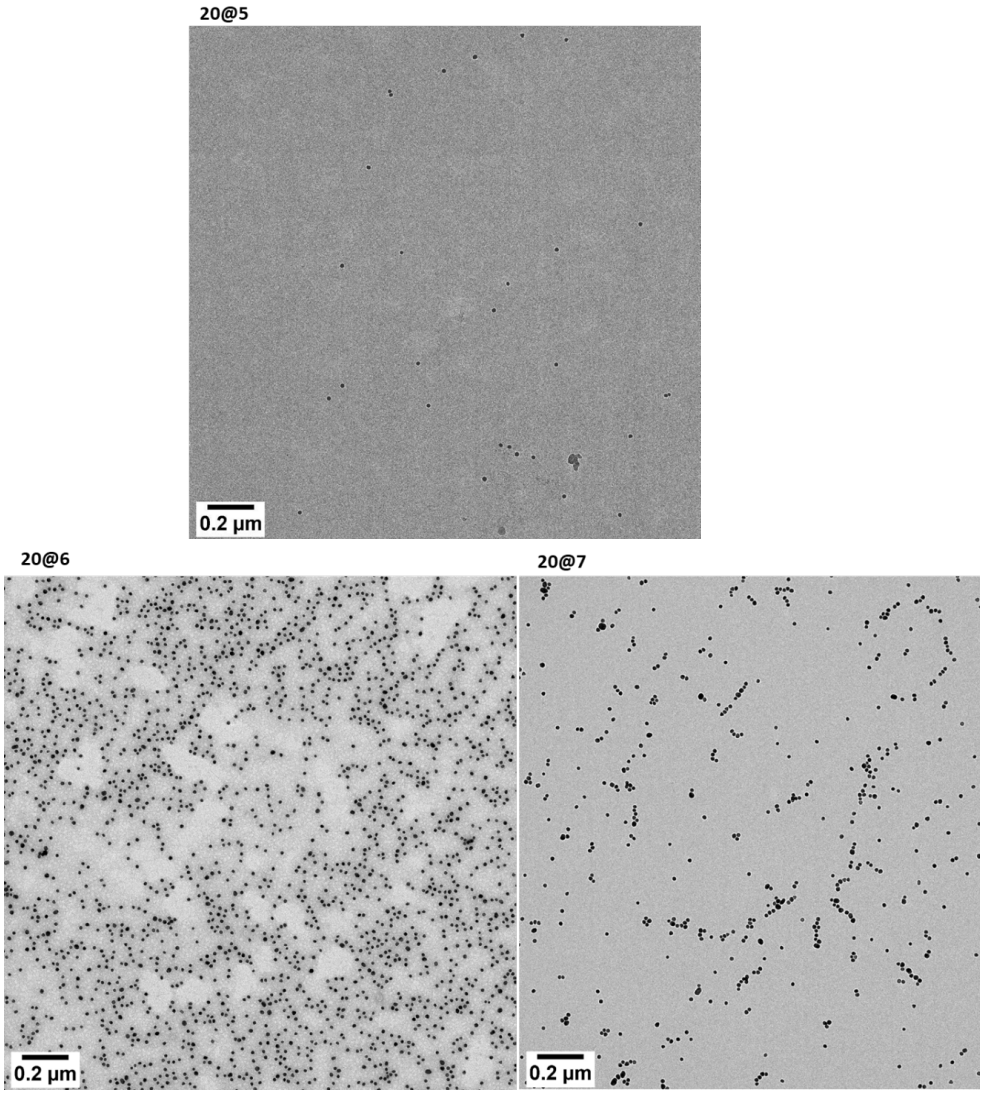

Figure S3.16. Low magnification images of 20 nm GNPs coated with molecules **5-7**.

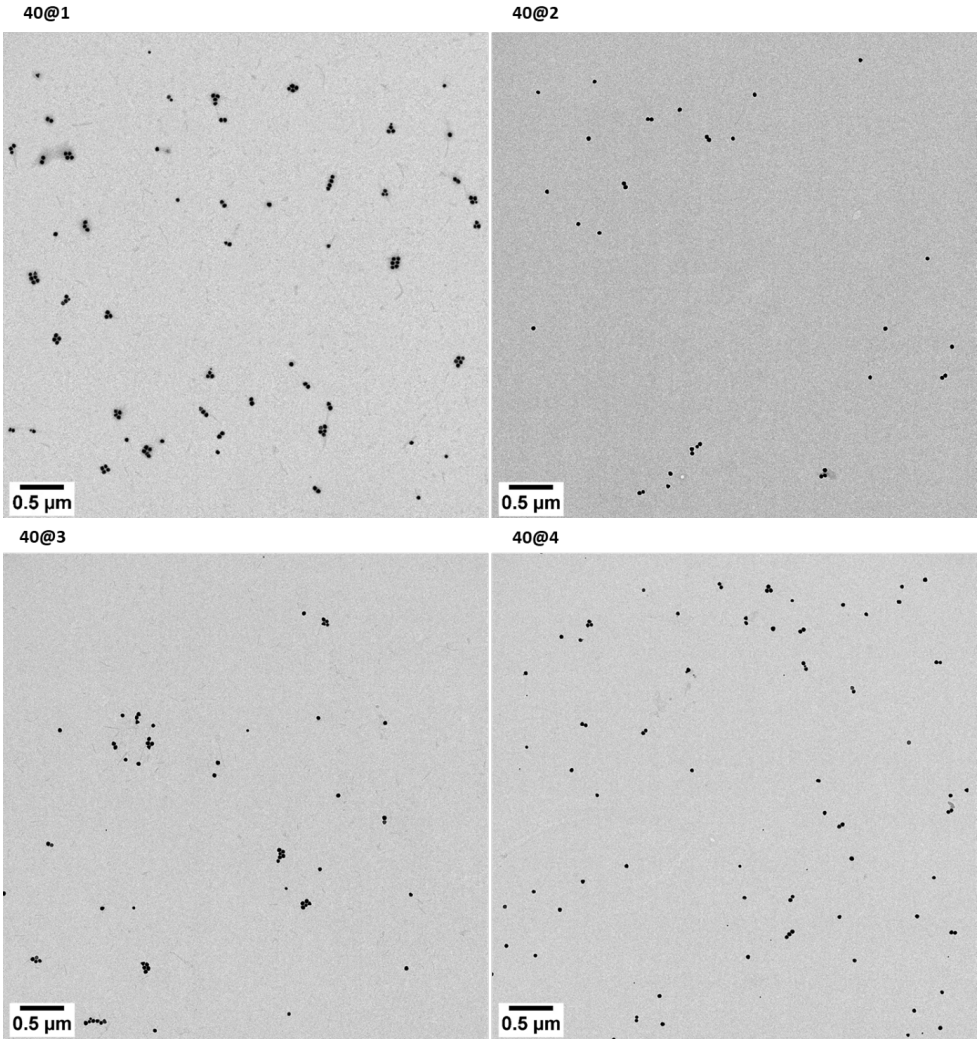

Figure S3.17. Representative low magnification images of 40 nm GNPs coated with molecules **1**-**4.**

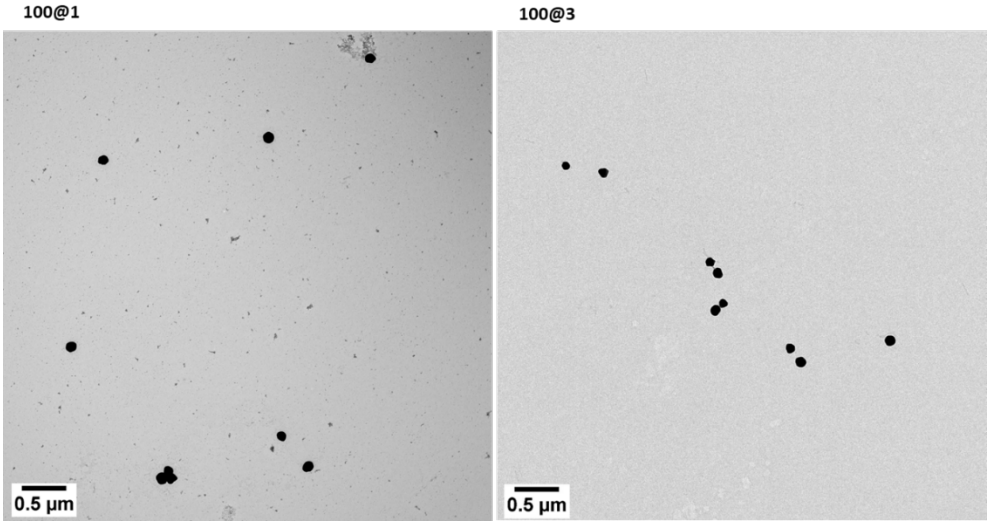

Figure S3.18. Representative low magnification images of 100 nm GNPs coated with molecules **1** and **3**.

Self-assembly of the peptide amphiphile monolayer attached to the GNP surface:

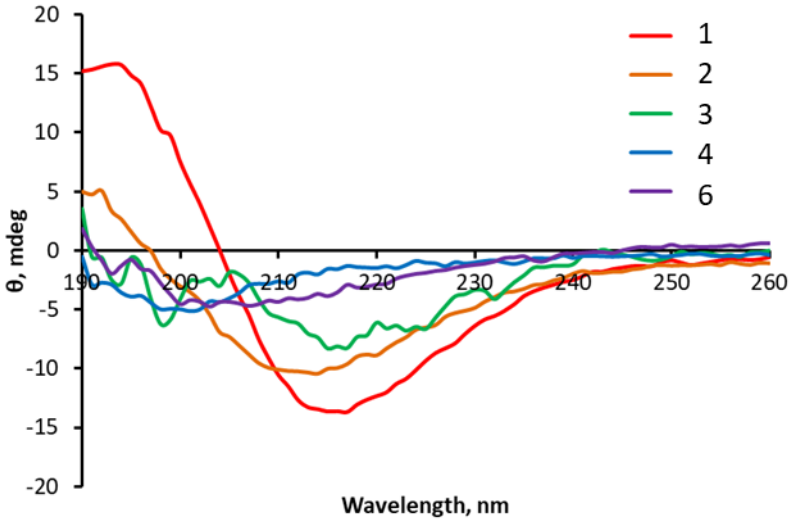

Figure S3.19. CD spectra of 20 nm coated GNPs illustrating the self-assembly of the amphiphilic molecules on the gold surface. Conditions: [GNP] = 6 nM, PBS, pH 7.2.

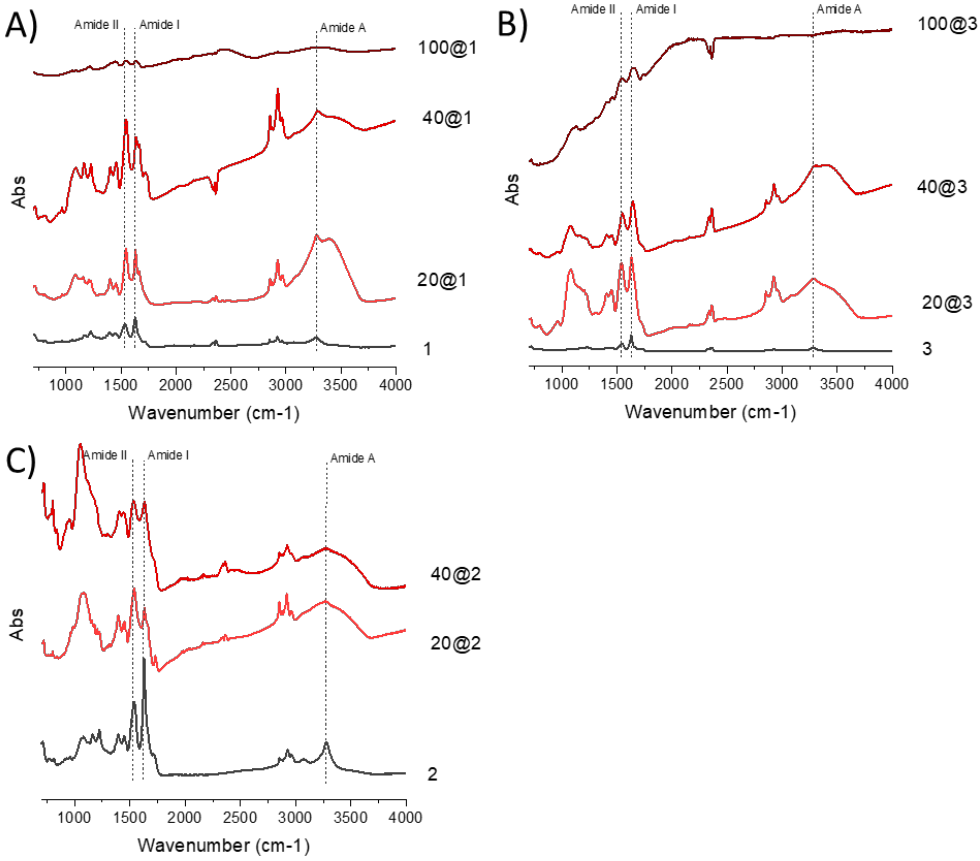

Figure S3.20. Full ATR-IR spectra of amphiphiles: (A) **1**, (B) **3**, and (C) **2**.

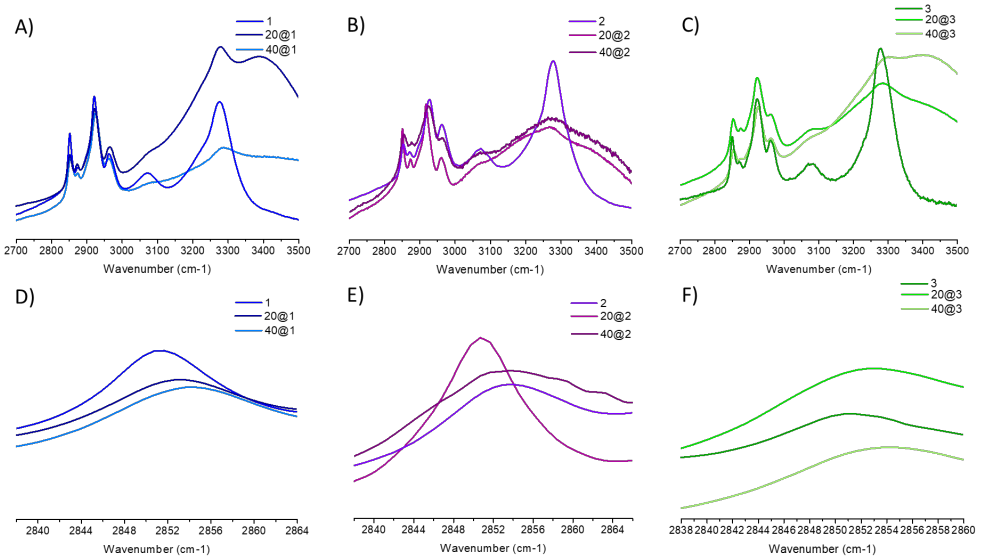

Figure S3.21. ATR-IR spectra in the range 2700-3500 cm^{-1} (A-C) and a close-up of the -CH_2- vibrational peak of the alkyl chain (D-F). Spectra are shown for the molecules by themselves and on 20 and 40 nm GNPs. For 100 nm GNPs it was not possible to distinguish individual peaks in this region due to a low intensity and high signal-to-noise ratio.

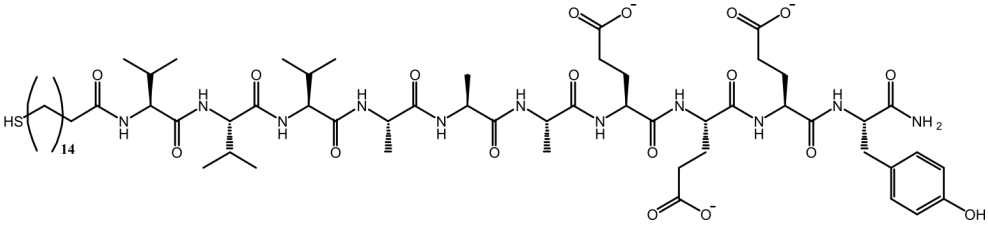

Scheme S3.1. Structure of the peptide used to evaluate coverage densities.

GNP aggregation tests based on charge screening effects and competition with thiolated ligands:

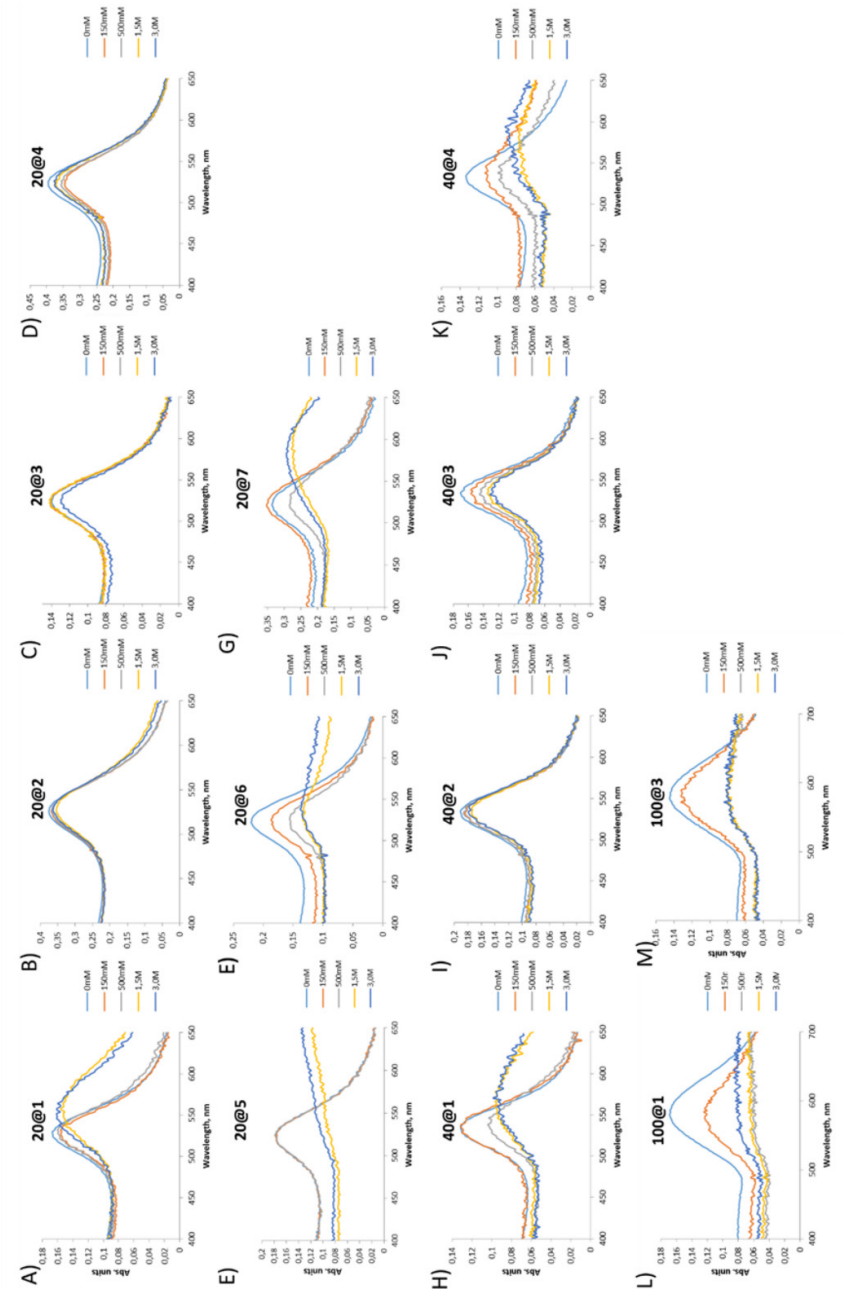

Figure S3.22. Overlays of UV-Vis spectra for 20, 40 and 100 nm GNPs coated with different stabilizing molecules at different concentrations of NaCl.

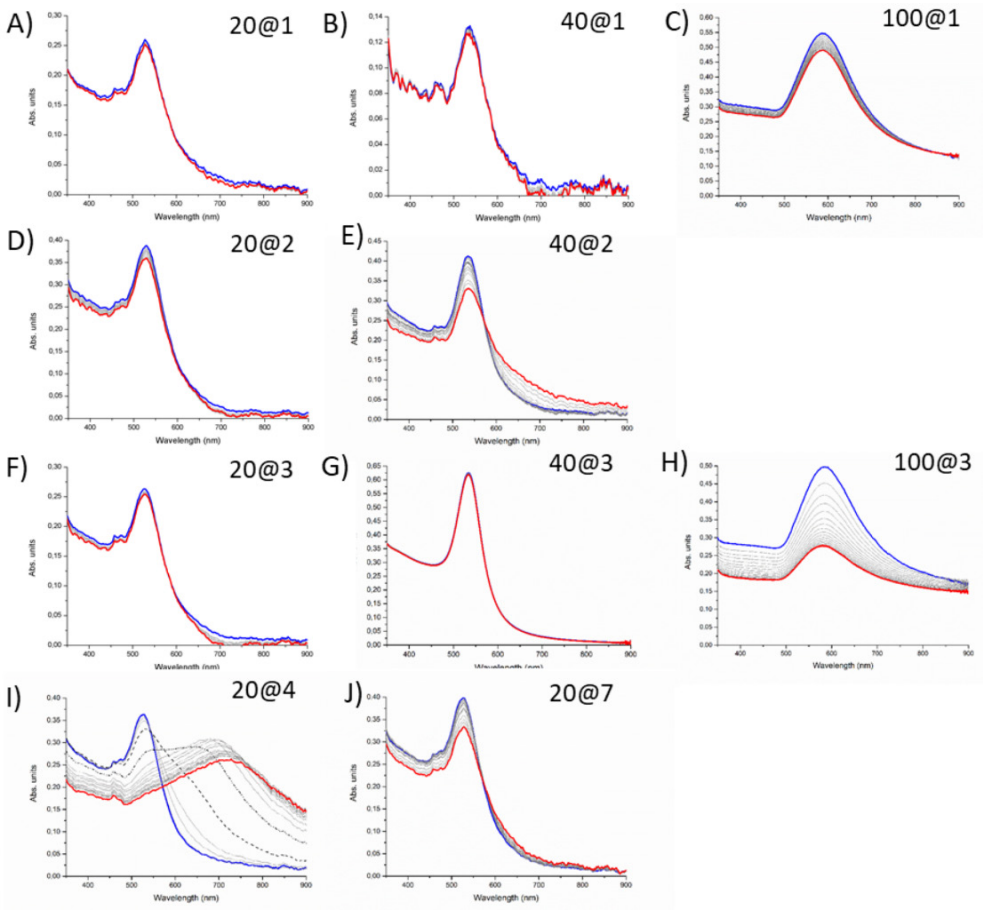

Figure S3.23. UV-Vis spectra for the DTT competition experiment with: (A) **1** on 20 nm GNPs; (B) **1** on 40 nm GNPs; (C) **1** on 100 nm GNPs; (D) **2** on 20 nm GNPs; (E) **2** on 40 nm GNPs; (F) **3** on 20 nm GNPs; (G) **3** on 40 nm GNPs; (H) **3** on 100 nm GNPs; (I) **4** on 20 nm GNPs, and; (J) **7** on 20 nm GNPs.

CHAPTER 4

Peptidic stabilization of gold nanorods

4.1 Abstract

Gold nanorods (GNRs) are a particularly interesting class of nanoparticles: their dimensions can be tuned to produce rods of different aspect ratios (a.r.) providing well-defined optical properties due to the localized surface plasmon resonance (LSPR) position. GNRs are commonly employed in nanophotonics, biosensing, and surface-enhanced Raman scattering (SERS) applications, and they are also believed to have different effects in immunological and biomedical applications when compared to spherical gold nanoparticles (GNPs). However, the wider use of GNRs is restricted due to difficulties associated with their surface stabilization. Reagents that are used as stabilizers during GNR synthesis are toxic, and need to be displaced from the gold surface before being employed in biological applications. Polymer or silica coatings commonly employed to stabilize GNRs are typically thick (>10 nm), negatively affecting the use of GNRs in applications based on their optical properties. Previously, it was shown that peptide amphiphiles effectively stabilized spherical GNPs in the 20-100 nm size range. The peptide amphiphiles formed a self-assembled monolayer (SAM) on the gold surface with a thickness of <5 nm. In this chapter, the use of peptide amphiphiles as a stabilizing coating for GNRs is reported. The procedure reported for peptide amphiphile-stabilized GNPs was optimized for GNR stabilization, resulting in long-term stability and resistance to external factors inducing aggregation. Moreover, the formed SAMs were probed for their secondary structure distribution and coverage density. All tested peptide amphiphiles formed dense (2.62-3.87 peptides/nm^2) and highly ordered (51.8-58.8% β-content) shells on the GNR surface. Due to their high stability and thin coating, peptide amphiphile-stabilized GNRs are of particular interest as a tool in biophysical and biomedical applications.

4.2 Introduction

Gold nanorods (GNRs) first emerged in 1999 and provided an opportunity to synthesize asymmetric nanoparticles with finely tunable physical dimensions and optical properties.[1-4] The GNR aspect ratio (a.r.), which is the relationship between their length and width, defines the optical properties of these nanoparticles and is reflected in the localized surface plasmon resonance (LSPR) position. The LSPR can therefore vary between 600 nm and 1200 nm. Also, due to the fact that the LSPR position is in the near-infrared (NIR) region of the electromagnetic spectrum, outside of the region where water and biological molecules absorb, GNRs are considered to be highly suitable for biological applications. Upon excitation with a laser matching their plasmon frequency, these nanoparticles emit an enhanced multiphoton signal. GNRs have been extensively used as extraordinarily bright substrates for *in vitro* and *in vivo* two-photon (2P) luminescence imaging that minimizes the damage to biological samples and prolongs imaging time.[5-9] GNRs have also been utilized as contrast agents in photoacoustic imaging,[10] and other SPR-enhanced imaging and detection techniques.[7, 11, 12] In addition, GNRs are insensitive to photobleaching,[13] provide a 3D spatial resolution of the read-out signal,[5] and their spatial orientation can be deduced from their polarized light scattering.[14] GNR excitation can also result in the conversion of optical energy into heat, therefore GNRs are used in cancer photothermal therapy.[7, 15, 16] Finally, GNR optical properties are extremely sensitive to changes in the environment which is especially attractive for label-free bio-sensor development.[17, 18]

The shape of GNRs, which gives rise to their unique optical properties, is achieved *via* seed-mediated growth in the presence of silver nitrate ($AgNO_3$)

and high excesses of specific cationic surfactants such as cetyltrimethylammonium bromide (CTAB),[19] cetyltrimethylammonium chloride (CTAC),[20] benzyldimethylhexadecylammonium chloride (BDAC), or mixtures thereof.[3] These molecules form a bilayer on the gold surface and are essential for the shape control and stability of GNRs. These non-covalent interactions are weak enough to allow surface modification of GNRs *via* displacement of the surfactant. Moreover, due to the cationic and amphiphilic nature of these molecules, surfactant-protected GNRs are unstable under physiological conditions and cause severe cytotoxicity.[12] Displacement of CTAB is achieved through common nanoparticle stabilization approaches including polymer coating (*e.g.* thiolated PEG molecules[21, 22] and other polymers[23]), silica condensation,[24] or alternatively, CTAB can be replaced by thiolated analogues.[25, 26] The first two methods rely on creating a steric barrier between individual GNRs. Thiolated PEGs displace CTAB *via* ligand exchange and form a shell attached to the gold surface through Au-S bonds. It was shown that 5-10 kDa thiolated PEGs are optimal for stabilization of GNRs.[21] This PEG size corresponds to a substantial contour length: at least 30 nm and longer for a fully "stretched" molecule.[27, 28] Silica precursors can condense on the GNR surface, but the resulting coatings are typically thick as well (>10 nm).[29]

GNRs are utilized to study ligand-receptor interactions, and hence the choice of the protective molecule is crucial. The formed shell has to meet several requirements: (i) be suitable for further functionalization with a ligand of interest; (ii) be of minimal thickness to allow detection of biomolecule interactions close to the GNR surface. Since the LSPR is defined by the local refractive index close to the particle's surface, the studied interactions should take place as close to the gold surface as possible. This way the shift of LSPR band is a direct measure of such interactions.[18] Also, when *in vitro* or

in vivo applications are envisioned, a significant increase in GNR dimensions due to the presence of a shell can alter the pathways by which the nanoparticles are taken up by cells and cleared from the blood stream. From this point of view the common stabilization approaches are not ideal and a new stabilization method is desired. In this chapter thiolated peptide amphiphiles are studied as potential GNR stabilizers. These amphiphiles comprise a beta-sheet forming peptide domain conjugated, at the N-terminus, to a thiolated alkyl chain. The presence of the alkyl chain is likely to lead to increased stability as it was previously shown that conjugation of thiolated PEG (2000 Da) with 11-mercaptoundecanoic acid (MUA) improved the stability of the resulting GNR conjugates.[22] Additionally, the coverage densities increased from <1 to up to 3.3 molecules/nm^2. This was attributed to better penetration of the hydrophobic tails into the CTAB bilayer in comparison to the hydrophilic thiolated PEGs. It was also shown that use of a thiolated analogue of CTAB, 16-mercaptohexadecyl-trimethylammonium bromide (MTAB), improved the ligand density from 0.9 (± 0.2) to 3.6 (± 1.0) molecules/nm^2.[24] Interestingly, MTAB formed a uniform monolayer at the GNR surface, while CTAB coatings are less dense at the rod tips. Also, no significant difference in MTAB coverage was detected for GNRs of different a.r. (1.4, 2.3, 3.2, and 3,9 respectively).[26] These findings emphasize the importance of a thiolated alkyl chain presence, implying peptide amphiphiles are likely to act as effective stabilizing coatings.

In **Chapter 3** of this thesis, the use of thiolated peptide amphiphiles for stabilization of spherical gold nanoparticles (GNPs) by formation of a self-assembled monomer (SAM) was described.[30] It was shown that peptide amphiphiles stabilized GNPs of different diameters under physiological conditions and at high salt or dithiothreitol (DTT) concentrations. This extraordinary stability of the peptide amphiphile-coated GNPs was attributed

to a combination of effects arising from their amphiphilic nature: firstly, alkyl chains are bound to the gold surface *via* an Au-S bond and create a hydrophobic environment around the core. This depletes the presence of water, and the molecules dissolved in it, from the surface of the GNP. Secondly, peptide self-assembly leads to the formation of a dense self-assembled monolayer (SAM) on the surface of the GNPs. Finally, a correlation between the surface curvature and the stabilizing capacity of the peptide or peptide amphiphile was also implicated in the stabilizing effect.

To probe these stabilizing effects further, the same coating approach was applied to gold nanorods in this chapter. As before, a ligand exchange procedure was used to replace the original CTAB bilayer on the GNR surface with molecules **1-4** (**Scheme 4.1**).[30] As both the shape and the original surface chemistry of GNRs differed from GNPs, this had implications for the ligand exchange as well as for the overall stability that was achieved. The rod-like shape is a combination of high (at the tips) and low (in the center of the rods) curvature areas, while CTAB creates a hydrophobic environment shown to be difficult to penetrate with hydrophilic molecules.[22] Both factors were suggested to contribute to the ligand density and secondary structure distribution within the peptide amphiphile shell attached to the GNR surface. Additionally, the protective capability of the thiolated peptide amphiphiles was simultaneously evaluated and explained though the coated-GNR behavior upon addition of molecules inducing aggregation (high-salt conditions or competition with thiol ligands). UV-Vis spectroscopy (UV-Vis) was used to elucidate the aggregation state of GNRs, while the resulting peptide amphiphile-based SAMs were analyzed with transmission electron microscopy (TEM) and Fourier-transform infrared spectroscopy (FTIR).

4.3 Results and Discussion

4.3.1 Peptide amphiphile design

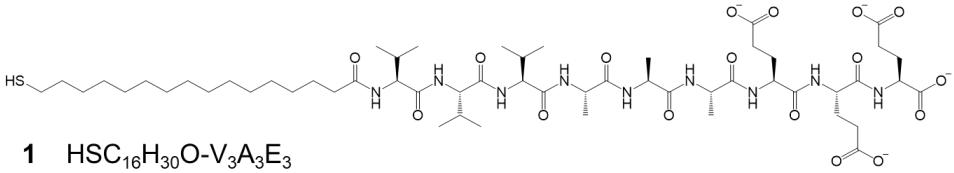

1 $HSC_{16}H_{30}O\text{-}V_3A_3E_3$

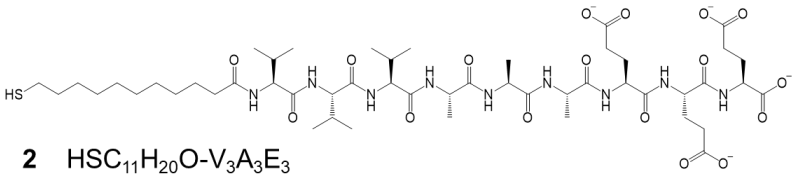

2 $HSC_{11}H_{20}O\text{-}V_3A_3E_3$

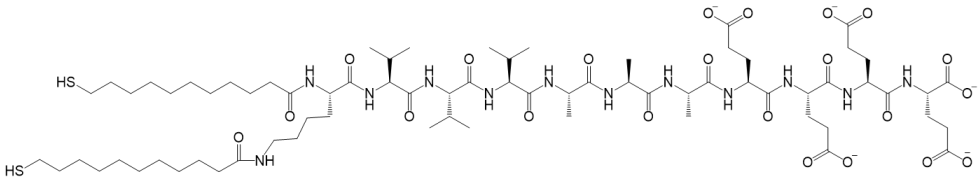

3 $(HSC_{11}H_{20}O)_2\text{-}KV_3A_3E_4$

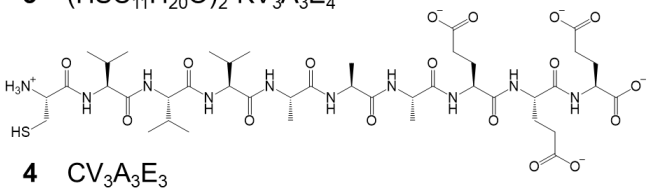

4 $CV_3A_3E_3$

Scheme 4.1. Sequences and structures of peptides and amphiphiles used in this study.

Similar to **Chapter 3** of this thesis, peptide amphiphiles comprising a thiolated alkyl chain of either 16 or 11 carbons in length and a peptide domain with the sequence $V_3A_3E_3$ were designed and synthesized. These are dubbed molecules **1** and **2** respectively (**Scheme 4.1**). A third construct with two C-11 alkyl chains, molecule **3**, possesses increased steric bulk within the hydrophobic domain and was also introduced to probe the effect of a

bidentate binding ligand. The sequence of **3** was extended with a fourth glutamic acid residue (Glu, E) for increased solubility. Peptide **4** contained a cysteine (Cys, C) amino acid instead of a thiolated alkyl chain and served as a reference molecule to study the impact of the hydrophobic alkyl chain domain of **1-3**.

All four molecules are suitable for displacement of citrate from the surface of GNPs, (**Chapter 3** of this thesis) and are therefore likely to be effective for the displacement of CTAB from the surface of GNRs as well. In addition to using molecule **4** as a reference molecule, GNRs were also coated with thiolated PEG-OMe with average molecular weights of 750 and 5000 Da. The reason thiolated PEG-OMe was chosen as a reference stabilizing molecule is that thiolated PEG_{5000} has been reported to be an optimal length for GNR stabilization, while thiolated PEG_{750} was chosen because its shorter contour length (in its extended conformation) is comparable to the length of the peptide amphiphiles used in this study (4.8 nm based on 0.28 nm per -CH_2CH_2O- repeat).[27, 28]

4.3.2 GNR coating protocol optimization

GNRs with an aspect ratio (a.r.) of 3.3 (LSPR 756 nm) were synthesized according to the seed-mediated overgrowth method (**Figure 4.1**). The average dimensions of the resulting rods were 46.4 (± 8.3) by 14.0 (± 2.9) nm. Rods with these dimensions were selected as they are suitable for potential future applications using two-photon microscopy.[18] As-synthesized GNRs were stabilized with a cetyltrimethylammonium bromide (CTAB) bilayer which was displaced from the GNR surface *via* ligand exchange with the thiol-containing ligands **1-4** and thiolated PEGs (750 and 5000 Da).

The thiolated peptide amphiphiles require an optimized coating procedure (**Chapter 3** of this thesis).[30] To prevent the undesired simultaneous formation of peptide amphiphile fibers, **1-3** were dissolved in pure DMSO prior to the ligand exchange, which was performed in aqueous DMSO. Previously, it was shown that ligand exchange between citrate resident on the GNP surface and thiolated peptide amphiphiles was successful in 25% DMSO (aq. v/v) (**Chapter 3** of this thesis): after 1h incubation, the excess ligand was removed *via* a combination of centrifugation and size-exclusion chromatography (SEC). Concomitantly, the medium was replaced with PBS (pH 7.2). The resulting peptide amphiphile-stabilized GNPs were fiber-free and dense well-defined peptide amphiphile monolayers around each gold core were observed with transmission electron microscopy (TEM). However, this approach resulted in a significant red-shift of the SPR band (>20 nm) of the GNRs (**Figure 4.1A**). TEM analysis indicated that this red-shift was caused by the presence of associated peptide amphiphile fibers, although coated GNRs were individually coated and separated from each other (**Figure 4.1B**). Fiber formation was particularly prevalent when **1** and **3** were used, while rods coated with **2** (**GNR@2**) were typically free of fibers. This was attributed to the different alkyl chain lengths, resulting in different fiber formation kinetics and critical fiber formation concentrations. Reduction of the alkyl chain length from C16 to C11 results in a slower fiber formation rate and a higher critical concentration in the case of **2** (**Chapter 2** of this thesis). Since free residual fibers could affect applications and stability of the coated GNRs, we optimized the coating procedure in order to obtain pure GNRs coated with **1** (**GNR@1**) or **3** (**GNR@3**) in the absence of peptide amphiphile fibers.

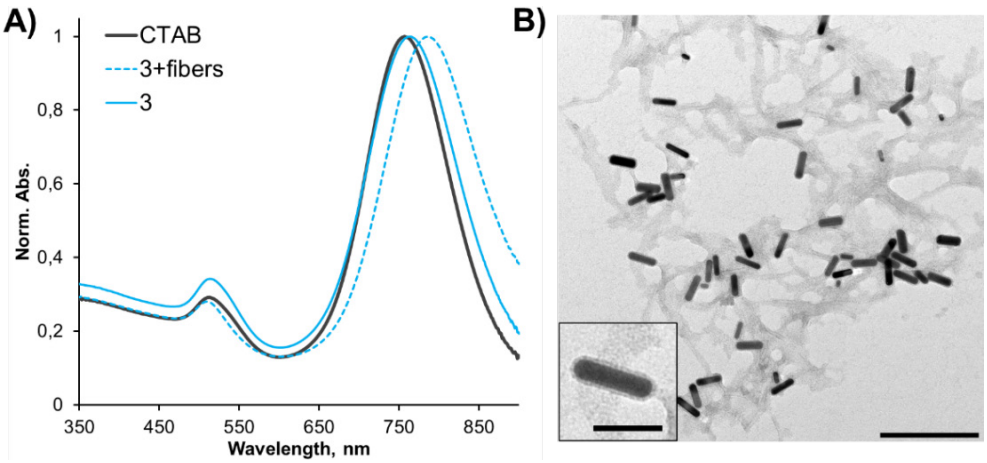

Figure 4.1. Optimization of the GNR coating procedure with molecule **3** (A) UV-Vis spectra of a **GNR@3** sample with associated fibers (dashed line) and a fiber-free sample (solid blue line), compared to the original CTAB-coated GNRs (black line); (B) a representative TEM image of fibers associated with **GNR@3**. TEM image: scale bar is 200 nm (insert - 50 nm); 0.5% uranyl acetate staining.

Fiber formation in solution can be disrupted or delayed if an appropriate solvent is added.[31] As DMSO had previously been shown to disrupt fiber formation,[30] the DMSO content was increased, from 25% (v/v) to 50% (v/v), and this coating procedure resulted in predominantly fiber-free GNR samples, as determined by UV-Vis spectroscopy (**Figure 4.2**) and TEM analysis (**Figure 4.3**). No broadening of the LSPR band was observed, and only a moderate red-shift (7-10 nm) was observed, indicative of a change in dielectric constant (**Figure 4.2**).[30] Individual shells formed by **1-3** were observed with TEM and accumulation of uranyl acetate revealed the shell thicknesses, which corresponded to the formation of a peptide amphiphile monolayer at the GNR surface (**Figure 4.3A-C**).

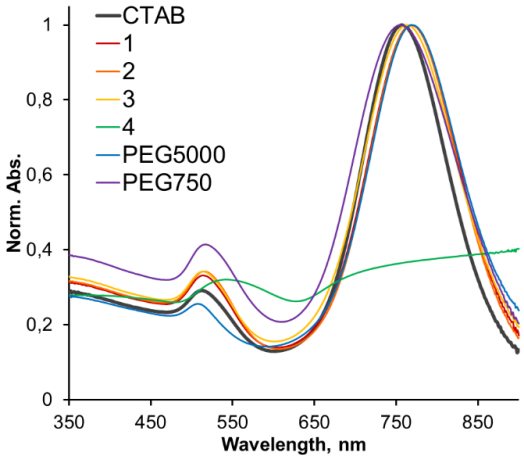

Figure 4.2. An overlay of UV-Vis spectra of GNRs with different coatings: peptide amphiphiles **1-3**, peptide **4**, and thiolated PEGs (750 and 5000 Da). Samples were prepared in PBS (pH 7.2).

Batch-to-batch variation influences the success of surface modification: some residual free fibers were observed even after increasing the DMSO content in the reaction mixture. Importantly, the initial CTAB content was found to influence fiber formation during the GNR modification protocol. Typically, CTAB is present in a high excess in GNR suspensions in order to maintain colloidal stability. When the coating with peptide amphiphiles was conducted in the presence of 10 mM CTAB (as in commercially available GNRs), the GNRs formed large aggregates visible to the naked eye within 5 mins after peptide amphiphile addition. From this, it was suspected that the cationic CTAB negatively influences the self-assembly process of the negatively charged peptide amphiphiles **1** and **3**. An imbalance between two simultaneous processes: fiber formation and Au-S bond formation, might induce the observed precipitation. Therefore, the coating procedure for GNR surface modification with peptide amphiphiles was optimized further. An additional centrifugation cycle, prior to mixing the amphiphiles and the GNRs,

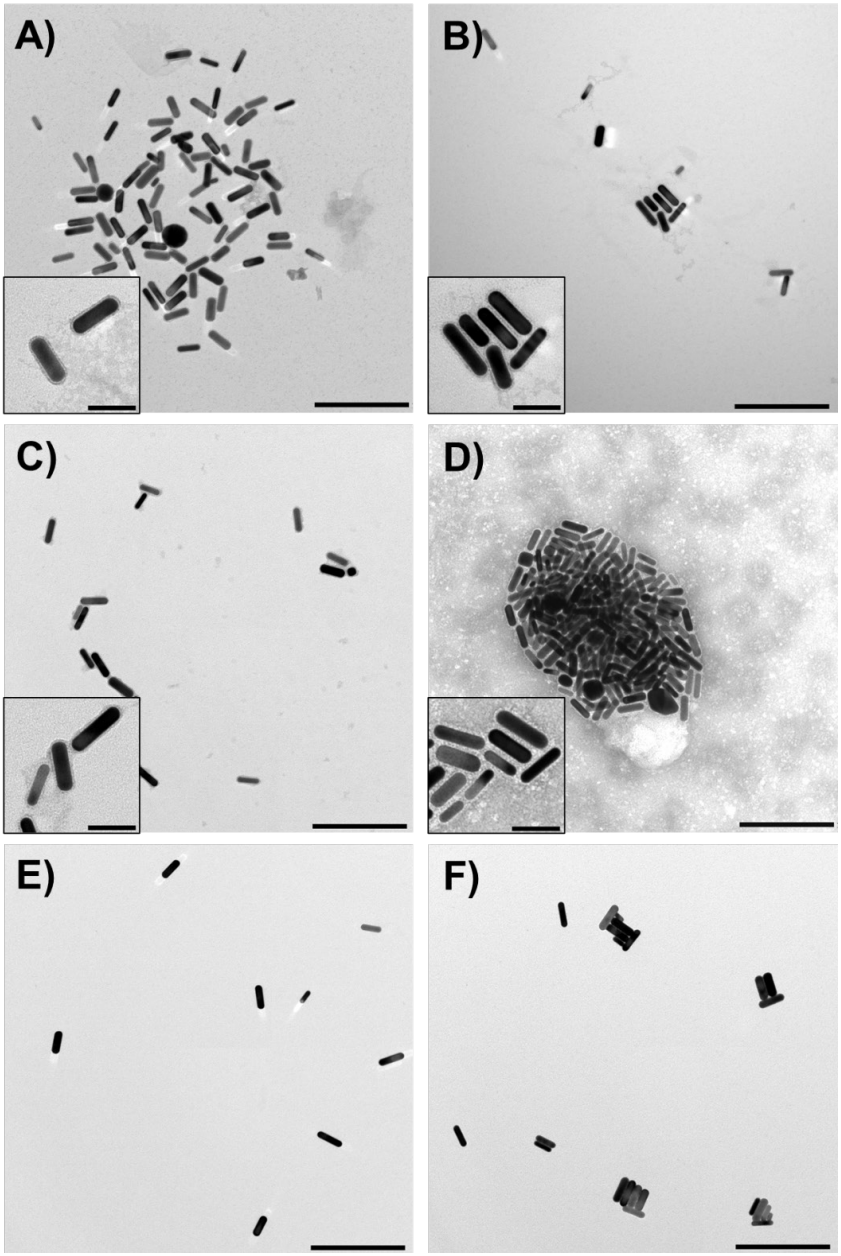

Figure 4.3. Representative TEM images of GNRs coated with: (A) **1**; (B) **2**; (C) **3**; (D) **4**; (E) PEG_{5000}; (F) PEG_{750}. Scale bars: 200 nm and 50 nm for the inserts. Samples were stained with 0.5% uranyl acetate. All samples (except **GNR@4**) were prepared in PBS (pH 7.2). Small white entities in (D) presumably derive from the peptide **4** itself, since this sample was not purified by SEC.

was added to the coating procedure to remove excess CTAB, thereby reducing GNR precipitation upon CTAB-to-peptide amphiphile exchange. GNRs, prepared according the method described in **4.5.2**, required two washing steps *via* centrifugation post-synthesis (14 000 rpm, 15 mins; the pellet was resuspended in 100 mL of water) and one extra round directly before the coating procedure. As a result, the residual CTAB concentration was sufficient to maintain colloidal stability of CTAB-protected GNRs ensuring that GNR precipitation was minimized during the peptide-amphiphile coating procedure.

Coating GNRs with molecules that did not contain an alkyl chain (molecules **4** and thiolated PEGs) was conducted in 10% (v/v) DMSO. The excess unbound molecules were removed by centrifugation, and SEC was used to exchange the buffer for PBS (pH 7.2). Coating GNRs with peptide **4** resulted in massive aggregation: UV-Vis revealed a complete loss of the LSPR band (**Figure 4.2)**. TEM imaging revealed some shell formation around the **GNR@4**, but it was not sufficient to maintain their stability in PBS (**Figure 4.3D**). The presence of the N-terminal alkyl chain indeed allowed for effective surface modification of GNRs, as reported by Schulz et al.[22] Thus, stabilization of GNRs with oligopeptides only might not be possible due to their hydrophilicity and limited penetration into the CTAB bilayer yielding incomplete coating of the GNRs.

PEGylation of GNRs resulted in a blue-shift (-1 nm) and broadening of the LSPR band for **GNR@PEG$_{750}$**, indicative of aggregation, while **GNR@PEG$_{5000}$** showed a red-shift (+11 nm) (**Figure 4.2**). This opposing behavior is explained by the change in the refractive index near the gold surface. The bandwidth was preserved in both cases, as was also observed in previous reports.[21] TEM imaging showed that **GNR@PEG$_{750}$** was present

as small compact aggregates, while **GNR@PEG$_{5000}$** consisted of well-dispersed single GNRs (**Figure 4.3E,F**). The PEG shells could not be visualized, most likely due to their low density and poor electron contrast.

All coated GNRs had a negative zeta potential in contrast to the original CTAB-stabilized GNRs, which were positively charged (-15.3 mV for **GNR@PEG$_{5000}$**, -27.3 mV for **GNR@1**, -21.1 mV for **GNR@2**, and -20.7 mV for **GNR@3** *versus* +36.6 mV for **GNR@CTAB**). This change in surface charge revealed the successful surface modification of GNRs with peptide amphiphiles.

Using the optimized coating protocol for GNRs, amphiphiles **1**-**3** proved to be effective stabilizing coatings, forming dense, well-defined shells resulting in well-dispersed single GNRs in suspension. Short peptides such as **4** are not effective as GNR stabilizers, as rapid aggregation occurred as soon as excess peptides and CTAB were removed from the GNR suspension.

4.3.3 Self-assembled monolayers formed by peptide amphiphiles on the GNR surface

TEM analysis of 21 GNRs coated with **3** showed that the shells around the **GNR@3** were not uniform in thickness (**Figure S4.1**). The shell thickness slightly differed on a rod-to-rod basis and in some cases thickness around the tips of a rod was different to the thickness around the sides (**Table S4.1**). Overall, the shell thickness distribution seemed to be curvature-independent. The average thickness was calculated to be 1.6 ± 0.3 nm both around the rod tips and around the rod sides. Interestingly, this value is lower than expected: the length of a fully-stretched molecule **3** (in a parallel β-sheet conformation and with the alkyl chain on the same axis as the peptide

backbone) was calculated to be 5.02 nm (**Scheme S4.2**). If peptide amphiphiles are situated perpendicularly to the gold surface, the expected shell thickness would be equal to the molecule length. This mismatch could be explained by several reasons. Firstly, drying effects during sample deposition on a TEM grid may cause a SAM collapse. This can implicate a change in conformation of both the peptide backbone and the alkyl chain, causing packing defects. Alternatively, it can mean that peptide amphiphiles are not positioned perpendicularly to the gold surface but at an angle. If the angle is small (<< 90°), then the peptide amphiphile shell thickness can be significantly reduced. Secondly, peptide amphiphiles consist of two segments (the alkyl chain and the peptide) with different properties and may exhibit different electron densities. The length of the C11 chain is 1.49 nm, and the rest of the molecule belongs to the peptide segment. The observed difference is most likely to be attributed to the difference in packing densities: alkyl chains undergo hydrophobic collapse and form a denser layer than the more hydrophilic peptide segments. The observed stain accumulation most likely indicates the dense part of the shell rather than the entire peptide amphiphile SAM. More information on SAM coverage densities and peptide secondary structure is needed to address this issue.

Coverage density is an important parameter defining a ligand's stabilizing capacity.[25] The coverage density of bound peptide amphiphiles was determined by UV-Vis spectroscopy as described in **Chapter 3** of this thesis.[30] For this, all three sequences were extended with a tryptophan (Trp, W) residue yielding three thiolated peptide amphiphiles **1-W**, **2-W**, and **3-W** (structures shown in **Figure S4.2**). GNRs were subsequently coated with these peptide amphiphiles. Using the extinction coefficient of Trp, $\varepsilon_{280}(W)=5600\ M^{-1}cm^{-1}$ the initial concentration of peptide amphiphiles and the amount of unbound peptide amphiphiles were determined and the number

of bound ligands was calculated. The GNRs molar concentration was calculated using $\varepsilon_{LSPR}=4.6^{\times}10^{9}\ M^{-1}cm^{-1}$ and the surface area of a rod was calculated to be 2041 nm^2.[32] Unfortunately, the protocol devised for determination of peptide amphiphile coverage on the surface of spherical GNPs was not successful when applied to GNRs (**Scheme S4.1A**). A DMSO content of 50% (v/v) during the coating procedure was not sufficient to completely eliminate fiber formation and as a result the calculated coverage density for **1-W** was determined to be 10.65 peptides/nm^2, which was unrealistically high. Therefore, the maximum theoretical coverage densities d_{theor} for molecules **1-3** were calculated to determine whether the determined coverage density was theoretically possible. For this, models of fully stretched, β-structured molecules **1-3** were built using PyMol and the distances between certain atoms were determined (for details see **Scheme S4.2A**). Each molecule was simplified to a geometrical shape and, using the obtained dimensions, the volume of the molecule was calculated (**Scheme S4.2B** and **Table S4.2**). The length of a fully-stretched molecule was taken as the shell thickness, and using a diameter of the rod (14.0 nm), the volume of the shell coating was calculated (**Scheme S4.2C** and **Table S4.2**). Dividing the volume of the shell by the volume of a molecule, the following d_{theor} values were determined: 4.89 peptide/nm^2 for **1**, 4.54 peptide/nm^2 for **2** and 3.84 peptide/nm^2 for **3**. It is important to remember that these values represent a situation when the molecules are tightly packed on the gold surface with almost no free volume within the shell. These values serve as a reference, and provide a theoretical upper limit of what coverage is achievable. This calculation revealed that the determined coverage density of 10.65 peptides/nm^2 for **1-W** cannot be realistic for a SAM and is most likely is due to the presence of fibers in the sample.

The coating protocol was therefore modified once more; 1,1,1,3,3,3-hexafluoro-2-propanol (HFIP) was used as a solvent for peptide amphiphiles (**Scheme S4.1B**). HFIP was successfully used previously to disrupt the fiber formation of analogous peptide amphiphiles,[31] and to remove amyloid-like fibrils from the peptide-coated GNPs.[33] Unfortunately, this procedure also yielded high coverage densities: 7.67 peptide/nm^2 for **1-W**, 17.22 peptide/nm^2 for **2-W**, and 14.28 peptide/nm^2 for **3-W**. Again, fiber formation was suspected to be the cause of the observed behavior, which leads us to believe that trace amounts of water could sustain the presence of fibers during the HFIP washing steps. Therefore, the coating protocol was further optimized with an additional lyophilization step, introduced after the coating mixture was separated from the GNRs *via* centrifugation (**Scheme S4.1C**). This ensured that no residual water was present in the sample when the GNRs were resuspended in HFIP. UV-Vis analysis resulted in realistic coverage densities: 3.87 peptides/nm^2 for **1-W**, 3.16 peptides/nm^2 for **2-W**, and 2.62 peptides/nm^2 for **3-W**. These values are within the d_{theor} limits and are in agreement with previously reported coverage densities on GNRs coated with thiolated fatty acids, analogous to the alkyl chain our peptide amphiphiles are comprised of.[25, 26]

It should be noted that the calculated coverage densities reflected a mean ligand density throughout the whole surface area of the rod (highly curved tips and cylindrical sides) and increased in the order **GNR@3**<**GNR@2**<**GNR@1** (2.62 < 3.16 < 3.87 peptide/nm^2). It is anticipated that different coverage densities can be observed at the tips (higher) *versus* the sides (lower) of the rod, but that is yet to be determined. The order of peptide amphiphile coverage densities was explained on the basis of the molecule's geometry. Shortening the alkyl chain length from C16 to C11 directs the peptide domain closer to the gold surface. The steric bulk

of the sidechains was altered in proportion to the alkyl chain length, causing increased steric hindrance resulting in a lower coverage density for **GNR@2** in comparison to **GNR@1**. Due to the bidentate nature of **3**, a lower peptide coverage was expected.

The following parameters indicate formation of a SAM: high coverage densities, and a tight peptide packing enabling effective hydrogen bonding (hence the high level of self-assembly) within the peptide shell. It was shown that **1-3** formed SAMs on the surface of spherical GNPs (**Chapter 3** of this thesis).[30] According to Fourier-transform infrared spectroscopy (FTIR) analysis, an increased particle size resulted in a decreased surface curvature, while the content of ordered structures within the SAMs decreased. It was hypothesized that high coverage densities and the steric bulk of the peptide side chains hindered effective hydrogen bonding when the surface curvature approached a near 'flat' state. From the curvature point of view, GNRs represent a peculiar entity. A rod can be subdivided into two half-spheres with a high curvature adjacent to a cylindrical shape formed by facets. Thus, GNRs possess a combination of high and low curvature domains.

After the coating protocol was optimized to yield fiber-free samples, attenuated total reflection IR (ATR-IR) spectra of the coated GNRs were recorded to investigate peptide secondary structure. The Amide I peak (1575-1725 cm^{-1} region) describes the conformation of the peptide backbones and is a superposition of signals caused by different secondary structure types.[34, 35] An absorption band centered between 1613-1637 cm^{-1} is attributed to β-structures, a band located between 1637-1645 cm^{-1} shows the presence of unordered structures, while a band at 1645-1662 cm^{-1} is indicative of α-structures, and a band around 1662-1682 cm^{-1} reveals the

presence of turns and other structures.[34-36] The Amide I region in these recorded spectra for peptide amphiphile-coated GNRs were fitted to give a sum of these four bands (**Figure 4.4**).

As shown previously, the peptide amphiphiles used in this study form predominantly β-structures in isolation (97.7% for **1**, 85.2% for **2**, and 94.8% for **3**).[30] Indeed, no unordered structures were observed for the peptide amphiphiles in the absence of a GNR surface (**Figure 4.4A-C** and **Table S4.3**). When the peptide amphiphiles were bound to the GNR surface, all three coatings still possessed a high β-content: 58.8% for **GNR@1**, 51.8% for **GNR@2**, and 57.1% for **GNR@3** (**Table S4.3**). The tendency to adopt unordered structures was low for all three coatings (< 7%), while a significant increase in the content of turns, α-, and other structures in comparison to the free peptide amphiphiles was observed (**Table S4.3**). It should be noted that FTIR analysis of secondary structure types across the whole rod surface provides a mean distribution within the peptide shells, therefore no information was obtained about potential differences between the rod tips or sides (**Figure 4.4D-F**). The above-mentioned secondary structures were caused by packing defects that could be linked to the peptide amphiphile's composition. Molecules **2** and **3** possess a shorter (C11) alkyl chain and show a higher α-content within the shells in comparison to molecule **1**, which possesses a longer (C16) alkyl chain. Having a double alkyl chain allowed molecule **3** to increase the β-content relative to the single chain **2**. Furthermore, lower coverage densities for **2** relative to **1** suggests that the distance between the peptides might be too long to establish effective hydrogen bonding. However, the coverage densities for **2** and **3** do not correlate with the β-content: **3** showed a lower coverage density but a higher β-content. This suggests that the distance between peptide segments when **3** is attached to a surface, is sufficient to allow effective hydrogen bonding,

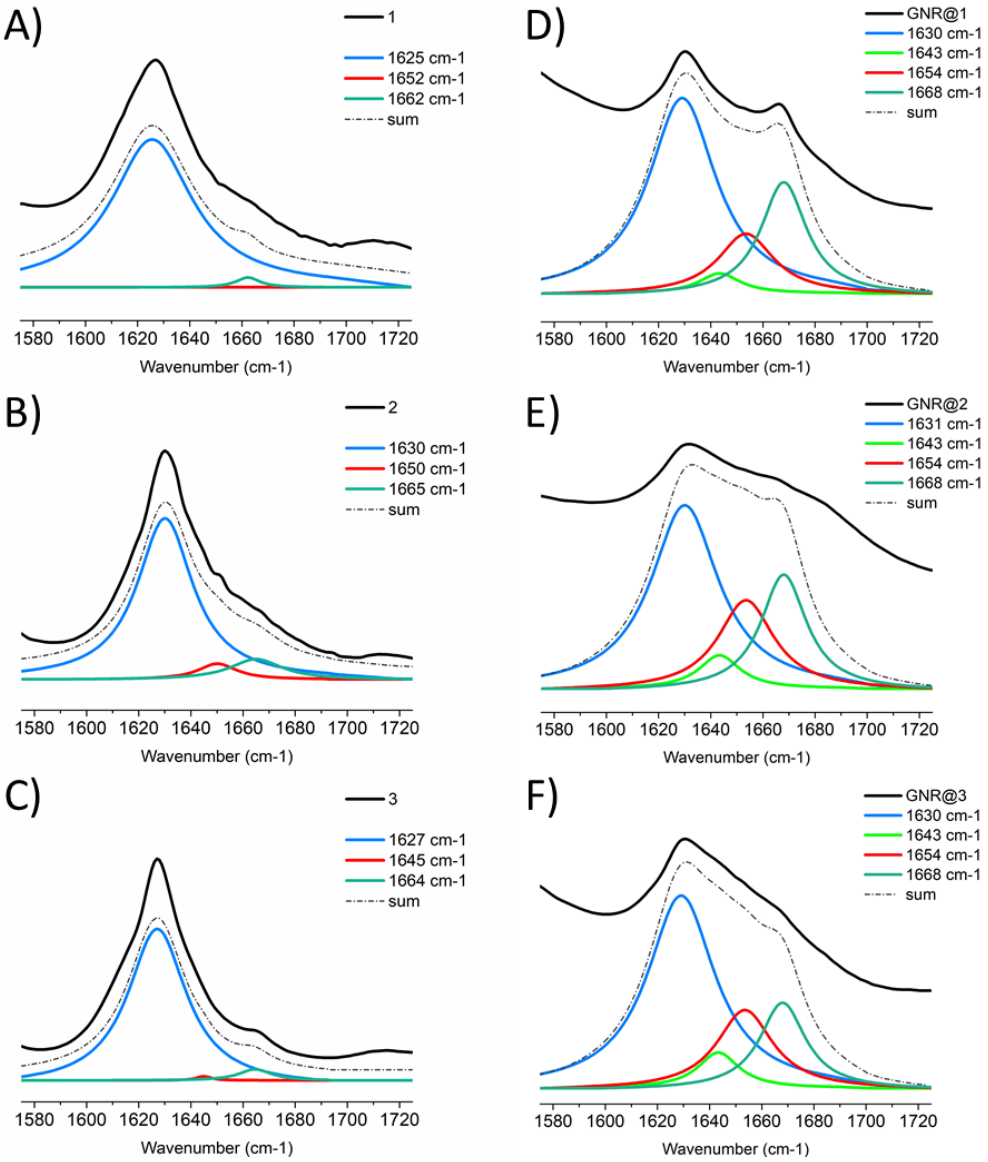

Figure 4.4. Amide I peaks were fitted to be a sum of four peaks corresponding to different secondary structure types (blue line – β-structures, green line – unordered structures, red line – α-structures, cyan line – turns). (A-C) show the Amide I fits for molecules **1-3** and were adapted from our previous work.[30] Amide I fits for GNRs coated with thiolated peptide amphiphiles are shown in (D) **1**; (E) **2**; and (F) **3**. Full ATR-IR spectra are available in the Supporting Information (**Figure S4.3**). The secondary structure distribution presented as a percentage of four different structure types is shown in **Table S4.3** (deduced from the area under the curve).

while the peptide segments of **2** are skewed by their closer proximity causing more packing defects leading to a lower β-content. In summary, a GNR coating composed of **1** or **3** is tight and restricted and therefore gives highly ordered assemblies on a surface, while **2** has more conformational freedom and packing defects, leading to less-ordered structures at the surface of a GNR.

4.3.4 Induced-aggregation behavior of peptide amphiphile-coated GNRs

Salt-induced aggregation and DTT ligand displacement assays were employed as induced-aggregation tests to investigate the ligand organization on the gold surface and the origin of the observed stability (**Chapter 3** of this thesis).[30] Furthermore, these assays probe colloidal stability of coated GNRs under extreme conditions using UV-Vis spectroscopy. For comparison to state of the art, peptide amphiphile protective coatings for GNRs were compared to PEG coatings.

NaCl induces GNR aggregation by screening surface charges, resulting in the nanoparticles reaching their isoelectric point. As a result, interparticle electrostatic repulsion is minimized, and the aggregated nanoparticles precipitate from suspension. In this assay, surface-modified GNRs were exposed to NaCl at concentrations of 150 mM, 500 mM, 1.5 M, and 3.0 M respectively for 15 min and UV-Vis spectra were recorded (**Figure S4.4**). The aggregation state was determined by the absorbance of the LSPR band: the decrease in the optical density at the LSPR wavelength (OD_{LSPR}) relative to the OD_{LSPR} of the sample in 0 mM NaCl indicated aggregation (equation is shown in **Figure 4.5B**).[30] Severe aggregation was considered to occur if the value of normalized OD_{LSPR} was below 0.5. GNRs coated with the single

chain amphiphiles **1** and **2** showed rapid (*i.e.* within 15 mins) aggregation when the NaCl concentration was increased from 150 to 500 mM, while GNRs coated with the double-chain amphiphile **3** were insensitive to high NaCl concentrations, even up to 3.0 M. PEGylated GNRs did not exhibit severe aggregation, but a 10-15% decrease in absorbance relative to the 0 M NaCl state indicated that PEGylated GNRs are more sensitive to charge screening than **GNR@3**. Rapid NaCl-induced aggregation of **GNR@1** and **GNR@2** most likely arises from their chemical structure, resulting in a different charge distribution on the surface of these coated GNRs in comparison to **3**. Interestingly, the zeta potential values were similar for all three peptide amphiphile coated GNRs (deviation ± 5 mV), and therefore cannot be used as a predictor of colloidal stability. These results suggest that the charge distribution, as well as the peptide chain conformation (its secondary structure) and coverage densities are dictated by the alkyl chain parameters (number of chains and their length). Presumably, the C-terminal glutamate residues of **3** are more exposed to the environment when coupled to a surface in comparison to **1** or **2** and therefore provide a stabilizing effect. It should be noted, that upon removal of NaCl (by means of centrifugation) the peptide amphiphile-stabilized GNRs regained their non-aggregated state, which means that the observed aggregation was reversible and should be considered agglomeration.

Next, the DTT competition assay was conducted to probe the accessibility of the gold surface and the stability of the Au-S bond: if ligands are displaced with DTT, GNRs aggregate. For this assay, coated GNRs were exposed to 1 M DTT and a UV-Vis spectrum was recorded every 5 mins (**Figure S4.5**). The aggregation factor (AF)[30, 37] was calculated as the ratio between the optical density at 610 nm (OD_{610}), a peak indicative of aggregation, and the

OD_{LSPR}. This value is then normalized to the initial value: AF_0 (equation is shown in **Figure 4.5C**).

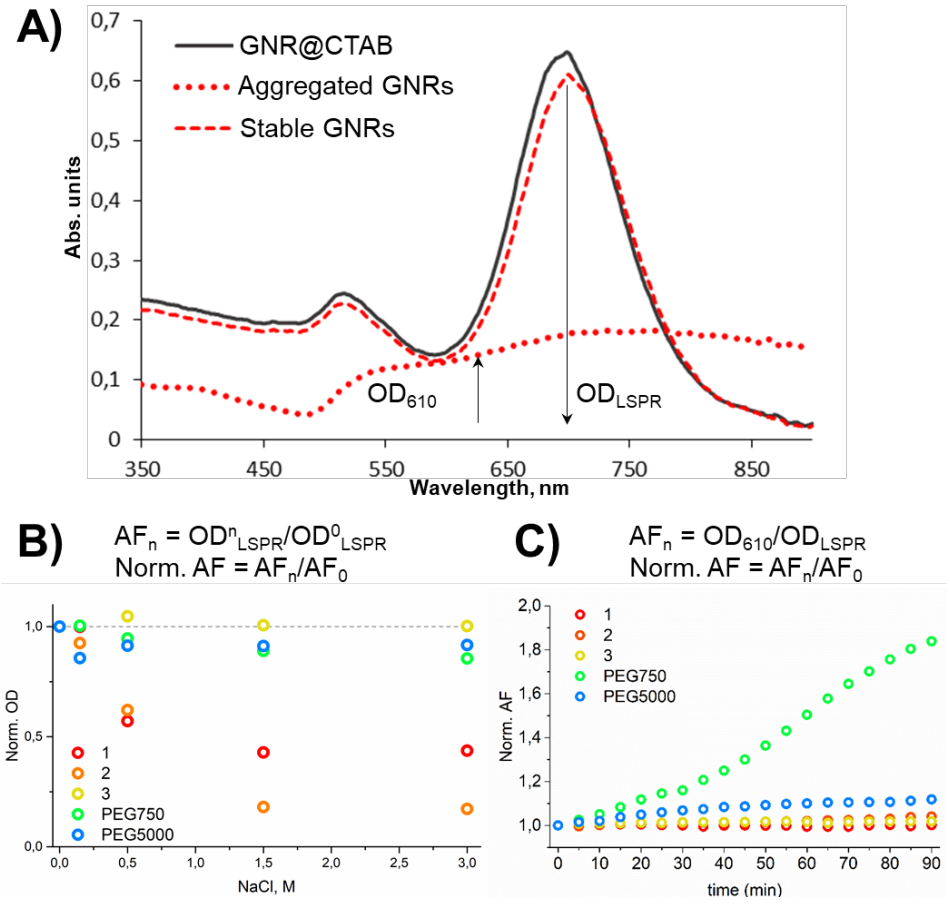

Figure 4.5. Aggregation behavior of coated GNRs was monitored as shown in schematic (A): upon aggregation the LSPR band is lost; its intensity significantly decreases in respect to the absorbance at 610 nm. Aggregation factors (AF) were calculated according to the equations and normalized to the value at t = 0 min. (B) Normalized AF calculated for coated GNRs in the presence of high salt concentrations; (C) Normalized AF calculated for coated GNRs in the presence of 1 M DTT. UV-Vis spectra the calculations were based on can be found in **Figure S4.4** and **Figure S4.5**.

From the normalized AF plot (**Figure 4.5C**) it was obvious that all three thiolated peptide amphiphiles protected and insulated the GNR surface by

forming an impenetrable monolayer. This was attributed to the high coverage densities provided by the alkyl chains, as well as to the presence of the hydrophobic environment created by the alkyl chains. Water and polar molecules dissolved in it cannot penetrate the hydrophobic barrier and are depleted from the gold surface. In contrast, the colloidal stability of PEGylated GNRs was shown to be strongly correlated to the molecular weight of the PEG. While **GNR@PEG$_{750}$** aggregated rapidly, **GNR@PEG$_{5000}$** did not exhibit signs of aggregation. GNR stabilization with PEG is based on a steric stabilization effect: the long polymer chain wraps around the surface providing good coverage and shielding. As a result, longer PEGs provide better coverage of the gold surface, while shorter PEG cannot not obtain a proper conformation to do so.[21]

Based on the combined results from both tests (**Figure 4.5B,C**), GNR coating with peptide amphiphile **3** outperformed thio-PEG$_{5000}$. **GNR@3** was completely insensitive to the surface charge screening, and did not dissociate from the gold surface upon addition of a competing thiolated ligand. At the same time the thiolated PEG$_{5000}$ coating, a molecule that greatly exceeds the length of **3**, did show some aggregation in both assays. The superior stability of **3** as a GNR coating was a result of the two alkyl tails providing an increased hydrophobic bulk and four Glu residues *versus* three residues in **1** and **2**. The contribution of the double chain was reflected in a different peptide chain arrangement allowing for the display of more charges on the shell surface than in the case of **1** or **2**. The bidentate nature of **3** is also beneficial because such coordination was proven to be more stable compared to monodentate counterparts.[37]

4.3.5 Peptide amphiphiles provide stabilizing coatings regardless of the GNR aspect ratio

GNR dimensions and aspect ratios (a.r.) can be tuned to provide desired optical properties,[4] and we validated whether thiolated peptide amphiphiles are able to stabilize GNRs with different dimensions. For this, GNRs with the a.r. range of 2.9-4.1 were used (**Table 4.1**). As expected, coating of GNRs with the more hydrophobic amphiphiles **1** and **3** resulted in shell formation alongside fiber formation: apparent from UV-Vis spectra and TEM images, while coating with **2** was not accompanied by fiber formation (**Figure 4.6A,B**). Well-defined shells for **1**, **2**, and **3** corresponding to a ligand monolayer were visible as well. Interestingly, the zeta potential values were within the -20 to -30 mV range, regardless of the GNR a.r. or applied peptide amphiphile coating.

Table 4.1. Size characteristic of GNRs used in this study.

Sample	Length, nm (± SD*)	Width, nm (± SD)	A.r.
GNR	46.4 ± 8.3	14.0 ± 2.9	3.3
s-GNR**	44.0 ± 4.0	14.8 ± 1.9	2.9
l-GNR***	49.0 ± 9.1	12.0 ± 2.6	4.1

Average size of GNRs was determined using TEM. *- SD = standard deviation. **- short GNRs (**s-GNR**) were synthesized according to the method described in **4.5.2**, but had different dimensions compared to the **GNR** sample (within batch-to-batch variations). ***- long GNRs (**l-GNR**) were purchased from Sigma-Aldrich.

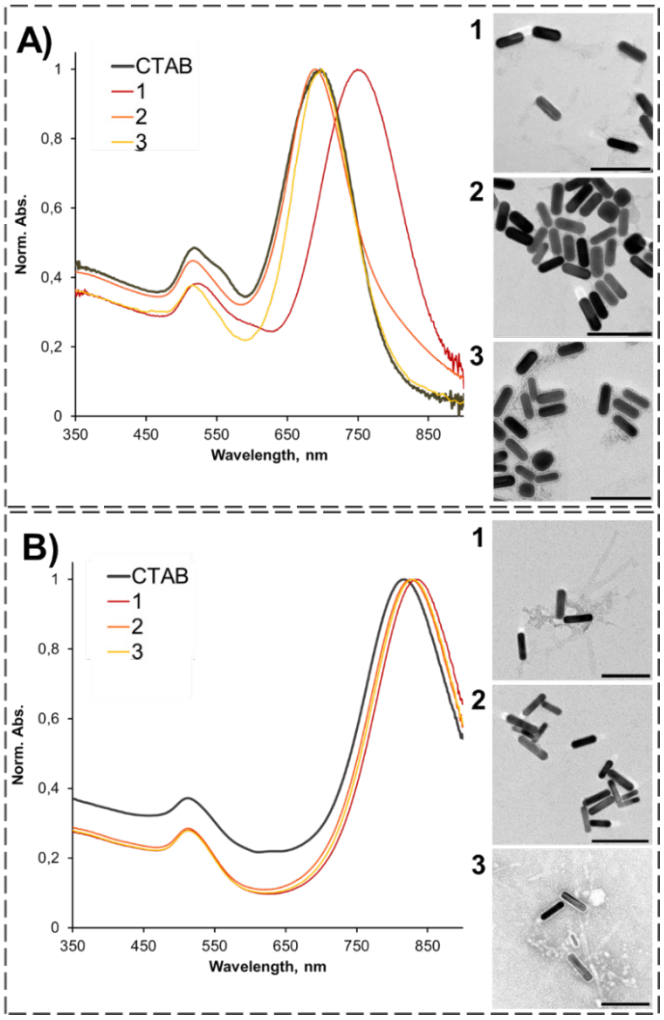

Figure 4.6. Sample characterization (UV-Vis spectroscopy on the left and TEM imaging on the right) for peptide amphiphile-coated GNRs with different a.r.: (panel A) **s-GNRs** and (panel B) **l-GNRs** Samples were prepared in PBS (pH 7.2). The non-optimized protocol was used to fabricate the samples; hence peptide amphiphile fibers are present. In the case of **s-GNR@1**, a significant red-shift was observed due to the presence of associated fibers triggering interparticle interactions. Scale bar is 100 nm. Negative staining (0.5% uranyl acetate) was used.

4.3.6 Positively charged peptide amphiphile-stabilized GNRs

Peptide amphiphiles can be designed to carry either net negative (as for molecules **1-3**) or positive charge.[38] Two thiolated peptide amphiphiles dubbed **1-K** and **2-K**, in which Glu residues were replaced by Lys residues, were synthesized (sequences are shown in **Figure S4.6**). Due to the opposite charge, the coating procedure had to be altered. As a result, fiber formation was not observed, possibly due to the electrostatic repulsion between the positively charged CTAB and lysine-rich peptide amphiphiles. Furthermore, the coating procedure was conducted in 10% DMSO (aq., v/v) and extended to 16 hours instead of 1 hour, and SEC purification was done with water as the eluent. UV-Vis spectroscopy revealed a small red-shift (+7 nm) for **GNR@1-K** and aggregation did not occur. Although a larger red-shift (+16 nm) was observed for **GNR@2-K**, TEM imaging revealed no aggregation, and no peptide amphiphile fibers, hence this red-shift cannot arise from association with peptide amphiphile fibers (**Figure 4.7**). The shifts were explained by a change in refractive index at the GNR surface upon CTAB exchange.[18] The zeta potential was positive for both coated samples (+23.6 mV for **GNR@1-K**, +18.7 mV for **GNR@2-K** *versus* +36.6 mV for **GNR@CTAB**). The NaCl-aggregation assay was applied to the positively charged **GNR@1-K** and **GNR@2-K**. The samples were exposed to increasing NaCl concentrations for 15 min and the OD_{LSPR} was monitored. (**Figure 4.7C** and **Figure S4.6**). GNRs coated with positively charged **1-K** and **2-K** already aggregated at 50 mM NaCl, when all surface charges were screened and the isoelectric point was reached. This implies that **GNR@1-K** and **GNR@2-K** cannot be used in biologically relevant conditions.

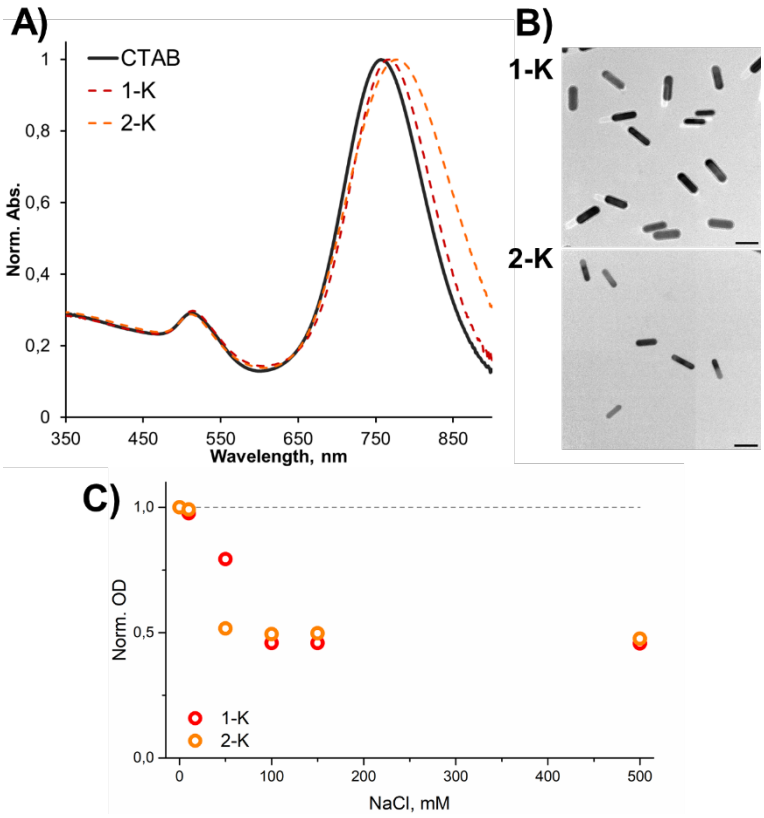

Figure 4.7. Characterization of GNRs coated with positively charged **1-K** and **2-K**: (A) UV-Vis spectroscopy and (B) TEM imaging. Samples were prepared in MQ water. Scale bar is 50 nm. Negative staining (0.5% uranyl acetate) was used. (C) Normalized AF calculated for coated GNRs in the presence of high salt concentrations. Aggregation factor values (AF) were calculated according to the equations shown in **Figure 4.5B** and were normalized to the value at t = 0 min. UV-Vis spectra the calculations were based on can be found in **Figure S4.6**.

4.4 Conclusions

Thiolated peptide amphiphiles were evaluated for their ability to form a protective coating at the GNR surface. Peptides that did not contain an alkyl chain failed to stabilize GNRs. However, it was proven that both negatively charged amphiphiles **1-3** and positively charged **1-K** and **2-K** are capable of displacing CTAB from the GNR surface and stabilize GNRs irrespective of their aspect ratio. The negatively charged peptide amphiphile-stabilized GNRs possess long-term stability under physiologically relevant conditions. Thiolated, negatively-charged, peptide amphiphiles provide greater stability compared to commonly used thiolated PEG of the same molecule length. Furthermore, thiolated peptide amphiphiles provide a much thinner coating with equal stabilizing capacity in comparison to long thiolated PEG. Peptide amphiphiles also offer relatively easy pathways for modification with ligands, while modification of long thiolated PEGs is not trivial. Moreover, PEGs were reported to induce specific immune responses,[39] while peptide amphiphiles are not recognized by the immune system.[40]

The stabilizing effect of the amphiphiles was attributed to the presence of an alkyl chain and to the formation a self-assembled monolayer (SAM) bound to the GNR surface. Both the number and length of the alkyl chain proved to be important factors influencing the peptide amphiphile self-assembly on the surface. Peptide amphiphiles with a single alkyl chain **1** (C16 length) and **2** (C11 length) showed higher coverage densities with respect to the bidentate peptide amphiphile **3** (double C11). ATR-IR analysis of the secondary structure of the GNR-bound peptide amphiphiles revealed that all three peptide amphiphiles formed ordered assemblies on the GNR surface in comparison to peptide amphiphile **2**, with a slightly lower β-content (<7%). At

NaCl concentrations exceeding biologically relevant levels, GNRs coated with the single chain peptide amphiphiles **1** and **2** showed that the surface charge of such GNRs is more easily screened than in the case of GNRs coated with the double chain **3**. These findings suggest that despite similar self-assembly behavior and high coverage densities, there is a delicate difference in the peptide domain assembly at the GNR surface. According to the induced aggregation tests, peptide amphiphile **3** was considered to be the best stabilizer for GNRs as **GNR@3** was stable at high NaCl and DTT concentration.

Coatings based on peptide amphiphiles **1-3** were previously applied to stabilize spherical GNPs (**Chapter 3** of this thesis).[30] Similarly to the behavior of **3** on the surface of 20 and 40 nm GNPs, **GNR@3** showed superior stability even in 3.0 M NaCl (**Figure 4.5B**). Both single chain peptide amphiphiles **1** and **2** could not prevent reversible nanoparticle agglomeration at 500 mM NaCl. GNPs and GNRs possess different kinds of curvature: GNRs have both spherical (tips) and cylindrical (sides) parts. This seems to suggest that the charge distribution on the cylindrical surface did not differ significantly from the charge distribution on the spherical surface.

Obtained guidelines on the coating protocol and data on peptide amphiphile-stabilized GNRs encourage the use of these nanoparticles in biological applications *in vitro* and *in vivo*. Peptide amphiphile-stabilized GNRs equipped with specific ligands can be used in label-free biosensing, as well as in imaging, and as a delivery platform. **Chapter 5** of this thesis will focus on employing peptide amphiphile-stabilized GNPs and GNRs in vaccine development.

4.5 Experimental section

4.5.1 Materials

All chemicals were purchased from Sigma-Aldrich unless stated otherwise. For GNR and GNP synthesis, the purity of CTAB and the composition of the gold salt are critical for reliable particle formation. CTAB (≥ 99%, H6269) and $HAuCl_4 \times 3\ H_2O$ (49% Au basis, G4022) were purchased from Sigma-Aldrich. Silver nitrate (99,9999%, 4500.1) and Oxyma Pure were purchased from Carl Roth GmbH. TFA, piperidine, DMF, DCM, methanol, and acetonitrile were purchased from Biosolve. Thiolated PEGs ($HS\text{-}PEG\text{-}OCH_3$ with average MW of 750 Da and 5000 Da) were supplied by Rapp Polymere GmBH. TEM grids (Formvar/Carbon, 200 mesh, on copper support) were purchased from Electron Microscopy Sciences. Gold nanorods (GNRs) with an a.r. of 4.1 were purchased from Sigma-Aldrich (LSPR at 810 nm).

4.5.2 GNRs synthesis

Gold nanorods (GNRs) were synthesized in the presence of CTAB in the two-step process commonly described as seed-mediated approach.[3] Briefly, 2-3 nm seeds were prepared by mixing the following solution: CTAB (5 mL, 0.20 M), $HAuCl_4$ (5 mL, 0.50 mM) with ice-cold $NaBH_4$ (0.60 mL, 10 mM) added under intense stirring at room temperature.[32] After 2 mins of vigorous stirring, the solution was left undisturbed at room temperature for 2 hours. For the overgrowth, solutions of $HAuCl_4$ (50 mL, 1.0 mM) and $AgNO_3$ (200 µL,100 mM) were gently mixed with CTAB (50 mL, 0.20 M) at 25 ºC. The amount of silver added is the major determinant for the aspect ratio (a.r.) of the resulting GNRs. After 2 min of stirring, ascorbic acid (550 µL, 100 mM) was added. The growth solution underwent a color change from dark yellow

to colorless due to reduction of gold. Next, 120 µL of the seed solution was added to the growth solution under vigorous stirring at room temperature. After 6 hours the rods were washed with MilliQ twice (2 × 100 mL) by means of centrifugation to remove the CTAB excess. Average dimensions were found to be 46.4 by 14.0 nm as determined by TEM.

Due to the high sensitivity of this synthetic procedure to the quality of some reagents, slight alterations to the protocol may be needed. Increasing the volume of 100 mM $AgNO_3$ to 400 µL may be necessary to make GNRs with an a.r. of 3.0. If shape control is lost and non-rodlike particles are formed instead of GNRs, it is recommended to adjust the ratio between $HAuCl_4$ and ascorbic acid.

4.5.3 Peptide and peptide amphiphile synthesis

All peptide amphiphile and peptide sequences were synthesized by solid-phase peptide synthesis using standard Fmoc-chemistry protocols (9-fluorenylmethyloxycarbonyl-protected amino acids were used to propagate the peptide chain). The synthesis was performed on an automated microwave peptide synthesizer Liberty Blue (CEM) using standard settings. 5 equivalents (relative to the resin loading) of Fmoc-protected amino acids were used to propagate the peptide chain. 20% piperidine in dimethylformamide (DMF) was used as the deprotection agent (90 °C, 60 secs) and N,N'-diisoprorylcarbodiimide (DIC)/OxymaPure were employed as the activator/activator base pair (5 equivalents relative to the resin loading, 95 °C, 4 mins). The sequences were synthesized on a high-loading Wang resin (**1-4**, **1-W**, **2-W**, **3-W**) or a high-loading Rink Amide resin (**1-K** and **2-K**), yielding either a C-terminal acid (**1-4**) or an amide (**1-K** and **2-K**) at 0.1 mmol scale. Used resin loadings were within the range of 0.5-0.8 mmol/g. The alkylation was performed using Liberty Blue *via* an on-resin coupling of

the corresponding chain to the terminal amine of the corresponding peptide (the same protocol as for amino acids). The terminal thiol of acyl chains was blocked with 2,2′-Dithiobis(5-nitropyridine) (DTNP, 1 eq. in DMF, 3 hours). Peptide **4** was not alkylated, thus preserving a free amine at the N-terminus. All the molecules were cleaved from the resin using a trifluoroacetic acid (TFA) cocktail: 1.5% deionized water, 2.5% triisopropylsilane (TIS), and in the case of **4**, 2.5% 3,4-ethylenedioxythiophene (EDOT) was added. The crude peptide amphiphiles were precipitated into cold diethyl ether, pelleted by centrifugation, redissolved in water, and lyophilized prior to purification.

4.5.4 Peptide amphiphile purification

A Shimadzu HPLC system equipped with two LC-20AR pumps, an SPD-20A UV-Vis detector and a Phenomenex Kinetex EVO C18 column (21.2 by 150 mm) was used to perform HPLC purification of the peptidic molecules. The mobile phases were water and acetonitrile, containing either 0.1% NH_3 (for **1-3**) or 0.1% TFA (for **4**, **1-K**, and **2-K**). Acetonitrile gradients were run over 25 min with a flow rate of 12 mL/min: **1-3** were purified on a 5-55% gradient of acetonitrile; **1-K** – 20-100%; and **2-K** – 15-75%. Prior to purification of **1-3**, the protecting TNP group was removed by Tris(2-carboxyethyl)phosphine hydrochloride (TCEP, added in excess, 30 mins incubation). The purity of the compounds was assessed using LC-MS (**Figures S4.7-15**). All purified molecules were lyophilized and stored at -20 °C until needed.

4.5.5 Coating GNRs with thiolated peptide amphiphiles

GNRs were coated using a ligand exchange approach. The ligand (*i.e.* peptide amphiphiles) was dissolved in DMSO and added to a stirred GNR suspension. The ligand excess was at least 100 000-fold (molar) relative to

the GNR concentration obtained using extinction coefficients for GNRs with different a.r. published by Orendorff *et al*.[32] In other words, for every mL of GNR suspension with the optical density of absorbance maximum (OD_{LSPR}) of 1, at least 0.05 mg of a peptide amphiphile was added. The two components were mixed in such a ratio (v/v) to assure that the final concentration of DMSO in the mixture was 50% (v/v) for **GNR@1**, **GNR@2**, and **GNR@3**, and 10% (v/v) for **GNR@4**, **GNR@1-K**, and **GNR@2-K**. After the incubation (1 hour for **1-3**; 16 hours for **1-K** and **2-K**) the samples were centrifuged (Eppendorf Centrifuge 5425, 14 000 rpm, 15 mins), the supernatants were discarded and replaced with 25% DMSO in water (**GNR@1**, **GNR@2**, and **GNR@3**) or 5% DMSO in water (**GNR@4**, **GNR@1-K**, and **GNR@2-K**). **GNR@4**, **GNR@1-K**, and **GNR@2-K** were directly loaded on a size exclusion chromatography column (SEC, NAP-25 columns, GE Healthcare) to remove any remaining free ligand and exchange for phosphate buffered saline (PBS). The **GNR@1**, **GNR@2**, and **GNR@3** samples were incubated in DMSO, 25% (v/v) overnight to dissolve unbound peptide amphiphiles. After centrifugation, supernatants were discarded and the GNRs were resuspended in 5% DMSO (v/v) the same SEC purification was performed. If fiber formation by **1** and **3** occurred, the samples were lyophilized, resuspended in pure DMSO, incubated overnight and SEC-purified as described above.

4.5.6 PEGylation of GNRs

Thiolated PEGs were dissolved in DMSO (10 mg/mL). The added PEG excess was at least 100 000-fold relative to GNR molar concentration. For every mL of a GNR suspension with the OD_{LSPR} of 1 at least 0.2 mg of PEG was added. The PEG solution and GNR suspension were mixed resulting in a 10% (v/v) final concentration of DMSO. GNRs were PEGylated in 10% DMSO (v/v) mixtures overnight and PEG was removed *via* centrifugation

(14 000 rpm, 15 mins). GNRs were resuspended in MQ and directly purified by means of SEC (NAP-25 column, GE Healthcare) with PBS as the eluent according to the manufacturer's manual.

4.5.7 UV-Vis spectroscopy

Spectra were recorded using a Cary 300 UV-Vis spectrophotometer (Agilent). Samples were placed in 1 mm quartz cuvettes and spectra were recorded between 900-350 nm unless otherwise stated. Samples were diluted with either MQ water or PBS as appropriate to provide a maximum absorbance in the range of 0.6-1.0. All spectra were normalized to a maximum absorbance of 1.0, except for the induced aggregation experiments where spectra were not normalized and aggregation factors were calculated as described in **4.5.12** and **4.5.13**. To calculate peptide amphiphile and GNR concentration, Lambert-Beer law was used (equation 1):

$$A = \varepsilon \cdot l \cdot c \cdot N, \quad (1)$$

where A is absorption, ε is extinction coefficient (in $M^{-1}cm^{-1}$), l is the optical path length (l = 1 mm), c is molar concentration (in M), and N is the dilution factor. For GNRs with an a.r. of 3.3, $\varepsilon_{LSPR}(GNR)=4.6\times10^9$ $M^{-1}cm^{-1}$ was used.[32] For tryptophan absorbance $\varepsilon_{280}(W)=5600$ $M^{-1}cm^{-1}$ was used.

4.5.8 Transmission electron microscopy

Grid preparation for transmission electron microscopy (TEM) measurements involved the following steps: a 10 µL GNR sample droplet was placed on a continuous carbon grid (200 mesh copper support) and left undisturbed for 10 mins. The excess sample was removed by manually blotting with a fibreless paper tissue (Kimtech Science). A water droplet (10 µL) was put on

the grid to wash off the unbound sample and blotted once again right away. Uranyl acetate staining (0.5% w/v, 10 µL, t = 10 secs) was applied, followed immediately by blotting. Images were acquired on a JEM1400 Plus (JEOL) transmission electron microscope operated at 80 kV and equipped with a CCD camera.

4.5.9 Zeta potential measurements

A Zetasizer Nano-7 S (Malvern Instruments) equipped with a 633 nm laser wavelength and a 173° fixed scattering angle was used to perform zeta potential measurements. Samples in PBS were diluted 10 times with deionized water to obtain a salt concentration below 20 mM. Sample aliquots of 1 mL were placed in a universal dip cuvette and the zeta potential was calculated from an average of three measurements.

4.5.10 Coverage density measurements

Coverage densities were determined through the unbound ligand content.[41] The three thiolated peptide amphiphiles were extended with a Tyr coupled *via* a glycine spacer to yield **1-W**, **2-W**, **3-W** (**Figure S4.2**). These three molecules were used to coat GNRs in an altered setup: three different protocols were devised (workflows schematically shown in **Scheme S4.1**). The ratio between GNR and peptide amphiphile concentrations was preserved (see, **4.5.5**). Lambert-Beer was used to determine peptide and GNR concentrations (equation 1: $\varepsilon_{280}(W)=5600\ M^{-1}cm^{-1}$; $\varepsilon_{LSPR}(GNR)=4.6\times10^{9}\ M^{-1}cm^{-1}$).

Protocol #1 (**Scheme S4.1A**). Tryptophan-tagged peptide amphiphiles **1-W**, **2-W**, and **3-W** were dissolved in DMSO and mixed with CTAB-protected GNRs in the same molar ratio as described above (**4.5.5**), yielding a final

DMSO concentration of 50% (v/v). After a 1-hour incubation, the supernatant of the first centrifugation cycle was collected and combined with the supernatant of the following wash with 25% DMSO (v/v). The supernatants were analyzed by UV-Vis with absorbance at 280 nm. As the concentration of **1-W**, **2-W**, and **3-W** added to the GNR suspension was known, the concentration of unbound ligands in the combined supernatants was determined using UV-Vis, the number of bound ligands was calculated. The number of ligands per particle was calculated by dividing the concentration of the bound ligands by the molar concentration of original GNRs (calculated as described elsewhere).[32] The coverage density expressed in peptide/nm^2 was derived from the average surface area of a rod.

Protocol #2 (**Scheme S4.1B**). Tryptophan-tagged molecules **1-W**, **2-W**, and **3-W** were dissolved in 1,1,1,3,3,3-hexafluoro-2-propanol (HFIP) and mixed with CTAB-protected GNRs in the same molar ratio as described above (**4.5.5**), but yielding a final HFIP concentration of 33% (v/v). After a 1-hour incubation, the supernatant of the first centrifugation cycle was collected and combined with the supernatant of the following wash with HFIP. The supernatants were analyzed using UV-Vis and absorbance at 280 nm was determined. As the concentration of **1-W**, **2-W**, and **3-W** added to the GNR suspension was known, the concentration of unbound ligands in the combined supernatants was determined using UV-Vis, and it was possible to deduce the amount of bound ligands. The number of ligands per particle was calculated by dividing the concentration of the bound ligands by the molar concentration of original GNRs (calculated as described elsewhere).[32] The coverage density expressed in peptide/nm^2 was derived from the average surface area of a rod.

Protocol #3 (**Scheme S4.1C**). Tryptophan-tagged molecules **1-W**, **2-W**, and **3-W** were dissolved in HFIP and mixed with CTAB-protected GNRs in the

same molar ratio as described above (**4.5.5**), but yielding a final HFIP concentration of 33% (v/v). After a 1-hour incubation, the supernatant of the first centrifugation cycle was collected. The GNR pellets were resuspended in water and lyophilized. Next, GNRs were resuspended in HFIP and were pelleted again. The supernatants were analyzed using UV-Vis and absorbance at 280 nm was determined. Since the concentration of **1-W**, **2-W**, and **3-W** added to the GNR suspension was known, the concentration of the unbound ligands in the combined supernatants was determined using UV-Vis, and the number of bound ligands was calculated. Next, the number of ligands per particle was calculated by dividing the concentration of bound ligands by the molar concentration of original GNRs (calculated as described elsewhere).[32] The coverage density expressed in peptide/nm^2 was derived from the average surface area of a rod.

4.5.11 Infra-red spectroscopy measurements

Attenuated total reflection-infrared (ATR-IR) spectra were recorded on an Excalibur FTS 4000 setup equipped with a “golden gate” accessory. Samples were analyzed in the solid state (both thiolated peptide amphiphiles and coated GNRs). A lyophilized powder was placed on top of the crystal and spectra were recorded (512 scans at 2 cm^{-1} aperture). Deconvolution and fitting of the Amide I peaks to the Lorenz function were performed using Origin Pro. Surface areas under the individual peaks were taken to determine the distribution of different peptide secondary structure types.

4.5.12 Stability to electrolyte-induced aggregation

GNRs coated with **1-3**, thio-PEG$_{5000}$, and thio-PEG$_{750}$ were mixed with a 4.5 M NaCl solution to yield samples with the following final concentrations of salt: 150 mM, 500 mM, 1.5 M and 3.0 M. The GNR concentration

remained constant (OD_{LSPR} ~ 0.2-0.4) while only the salt concentration was varied. A spectrum from 500–800 nm was recorded using an Infinite M1000 plate-reader (Tecan). The optical densities at the peak maximum of the LSPR (OD_{LSPR}) of each sample were compared to that of a GNR suspension with no salt added (0 mM NaCl). When GNRs aggregate, they exhibit a red-shift and often a broadening of the plasmon band. The OD of the samples with increasing amounts of NaCl were monitored and a decrease in the OD_{LSPR} value indicated aggregation.

4.5.13 Stability to DTT-competition induced aggregation

A DL-Dithiothreitol (DTT) competition assay was used to assess permeability of the peptide amphiphile shells formed around the GNRs. The protocol used in this study was a modification of that published by the Mattoussi group.[37] Briefly, 4 M DTT, deionized water and the coated GNRs were mixed in a proportion to set the final concentration of DTT to 1 M. The OD_{LSPR} value was monitored by UV-Vis for 90 mins with a 5 min interval between the data points to assess the aggregation state. The OD_{LSPR} at the 0 min time point was maintained within a range of 0.5-0.9 for all GNR samples. The ratio between the OD at 610 nm and OD_{LSPR} gave rise to the aggregation factor (AF), which was normalized to the value at t = 0 min.

4.6 References

1. Lohse, S. E.; Murphy, C. J., The Quest for Shape Control: A History of Gold Nanorod Synthesis. *Chem Mater* **2013,** *25* (8), 1250-1261.

2. Link, S.; Burda, C.; Mohamed, M. B.; Nikoobakht, B.; El-Sayed, M. A., Laser photothermal melting and fragmentation of gold nanorods: Energy and laser pulse-width dependence. *J Phys Chem A* **1999,** *103* (9), 1165-1170.

3. Nikoobakht, B.; El-Sayed, M. A., Preparation and growth mechanism of gold nanorods (NRs) using seed-mediated growth method. *Chem Mater* **2003,** *15* (10), 1957-1962.

4. Gonzalez-Rubio, G.; Kumar, V.; Llombart, P.; Diaz-Nunez, P.; Bladt, E.; Altantzis, T.; Bals, S.; Pena-Rodriguez, O.; Noya, E. G.; MacDowell, L. G.; Guerrero-Martinez, A.; Liz-Marzan, L. M., Disconnecting Symmetry Breaking from Seeded Growth for the Reproducible Synthesis of High Quality Gold Nanorods. *ACS Nano* **2019,** *13* (4), 4424-4435.

5. Wang, H. F.; Huff, T. B.; Zweifel, D. A.; He, W.; Low, P. S.; Wei, A.; Cheng, J. X., In vitro and in vivo two-photon luminescence imaging of single gold nanorods. *P Natl Acad Sci USA* **2005,** *102* (44), 15752-15756.

6. Durr, N. J.; Larson, T.; Smith, D. K.; Korgel, B. A.; Sokolov, K.; Ben-Yakar, A., Two-photon luminescence imaging of cancer cells using molecularly targeted gold nanorods. *Nano Letters* **2007,** *7* (4), 941-945.

7. Tong, L.; Wei, Q. S.; Wei, A.; Cheng, J. X., Gold Nanorods as Contrast Agents for Biological Imaging: Optical Properties, Surface Conjugation and Photothermal Effects. *Photochem Photobiol* **2009,** *85* (1), 21-32.

8. Zhang, W. C.; Caldarola, M.; Lu, X. X.; Orrit, M., Plasmonic Enhancement of Two-Photon-Excited Luminescence of Single Quantum Dots by Individual Gold Nanorods. *ACS Photonics* **2018,** *5* (7), 2960-2968.

9. van den Broek, B.; Ashcroft, B.; Oosterkamp, T. H.; van Noort, J., Parallel Nanometric 3D Tracking of Intracellular Gold Nanorods Using Multifocal Two-Photon Microscopy. *Nano Letters* **2013,** *13* (3), 980-986.

10. Knights, O. B.; Ye, S. J.; Ingram, N.; Freear, S.; McLaughlan, J. R., Optimising gold nanorods for photoacoustic imaging in vitro. *Nanoscale Adv* **2019,** *1* (4), 1472-1481.

11. Xu, K. Y.; Shi, J. W.; Pourmand, A.; Udayakumar, T. S.; Dogan, N.; Zhao, W. Z.; Pollack, A.; Yang, Y. D., Plasmonic Optical Imaging of Gold Nanorods Localization in Small Animals. *Sci Rep-Uk* **2018,** *8*: e9342.

12. Bhamidipati, M.; Fabris, L., Multiparametric Assessment of Gold Nanoparticle Cytotoxicity in Cancerous and Healthy Cells: The Role of Size, Shape, and Surface Chemistry. *Bioconjugate Chem* **2017,** *28* (2), 449-460.

13. Yelin, D.; Oron, D.; Thiberge, S.; Moses, E.; Silberberg, Y., Multiphoton plasmon-resonance microscopy. *Opt Express* **2003,** *11* (12), 1385-1391.

14. Sonnichsen, C.; Alivisatos, A. P., Gold nanorods as novel nonbleaching plasmon-based orientation sensors for polarized single-particle microscopy. *Nano Letters* **2005,** *5* (2), 301-304.

15. Abadeer, N. S.; Murphy, C. J., Recent Progress in Cancer Thermal Therapy Using Gold Nanoparticles. *J Phys Chem C* **2016,** *120* (9), 4691-4716.

16. Wu, Y.; Ali, M. R. K.; Dong, B.; Han, T. G.; Chen, K. C.; Chen, J.; Tang, Y.; Fang, N.; Wang, F. J.; El-Sayed, M. A., Gold Nanorod Photothermal Therapy Alters Cell Junctions and Actin Network in Inhibiting Cancer Cell Collective Migration. *ACS Nano* **2018,** *12* (9), 9279-9290.

17. Cao, J.; Sun, T.; Grattan, K. T. V., Gold nanorod-based localized surface plasmon resonance biosensors: A review. *Sensor Actuat B-Chem* **2014,** *195*, 332-351.

18. Paulo, P. M. R.; Zijlstra, P.; Orrit, M.; Garcia-Fernandez, E.; Pace, T. C. S.; Viana, A. S.; Costa, S. M. B., Tip-Specific Functionalization of Gold Nanorods for Plasmonic Biosensing: Effect of Linker Chain Length. *Langmuir* **2017,** *33* (26), 6503-6510.

19. Scarabelli, L.; Sanchez-Iglesias, A.; Perez-Juste, J.; Liz-Marzan, L. M., A "Tips and Tricks" Practical Guide to the Synthesis of Gold Nanorods. *J Phys Chem Lett* **2015,** *6* (21), 4270-4279.

20. Ye, X. C.; Gao, Y. Z.; Chen, J.; Reifsnyder, D. C.; Zheng, C.; Murray, C. B., Seeded Growth of Monodisperse Gold Nanorods Using Bromide-Free Surfactant Mixtures. *Nano Letters* **2013,** *13* (5), 2163-2171.

21. Bogliotti, N.; Oberleitner, B.; Di-Cicco, A.; Schmidt, F.; Florent, J. C.; Semetey, V., Optimizing the formation of biocompatible gold nanorods for cancer research: Functionalization, stabilization and purification. *J Colloid Interf Sci* **2011,** *357* (1), 75-81.

22. Schulz, F.; Friedrich, W.; Hoppe, K.; Vossmeyer, T.; Weller, H.; Lange, H., Effective PEGylation of gold nanorods. *Nanoscale* **2016,** *8* (13), 7296-7308.

23. Burrows, N. D.; Lin, W.; Hinman, J. G.; Dennison, J. M.; Vartanian, A. M.; Abadeer, N. S.; Grzincic, E. M.; Jacob, L. M.; Li, J.; Murphy, C. J., Surface Chemistry of Gold Nanorods. *Langmuir* **2016,** *32* (39), 9905-9921.

24. Hanske, C.; Sanz-Ortiz, M. N.; Liz-Marzan, L. M., Silica-Coated Plasmonic Metal Nanoparticles in Action. *Adv Mater* **2018,** *30* (27): e1707003.

25. Janicek, B. E.; Hinman, J. G.; Hinman, J. J.; Bae, S. H.; Wu, M.; Turner, J.; Chang, H. H.; Park, E.; Lawless, R.; Suslick, K. S.; Murphy, C. J.; Huang, P. Y., Quantitative Imaging of Organic Ligand Density on Anisotropic Inorganic Nanocrystals. *Nano Letters* **2019,** *19* (9), 6308-6314.

26. Wu, M.; Vartanian, A. M.; Chong, G. N.; Pandiakumar, A. K.; Hamers, R. J.; Hernandez, R.; Murphy, C. J., Solution NMR Analysis of Ligand Environment in Quaternary Ammonium-Terminated Self -Assembled Monolayers on Gold Nanoparticles: The Effect of Surface Curvature and Ligand Structure. *J Am Chem Soc* **2019,** *141* (10), 4316-4327.

27. Ma, Z. Y.; LeBard, D. N.; Loverde, S. M.; Sharp, K. A.; Klein, M. L.; Discher, D. E.; Finkel, T. H., TCR Triggering by pMHC Ligands Tethered on Surfaces via Poly(Ethylene Glycol) Depends on Polymer Length. *Plos One* **2014,** *9* (11): e112292.

28. Sedlak, S. M.; Bauer, M. S.; Kluger, C.; Schendel, L. C.; Milles, L. F.; Pippig, D. A.; Gaub, H. E., Monodisperse measurement of the biotin-streptavidin interaction strength in a well-defined pulling geometry. *Plos One* **2017,** *12* (12): e0188722.

29. Abadeer, N. S.; Brennan, M. R.; Wilson, W. L.; Murphy, C. J., Distance and Plasmon Wavelength Dependent Fluorescence of Molecules Bound to Silica-Coated Gold Nanorods. *ACS Nano* **2014,** *8* (8), 8392-8406.

30. Egorova, E. A.; van Rijt, M. M. J.; Sommerdijk, N.; Gooris, G. S.; Bouwstra, J. A.; Boyle, A. L.; Kros, A., One Peptide for Them All: Gold Nanoparticles of Different Sizes Are Stabilized by a Common Peptide Amphiphile. *ACS Nano* **2020**, *14* (5), 5874-5886.

31. Korevaar, P. A.; Newcomb, C. J.; Meijer, E. W.; Stupp, S. I., Pathway selection in peptide amphiphile assembly. *J Am Chem Soc* **2014,** *136* (24), 8540-8543.

32. Orendorff, C. J.; Murphy, C. J., Quantitation of metal content in the silver-assisted growth of gold nanorods. *J Phys Chem B* **2006,** *110* (9), 3990-3994.

33. Shaw, C. P.; Middleton, D. A.; Volk, M.; Levy, R., Amyloid-derived peptide forms self-assembled monolayers on gold nanoparticle with a curvature-dependent beta-sheet structure. *ACS Nano* **2012,** *6* (2), 1416-1426.

34. Susi, H.; Byler, D. M., Resolution-Enhanced Fourier-Transform Infrared-Spectroscopy of Enzymes. *Method Enzymol* **1986,** *130*, 290-311.

35. Chirgadze, Y. N.; Nevskaya, N. A., Infrared-Spectra and Resonance Interaction of Amide-One Vibration of Parallel-Chain Pleated Sheet. *Biopolymers* **1976,** *15* (4), 627-636.

36. Kong, J.; Yu, S., Fourier transform infrared spectroscopic analysis of protein secondary structures. *Acta Bioch Bioph Sin* **2007,** *39* (8), 549-559.

37. Mei, B. C.; Oh, E.; Susumu, K.; Farrell, D.; Mountziaris, T. J.; Mattoussi, H., Effects of Ligand Coordination Number and Surface Curvature on the Stability of Gold Nanoparticles in Aqueous Solutions. *Langmuir* **2009,** *25* (18), 10604-10611.

38. Hendricks, M. P.; Sato, K.; Palmer, L. C.; Stupp, S. I., Supramolecular Assembly of Peptide Amphiphiles. *Acc Chem Res* **2017,** *50* (10), 2440-2448.

39. Shiraishi, K.; Yokoyama, M., Toxicity and immunogenicity concerns related to PEGylated-micelle carrier systems: a review. *Sci Technol Adv Mat* **2019,** *20* (1), 324-336.

40. Sahoo, J. K.; Braegelman, A. S.; Webber, M. J., Immunoengineering with Supramolecular Peptide Biomaterials. *J Indian I Sci* **2018,** *98* (1), 69-79.

41. Mikolajczak, D. J.; Heier, J. L.; Schade, B.; Koksch, B., Catalytic Activity of Peptide-Nanoparticle Conjugates Regulated by a Conformational Change. *Biomacromolecules* **2017,** *18* (11), 3557-3562.

4.7 Supporting Information

Thickness of the shell formed by **3** was determined from the TEM images:

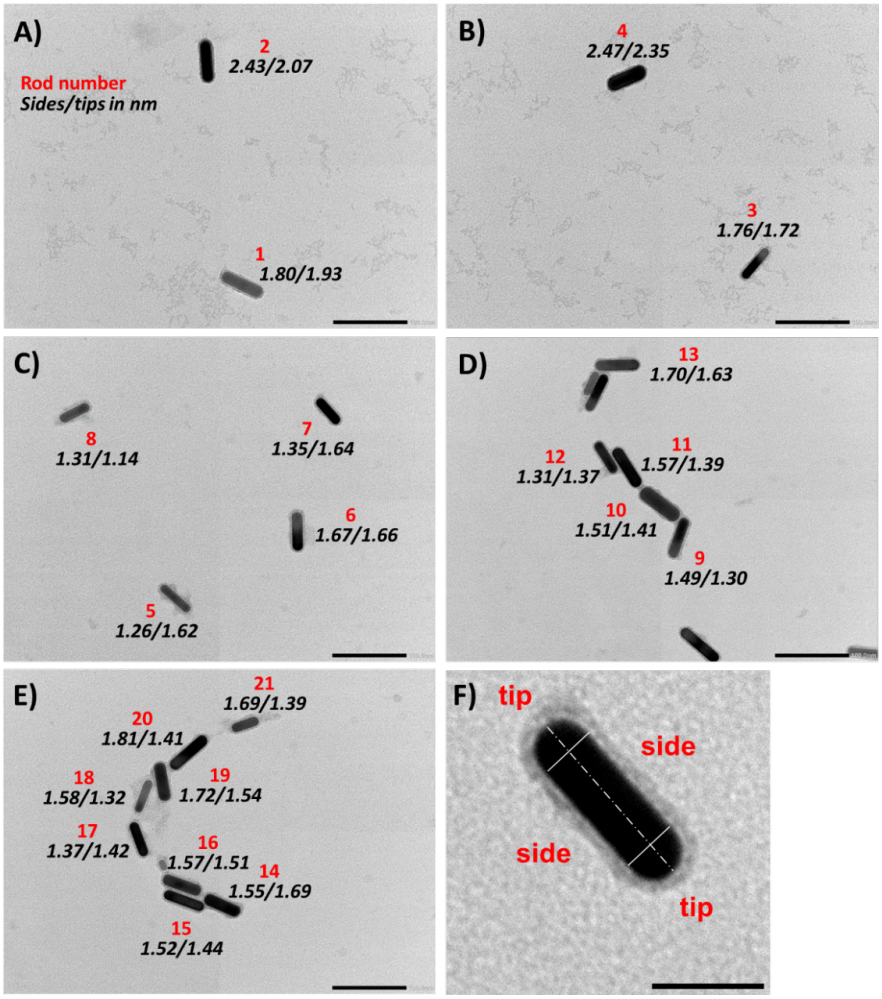

Figure S4.1. Analysis of the shell thickness of **GNR@3** as an example, based on the TEM images. Individual GNRs were numbered: (A) #1,2; (B) #3,4; (C) #5-8; (D) #9-13; (E) 14-21. To compare the shell thickness, the rod was divided as shown in (F). GNR numbers are shown in red, while the shell thickness is expressed in nm (first number indicates shell thickness at the sides of a rod, second number – at the tips). Negative staining was used to visualize the shells (0.5% uranyl acetate). Scale bar is 100 nm (A-E) and 25 nm (F).

Table S4.1. Analysis of the shell thickness derived from the TEM images of 21 individual GNRs. Mean parameters are given at the bottom of the table.

Rod #	Shell thickness, nm		SD*, nm		Ratio, %	
	sides	tips	sides	tips	sides	tips
1	1,80	1,93	0,23	0,28		107
2	2,43	2,07	0,19	0,23		85
3	1,76	1,72	0,21	0,25		98
4	2,47	2,35	0,25	0,29		95
5	1,26	1,62	0,19	0,23		128
6	1,67	1,66	0,30	0,30		100
7	1,35	1,64	0,23	0,19		121
8	1,31	1,14	0,19	0,22		87
9	1,49	1,30	0,24	0,32		87
10	1,51	1,41	0,39	0,30		93
11	1,57	1,39	0,40	0,31	100	89
12	1,31	1,37	0,30	0,29		104
13	1,70	1,63	0,32	0,38		96
14	1,55	1,69	0,31	0,59		109
15	1,52	1,44	0,37	0,21		95
16	1,57	1,51	0,29	0,34		96
17	1,37	1,42	0,26	0,26		104
18	1,58	1,32	0,44	0,46		84
19	1,72	1,54	0,36	0,34		89
20	1,81	1,41	0,28	0,29		78
21	1,69	1,39	0,27	0,32		82
av	1,64	1,57	0,29	0,30	100	97

* SD – standard deviation. The rod was divided into tips and sides as shown in **Figure S4.1F**.

Determination of coverage density provided by thiolated peptide amphiphiles:

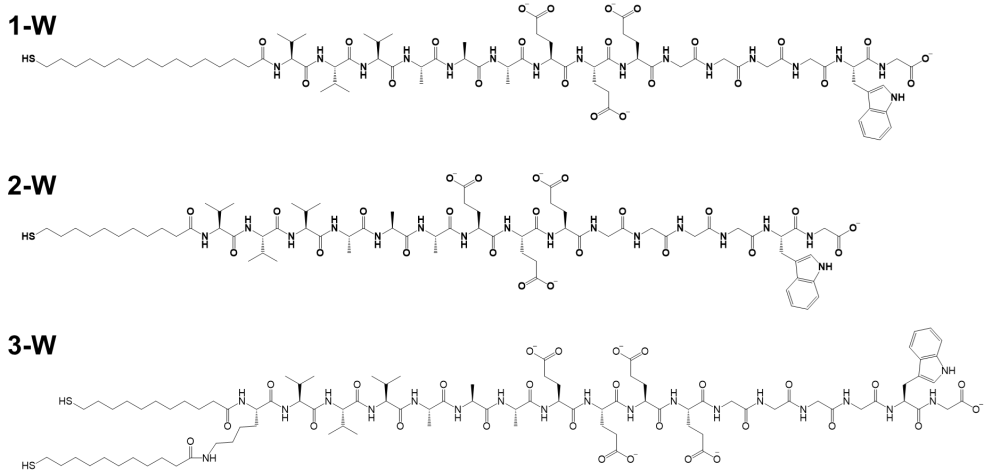

Figure S4.2. Chemical structures of thiolated peptide amphiphiles used to determine the coverage densities of the ligand on the GNR surface (46.4 by 14.0 nm, a.r. of 3.3): **1-W** was used to determine the coverage density of **1**, **2-W** – of **2**, **3-W** – of **3**.

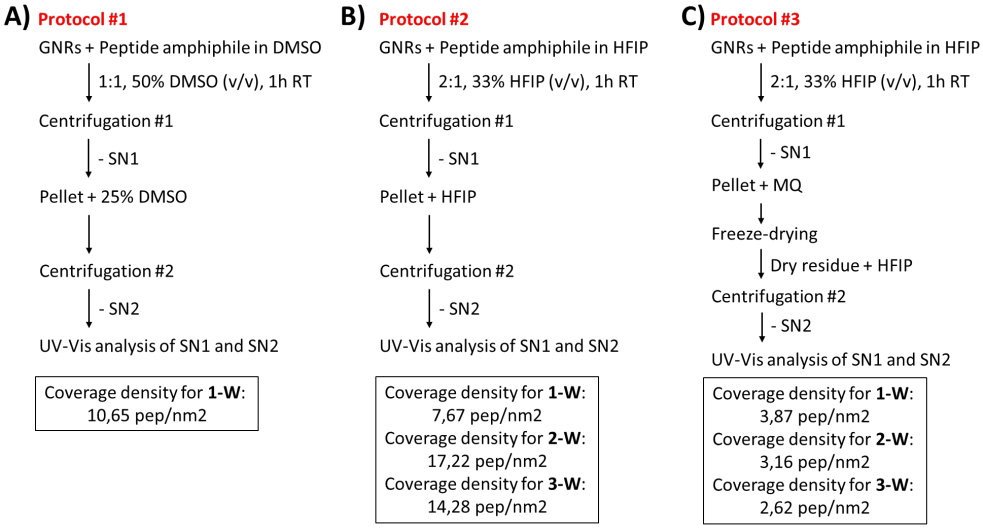

Scheme S4.1. Workflows illustrating the protocols tested to determine peptide amphiphile coverage density: (A) protocol #1, (B) protocol #2, and (C) protocol #3. Calculated coverage densities are given below the workflows.

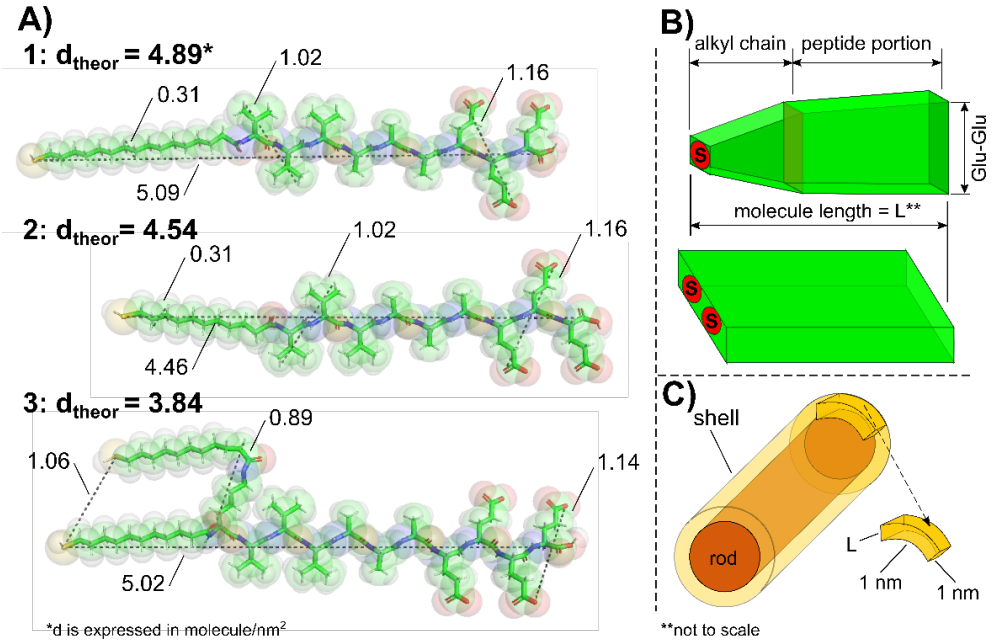

Scheme S4.2. Simulation of theoretical coverage density of peptide amphiphiles on a cylindrical surface: (panel A) contour length and possible dimensions of peptide amphiphile molecules **1-3**; (panel B) schematics illustrating simplified geometries given to molecule **1,2** (top) and **3** (bottom) to calculate the molecule volume; (panel C) a shell segment corresponding to 1 nm^2 of the gold surface occupied by 4.89 molecules of **1**, 4.54 molecules of **2**, or by 3.84 molecules of **3**. Theoretical coverage density (d_{theor}) was expressed as the ratio between the shell volume and the volume of one molecule. Models were built using PyMol. The dimensions are given in nm.

The following equations (2-11) describe how the d_{theor} values in **Scheme S4.2** were calculated.

Molecules **1** and **2** were simplified into two adjacent right frustums: one describing the alkyl chain and the other - the peptide segment (**Scheme S4.2**). The fully stretched molecules, as well as fully β-structured molecules, are flat and have a thickness corresponding to the alkyl chain (0.31 nm for all three molecules). Molecule volumes were calculated as follows:

$$V_{molecule} = V_I + V_{II}, \quad (2)$$

where $V_{molecule}$ is the volume of a molecule **1** or **2** (dimensions shown in **Scheme S4.2**), V_I is the volume of the alkyl chain, and V_{II} is the volume of the peptide segment.

$$V_I = {}^1\!/_3 \cdot L_I \cdot \left(S_1 + S_2 + \sqrt{S_1 \cdot S_2}\right), \quad (3)$$

where L_I is the distance between the sulfur atom and the amide bond formed due to the coupling of the alkyl chain to the N-terminus of the peptide segment (L_I = 2.11 nm for molecule **1** and L_I = 1.49 nm for molecule **2**); where S_1 is the (square) area with the alkyl chain distance in the base (S_1 = (0.31 nm)^2 for both molecules); S_2 is the (rectangular) area with the Val-to-Val distance in the base (S_2 = (1.02 nm) × (0.31 nm) for both molecules),

$$V_{II} = {}^1\!/_3 \cdot L_{II} \cdot \left(S_2 + S_3 + \sqrt{S_2 \cdot S_3}\right), \quad (4)$$

where L_{II} is the distance between the termini of the peptide segment (L_{II} = 2.98 nm for both molecules) and where S_3 is the (rectangular) area with the Glu-to-Glu distance in the base (S_3 = (1.16 nm) × (0.31 nm) for both molecules).

Molecule **3** was simplified in a different way: it was presented by a rectangular box with a base of $D_{alkyl\ chain}$ = 0.31 nm (the thickness of alkyl chain) by $D_{Glu-Glu}$ = 1.14 nm (Glu-to-Glu distance):

$$V_3 = L_{S-Cterm} \cdot D_{Glu-Glu} \cdot D_{alkyl\ chain}, \quad (5)$$

where $L_{S-Cterm}$ is the distance between the sulfur atom and the peptide C-terminus ($L_{S-Cterm}$ = 5.02 nm).

To calculated the shell volume V_{shell}, the volume of a gold rod segment V_{rod} and the volume of a coated rod segment $V_{rod+shell}$ were determined:

$$V_{rod} = \pi \cdot r_{rod}^2 \cdot h_{rod}, \quad (6)$$

where r_{rod} is the diameter of the rod (r_{rod} = 7.00 nm) and where h_{rod} is the rod length,

$$V_{rod+shell} = \pi \cdot (r_{rod} + L_{molecule})^2 \cdot h_{rod}, \quad (7)$$

where the length of the molecule $L_{molecule}$ is the distance between the sulfur atom and the C-terminus of the peptide segment (see **Scheme S4.2**). The shell volume is then:

$$V_{shell} = V_{rod+shell} - V_{rod}. \quad (8)$$

The lateral surface area of a rod is given by:

$$S_{lateral} = 2\pi \cdot r \cdot h_{rod}. \quad (9)$$

Next, we determine the number of molecules $N_{molecules}$ in a shell by dividing the shell volume by the volume of a single molecule:

$$N_{molecules} = {}^{V_{shell}}/_{V_{molecule}}. \quad (10)$$

Finally, the theoretical coverage density d_{theor} was calculated by dividing the number of molecules in a shell by the lateral surface area of a rod:

$$d_{theor} = {}^{N_{molecules}}/_{S_{lateral}} = {}^{L_{molecule}}/_{V_{molecule}} \cdot \left(1 + {}^{L_{molecule}}/_{2r_{rod}}\right). \quad (11)$$

The numerical values for the theoretical coverage density d_{theor} for the three types of molecule are presented in **Table S4.2**.

Table S4.2. Calculation of theoretical coverage densities for molecules 1-3 displayed on a cylindrical surface of 14 nm in diameter.

Molecule	$V_{molecule}$ (nm^3)	$L_{molecule}$ (nm)	d_{theor} (molecule/nm^2)
1	1.419	5.09	4.89
2	1.296	4.46	4.54
3	1.774	5.02	3.84

Self-assembly of the peptide amphiphile monolayer attached to the GNR surface:

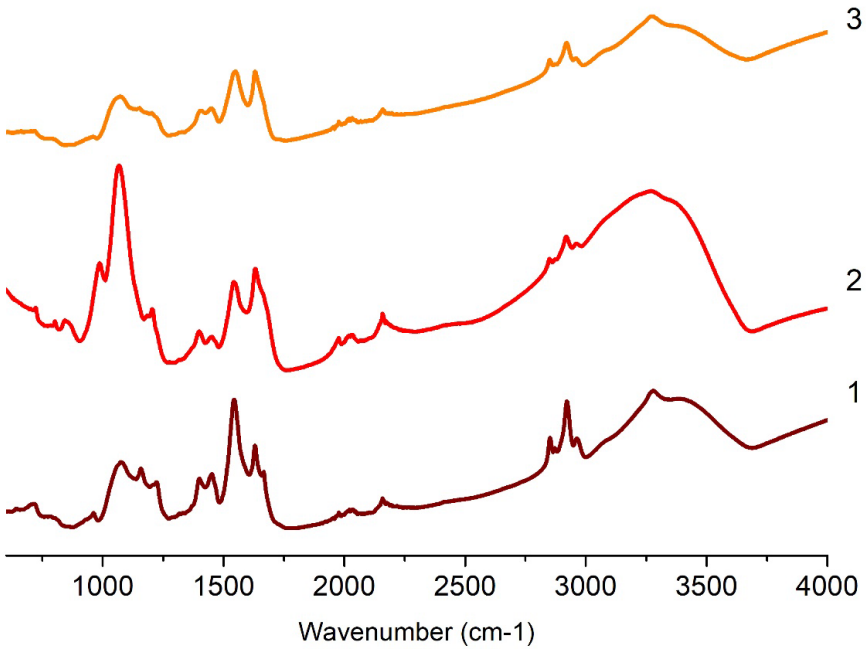

Figure S4.3. Full ATR-IR spectra of the coated GNRs with the thiolated peptide amphiphiles: brown line - **GNR@1**, red line - **GNR@2**, and orange line - **GNR@3**. Full FTIR-IR spectra for the corresponding peptide amphiphiles can be found in **Chapter 3**.

Table S4.3. Secondary structure distribution of peptide amphiphiles **1-3** in isolation and bound to the GNR surface.

Sample	β, %	Unordered, %	α, %	Others, %
1	97.7	0	0	2.3
GNR@1	58.8	3.9	14.8	22.5
2	85.2	0	5.4	9.4
GNR@2	51.8	6.0	20.5	21.7
3	94.8	0	0.8	4.4
GNR@3	57.1	6.8	19.0	17.1

The distribution is based on a fitting of Amide I peaks into 4 individual peaks and is shown as a percentage (deduced through area under the curve). Fitting into the Lorenz function were done using Origin Pro. ATR-IR spectra are shown in **Figure 4.4** and **Figure S4.3**.

GNR aggregation tests based on charge screening effects and competition with thiolated ligands:

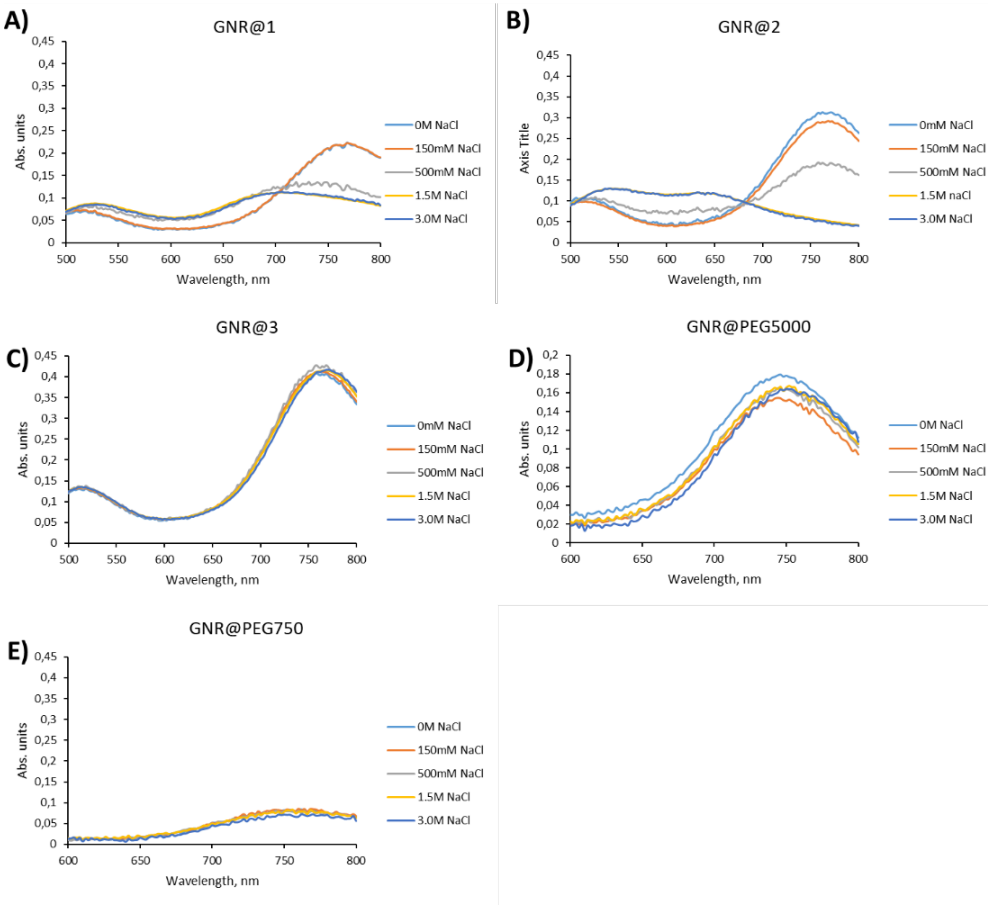

Figure S4.4. UV-Vis spectra recorded during the salt-induced aggregation assay for GNRs coated with (A) **1**; (B) **2**; (C) **3**; (D) **PEG$_{5000}$**; (E) **PEG$_{750}$** used to obtain normalized aggregation factor (AF). Coated GNRs (originally dispersed in MilliQ water) were mixed with NaCl to yield final salt concentrations of: 150 mM (orange line), 500 mM (gray line), 1.5 M (yellow line), and 3.0 M (blue line). After mixing, samples were incubated 15 min at room temperature. The sample with no salt added (0 M NaCl, light blue line) served as a reference to calculate AF (for results, see **Figure 4.5**). Measurements were carried out at room temperature.

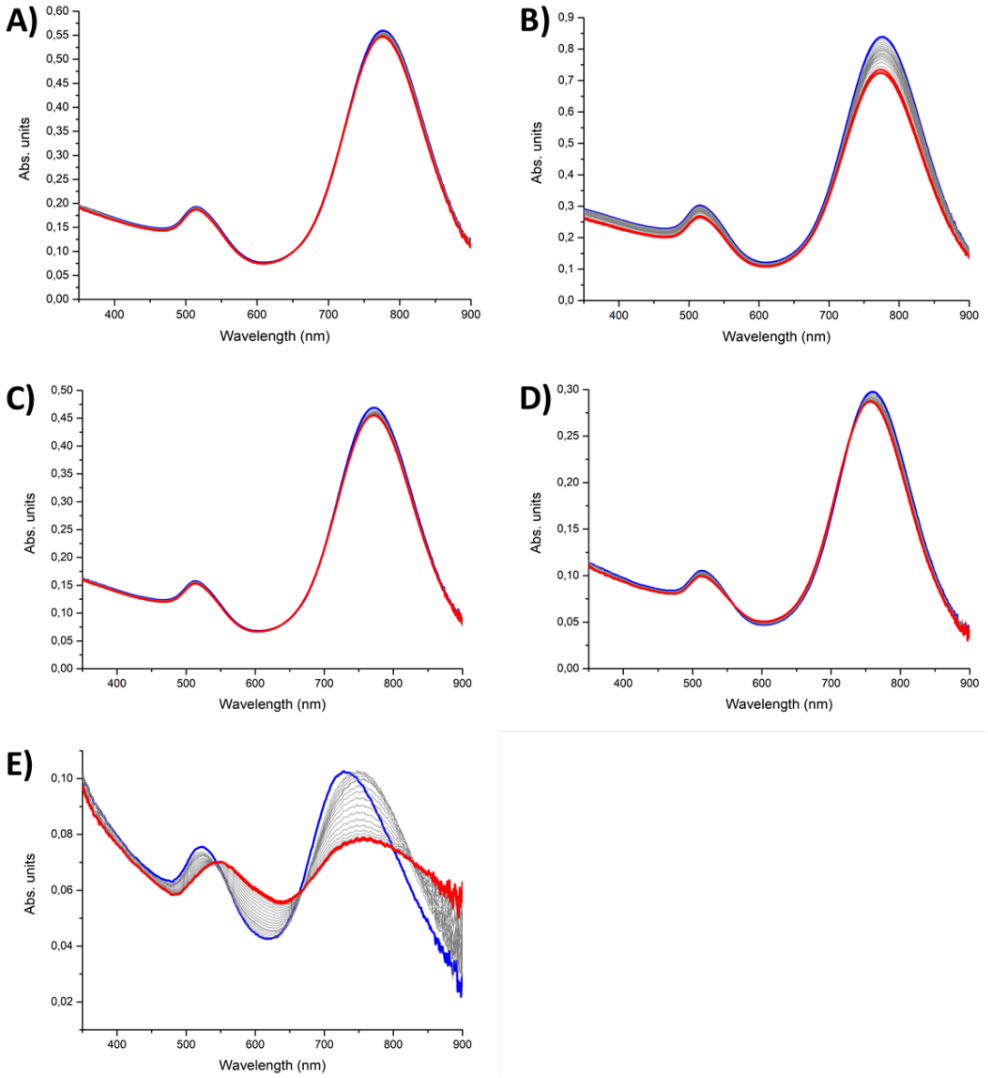

Figure S4.5. UV-Vis spectra recorded during the DTT competition assay to obtain normalized aggregation factor (AF) for GNRs coated with: (A) **1**; (B) **2**; (C) **3**; (D) **PEG$_{5000}$**; (E) **PEG$_{750}$**. Coated GNRs (originally dispersed in MilliQ water) were mixed with DTT to yield a final DTT concentration of 1 M (blue line, t = 0 min), a UV-Vis spectrum was recorded every 5 mins (gray lines) over a course of 90 mins (red line, t = 90 mins). The sample at t = 0 min (blue line) served as a reference to calculate AF (for results, see **Figure 4.5**). Measurements were carried out at room temperature.

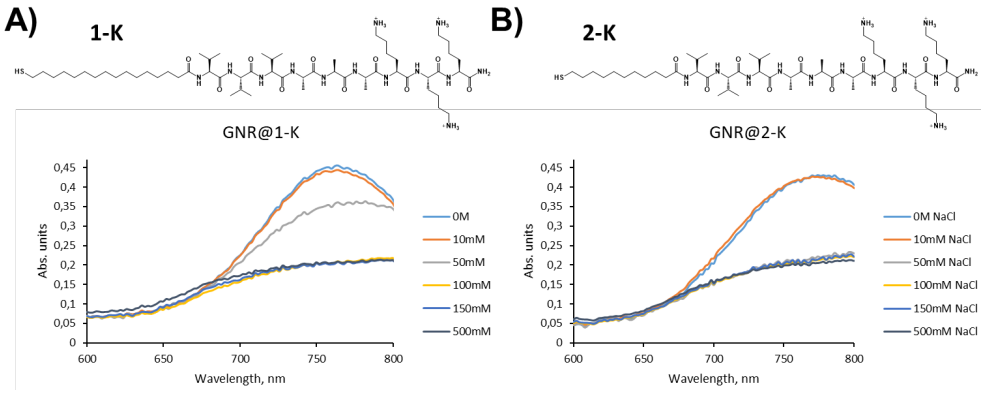

Figure S4.6. Salt-induced aggregation of GNRs coated with positively charged peptide amphiphiles was monitored with UV-Vis spectroscopy to obtain normalized aggregation factor (AF) for GNRs coated with (A) **1-K** and (B) **2-K**. Coated GNRs (originally dispersed in MilliQ water) were mixed with NaCl to yield final salt concentrations of: 10 mM (orange line), 50 mM (gray line), 100 mM (yellow line), 150 M (blue line), and 500 mM (dark gray line). After mixing samples were incubated 15 min at room temperature. The sample with no salt added (0 M NaCl, light blue line) served as a reference to calculate AF (for results, see **Figure 4.6**). Measurements were carried out at room temperature. Chemical structures of **1-K** and **2-K** are shown above the UV-Vis spectra.

Characterization of the synthesized peptides and peptide amphiphiles by LC-MS:

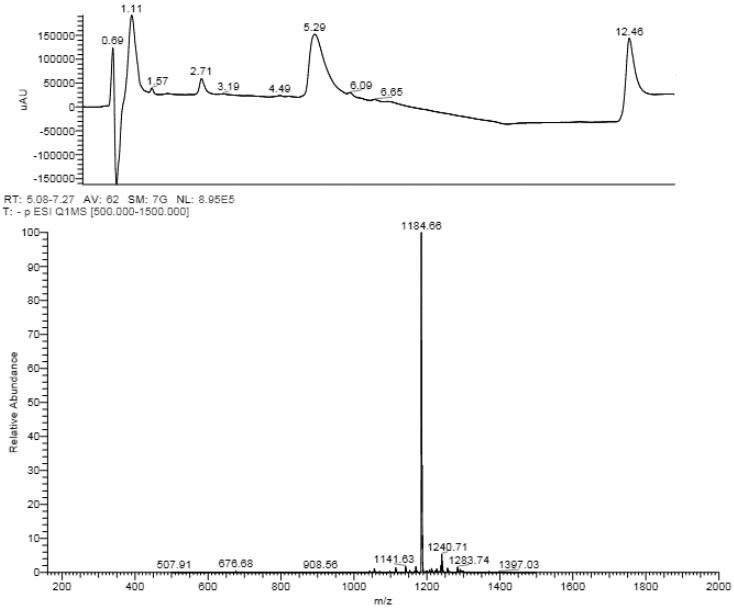

Figure S4.7. LC-MS spectrum for **1**. $[M\text{-}H]^{1-}_{theor}$ =1184.65.

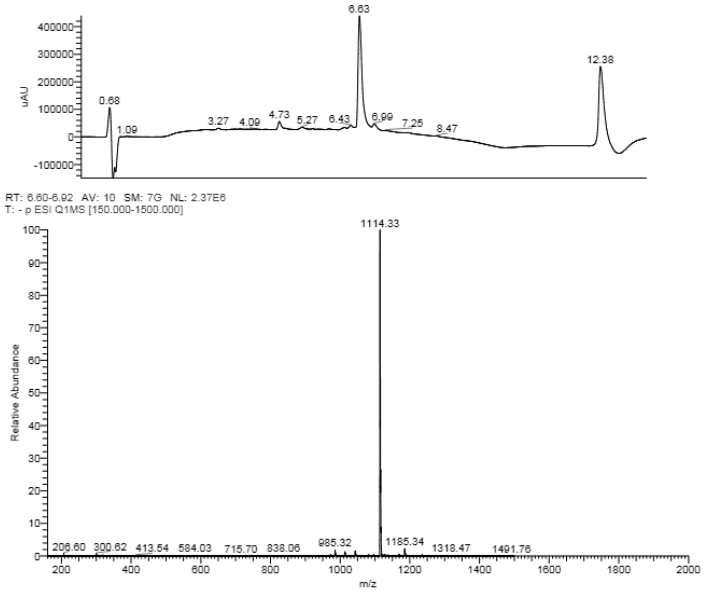

Figure S4.8. LC-MS spectrum for **2**. $[M\text{-}H]^{1-}_{theor}$ =1114.57.

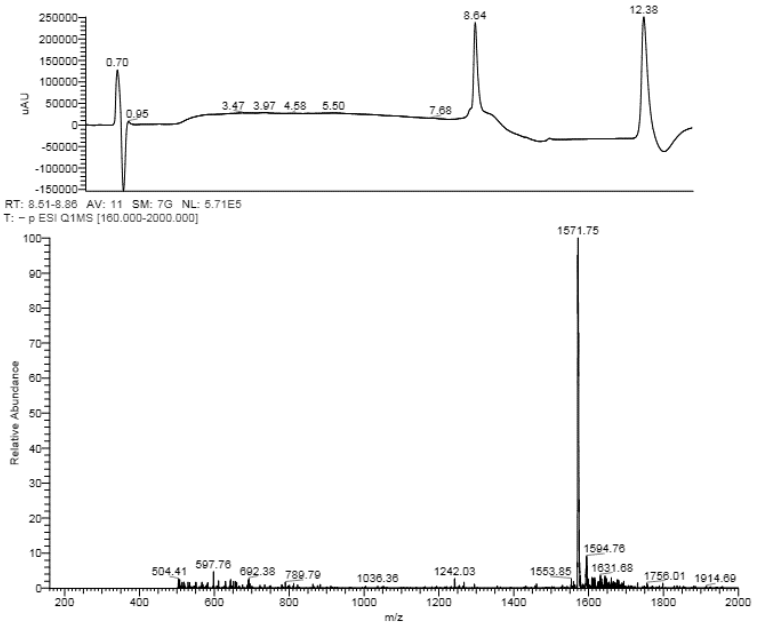

Figure S4.9. LC-MS spectrum for **3**. $[M\text{-}H]^{1-}_{theor}$ =1571.83.

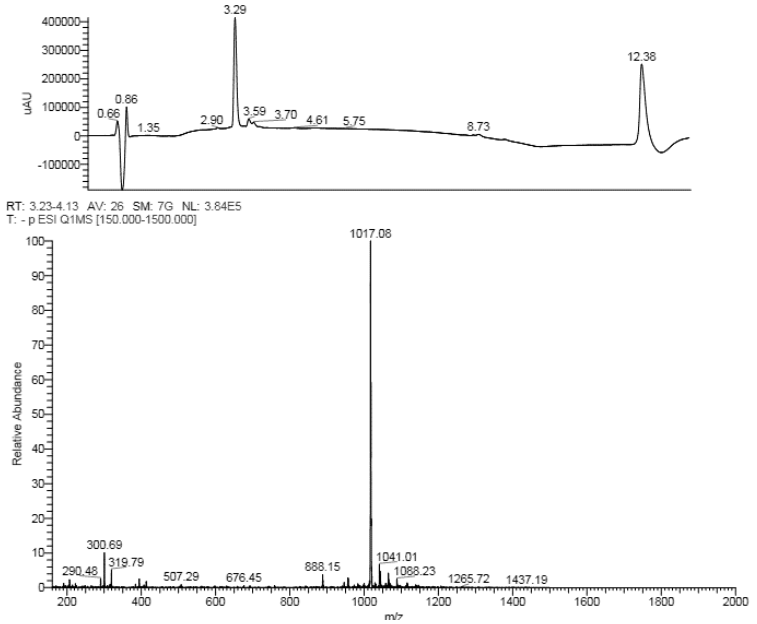

Figure S4.10. LC-MS spectrum for **4**. $[M\text{-}H]^{1-}_{theor}$ =1017.45.

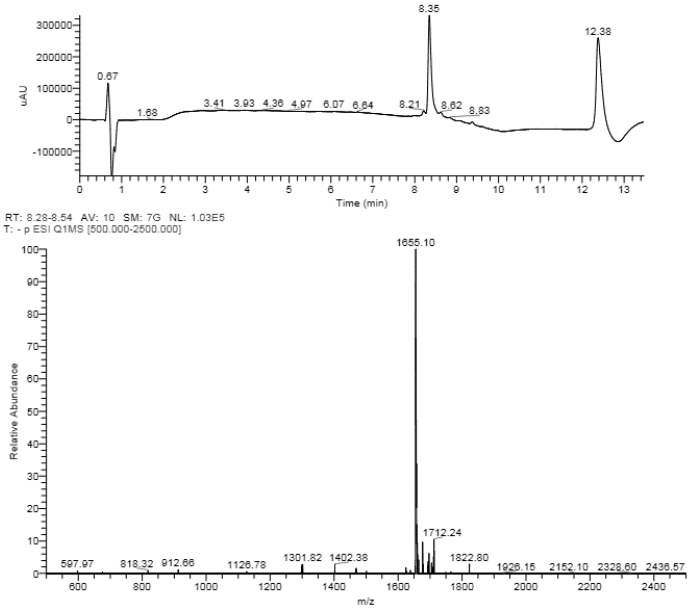

Figure S4.11. LC-MS spectrum for **1-W**. $[M-H]^{1-}_{theor}$ =1654.82.

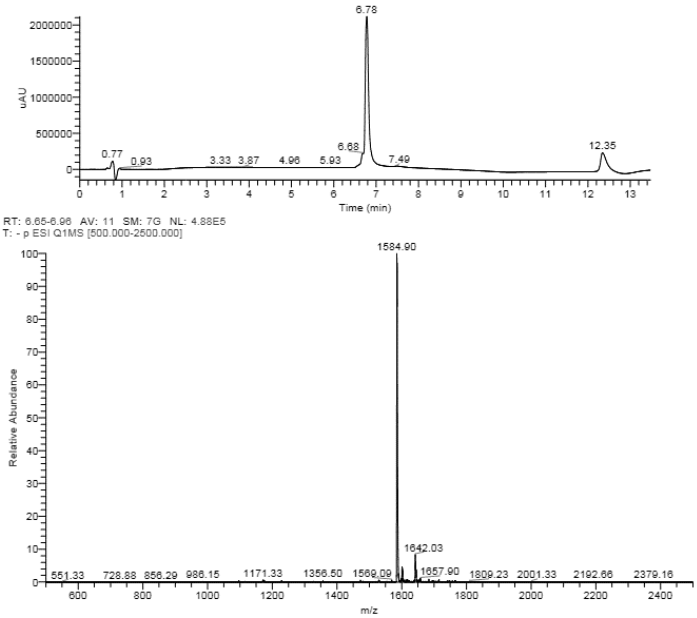

Figure S4.12. LC-MS spectrum for **2-W**. $[M-H]^{1-}_{theor}$ =1585.75.

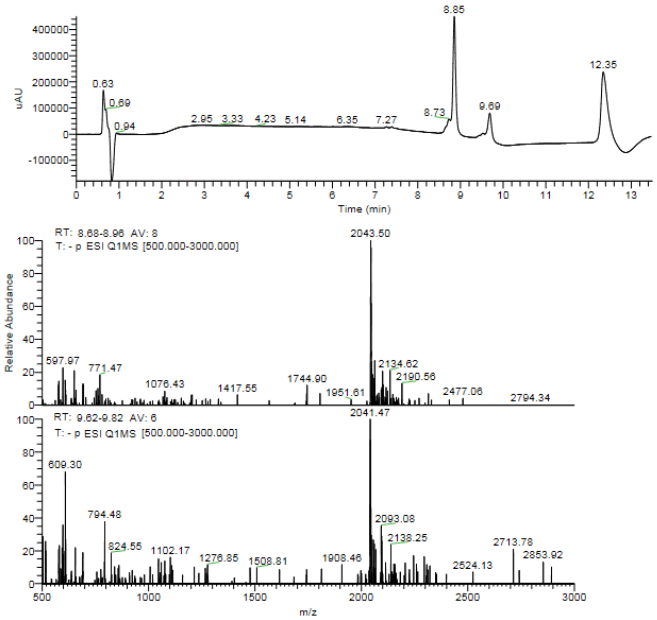

Figure S4.13. LC-MS spectrum for **3-W**. $[M-H]^{1-}_{theor}$ =2043.03; for the dimeric species $[M-2H]^{2-}_{theor}$ = 2041.50.

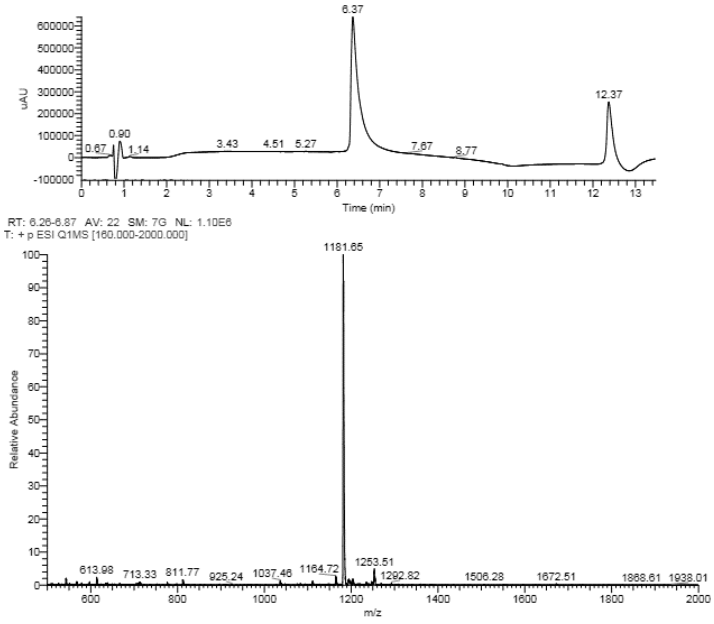

Figure S4.14. LC-MS spectrum for **1-K**. $[M+H]^{1+}_{theor}$ =1181.83.

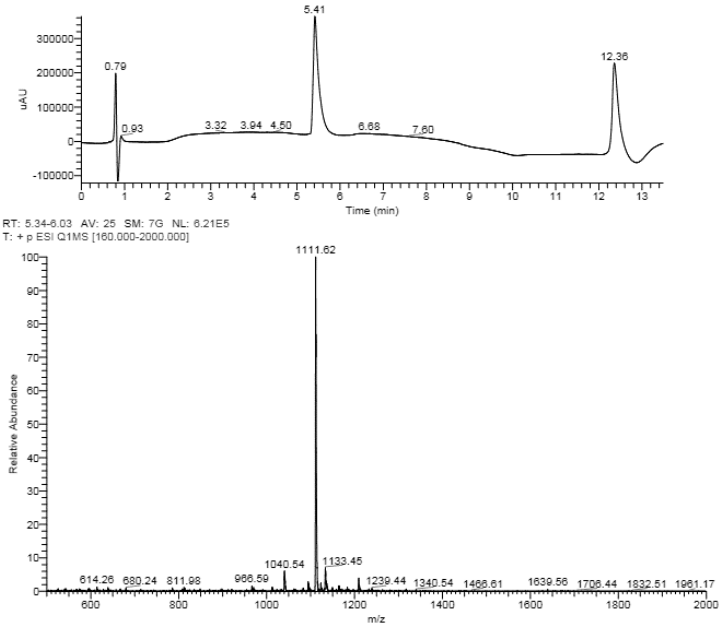

Figure S4.15. LC-MS spectrum for **2-K**. $[M+H]^{1+}_{theor}$ = 1111.75.

CHAPTER 5

GNPs decorated with ovalbumin-derived epitopes: effect of shape and size on T-cell immune responses

5.1 Abstract

Due to their ease of detection, unique optical properties, and large surface areas, gold nanoparticles (GNPs) are attractive nano-sized delivery vehicles. They have been employed to study multiple biological processes including cellular uptake, immune response, nanoparticle-mediated cytotoxicity, and apoptosis. As GNPs can be manufactured in various shapes and their size is programmable, the effects that their size and shape impose on biological processes can be studied. However, there is currently no clear evidence that a certain shape or size of nanoparticle is beneficial. To address this issue, we have utilized peptide amphiphile-coated GNPs and gold nanorods (GNRs). GNPs of 15 and 40 nm in diameter and 40 by 15 nm GNRs were coated with thiolated peptide amphiphiles and functionalised with model epitopes derived from chicken ovalbumin ($OVA_{257-264}$ and $OVA_{323-339}$). These particles were evaluated for their cytotoxicity *in vitro* in bone marrow-derived dendritic cells (BMDCs), and the cellular uptake was visualized using transmission electron microscopy (TEM) and quantified with inductively coupled plasma mass spectrometry (ICP). Subsequently, epitope-decorated GNPs and GNRs were tested for their immunogenicity in an *ex vivo* assay using transgenic ovalbumin mice (OT-I and OT-II). By using two distinct epitopes, it was possible to draw conclusions regarding the impact of shape and size of the nanoparticles on different aspects of the immune response.

Our findings indicate that the shape and size of GNPs and GNRs does indeed influence immune response. We were able to draw the following conclusions: (i) there is a size threshold below which antigen delivery efficacy drops (~15 nm in diameter), and (ii) there is a mass (or volume) threshold below which no effective antigen presentation *via* the major histocompatibility

complex class I (MHC-I) is possible (~40 nm in diameter). We believe these findings will have implications for vaccine development, and lead to a better understanding of cellular uptake as well as antigen egress from lysosomes into the cytosol.

5.2 Introduction

The field of nanomedicine focuses on the use of nanoparticles to diagnose, monitor and treat disease. Within this field, there is a particular focus on using nanoparticles as drug delivery vehicles or as vaccine platforms.[1-5] One reason that nanoparticles are suited to this purpose is that their nanometer size range imposes certain interactions between the particles and biological systems, for instance cellular uptake pathways, recognition by immunocompetent cells and clearance from the blood flow.[6-8] However, researchers have reported contradictory data on the effects of nanoparticle size and shape on immune response,[9] or effects of nanoparticle charge on cellular uptake, clearance, and immune response,[10] and cytotoxicity.[11-15] Often, these reports do not provide sufficient information on the antigen loading or particle concentration. Literature may also lack normalization of the obtained results to a common parameter to aid comparison. Moreover, it is not always possible to find only one determinant parameter attributed to the biological effect of the studied nanoparticles. Parameters including size,[16] shape,[2, 17] charge,[11, 18] rigidity,[6] drug or antigen loading,[1, 2] particle concentration,[19, 20] total mass of nanoparticles,[12, 21] and mean surface area available for contact[2, 19] have all been proposed to affect the biological fate of studied particles.

Studying the effect of all these parameters on vaccine efficacy is an enormous undertaking. In order to make a new system suitable for screening the effects of the abovementioned parameters, a new approach is needed. This approach has to allow for thorough control over one parameter while other parameters, such as size, shape, charge, and/or surface chemistry are fixed. Gold nanoparticles (GNPs) can be synthesized in a range of sizes and

shapes therefore they are ideal for studying the shape and size dependency of a biological response. Through the use of different sizes and shapes of GNPs, the dependence of cellular uptake,[17, 20, 21] cytotoxicity,[12, 17] and immune response[22] on physico-chemical properties can be studied. In addition, the surface chemistry of GNPs can be easily modified, and as a result, low toxicity and modulation of chronic inflammation risk caused by the antigen delivery particles are expected. Another advantage is that antigens are displayed on the GNP surface and cannot be compromised by non-specific interactions with the delivery vehicle itself. For example, peptide-decorated liposomes can show partial encapsulation of the displayed peptides *via* engulfment into the lipid membrane.[23]

In this chapter, we studied the effect of nanoparticle shape and size on antigen processing and presentation. For this, gold nanorods (GNRs) of 40 by 15 nm in size and spherical GNPs of 15 and 40 nm in diameter were synthesized (**Scheme 5.1** and **Scheme 5.2**). The choice of these sizes was dictated by multiple lines of evidence showing that nanoparticles of 40-50 nm in diameter exhibit more efficient cellular uptake[7, 20] and immune response compared to other sizes.[2, 9] GNPs with a dimeter of 15 nm are often used in literature[3, 16, 18, 24] and were chosen to serve as a reference for GNRs' width. GNRs were introduced to elucidate the effect of shape and their length matched the diameter of the larger GNPs. Incorporation of two spherical particle sizes matching the GNRs dimensions was intended to decouple the effects of shape and size.

A protective coating on the gold surface is required to maintain particle stability in biological media, to prevent aggregation, and to eliminate potential cytotoxicity.[11, 18, 24-27] It was previously shown that, depending on the aggregation state, endocytosis pathways may vary for the same nanoparticle

formulation.[28] In addition to stabilizing molecules, antigens can be attached to the GNP surface to modulate antigen processing in dendritic cells (DCs).[1] Using a common stabilizing molecule for the three selected nanoparticle types results in an identical surface chemistry allowing for a fair comparison of the elicited cellular responses. Previously, we reported the use of thiolated peptide amphiphiles as stabilizers for both GNPs and GNRs (**Chapters 3** and **4** of this thesis).[29] These coatings insulate the gold surface, prevent particle aggregation under harsh conditions (up to 3 M NaCl, or 1 M competing thiol), and provide GNPs with surface chemistry described as "protein-like".[30] Published data suggests that active moieties displayed on the surface of peptide-capped GNPs preserve their biological function and their availability.[30-33] Several reports suggest that GNPs do not impair immune functions of DCs or B cells.[18, 25, 26] Unlike most other metallic nanoparticles, GNPs do not give rise to reactive oxygen species (ROS) *in vitro*, hence oxidative stress and ROS-related cytotoxicity are less common.[24]

In this study, 15 nm and 40 nm GNPs and 15 by 40 nm GNRs were coated with a stabilizing peptide amphiphile,[29] and model epitopes derived from the chicken ovalbumin (OVA) protein ($OVA_{257-264}$ or $OVA_{323-339}$, **Scheme 5.2**). The peptide amphiphile stabilizer, herein referred to as the **base** molecule, comprised a doubly-thiolated C11 alkyl chain conjugated to a KVVVAAAEEE peptide sequence *via* the N-terminus and the side-chain of the lysine. The two bioactive peptide amphiphiles were bound *via* Au:S bonds to form epitope-decorated GNPs and GNRs. Both peptide amphiphiles comprised a thiolated C11 alkyl chain, a VVVAAAEEE peptide sequence, a tetraethyleneglycol spacer, and one of the two epitope sequences. The bioactive peptide amphiphile coupled to $OVA_{257-264}$, the major histocompatibility complex class I (MHC-I) restricting epitope, was

abbreviated as **1**, and the peptide amphiphile coupled to $OVA_{323-339}$, the major histocompatibility complex class II (MHC-II) restricting epitope, was denoted as **2**. Since the same coating procedure was applied to all chosen GNPs, their immunological effects could be compared on the basis of antigen loading or available area.

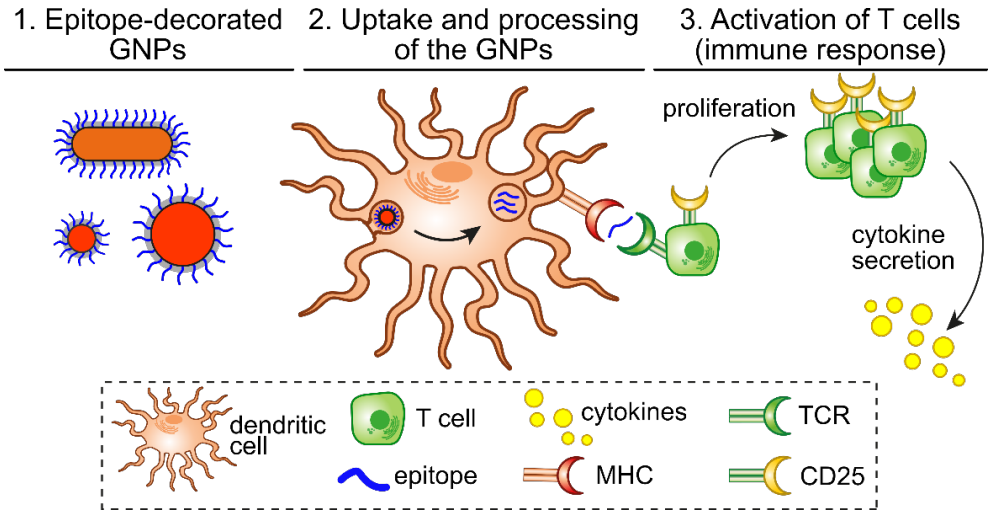

Scheme 5.1. Immune response to epitope-decorated GNPs was studied in 3 steps: (1) GNPs of different shape and size were synthesized and coated with epitope/base constructs. Two epitopes were chosen as models: $OVA_{257-264}$ and $OVA_{323-339}$. (2) Uptake of the epitope-decorated GNPs by dendritic cells (DCs) was studied. (3). Activation of specific T-cells by DCs *via* MHC/epitope/T-cell receptor (TCR) contact led to T-cell proliferation and release of cytokines.

Immunogenicity of the epitope-decorated GNPs and GNRs was studied using cells derived from the ovalbumin transgenic OT-I and OT-II mice. T cells of these transgenic mice express T-cell receptors (TCRs) that are specific for either $OVA_{257-264}$ (OT-1) or $OVA_{323-339}$ (OT-2) epitopes and pair with either CD8 or CD4 coreceptors.[34] Previously, TCR-ligand interactions, and the T-cell activation, as well as their function in the development of autoimmunity and tolerance were studied using these mouse lines.[1, 16, 35-37] 'Splitting' the immune response into two components ($OVA_{257-264}$ modulates

cytotoxic T-cell response, while $OVA_{323-339}$ – is a helper T-cell response) should provide more clarity as to how the immune system reacts to more complex antigens, depending on their size and shape.

This study covers three distinct stages in the immune response pathway summarized in **Scheme 5.1**. Before studying the elicited immune responses, the peptide amphiphile-coated GNPs and GNRs were characterized using UV-Vis spectroscopy and transmission electron microscopy (TEM). Next, cellular uptake and cytotoxicity of these GNPs and GNRs were evaluated in a population of DCs derived from mouse bone marrow (bone marrow-derived dendritic cells, BMDCs). After incubation with BMDCs, the cellular uptake by these DCs was studied with TEM and inductively coupled plasma mass spectrometry (ICP-MS). Upon cellular uptake, antigen-decorated nanoparticles are delivered into the cells. To initiate an immune response, antigens are cleaved and processed into epitopes inside lysosomes or in the cytosol to be later presented in the groove of MHC-II (inside lysosomes) or MHC-I (in the cytosol).[38] Next, an immune response is triggered by contact of the epitope-loaded MHC with a TCR of specific T cells and is accompanied by cytokine release and upregulation of cellular markers.[39] In this study, DCs activation by OVA epitope-decorated GNPs and GNRs and antigen processing were quantified using enzyme-linked immunosorbent assay (ELISA) and flow cytometry. The capability of epitope-decorated GNPs to mediate effective antigen processing and MHC/epitope/TCR binding, as well as cause CD25 upregulation (a T-cell activation marker) was assessed using flow cytometry.

5.3 Results and Discussion

5.3.1 Characterization of peptide-gold conjugates.

In order to keep the surface chemistry identical, GNPs of different shape and size were coated with a mixture comprising 9 molar parts of the **base** peptide and 1 molar part of the active peptide **1** or **2** (**Scheme 5.2**). The **base** composition was inspired by previous work (see **Chapters 3** and **4** of this thesis) and comprised a double thiolated C_{11} chain conjugated to a KVVVAAAEEEE peptide domain *via* the N-terminus and the lysine side-chain.[29] The thiol group enabled coordination of the ligands to the gold surface *via* an Au-S bond. This peptide amphiphile formed a self-assembled monolayer on the gold surface and stabilized GNPs in the 20-100 nm size range. The active peptides comprised a single thiolated C_{11} chain conjugated, *via* the N-terminus, to a peptide with the sequence $V_3A_3E_3$ while the epitopes were coupled to the C-terminus of this peptide sequence *via* a PEG_4-spacer. Epitope sequences corresponded to OVA-derived T-cell epitopes (SIINFEKL, $OVA_{257-264}$, is an MHC-I binding epitope, and ISQAVHAAHAEINEAGR, $OVA_{323-339}$, is an MHC-II binding epitope). The active peptides **1** and **2** were conjugated to a single alkyl chain instead of a double chain to aid solubility of the resulting compounds.

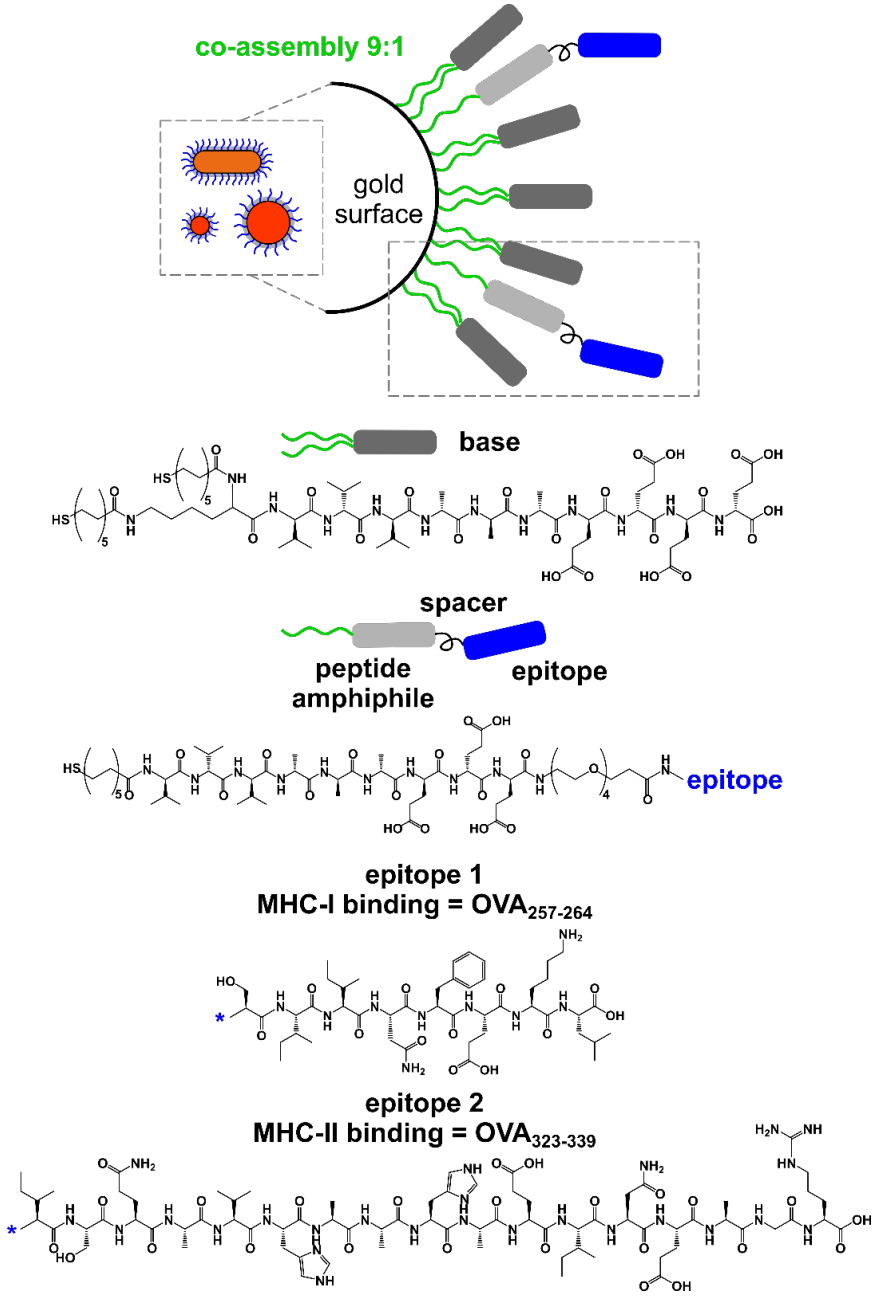

Scheme 5.2. Schematic representation of the shell composition (**base** peptide and epitope-bound peptides **1** and **2**) used to stabilize GNPs and GNRs. **Base** peptide was mixed with either **1** or **2** at a 9:1 molar ratio to form shells around GNPs and to provide near-identical surface chemistries.

The stabilizing effect of the **base** sequence was ascribed to increased hydrophobicity within the shell around the gold core and effective self-assembly (up to 73% β-content within the shell).[29] It was anticipated that addition of 10 mol % of single chain amphiphiles **1** or **2** to the double chain **base** amphiphile would not disturb peptide amphiphile self-assembly on the gold surface. The resulting assemblies (in the absence of gold) were probed with circular dichroism spectroscopy to confirm this assumption (CD, **Figure S5.1**).

Peptide amphiphiles were synthesized using protocols described in **Chapter 3** of this thesis, dissolved in 1,1,1,3,3,3-Hexafluoro-2-propanol (HFIP), mixed in a 9:1 ratio and the solvent was evaporated yielding a thin film. Upon rehydration with PBS (pH 7.2), supramolecular assemblies were formed. The **base** sequence in PBS adopted a typical β-structured profile as evidenced by the pronounced ellipticity minimum at 222 nm. Incorporation of 10 mol % of **2** did not affect the overall spectral shape, or position of the ellipticity minimum, indicating that **2** did not interfere with the self-assembly of the **base** amphiphile. However, **1** did influence the resulting assemblies to some extent: the ellipticity minimum did not shift, but the band became narrower and its intensity increased in comparison to the effect **2** demonstrated. This suggests a decrease in contributions from other secondary structures. Absence of unordered structures or significant changes in the CD spectra caused by addition of **1** or **2** implies that the mode of self-assembly was preserved, and it was not disrupted by interactions with the epitopes. Our previous study showed that the self-assembly behavior of these peptide amphiphiles in solution was translated well to self-assembly on the gold surface.[29] In this study, the peptide amphiphiles mixtures were deemed to follow the same trend. Thus, when the epitopes are displayed on

the GNP surface, they are expected to be available for interaction and not buried within the peptide amphiphile shell.

Citrate-stabilized GNPs of different sizes and CTAB-protected GNRs were prepared using standard protocols described in **Chapter 3** and **Chapter 4** of this thesis. GNPs were characterized with dynamic light scattering (DLS), ultraviolet-visible spectroscopy (UV-Vis), and transmission electron microscopy (TEM) to confirm their size and monodispersity (**Table 5.1**, **Figure 5.1**, **Figure S5.2**). Due to their rod-like shape, GNRs were not analyzed by DLS, instead only UV-Vis spectroscopy and TEM data were collected.

Table 5.1. GNPs size characteristics before/after modification using TEM and DLS.

Sample	**15 nm GNPs**	**40 nm GNPs**
Av. size of the core (TEM)	15.0 ± 1.4*	43.5 ± 3.3
Citrate	15.5 ± 0.2	40.4 ± 0.5
Base	26.8 ± 0.3	50.8 ± 0.1
1	25.9 ± 0.3	50.8 ± 0.8
2	26.6 ± 0.6	54.3 ± 0.2

To determine the core size, citrate-stabilized GNPs were imaged using TEM. *-standard deviation. The size of peptide amphiphile-coated GNPs was determined using DLS. Both average size and mean hydrodynamic diameter are given in nm. Peptide amphiphile-coated samples were prepared in PBS (pH 7.2).

Upon modification with the peptide amphiphiles, a slight increase in size for all peptide-gold conjugates was observed with DLS. The incorporation of the extended sequences **1** or **2** (10 mol%) into the **base** peptide shell did not lead to agglomeration of GNPs (**Figure 5.1**; for intensity size distributions see **Figure S5.2**). The UV-Vis spectroscopy supported these findings: the absence of plasmon band broadening for **15-base**, **15-1**, and **15-2** relative to **15-citrate** indicated that no aggregation occurred after the peptide coating

was applied (**Figure 5.1A**). The same was true for 40 nm GNPs and GNRs. The small (1-7 nm) red-shift of the plasmon band is related to substitution of citrate or CTAB on the gold surface with other molecules, which leads to a change in the dielectric constant.[40] Since neither DLS (**Figure S5.2A,B**) or TEM (**Figure 5.1B**) indicated aggregation, the peptide-coated GNPs and GNRs were presumed to be monodisperse. TEM imaging revealed particle clustering, which can be explained by drying effects during deposition of samples on a TEM grid. This clustering was also facilitated by the presence of salts, since all tested samples were prepared in PBS (pH 7.2).[29] Zeta potential values of as-synthesized citrate-capped GNPs and amphiphile-coated GNPs showed that particles had a negative surface charge (up to -30 mV, **Figure S5.2C-E**). A slight deviation of surface charge for GNPs coated with **1** and **2** from the samples coated with the **base** sequence was explained by a slight change in the surface chemistry when the active peptides were incorporated in the peptide amphiphile shell. The GNRs showed a zeta potential change from positive to negative, indicative of CTAB displacement from the GNR surface by the peptide amphiphiles (**Figure S5.2E**). A negative net charge for peptide amphiphile-coated GNPs and GNRs is advantageous for two reasons: negatively charged particles cause less cytotoxicity compared to positively charged counterparts, and better cellular uptake than neutral nanoparticles.[7]

TEM analysis revealed the presence of well-defined peptide shells surrounding the gold core (**Figure 5.1B**). The shell around the GNPs and GNRs ensured that particles were separated from each other with the interparticle distance corresponding to the shell thickness. This thickness of the shells (<5 nm) is in agreement with a peptide-amphiphile monolayer around the particles. It was previously shown that these peptide amphiphile monolayers are well-structured.[29] Notably, in the TEM images there is no

obvious difference in the shell thickness for samples with the functional peptides **1** or **2** incorporated, possibly due to a low epitope display density.

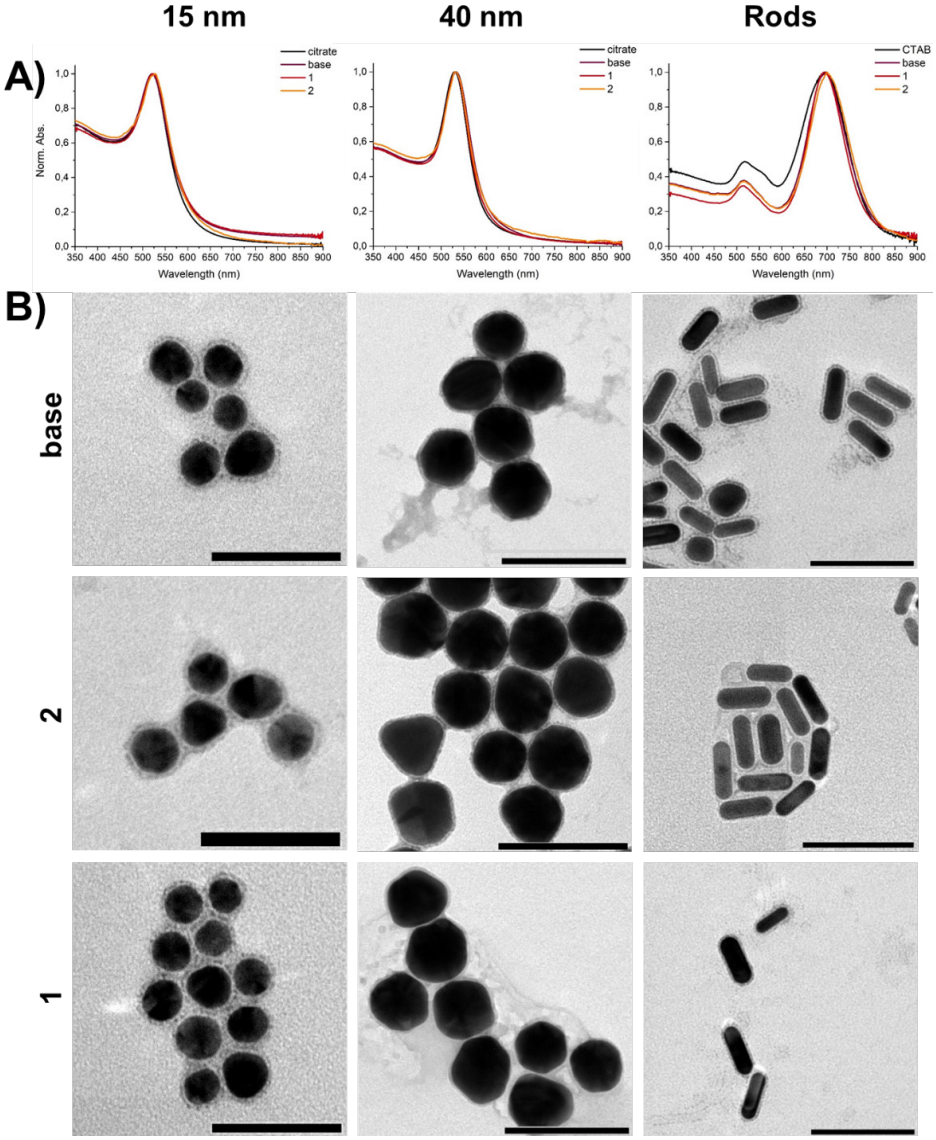

Figure 5.1. Sample characterization of the GNPs used in this study: (panel A) UV-Vis spectra for coated 15 nm GNPs, 40 nm GNPs, and GNRs; (panel B) TEM images of the peptide-gold conjugates evaluated in this work. Modified samples were prepared in PBS (pH 7.2). Scale bars: 50 nm for **15-base**, **15-1**, and **15-2**; 100 nm for others. Staining – 1% uranyl acetate. The visible shells are the peptide coatings.

According to our previous work, GNPs coated with these amphiphilic molecules are highly stable at elevated salt concentrations and are resistant towards thiols,[29] thus the GNPs and GNRs presented in this work were expected to be stable under biologically relevant conditions.

5.3.2 Number concentration and epitope dosage

To study biological effects elicited by nanoparticles of different size and shape, a defined parameter should be adopted to enable comparison. It can be particle number, particle area available for interaction,[2, 19] or drug/active molecule loading/dosage.[19, 20, 41] Unfortunately, reports with a normalization used to truly determine the effect of a particle parameter (*e.g.* of an antigen loading rather than particle mass) on biological response are scarce.[2, 12, 21] To calculate the above-mentioned parameters, the number concentration of the nanoparticles should be known. For this, inductively coupled plasma mass spectrometry (ICP-MS) is the most appropriate technique. This technique has also been employed to determine the thiol-containing ligand coverage on GNPs,[42] as well as metal content in cells and tissues.[2, 12, 16, 18, 19, 24, 43]

Peptide amphiphile-coated GNPs and GNRs were digested in *aqua regia* and analyzed with ICP-MS to determine gold mass concentration, which was later translated to particle number concentration (**Figure S5.3** and **Table S5.1**). Determined concentrations were linked to the optical density (OD) of the GNP or GNR suspension (**Table 5.2**). This enables accurate dosing of the GNP and GNR samples according to their OD, acquired with UV-Vis spectroscopy. We determined that a suspension of peptide amphiphile coated GNPs with an OD_{LSPR} = 1 corresponds to number concentrations within the 10^{11}-10^{12} particle/mL range regardless of the

applied coating, which is in agreement with published data for citrate-capped GNPs.[44] Moreover, normalized number concentrations for GNPs with the same gold core but different peptide amphiphile coatings showed similar values, signifying that the employed coating strategy did not result in different optical properties arising from the applied stabilizer. Furthermore, incorporation of 10 mol % of the epitope-displaying peptide amphiphile **1** or **2** did not affect the optical properties either.

Table 5.2. Number concentrations and epitope dosage of GNPs and GNRs.

	Number concentration, particles/mL			Epitope dosage, µg/mL		
	15 nm GNPs	**40 nm GNPs**	**GNRs**	**15 nm GNPs**	**40 nm GNPs**	**GNRs**
base	4.03×10^{12}	1.49×10^{11}	3.54×10^{11}	n/a	n/a	n/a
1	3.83×10^{12}	1.25×10^{11}	4.06×10^{11}	2.5	0.4	0.6
2	3.46×10^{12}	1.46×10^{11}	3.93×10^{11}	4.2	0.9	1.1

Samples were prepared in PBS (pH 7.2). For normalized mass concentrations and areas available for contact, see **Figure S5.3B,C**. The obtained mass concentrations were divided by the mass of one particle and normalize to OD_{LSPR} = 1.0.

To quantify the epitope dosage another peptide amphiphile was synthesized. Mercapto-undecanoyl-$V_3A_3E_3G_5WG$ (denoted as **W**, see **Scheme S5.1**) was composed of a single C_{11} alkyl chain, the same peptide domain as **1** or **2**, and a single Trp (tryptophan, W), conjugated *via* a Gly_5 spacer (glycine, G). GNPs and GNRs were coated with 9 molar parts of the **base** amphiphile and 1 molar part of **W**. The amount of the unbound peptide was determined through an absorbance measurement at A_{280} (ε_{280}=5600 $M^{-1}cm^{-1}$) and by relating this to the Lambert-Beer law, the concentration of unbound (and hence bound) peptide could be calculated. From the amount of the bound **W** together with the known relationship between OD and number concentration,

the epitope loading per mL of a sample and/or epitope molecules per particle was calculated (**Table 5.2**).

Due to high relative surface area and the high number concentration, 15 nm GNPs carry a significant epitope load, while carrying a low number of epitopes per particle. Consequently, 40 nm GNPs had a lower number concentration but higher antigen load per particle. Due to their shape, GNRs have a higher relative surface area and number concentration than 40 nm GNPs.

For *in vitro* experiments a defined concentration range was used in order to determine a dose-response effect of GNPs of different shape and size. The selection was based on the epitope loading, while the other parameters including particle number concentration and OD are shown in **Table S5.2**. The dosage window for GNPs and GNRs decorated with $OVA_{257-264}$ covered the 0.03-1.89 µg/mL range, while for $OVA_{323-339}$ it was 0.06-3.15 µg/mL (molar concentration ranges were identical). For studies of cytotoxicity and cellular uptake in bone marrow-derived dendritic cells (BMDCs) only the highest concentrations, and 4x, and 16x dilutions were tested. For OT-I and OT-II experiments a serial dilution (1x, 2x, 4x, 8x, and 16x) was used.

5.3.3 Cytotoxicity of coated GNPs and GNRs

An *in vitro* cytotoxicity test was performed prior to studying immune response, to ensure that the peptide amphiphile-coated GNPs and GNRs were not harmful to cells. BMDCs were used in this assay for two reasons. BMDCs, like other types of dendritic cells (DCs), are antigen-presenting cells and are the cell type most likely to first encounter pathogens. Moreover, the *ex vivo* assay using transgenic ovalbumin mice (OT-I and OT-II) to probe the immunogenicity require DCs treatment as the first step.

The assay consisted of the following steps: BMDCs were differentiated from bone marrow progenitor cells over the course of 10 days; BMDCs were exposed to peptide amphiphile-coated GNPs and GNRs at different concentrations for 4 hours; then the cytotoxicity was determined with a Lactate Dehydrogenase (LDH) assay. LDH is naturally present in the cytosol and is released into the cell culture upon cellular membrane damage caused by nanoparticle toxicity. The LDH level determined for BMDCs treated with PBS was taken as 0% cytotoxicity (negative control), while the LDH level determined for BMDCs treated with the assay lysis buffer was taken as 100% cytotoxicity (positive control).

The observed peptide-gold nanoconjugates cytotoxicity was found to be <10% after 4-hours of exposure and <20% after 24 hours for all tested GNPs and GNRs (**Figure 5.2** and **Figure S5.4**). This was true for all concentrations tested. Notably, **15-base** showed the highest toxicity, most likely attributed to the high number concentration of particles.[19, 21] On average, cytotoxicity of spherical GNPs increased after 24 hours compared to 4-hours exposure for all tested particles. Moreover, there was no statistically significant difference between the cytotoxicity demonstrated by GNPs and GNRs after 24-hours exposure (only the highest concentrations were compared).

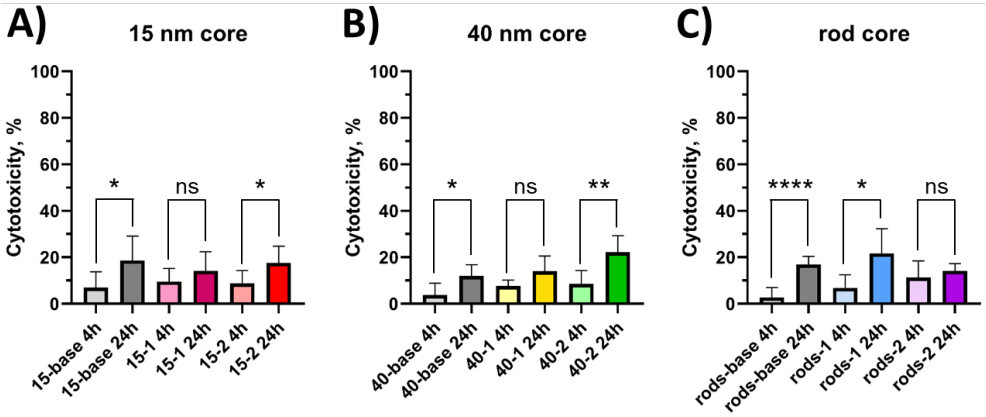

Figure 5.2. Cytotoxicity profiles for the peptide-coated GNPs and GNRs at the highest concentration used for each experimental group (**Table S5.2)** at 4 (light colors) and 24h (darker colors) exposure times: (A) 15 nm GNPs; (B) 40 nm GNPs; and (C) GNRs. Cytotoxicity was evaluated with the LDH release assay. Each data point was recorded in triplicate. The graphs present an average of two independent repeats; error bars indicate standard deviations calculated using GraphPad Prism software. Unpaired t-test was used to calculate the significance (ns = not significant, p ≥0.05; * = p within 0.01-0.05; ** = p within 0.001-0.01; *** = p within 0.0001-0.001). For the cytotoxicity profiles covering the full nanoparticle concentration range see **Figure S5.4**.

This data is consistent with published results of different GNP samples in different cell types. PEGylated GNPs and GNRs were shown to have a limited effect on LDH release (<20% after 24-hours exposure)[13, 24] and cell death (<15% after 24-hours exposure).[1, 16, 18, 24] According to Fytianos *et al.* polymer-coated GNPs (15 nm in diameter) did not induce cell death independent of the surface charge,[18] while Bhamidipati *et al.* reported that surface chemistry contributes towards cytotoxicity, but not the shape when spherical (20 nm in diameter), rod-like (53 by 23 nm), and star-like GNPs (63 nm) were compared.[24] Kang *et al* reported that neither 10, 22, or 33 nm OVA protein-coated GNPs induced cytotoxicity.[16] It has also been reported that PEGylation of GNRs abolishes cytotoxicity for CTAB-stabilized GNRs.[24, 27] The results presented here suggest that employing thiolated peptide amphiphiles as GNP and GNR stabilizers abolishes the cytotoxicity reported

for citrate-capped GNPs and CTAB-protected GNRs. Additionally, changing the surface chemistry by addition of a bioactive peptide did not induce acute cytotoxicity.

5.3.4 Cellular uptake of OVA-decorated GNPs and GNRs by BMDCs

Cellular uptake defines the antigen fate inside the cell and is crucial for establishing a link between the evoked immune reaction and the nanoparticle type. Cellular uptake of peptide-gold nanoconjugates by DCs was quantified using ICP-MS and the subcellular localization of endocytosed GNPs and GNRs was visualized with TEM. For this study, BMDCs were differentiated from bone marrow progenitor cells and exposed to epitope-bearing GNPs and GNRs for 4 hours. Particles in exposure medium were removed and the cells were subsequently washed with PBS and examined as described in **5.5.11**.

In order to analyze subcellular localization of GNP- and GNR-treated cells were embedded in a resin, cut into thin (100 nm) sections, and stained. GNPs and GNRs were found inside subcellular vesicles but not dispersed in the cytosol, or accumulated in organelles (**Figure 5.3** and **Figure S5.5**). There was no apparent difference in nanoparticle distribution as a function of peptide amphiphile composition. However, the appearance of these vesicles and number of entrapped particles depended on the nanoparticle core shape and size. For example, **40-1** and **40-2** showed fewer particles per vesicle (<10) than **15-1**, **15-2**, **Rods-1**, or **Rods-2**. For **40-1** and **40-2** the volume of some vesicles was very low: particles appeared to be encased in the endosomal membrane. For 15 nm GNPs and GNRs, the vesicles looked

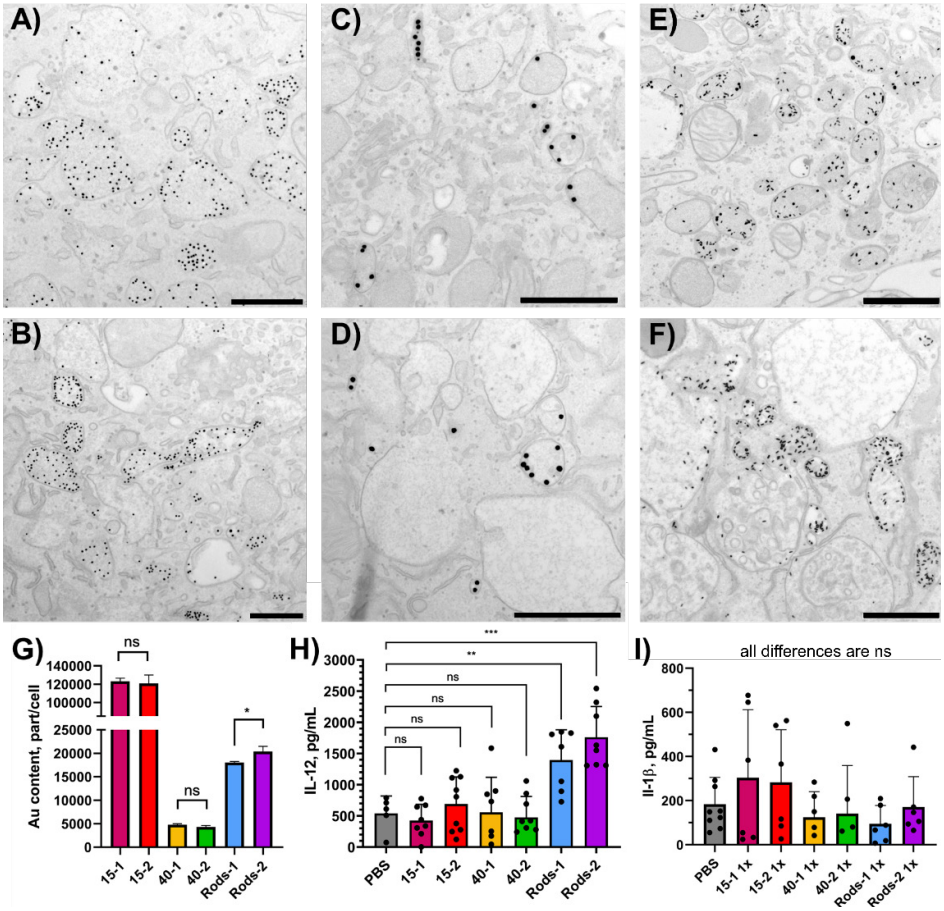

Figure 5.3. GNPs uptake was studied using TEM imaging (A-F), and quantified with ICP-MS (G), while BMDCs activation was checked *via* IL-12 (H) and IL-1β (I) levels in cell culture medium. Localization of GNPs and GNRs inside BMDCs sections after a 4-hour incubation was studied using TEM: (A) **15-1**; (B) **15-2**; (C) **40-1**; (D) **40-2**; (E) **Rods-1**; and (F) **Rods-2**. All studied particles were trapped in vesicles. Scale bars: 500 nm for A-B and E-F, and 1 µm for C-D. A representative image of a DC treated with PBS and low magnification images can be found in **Figure S5.5**. For more uptake quantification using ICP-MS, see **Figure S5.7** (measured in triplicate). Only IL-12 and IL-1β levels for the highest GNP concentration (1x) in exposure medium after a 24-hour incubation are shown in (H and I), for 4x and 16x concentrations see **Figure S5.9, S5.10** (for H, three independent experiments, three test wells each, were tested; for I, two independent experiments were tested; negative values are not shown; values above 3000 pg/mL of IL-12 were excluded). Error bars indicate standard deviations and were calculated in GraphPad Prism software, as well as the results significance (ns = not significant, p ≥0.05; * = p within 0.01-0.05; ** = p within 0.001-0.01; *** = p within 0.0001-0.001). Unpaired t-test (G) or two-way ANOWA (H) were used to calculate the significance.

similar: larger vesicles with high particle numbers (>10) dominated, although small vesicles (< 100 nm) containing fewer particles were also observed.

The type and function of these vesicles could not be determined from TEM analysis, but these vesicles could be divided into several groups based on their size. Small vesicles with a low number of particles inside are most likely to be endocytic vesicles that are to be fused with endosomes to start the endo-lysosomal pathway.[7, 8] Reformed endosomes undergo a maturation process and subsequently fuse with lysosomes. Lysosomes can be distinguished by their darker contents in the TEM images.[45] Reformed lysosomes perform antigen digestion, which is crucial for antigen presentation through MHC-epitope interactions. Analysis of the TEM images (**Figure 5.3**) for the vesicles' dimensions and number of entrapped particles showed differences between the different gold nanoparticles (**Figure S5.6,S5.7**). It should be noted that this analysis was based not on a full volume of a vesicle, but on its partial volume restricted to a thin section with a thickness of 100 nm. The analysis was carried out for nanoparticles decorated with **1** ($OVA_{257-264}$). Based on the analysis of 177 vesicles inside the thin sections of BMDCs exposed to **40-1**, there were no vesicles with more than eight particles inside and 65.5% of the vesicles contained only one particle (**Figure S5.6B,C**). Interestingly, it was possible to divide vesicles into groups based on their size and particle number. Small vesicles (40-120 nm) with low particle numbers (<6) are likely to be endocytic vesicles.

Vesicles with an average size up to 500 nm could be both endosomes and lysosomes, and large vesicles (up to 1200 nm) are either lysosomes or multivesicular bodies (MVB). It was also possible to detect fusion of two vesicles: presumably a small vesicle released its content into a larger vesicle (**Figure S5.7D**). On the other hand, **15-1** and **R-1** showed a different

behavior. Only 15.3% of vesicles (n = 137) contained one **15-1** particle, while for **R-1** this value was 13.0% (n = 200, **Figure S5.6A,B,E,F**). At the same time, vesicles with ≤10 entrapped particles were moderately present in BMDCs exposed to **15-1** (48.9%), but formed the majority in the case of **R-1**-exposed cells (74.0%). In some images it was possible to see formation of endocytic vesicles: **15-1** was endocytosed in vesicles with one particle inside or by interactions between the plasma membrane and multiple particles (**Figure S5.7A-C**). This suggests that multiple endocytosis pathways are involved for **15-1** uptake. Interestingly, **R-1** exposed cells showed the presence of endosomes with two kinds of membrane: rough and smooth, although no significant deviation in vesicle size was observed (**Figure S5.7E,F**). Also, nanoparticles were seen in the cytosol, but these events were rare (<0.5% for all samples).

These findings indicate that different endocytosis pathways might be involved in GNP/GNR uptake. Published data suggests the following pathways for coated GNPs and GNRs: receptor-mediated[20, 41] and macropinocytosis[21] for GNPs within the 15 - 40 nm size range; and receptor-independent[21] and a combination of clathrin-/caveolae- and lipid raft-mediated pathways for GNRs.[17] Ding *et al.* also reported that endocytosis pathways for GNPs can be influenced through their surface chemistry.[21] Solely based on the TEM images it was not possible to distinguish what specific endocytosis pathways peptide amphiphile-coated GNPs and GNRs employ. To address this, more uptake studies focusing on the use of endocytosis inhibitors should be conducted.[17, 21, 46]

In order to study the immunological impact of nanoparticles of different size and shape, it was important to determine the gold content per cell. Quantification of cellular uptake based on the TEM images would not be

reflective of the entire cell population since the images provide information on only one section of a cell. For that reason, inductively coupled plasma mass spectrometry (ICP-MS) was used. BMDCs were subjected to GNPs in the same manner as described above: after a 4-hour incubation, the cells were thoroughly washed with PBS, and digested in *aqua regia*.

The gold content per cell was calculated by dividing the determined gold mass derived from gold mass concentration by the number of cells digested. Based on the dimensions of a nanoparticle, the mass of a single particle could be determined and thus the average number of particles per cell could be calculated. To make a fair comparison, the number of added nanoparticles was fixed to the gold core size, meaning the same number of **15-1** or **15-2** was added. After the 4-hour exposure time **15-1** and **15-2** were taken up to the same extent (123×10^3 *versus* 121×10^3 particle/cell), and 40 nm GNPs and GNRs showed the same trend (**Figure 5.3G**). This suggests that altering the active peptide in the shell composition did not have an effect on GNPs or GNRs uptake by BMDCs. It should be noted that 15 nm and 40 nm GNPs, although taken up in the same mass (in the range of 3.6-4.0 pg/cell), significantly differed in number (~25x times more 15 nm GNPs) and delivered total surface area (~3x times more for 15 nm GNPs, see **Figure S5.8**). The surface area available for contact that was delivered into the cells could be correlated to the number of delivered antigens and it decreases in the following order: 15 nm GNPs > GNRs > 40 nm GNPs. In our study epitope-decorated 15 nm GNPs could deliver ~3x times more antigens than 40 nm GNPs and ~2x times more than GNRs.

As part of the uptake studies, cytokine release by BMDCs was studied. Interleukin 1 beta (IL-1β) and interleukin 12 (IL-12) cytokines provide information on activation of DCs by particulate formulations.[2, 3, 18, 47, 48] For

this, BMDCs were exposed to epitope-decorated GNPs and GNRs at three concentrations (1x, 4x, and 16x) for 24 hours and the cytokine levels were determined with an enzyme-linked immunosorbent assay (ELISA) (**Figure 5.3H,I** and **Figure S5.9,S5.10**).

IL-12 is a cytokine secreted by DCs in response to Pathogen Recognition receptor (PRR) stimulation and promotes differentiation of naïve T cells into Th1 cells and stimulates production of IFN-γ from T cells.[36, 47] IL-12 also mediates enhancement of CD8+ cytotoxic T lymphocytes activity. Compared to the PBS negative control, only GNRs showed significant levels of IL-12 secretion when comparing the highest concentration of nanoparticles in the exposure medium (**Figure 5.3H**). Interestingly, all tested concentrations of **15-1** and **15-2** failed to induce IL-12 secretion, which indicates that 15 nm GNPs do not activate DCs, although they showed potential in delivering high antigen loads (**Figure S5.9A**). On the other hand, 40 nm GNPs showed a peculiar behavior: high number concentrations had less impact than lower number concentrations. This was attributed to possible overstimulation of BMDCs, since it was determined that at these doses 40 nm GNPs do not cause cytotoxicity. It is remarkable that such low number concentrations of 40 nm GNPs were as effective as high number concentrations of GNRs (**Figure S5.9B,C**). GNRs showed a concentration-dependent effect on IL-12 secretion. Previously, protein-coated GNPs (40 nm in diameter) and gold nanocubes (40 by 40 nm) were reported to induce IL-12 secretion, but not smaller GNPs (20 nm in diameter) or GNRs.[2] This data therefore supports this previous assertion that small GNPs do not induce IL-12 secretion, but contradicts the previous report as GNRs are capable of inducing IL-12 secretion in this study.

Additionally, the capacity of epitope-decorated GNPs and GNRs to induce inflammation was studied through IL-1β secretion (**Figure 5.3l** and **Figure S5.10**). None of the tested particles induced significantly elevated levels of IL-1β compared to the negative control (PBS) indicating that the observed activation of BMDCs did not follow an inflammasome-mediated pathway. These findings are in agreement with previous studies using spherical GNPs: irrespective of the GNP size or coating, they did not induce inflammasomes formation.[2, 18] Interestingly, there is no consensus between the results presented here and published data on GNRs. Depending on the coating, GNRs were reported to cause significant levels of IL-1β secretion. For example, this was observed for GNRs coated with the West Nile virus envelope protein, while spherical and cubical gold nanoparticles did not induce IL-1β secretion.[2] GNRs coated with recombinant Sm29 proteins derived from *Schistosoma mansoni* also induced high levels of IL-1β, however CTAB-stabilized or cysteamine-stabilized GNRs did not.[48] Furthermore, PEGylated GNRs also did not induce IL-1β.[27]

In summary, both GNPs and GNRs are likely taken up *via* an endo-lysosomal pathway. Cellular uptake was governed by the core size but not by the displayed epitope. Moreover, despite the potential of 15 nm GNPs to deliver antigens, they failed to activate BMDCs, while 40 nm GNPs possibly caused cell overstimulation. GNRs were capable of delivering significant antigen loads and caused concentration-dependent activation of BMDCs. None of the tested particles caused inflammation. These results are in agreement with previously published studies for GNPs, but contradict published data for GNRs.

5.3.5 Activation of CD25 and induced proliferation of CD4+ and CD8+ cells in OT-I and OT-II mouse models

Studying T-cell immune response is a challenging task as there is no direct *in vitro* method for detection. Classical approaches require a significant number of lab animals for intensive *in vivo* or *ex vivo* experiments. OT-I and OT-II mouse lines are transgenic lines that have T cells specific to the OVA-derived epitopes.[34] CD8+ T cells in the OT-I mice only express the TCR specific towards the cytotoxic epitope $OVA_{257-264}$, while CD4+ T cells of OT-II mice are specific to the T-helper epitope $OVA_{323-339}$. This model is of particular use for vaccine platform evaluation since immunization of animals is not required and challenging of the T cells with the epitope-decorated formulations can be done directly in an *ex vivo* assay. The OT-I/OT-II technique saves time and allows for faster and more thorough screening of potential vaccine platforms with the minimal number of animals required.

The strategy used in this study included differentiation of bone marrow progenitor cells into BMDCs with exposure of the latter to the epitope-decorated GNPs and GNRs. BMDCs will endocytose the nanoparticles and antigens will be cleaved from the gold surface and presented back to the surface of the DCs, waiting for interaction with specific T cells. DCs differentiation time was kept constant (10 days) for all experiments. After 4h exposure to the BMDCs, the GNPs were removed and isolated CD8+ (OT-I) or CD4+ T (OT-II) cells were added to the activated BMDCs and the cells proliferated for 72 hours. To track proliferation, CD8+ and CD4+ cells were stained with 5(6)-carboxyfluorescein diacetate N-succinimidyl ester (CFSE) after isolation. The degree of T-cell activation was determined with FACS using CD25 gated *versus* CFSE stained signals ($CD25^{+}CFSE^{low}$ T-cell subset, for gating strategy see **Figure S5.11**). CD25 is the high-affinity IL-2

receptor present in T cells and it is upregulated and moved to the cell surface upon activation by cytokines.[39, 49] This cell population positive for CD25+ and showing CFSE dilution (a decrease in fluorescence with respect to the negative control related to cell division) represent proliferated T cells. Next, proliferation rates as a function of epitope dosage were transformed into dose-response curves shown in **Figure 5.4**.

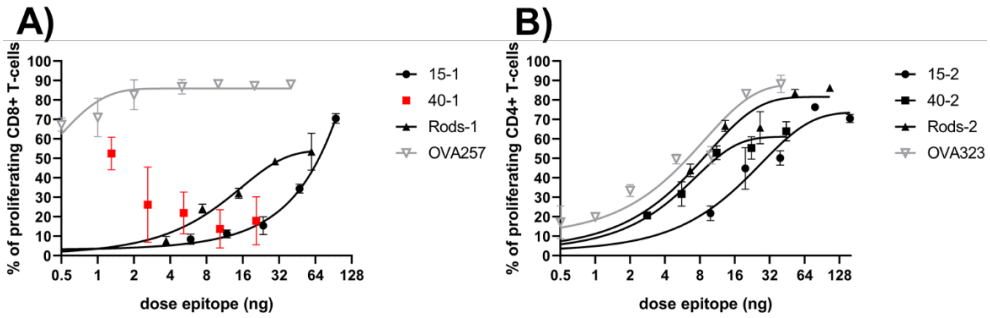

Figure 5.4. Dose-response curves reflecting proliferation rates of: (A) OT-I mice derived CD8+ cells and (B) OT-II mice derived CD4+ cells in response to OVA epitope-carrier GNPs (15 and 40 nm in diameter) and GNRs. % of proliferating cells was calculated from FACS data as CD25+/CFSE dilution (arising from the specific T-cells; for gating strategy, see **Figure S5.11**). The gray line shows the positive controls free epitopes. Three independent experiments were conducted for each GNP preparation, and a representative example is shown here. Data points represent a mean result of three individual wells. Error bars indicate standard deviations. Data sets were fitted into a dose-response curve using GraphPad Prism software.

The assays revealed a striking difference in GNPs and GNRs ability to induce different T-cell mediated responses. As expected, 15 nm GNPs were the least effective carriers in both cases. It was attributed to their inability to induce IL-12 secretion, hence there was no activation of BMDCs. 40 nm GNPs were more effective than 15 nm GNPs for induction of CD4+ cells (T-helper cells), but the CD8+ response was not trivial to interpret. **40-1** was the only formulation that did not show a typical S-shaped dose-response curve: proliferation of CD8+ cells was suppressed for all **40-1** concentrations except

the lowest. To test the overstimulation hypothesis drawn from the IL-12 secretion and CD8+ proliferation profiles, the number of BMDCs was doubled, while the ratio between BMDCs and CD8+ T cells was preserved. This alteration resulted in lower proliferation rates for all three formulations: almost negligible CD8+ proliferation in case of **15-1** and **Rods-1** formulations (**Figure 5.5**). On the other hand, **40-1** did cause significant levels of CD8+ proliferation in a concentration-dependent manner. This observation indicates that, indeed, **40-1** are capable of causing BMDCs overstimulation. The difference between the effect caused by **40-1** and **40-2** can be explained by different pathways that different MHC molecules employ to present processed antigens back to the plasma membrane. MHC-I (involved in CD8+ activation) is supplied with antigens present in the cytosol, while MHC-II (involved in CD4+ activation) loads antigens directly inside lysosomes.[38] Egress of antigens from lysosomes into the cytosol is a complex process that is not well understood.[50, 51] The data presented here suggests that 40 nm GNPs lead to significantly more cleaved epitopes escaping into the cytosol than GNRs, possibly defining a size-dependent trend. Following the idea of MHC-II loading inside lysosomes, **Rods-2** were expected to outperform **40-2**, since the former deliver more antigens in cells (**Figure 5.3G**), and this trend was proven experimentally (**Figure 5.4B**). Importantly, neither the **base**-coated GNPs or GNRs evoked any CD25 upregulation in both OT-I and OT-II experiments (**Figure S5.12**).

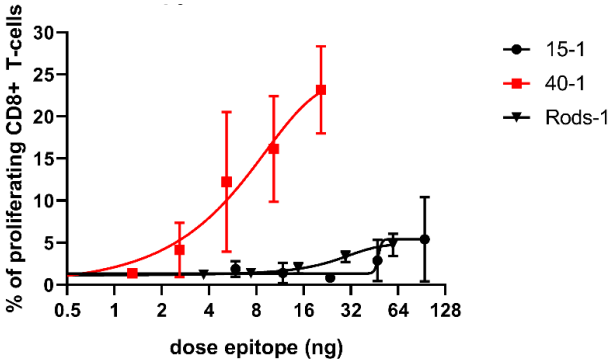

Figure 5.5. Dose-response curves showing proliferation rates of OT-I mice derived CD8+ cells exposed to BMDCs activated with GNPs and GNRs after the ratio between BMDCs and nanoparticles was doubled relative to **Figure 5.4**. % of proliferating cells was calculated from FACS data as CD25+/CFSE dilution (arising from the specific T-cells; for gating strategy, see **Figure S5.11**). Data points represent a mean of three individual wells. Error bars indicate standard deviation. Data sets were fitted into a dose-response curve using GraphPad Prism software.

'Splitting' the T-cell immune response into two components (cytotoxic and T-helper) highlighted several aspects. Firstly, there is potentially a size threshold below which DCs and hence T cells only become activated when a very high antigen loading is applied (**Figure 5.4B**). Secondly, CD4+ activation is less sensitive to the size or shape of a carrier particle, but is governed by cellular uptake and the number of delivered antigens. Thirdly, CD8+ activation does not seem to be directly linked to uptake, but is influenced by the size and/or shape of carrier nanoparticles. These aspects should be taken into account when a new vaccine platform is being developed and one type of immune response is preferred over the other.

In order to obtain additional details on the performance of GNPs and GNRs decorated with $OVA_{257-264}$, and to clarify the effect **40-1** exhibits on BMDCs, the cell activation through upregulation of cellular receptors was studied.

5.3.6 DCs activation monitored through cellular receptors upregulation

Mature BMDCs were exposed to **15-1**, **40-1** and **Rods-1** for 4 hours. The cell number per well was increased to 50×10^3 cells instead of the previously used 20×10^3 cells, but the particle concentrations added to the wells were not changed. Nanoparticles were subsequently removed and the cells were analyzed with FACS directly after NP removal and after 24 hours. CD80, CD86, and the full complex of MHC-I/$OVA_{257-264}$ were chosen to monitor BMDCs activation (**Figure S5.13-S5.16**).

Both CD80 and CD86 are necessary for T-cell activation and survival through co-stimulation with CD28 expressed on T cells.[36, 39] Both receptors are already upregulated on BMDCs due to their handling during the culture procedure, which is reflected in their staining in the negative control sample (DMEM). With respect to the negative control, geometric mean fluorescent intensity (GMFI) of the CD80 channel did not significantly differ in the positive control (free $OVA_{257-264}$), **15-1**, or **Rods-1** at both time points, with one notable exception: **40-1**, which raised the CD80 level to a statistically significant level (**Figure 5.6A** and **Figure S5.14**). Interestingly, CD86 was more readily activated by **40-1** and less by **Rods-1**, but not by **15-1** or free $OVA_{257-264}$ (**Figure 5.6B** and **Figure S5.15**). Enhancement provided by **40-1** was almost double compared to the effect of **Rods-1**, and showed a dose dependence. This assay helped clarify the effect of 40 nm GNPs on BMDCs activation: most likely, suppressed secretion of IL-12 (**Figure 5.3H**) and CD8+ T-cell proliferation (**Figure 5.4A**) observed earlier at higher particle concentrations could be attributed to BMDCs overstimulation, when lower cell numbers are exposed to the particles (50×10^3 cells *versus* 20×10^3 cells).

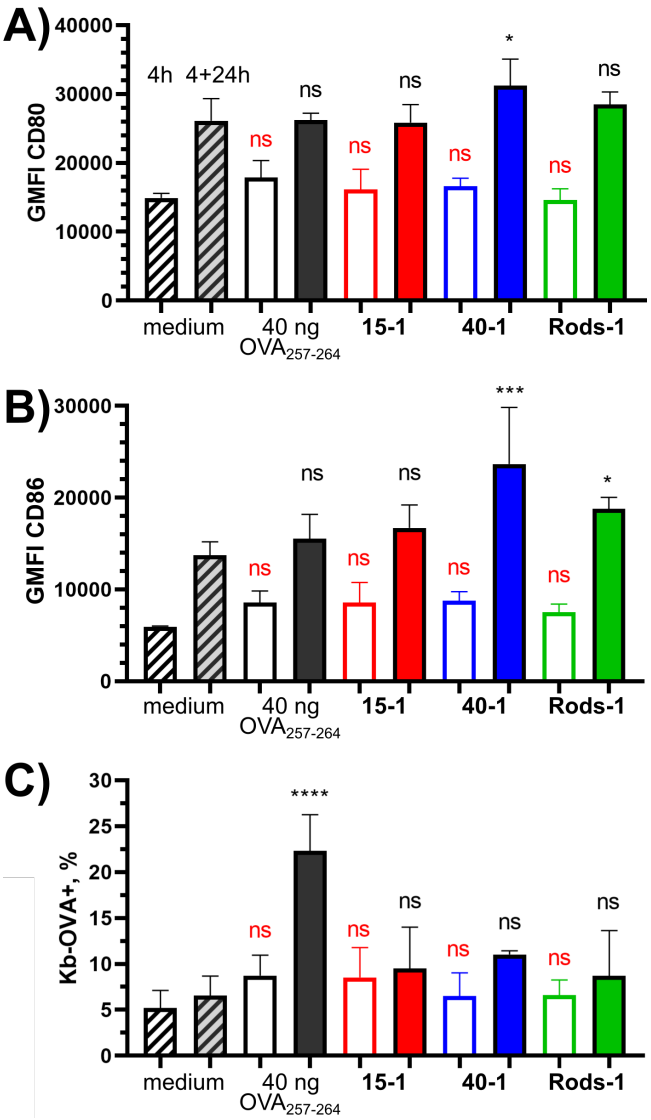

Figure 5.6. Activation of BMDCs upon exposure to GNPs and GNRs decorated with the $OVA_{257-264}$ epitope though cellular receptors upregulation: (A) CD80;(B) CD86; and (C) K_b-$OVA_{257-264}$. CD80 and CD86 datasets were calculated using the geometric mean fluorescent intensity (GMFI) of corresponding channels (**Figure S5.13-S5.15**), and for K_b-$OVA_{257-264}$ the positive cell subset is shown (**Figure S5.16**). Significance of the datasets mean values was determined through comparison to the negative control (supplemented DMEM). Empty columns correspond to 4-hour exposure time, and solid columns correspond to 24 hours post exposure. Only highest particle concentrations are shown here, for more detail, see **Figure S5.13-S5.16**.

The results of CD80 and CD86 activation of BMDCs are consistent with previously reported data: 33 nm GNPs coated with full OVA were shown to induce greater upregulation in both CD80 and CD86 expression than 10 or 22 nm GNPs coated with OVA.[16] Additionally, antigen-coated GNRs were able to induce simultaneous upregulation of CD86, MHC-I, and MHC-II.[48]

To investigate antigen processing and presentation mediated by GNPs of different shape and size, the ability of BMDCs to present MHC-I loaded with $OVA_{257-264}$ was assessed by means of FACS using an antibody specific towards the whole complex (K_b-$OVA_{257-264}$, **Figure 5.6C**). Consistent with the T-cell proliferation data, 15 nm GNPs did not induce significant epitope presentation, while GNRs induced very low presentation at 24 hours post exposure. However, 40 nm GNPs showed slight epitope presentation directly after exposure, but after 24 hours there was no significant MHC-I/$OVA_{257-264}$ upregulation detected. Taking into account suppressed IL-12 production and CD8+ T-cell proliferation, the Kb-OVA data shows that with decreasing concentration of **40-1**, an increase in antigen presentation is detected. Clearly, when the BMDCs are overloaded with 40 nm GNPs, this affects cross presentation. Other possible reasons for such seemingly poor presentation can be: (i) insufficient time after exposure to process most of the antigen and present it back to the cell membrane; (ii) the K_b-$OVA_{257-264}$ antibody was suitable for detection of direct MHC-I loading with free SIINFEKL, but it is not sensitive enough for detection of processed SIINFEKL; (iii) the epitope is being cleaved off the gold surface into a set of fragments that, when loaded onto MHC-I, cannot be recognized by the K_b-$OVA_{257-264}$ antibody with the same specificity as $OVA_{257-264}$ itself.

The results of upregulation of cellular receptors of DCs upon activation with GNPs of different size and shape were consistent with the other results.

Despite high loading and intense cellular uptake, 15 nm GNPs did not stimulate BMDCs on multiple levels (IL-12 secretion, CD80 and CD86 upregulation) and, hence, failed to induce T-cell proliferation. 40 nm GNPs showed great potential in delivering epitopes into cells and inducing BMDCs activation, even causing overstimulation in some cases. Also, 40 nm GNPs seem to be more effective in directing processing epitopes into the cell cytosol. GNRs took the middling position: they are capable of inducing activation of BMDCs and CD8+ cells, but to a lesser extent in comparison with 40 nm GNPs.

5.4 Conclusions

The data reported here on peptide-gold nanoconjugates comprising a gold core of differing shape and size (15 and 40 nm in diameter, and rods of 44 by 15 nm) and a peptide shell, showed that these nanoconjugates are safe in terms of their stability under physiological conditions and do not cause cytotoxicity. Cellular uptake of GNPs and GNRs by BMDCs was governed by the gold core parameters, irrespective of the displayed antigen. All three types of nanoparticles were trapped inside subcellular vesicles, which were analyzed for their size and number of entrapped particles. Observed differences might indicate that every type of GNPs and GNRs utilizes a different endocytosis pathway or mixed pathways. Despite potential in delivery of high antigen loads, 15 nm GNPs failed to activate BMDCs while both 40 nm GNPs and GNRs caused significant BMDCs activation through IL-12 secretion and upregulation of CD80 and CD86. Using the OT-I/OT-II mouse model, it was possible to decouple the cytotoxic and helper T-cell immune responses and show that larger spherical conjugates (40 nm in diameter) caused better CD8+ induction (cytotoxic response), while rod-shaped conjugates (44 by 15 nm) caused better CD4+ activation (T-helper response). In terms of CD4+ T-cell proliferation, GNRs consistently showed higher rates than GNPs of 40 nm in diameter. However, it cannot be concluded that GNRs are superior to the GNPs, as the latter also induced significant CD4+ proliferation. 15 nm GNPs induced both responses but only at very high doses. The observed difference in CD8+ T-cell proliferation can possibly be attributed to more effective egress of processed epitopes from lysosomes with 40 nm carrier GNPs in comparison to GNRs. This way epitopes are delivered into the cytosol more efficiently and have a higher chance of being loaded onto MHC-I and inducing a cytotoxic response. The

observed difference in CD4+ T-cell proliferation was attributed to the difference in epitope loading: GNRs due to their higher relative surface area carry more antigen than 40 nm GNPs, thus GNRs are more likely to load antigens onto MHC-II inside the lysosomes. It should be noted that the difference between different NPs in CD8+ T-cell activation had a more dramatic character than the difference observed in CD4+ T-cell activation. These findings allow for rational design of a carrier nanoparticle in vaccine development.

5.5 Experimental Section

5.5.1 Materials

All chemicals were purchased from Sigma-Aldrich unless stated otherwise. For GNR and GNP synthesis, the purity of CTAB and the composition of the gold salt are critical for reliable particle formation. For synthesis of the particles described in this chapter CTAB (≥ 99%, H6269) and $HAuCl_4 \times 3\ H_2O$ (49% Au basis, G4022) were purchased from Sigma-Aldrich. Silver nitrate (99.999%) and Oxyma Pure were purchased from Carl Roth GmbH. TFA, piperidine, DMF, DCM, methanol, and acetonitrile were purchased from Biosolve. TEM grids (Formvar/Carbon, 200 mesh, on copper support) were purchased from Electron Microscopy Sciences. FCS, penicillin/streptomycin mixture, L-glutamate, DMEM and RPMI 1640 cell culture media were purchased from Lonza. Mouse granulocyte-macrophage colony-stimulating factor (GM-CSF) was purchased from PeproTech. CD4+ and CD8+ isolation kits (*via* MACS magnetic separation) were purchased from Miltenyi Biotech. LDH leakage assay (LDH-Cytox™ Assay Kit) and the specific antibody against the whole MHC-I/$OVA_{257-264}$ complex (PE anti-mouse H-2Kb bound to $OVA_{257-264}$ antibody, K_b-$OVA_{257-264}$) were purchased from Biolegend. ELISA standards (IL-12 and IL-1β) and antibodies, TMB substrate, as well as FACS immunostaining antibodies were purchased from eBioscience.

5.5.2 Gold Nanoparticles Synthesis

Spherical particles (GNPs) of 15 and 40 nm in diameter were synthesized *via* citrate reduction and overgrowth as described in **Chapter 3** of this thesis.[29] The average size of the GNPs in suspension was analyzed using dynamic light scattering (DLS), and the results are shown in **Table 5.1**. Size

parameters of the obtained GNPs were also determined by transmission electron microscopy (TEM): mean diameters were 15.0 nm and 43.5 nm. The mass of one nanoparticle was calculated to be 34.1 and 832.2 ag (for 15 and 40 nm GNPs, respectively) and the surface areas were determined to be 707 and 5945 nm^2.[19, 52]

Gold nanorods (GNRs) were synthesized *via* the two-step seed-mediated approach as described in **Chapter 4** of this thesis.[53, 54] The average dimensions were 44.0 (± 4.0) by 14.8 (±1.9) nm. The mass of one nanorod was calculated to be 129.8 ag, and the surface area – 2046 nm^2.

5.5.3 Peptide and peptide amphiphile synthesis

Peptides and peptide amphiphiles were synthesized by solid-phase peptide synthesis using standard Fmoc-chemistry protocols. The synthesis was performed on an automated microwave peptide synthesizer, Liberty Blue (CEM), using standard settings. All peptides and amphiphiles were synthesized on a Wang resin preloaded with the corresponding C-terminal residue. 20% piperidine in DMF was employed as the deprotection solution, (deprotection was performed at 90 °C, for 60 secs), and N,N'-diisoprorylcarbodiimide (DIC)/OxymaPure (activator/activator base) were used to activate Fmoc-protected α-amino acids (5 equivalents relative to the resin loading were used, coupling was facilitated at 95 °C, 4 mins). 11-mercaptoundecanoic acid was coupled to the peptide N-terminus using the same protocol as for amino acid coupling but for a longer time (5 equivalents relative to the resin loading, 95 °C, 10 mins). The terminal thiol of the acyl chains was blocked with 2,2′-Dithiobis(5-nitropyridine) (DTNP, 1 eq. in DMF, 3 hours). The molecules were cleaved from the resin using a cleavage cocktail comprising 2.5% triisopropylsilane (TIS), 1.5% deionized water,

2.5% phenol in trifluoroacetic acid (TFA, RT, 2 hours). The crude peptide compounds were precipitated into cold diethyl ether, pelleted by centrifugation, redissolved in water, and lyophilized prior to purification. HPLC purification was performed on a Shimadzu system equipped with two LC-20AR pumps, an SPD-20A UV-Vis detector and a Phenomenex Kinetex EVO C18 column (21.2 by 150 mm) with water and acetonitrile as mobile phases. 0.1% TFA was added to the mobile phases, except for purification of the **base** sequence where 0.1% NH_3 was added. Purity of the compounds was confirmed with LC-MS (**Figure S5.17-S5.22**). The purified molecules were lyophilized and stored at -20 °C.

5.5.4 Preparation of Peptide Amphiphile-Capped GNPs

Coating of the GNPs was performed *via* the ligand exchange procedure as described in detail elsewhere.[29] Briefly, the desired coating molecules were dissolved in DMSO, mixed at 9:1 molar ratio (**base**:**1** or **base**:**2**), and added to a stirred GNP suspension. The peptide amphiphile molar excess over the GNPs was at least 200 000. The final concentration of DMSO in the mixture was 50% (v/v). After a 1-hour incubation the samples were centrifuged to pellet the modified GNPs and the supernatants were discarded and replaced with 25% DMSO (v/v). Samples were incubated overnight and after a final centrifugation cycle, the GNPs were dispersed in 5% DMSO. Size exclusion chromatography (SEC, NAP-25 columns, GE Healthcare) was performed with PBS as an eluent to remove free ligands and DMSO according to manufacturer's manual.

Particle size distributions, determined by dynamic light scattering (DLS), and Zeta-potential before and after modification were obtained using a Zetasizer Nano-7 S (Malvern Instruments). The average of three separate

measurements was reported. Transmission electron microscopy (TEM) measurements were performed on a JEM 1400 Plus (JEOL) microscope, with an accelerating voltage of 80 kV and with a CDD camera. Sample preparation was as follows: a 10 µL droplet of the sample was deposited on a carbon-coated copper grid for 20 mins. The excess sample was removed by blotting with a fibreless tissue. The grid was washed with MilliQ water once and blotted again. 1% (w/v) uranyl acetate staining was applied, followed by immediate blotting and drying.

UV-Vis spectra were recorded in the 900-350 nm range using a Cary 300 UV-Vis spectrometer (Agilent). Molar concentrations of GNPs and GNRs were determined by UV-Vis using extinction coefficients published by Haiss et al.[55] for spherical particles, and by Orendorff et al.[54] for rod-like particles. To calculate molar concentrations of nanoparticles, The Lambert-Beer law was used (equation 1):

$$A = \varepsilon \cdot l \cdot c \cdot N, \quad (1),$$

where A is absorption, ε is extinction coefficient (in $M^{-1}cm^{-1}$), l is the optical path length (l = 1 mm), c is molar concentration (in M), and N is the dilution factor.

5.5.5 Circular dichroism

Circular dichroism (CD) spectra of the amphiphiles were recorded using a JASCO J-815 spectropolarimeter, fitted with a Peltier temperature controller. All measurements were performed at 20 °C. Lyophilized powders of peptide amphiphiles were dissolved in 1,1,1,3,3,3-Hexafluoro-2-propanol (HFIP), mixed at the molar ratio of 1:9 = active peptide amphiphile (**1** or **2**):**base** peptide amphiphile, and dried under a nitrogen flow. The peptide amphiphile

thin film was rehydrated with PBS (pH 7.2) to achieve the following concentrations: 20 µM of active peptide amphiphile (**1** or **2**) and 180 µM of **base** peptide amphiphile. As a reference sample, **base** was dissolved in PBS (pH 7.2) to a final concentration of 200 µM. Samples were left in the dark in sealed vials for 14 days. Samples were measured in quartz cuvettes with a 2 mm path length, and spectra were recorded from 260 to 190 nm at 2 nm intervals with a 1 nm bandwidth. All spectra were converted to mean residue ellipticity (deg cm^2 dmol res^{-1}) using equation 2:

$$[\theta] = \frac{100 \times [\theta]obs}{((C_{base} \times n_{base}) + (C_X \times n_X)) \times l} \quad (2),$$

where $[\theta]_{obs}$ is the observed ellipticity in mdeg; C_{base} is the concentration of **base** in mM; n_{base} is the number of amino acids in **base** (n_{base} = 11); C_X is the concentration of **1** or **2** in mM; n_X is the number of amino acids in **1** or **2** (n_1 = 17 and n_2 = 26); and l is the path length of the cuvette in cm.

5.5.6 Number concentrations of GNPs and GNRs

Gold (Au) mass quantification using inductively coupled plasma mass spectrometry (ICP-MS) was conducted as follows: the concentration of Au in the samples was measured using a PerkinElmer NexION 2000 equipped with a quartz nebulizer and a glass cyclonic spray chamber operating in standard mode (1600 W radio frequency power; 18 mL/min plasma gas flow; 1.2 L/min nebulizer gas flow; and 1.12 L/min auxiliary flow). The peptide amphiphile-coated GNPs or GNRs (in suspension, OD ~0.3-0.5) were mixed 1:1 (v/v) with *aqua regia* (HNO_3:HCl = 1:3) and were subjected to digestion at 70 °C for 1 hour. Mixtures were diluted 25x times with MilliQ water and directly measured for ^{197}Au isotope content. Knowing the optical densities of the suspensions before digestion with *aqua regia*, the mass of digested gold, and

the calculated mass of one nanoparticle, it was possible to link optical density (OD) of GNP or GNR suspensions with their number concentration. Small deviations in the determined gold concentration between the samples with the same core were not significant (**Figure S5.3A**), and could be attributed to incomplete nanoparticle digestion and analysis error, which can lead to deviations of up to 10%.[19]

5.5.7 Antigen loading displayed onto GNPs and GNRs

Antigen loading was expressed as shown in equation 3:

$$AL = d_{\boldsymbol{W}} \times S_{NP} \times N_{NP} \quad (3),$$

where *AL* is the antigen loading that 1 mL of a GNP or GNR suspension with an optical density of 1.0 at the plasmon band (OD_{LSPR}) contains; $d_{\boldsymbol{W}}$ is coverage density of a model molecule **W** (see **Scheme S5.1**) displayed on the gold surface; S_{NP} is the square area of one nanoparticle; and N_{NP} is the number concentration of nanoparticles in a suspension with OD_{LSPR} = 1.0 (determined using ICP-MS as described in **5.5.6**).

Coverage density $d_{\boldsymbol{W}}$ was determined as described in **Chapter 4** of this thesis (protocol #3 in **4.5.10**). Briefly, **base** and **W** peptide amphiphiles were dissolved in 1,1,1,3,3,3-hexafluoro-2-propanol (HFIP, 1.0 mg/mL) and mixed at a molar ratio of 9:1. This mixture was diluted with HFIP to obtain a final concentration of **base** of 0.50 mg/mL. Next, it was added to the GNPs and GNRs as follows: for every 0.3 mL of the peptide amphiphile mixture, 0.5 mL of a citrate- or CTAB-protected nanoparticle suspension was taken (OD_{519} = 4.5 for 15 nm GNPs, OD_{530} = 2.5 for 40 nm GNPs, and OD_{756} = 3.2 for GNRs). After a 1-hour incubation under stirring, the nanoparticles were pelleted *via* centrifugation (Eppendorf Centrifuge 5425, 14 000 rpm, 40 mins

for 15 nm GNPs, 10 mins for 40 nm GNPs, and 20 mins for GNRs). The pellets were rehydrated and lyophilized. The dry residue was redissolved in HFIP and nanoparticles were pelleted again. Both supernatants were analyzed using UV-Vis spectroscopy and concentrations were determined using the Lambert-Beer law (equation 1, tryptophan absorbance was analyzed using $\varepsilon_{280}(W)=5600\ M^{-1}cm^{-1}$). Knowing the molar concentrations of GNPs and GNRs and their surface areas, as well as added concentrations of **W**, and the amount that did not bind to the gold surface, the following d_W values were calculated: 0.58 peptide/nm^2 for 15 nm GNPs; 0.35 peptide/nm^2 for 40 nm GNPs; and 0.46 peptide/nm^2 for GNRs. Using a simple proportion based on the molecular weight of $OVA_{257-264}$, and $OVA_{323-339}$, and particle number concentrations obtained using ICP-MS, the coverage densities were recalculated for epitope loading (**Table S5.1**).

5.5.8 Animals

C57BL/6, OT-I, and OT-II transgenic mice were purchased from Jackson Laboratory (CA, USA). The animals were bred in-house in agreement with standard laboratory conditions, and provided with water and food *ad libitum*. The animals were treated in compliance with the Dutch government guidelines and the Directive 2010/63/EU of the European Parliament. Experiments were approved by the Ethics Committee for Animal Experiments of Leiden University.

5.5.9 Isolation and maturation of bone marrow-derived dendritic cells (BMDCs)

Bone marrow was extracted from tibias, femurs, and thigh bones of C57BL/6 or OT-I/OT-II mice. A single-cell suspension of bone marrow cells was

prepared using a 70-µm cell trainer (Greiner Bio-One B.V.). The cell culture medium used for the maturation was DMEM supplemented with 2 mM L-glutamine, 5% (v/v) FCS, 100 U/mL penicillin/streptomycin. Bone marrow cells were seeded in 95 mm Petri dishes at a density of 8-10×10^6 cells per dish (Greiner Bio-One B.V.) and incubated at 37 °C and 5% CO_2 for 10 days. Medium was refreshed four times during the 10-day period, 20 ng/mL GM-CSF was added to the medium to induce and maintain the maturation of progenitor cells into BMDCs.

5.5.10 LDH leakage assay

LDH leakage assay was performed to determine cytotoxicity of the peptide-gold conjugates in BMDCs. For the concentration range employed see **Table S5.2** (dilutions of 1x, 4x, and 16x were used for this assay). For this assay, BMDCs were cultured as described above. After 10 days of culturing, DCs (20×10^3 per well) were plated in 96-well plates (Greiner Bio-One B.V.) and were exposed to GNPs and GNRs for 4 and 24 hours at 37 °C (5% CO_2). A negative control (50 µL of PBS) and a positive control (50 µL of the assay lysis buffer) were added to every plate. The added volumes of peptide-gold conjugate samples were kept the same for all experiments – 50 µL per well (200 µL total well volume). After the exposure, the plates were centrifuged (1500 rpm, 5 mins) and 30 µL of the supernatants were taken for analysis which was performed according to the manufacturer's manual (non-homogenous assay protocol). Cytotoxicity was expressed as the difference between the negative control and fully lysed cells (equation 4) and the results are shown in **Figure 5.2** and **Figure S5.4**.

$$Cytotoxicity\ (\%) = \frac{(A-C)}{(B-C)} \cdot 100 \qquad (4),$$

where *A* is the signal arising from the GNP- and GNR-treated wells, *B* - the signal from the cell treated with assay lysis buffer, and *C* - is the signal coming from the negative control wells (PBS-treated). Signals were derived from absorbance at 490 nm measured using a microplate reader (Infinite 200 PRO Tecan). Every sample was tested in three individual wells. The data shown is an average of two independent experiments.

5.5.11 GNPs and GNRs uptake by BMDCs

This step was duplicated for two independent experiments: measuring cellular uptake of GNPs and GNRs *via* direct detection of the gold content per cell (ICP-MS assisted) and visualization of subcellular localization with TEM. Samples analyzed were: **15-1**, **15-2**, **40-1**, **40-2**, **Rods-1**, and **Rods-2**.

Mature DCs were seeded at a density of 1×10^6 cell per well in 6-well plates (Greiner Bio-One B.V.). For the cell visualization experiment, a coverslip (Thermanox, 24 mm in diameter, Nunc) was added in each well. 250 µL of sample (top concentration in **Table S5.1**) were diluted 2x times with DMEM and added to the wells (3 mL total volume). The cells and the samples were incubated for 4 hours at 37 °C (5% CO_2). Next, the cells were washed with PBS (pH 7.2) to remove the non-associated nanoparticles.

For the visualization experiment, the cells were fixed with 2% (v/v) glutaraldehyde in sodium cacodylate buffer (0.1 M, pH 7.2, 2 hours at room temperature). After fixation, 1% (w/v) OsO_4 was applied for 1 hour at room temperature. Next, the cells were dehydrated through ethanol graded series and embedded into Agar 100 resin (Agar Scientific, AGR1043). Thin sections (100 nm) were cut from the resin using a Leica Ultramicrotome equipped with a diamond knife. The images were acquired on a JEM 1400 Plus microscope, fitted with a CCD camera, at an accelerating voltage of 80 kV. The vesicles

dimensions were determined using Fiji ImageJ software. Since vesicles are not completely spherical, each vesicle was measured across its longest and shortest axes, and a mean value was reported in **Figure S5.6**.

ICP-MS was also used to determine the average gold content per cell. After 4 hours of incubation time, the BMDCs were washed with PBS (pH 7.2, 3x times), detached with a cell scraper (Sarstedt) and counted (1 mL total volume). The cells were lysed with aqua regia (1:1 dilution, 1 hour at 70 °C). Lysates were diluted 25x times with MilliQ water and directly measured in triplicate using the method described in **5.5.6**. Since both the cell numbers and total gold content were known, the average gold content per cell could be calculated (**Figure 5.3G** and **Figure S5.8**).

5.5.12 Activation of BMDCs

Activation of BMDCs was monitored through cytokine release and upregulation in expression of cellular receptors.

Mature BMDCs (20×10^5 cell per well in 96-well plates) were treated with GNPs and GNRs for 24 hours in the same manner as described in **5.5.8**. The cell culture supernatants were checked for IL-12 and IL-1β levels using ELISA. A 'sandwich' ELISA was performed according to a standard protocol at room temperature and involved the following steps: (1) coating the 96-well plates (half area, Costar) with capture antibodies (eBioscience, overnight at 4 °C); (2) blocking the wells from non-specific interactions by incubation with BSA (2.5% w/v in PBS, 1 hour); (3) incubation (2 hours) with the supernatant of GNP-exposed cells (diluted with block buffer), PBS-treated samples, IL-12 standard at different concentrations, and blank wells (blocking buffer); (4) addition of detection antibodies and complexation with SAv-HRP (1 hour). The read out was based on the reaction of the HRP conjugate with an TMB

substrate (BD Bioscience). The reaction was stopped with 1 N H_2SO_4 when the blue color in the well became intense. Absorbance at 570 nm was subtracted from absorbance at 450 nm (recorded using a microplate reader Infinite 200 PRO Tecan). Based on the signals obtained for the cytokine standards, calibration curves were built. Samples from three independent experiments were analyzed. For results see **Figure 5.3H** and **Figure S5.9,S5.10**.

Next, mature BMDCs (50×10^5 cell per well in 96-well plates) were exposed to GNPs and GNRs for 4 hours. Cell culture supernatants were removed and half of the cells were analyzed directly, and the other half was supplied with fresh medium and analyzed after 24 hours. The procedure included immunostaining for CD80, CD86, and K_b-$OVA_{257-264}$, as well as for viability. Flowcytometry was performed on a CytoFLEX S (Beckman Coulter). FACS data analysis was done using FlowJo software (Treestar). The gating strategy can be found in **Figure S5.13** and the results are shown in **Figure S5.14-S5.16**.

5.5.13 Isolation of CD4+ and CD8+ T cells from OT-II and OT-I mice

BMDCs were cultured as described above for 10 days, and pulsed for 4 hours with GNPs and GNRs or controls (PBS or free epitopes) followed by complete removal of the particles from the cell culture. Spleens were removed from OT-I or OT-II mice and strained through a 70-µm cell strainer to yield a single-cell suspension. Red blood cells (erythrocytes) were lysed with Ammonium-Chloride-Potassium (ACK) lysis buffer (0.15 M NH_4Cl, 1 mM $KHCO_3$, 0.1 mM Na_2EDTA; pH 7.3). CD8+ or CD4+ T cells were isolated *via* magnetic separation using a CD8+ or CD4+ T cell isolation kit according to

the supplier's protocol. Enriched T-cell fractions were stained with CFSE-FITC and then added to the plates with BMDCs in the ratio of 3:1 = specific T cells:BMDCs in complete RPMI 1640 medium (supplemented with 2 mM glutamine, 5% FCS, 100 U/mL penicillin/streptomycin, and 50 µM β-mercaptoethanol). T cells were left to proliferate for 72 hours in the same plates (37 °C, 5% CO_2). Cells were immunostained for Thy1.2, CD4 or CD8, CD25, as well as for viability, and analyzed by flow cytometry. FACS data analysis was done using FlowJo software. Each experiment was repeated three times, and a representative example is shown in **Figure 5.4**. The gating strategy can be found in **Figure S5.11**. The proliferation rate was expressed through a CD25+ cell subset showing lowered CFSE-FITC fluorescence of daughter (divided) cells. GraphPad Prism version 7.00 for Windows (GraphPad Software) was used to analyze the data and to plot the dose-response curves.

5.6 References

1. Lin, A. Y.; Lunsford, J.; Bear, A. S.; Young, J. K.; Eckels, P.; Luo, L.; Foster, A. E.; Drezek, R. A., High-density sub-100-nm peptide-gold nanoparticle complexes improve vaccine presentation by dendritic cells in vitro. *Nanoscale Res Lett* **2013,** *8*: e72.

2. Niikura, K.; Matsunaga, T.; Suzuki, T.; Kobayashi, S.; Yamaguchi, H.; Orba, Y.; Kawaguchi, A.; Hasegawa, H.; Kajino, K.; Ninomiya, T.; Ijiro, K.; Sawa, H., Gold Nanoparticles as a Vaccine Platform: Influence of Size and Shape on Immunological Responses *in Vitro* and *in Vivo*. *ACS Nano* **2013,** *7* (5), 3926-3938.

3. Climent, N.; Garcia, I.; Marradi, M.; Chiodo, F.; Miralles, L.; Maleno, M. J.; Gatell, J. M.; Garcia, F.; Penades, S.; Plana, M., Loading dendritic cells with gold nanoparticles (GNPs) bearing HIV-peptides and mannosides enhance HIV-specific T cell responses. *Nanomed-Nanotechnol* **2018,** *14* (2), 339-351.

4. Spicer, C. D.; Jumeaux, C.; Gupta, B.; Stevens, M. M., Peptide and protein nanoparticle conjugates: versatile platforms for biomedical applications. *Chem Soc Rev* **2018,** *47* (10), 3574-3620.

5. Chariou, P. L.; Ortega-Rivera, O. A.; Steinmetz, N. F., Nanocarriers for the Delivery of Medical, Veterinary, and Agricultural Active Ingredients. *ACS Nano* **2020,** *14* (3), 2678-2701.

6. Benne, N.; van Duijn, J.; Kuiper, J.; Jiskoot, W.; Slutter, B., Orchestrating immune responses: How size, shape and rigidity affect the immunogenicity of particulate vaccines. *J Control Release* **2016,** *234*, 124-134.

7. Foroozandeh, P.; Aziz, A. A., Insight into Cellular Uptake and Intracellular Trafficking of Nanoparticles. *Nanoscale Res Lett* **2018,** *13*: e339.

8. Rathore, B.; Sunwoo, K.; Jangili, P.; Kim, J.; Kim, J. H.; Huang, M. N.; Xiong, J.; Sharma, A.; Yang, Z. G.; Qu, J. L.; Kim, J. S., Nanomaterial designing strategies related to cell lysosome and their biomedical applications: A review. *Biomaterials* **2019,** *211*, 25-47.

9. Fifis, T.; Gamvrellis, A.; Crimeen-Irwin, B.; Pietersz, G. A.; Li, J.; Mottram, P. L.; McKenzie, I. F. C.; Plebanski, M., Size-dependent immunogenicity: Therapeutic and protective properties of nano-vaccines against tumors. *J Immunol* **2004,** *173* (5), 3148-3154.

10. Campbell, F.; Bos, F. L.; Sieber, S.; Arias-Alpizar, G.; Koch, B. E.; Huwyler, J.; Kros, A.; Bussmann, J., Directing Nanoparticle Biodistribution through Evasion and Exploitation of Stab2-Dependent Nanoparticle Uptake. *ACS Nano* **2018,** *12* (3), 2138-2150.

11. Goodman, C. M.; McCusker, C. D.; Yilmaz, T.; Rotello, V. M., Toxicity of gold nanoparticles functionalized with cationic and anionic side chains. *Bioconjugate Chem* **2004,** *15* (4), 897-900.

12. Sonavane, G.; Tomoda, K.; Makino, K., Biodistribution of colloidal gold nanoparticles after intravenous administration: Effect of particle size. *Colloid Surface B* **2008,** *66* (2), 274-280.

13. Zhang, Q.; Hitchins, V. M.; Schrand, A. M.; Hussain, S. M.; Goering, P. L., Uptake of gold nanoparticles in murine macrophage cells without cytotoxicity or production of pro-inflammatory mediators. *Nanotoxicology* **2011,** *5* (3), 284-295.

14. Alkilany, A. M.; Murphy, C. J., Toxicity and cellular uptake of gold nanoparticles: what we have learned so far? *J Nanopart Res* **2010,** *12* (7), 2313-2333.

15. De Jong, W. H.; Hagens, W. I.; Krystek, P.; Burger, M. C.; Sips, A. J. A. M.; Geertsma, R. E., Particle size-dependent organ distribution of gold nanoparticles after intravenous administration. *Biomaterials* **2008,** *29* (12), 1912-1919.

16. Kang, S.; Ahn, S.; Lee, J.; Kim, J. Y.; Choi, M.; Gujrati, V.; Kim, H.; Kim, J.; Shin, E. C.; Jon, S., Effects of gold nanoparticle-based vaccine size on lymph node delivery and cytotoxic T-lymphocyte responses. *J Control Release* **2017,** *256*, 56-67.

17. Xie, X. P.; Liao, J. F.; Shao, X. R.; Li, Q. S.; Lin, Y. F., The Effect of shape on Cellular Uptake of Gold Nanoparticles in the forms of Stars, Rods, and Triangles. *Sci Rep-Uk* **2017,** *7*: e3827.

18. Fytianos, K.; Rodriguez-Lorenzo, L.; Clift, M. J. D.; Blank, F.; Vanhecke, D.; von Garnier, C.; Petri-Fink, A.; Rothen-Rutishauser, B., Uptake efficiency of surface modified gold nanoparticles does not correlate with functional changes and cytokine secretion in human dendritic cells in vitro. *Nanomed-Nanotechnol* **2015,** *11* (3), 633-644.

19. Monikh, F. A.; Fryer, B.; Arenas-Lago, D.; Vijver, M. G.; Darbha, G. K.; Valsami-Jones, E.; Peijnenburg, W. J. G. M., A Dose Metrics Perspective on the Association of Gold Nanomaterials with Algal Cellsy. *Environ Sci Tech Let* **2019,** *6* (12), 732-738.

20. Chithrani, B. D.; Ghazani, A. A.; Chan, W. C. W., Determining the size and shape dependence of gold nanoparticle uptake into mammalian cells. *Nano Letters* **2006,** *6* (4), 662-668.

21. Ding, L.; Yao, C. J.; Yin, X. F.; Li, C. C.; Huang, Y. A.; Wu, M.; Wang, B.; Guo, X. Y.; Wang, Y. L.; Wu, M. H., Size, Shape, and Protein Corona Determine Cellular Uptake and Removal Mechanisms of Gold Nanoparticles. *Small* **2018,** *14* (42): e1801451.

22. Dreaden, E. C.; Alkilany, A. M.; Huang, X. H.; Murphy, C. J.; El-Sayed, M. A., The golden age: gold nanoparticles for biomedicine. *Chem Soc Rev* **2012,** *41* (7), 2740-2779.

23. Rabe, M.; Aisenbrey, C.; Pluhackova, K.; de Wert, V.; Boyle, A. L.; Bruggeman, D. F.; Kirsch, S. A.; Bockmann, R. A.; Kros, A.; Raap, J.; Bechinger, B., A Coiled-Coil Peptide Shaping Lipid Bilayers upon Fusion. *Biophys J* **2016,** *111* (10), 2162-2175.

24. Bhamidipati, M.; Fabris, L., Multiparametric Assessment of Gold Nanoparticle Cytotoxicity in Cancerous and Healthy Cells: The Role of Size, Shape, and Surface Chemistry. *Bioconjugate Chem* **2017,** *28* (2), 449-460.

25. Villiers, C. L.; Freitas, H.; Couderc, R.; Villiers, M. B.; Marche, P. N., Analysis of the toxicity of gold nano particles on the immune system: effect on dendritic cell functions. *J Nanopart Res* **2010,** *12* (1), 55-60.

26. Hocevar, S.; Milosevic, A.; Rodriguez-Lorenzo, L.; Ackermann-Hirschi, L.; Mottas, I.; Petri-Fink, A.; Rothen-Rutishauser, B.; Bourquin, C.; Clift, M. J. D., Polymer-Coated Gold Nanospheres Do Not Impair the Innate Immune Function of Human B Lymphocytes in Vitro. *ACS Nano* **2019,** *13* (6), 6790-6800.

27. Grabinski, C.; Schaeublin, N.; Wijaya, A.; D'Couto, H.; Baxamusa, S. H.; Hamad-Schifferli, K.; Hussain, S. M., Effect of Gold Nanorod Surface Chemistry on Cellular Response. *ACS Nano* **2011,** *5* (4), 2870-2879.

28. Halamoda-Kenzaoui, B.; Ceridono, M.; Urban, P.; Bogni, A.; Ponti, J.; Gioria, S.; Kinsner-Ovaskainen, A., The agglomeration state of nanoparticles can influence the mechanism of their cellular internalisation. *J Nanobiotechnol* **2017,** *15*: e48.

29. Egorova, E. A.; van Rijt, M. M. J.; Sommerdijk, N.; Gooris, G. S.; Bouwstra, J. A.; Boyle, A. L.; Kros, A., One Peptide for Them All: Gold Nanoparticles of Different Sizes Are Stabilized by a Common Peptide Amphiphile. *ACS Nano* **2020,** *14* (5), 5874-5886.

30. Levy, R.; Thanh, N. T. K.; Doty, R. C.; Hussain, I.; Nichols, R. J.; Schiffrin, D. J.; Brust, M.; Fernig, D. G., Rational and combinatorial design of

peptide capping Ligands for gold nanoparticles. *J Am Chem Soc* **2004,** *126* (32), 10076-10084.

31. Andresen, H.; Mager, M.; Griessner, M.; Charchar, P.; Todorova, N.; Bell, N.; Theocharidis, G.; Bertazzo, S.; Yarovsky, I.; Stevens, M. M., Single-Step Homogeneous Immunoassays Utilizing Epitope-Tagged Gold Nanoparticles: On the Mechanism, Feasibility, and Limitations. *Chem Mater* **2014,** *26* (16), 4696-4704.

32. Wang, Z.; Levy, R.; Fernig, D. G.; Brust, M., The peptide route to multifunctional gold nanoparticles. *Bioconjugate Chem* **2005,** *16* (3), 497-500.

33. Zhao, C. L.; Qiu, L. H.; Lv, P.; Han, A. L.; Fang, G. Z.; Liu, J. F.; Wang, S., AuNP-peptide probe for caspase-3 detection in living cells by SERS. *Analyst* **2019,** *144* (4), 1275-1281.

34. Murphy, K. M.; Heimberger, A. B.; Loh, D. Y., Induction by Antigen of Intrathymic Apoptosis of Cd4+Cd8+Tcrlo Thymocytes *In vivo*. *Science* **1990,** *250* (4988), 1720-1723.

35. Benne, N.; van Duijn, J.; Vigario, F. L.; Leboux, R. J. T.; van Veelen, P.; Kuiper, J.; Jiskoot, W.; Stutter, B., Anionic 1,2-distearoyl-sn-glycero-3-phosphoglycerol (DSPG) liposomes induce antigen-specific regulatory T cells and prevent atherosclerosis in mice. *J Control Release* **2018,** *291*, 135-146.

36. Didierlaurent, A. M.; Collignon, C.; Bourguignon, P.; Wouters, S.; Fierens, K.; Fochesato, M.; Dendouga, N.; Langlet, C.; Malissen, B.; Lambrecht, B. N.; Garcon, N.; Van Mechelen, M.; Morel, S., Enhancement of Adaptive Immunity by the Human Vaccine Adjuvant AS01 Depends on Activated Dendritic Cells. *J Immunol* **2014,** *193* (4), 1920-1930.

37. Miyagawa, F.; Gutermuth, J.; Zhang, H.; Katz, S. I., The use of mouse models to better understand mechanisms of autoimmunity and tolerance. *J Autoimmun* **2010,** *35* (3), 192-198.

38. Trombetta, E. S.; Mellman, I., Cell biology of antigen processing in vitro and in vivo. *Annu Rev Immunol* **2005,** *23*, 975-1028.

39. Mempel, T. R.; Henrickson, S. E.; von Andrian, U. H., T-cell priming by dendritic cells in lymph nodes occurs in three distinct phases. *Nature* **2004,** *427* (6970), 154-159.

40. Paulo, P. M. R.; Zijlstra, P.; Orrit, M.; Garcia-Fernandez, E.; Pace, T. C. S.; Viana, A. S.; Costa, S. M. B., Tip-Specific Functionalization of Gold Nanorods for Plasmonic Biosensing: Effect of Linker Chain Length. *Langmuir* **2017,** *33* (26), 6503-6510.

41. Chithrani, B. D.; Chan, W. C. W., Elucidating the mechanism of cellular uptake and removal of protein-coated gold nanoparticles of different sizes and shapes. *Nano Letters* **2007,** *7* (6), 1542-1550.

42. Hinterwirth, H.; Kappel, S.; Waitz, T.; Prohaska, T.; Lindner, W.; Lammerhofer, M., Quantifying Thiol Ligand Density of Self-Assembled Monolayers on Gold Nanoparticles by Inductively Coupled Plasma-Mass Spectrometry. *ACS Nano* **2013,** *7* (2), 1129-1136.

43. Huo, S. D.; Ma, H. L.; Huang, K. Y.; Liu, J.; Wei, T.; Jin, S. B.; Zhang, J. C.; He, S. T.; Liang, X. J., Superior Penetration and Retention Behavior of 50 nm Gold Nanoparticles in Tumors. *Cancer Res* **2013,** *73* (1), 319-330.

44. Sigma Aldrich Gold Nanoparticle Properties and Applications. sigmaaldrich.com/technical-documnets/articles/materials-science/nanomaterials/gold-nanoparticles.html (accessed 20 September 2020).

45. Hagglund, H. G.; McSweeney, P. A.; Mathioudakis, G.; Bruno, B.; Georges, G. E.; Gass, M. J.; Moore, P.; Sale, G. E.; Storb, R.; Nash, R. A., Ex vivo expansion of canine dendritic cells from CD34(+) bone marrow progenitor cells. *Transplantation* **2000,** *70* (10), 1437-1442.

46. Mager, I.; Langel, K.; Lehto, T.; Eiriksdottir, E.; Langel, U., The role of endocytosis on the uptake kinetics of luciferin-conjugated cell-penetrating peptides. *Bba-Biomembranes* **2012,** *1818* (3), 502-511.

47. Kalinski, P.; Hilkens, C. M. U.; Snijders, A.; Snijdewint, F. G. M.; Kapsenberg, M. L., IL-12-deficient dendritic cells, generated in the presence of prostaglandin E-2, promote type 2 cytokine production in maturing human naive T helper cells. *J Immunol* **1997,** *159* (1), 28-35.

48. Assis, N. R. G.; Caires, A. J.; Figueiredo, B. C.; Morais, S. B.; Mambelli, F. S.; Marinho, F. V.; Ladeira, L. O.; Oliveira, S. C., The use of gold nanorods as a new vaccine platform against schistosomiasis. *J Control Release* **2018,** *275*, 40-52.

49. Triplett, T. A.; Curti, B. D.; Bonafede, P. R.; Miller, W. L.; Walker, E. B.; Weinberg, A. D., Defining a functionally distinct subset of human memory CD4(+) T cells that are CD25(POS) and FOXP3(NEG). *Eur J Immunol* **2012,** *42* (7), 1893-1905.

50. Cohn, L.; Delamarre, L., Dendritic cell-targeted vaccines. *Front Immunol* **2014,** *5*: e255.

51. Gros, M.; Amigorena, S., Regulation of Antigen Export to the Cytosol During Cross-Presentation. *Front Immunol* **2019,** *10*: e41.

52. Mei, B. C.; Oh, E.; Susumu, K.; Farrell, D.; Mountziaris, T. J.; Mattoussi, H., Effects of Ligand Coordination Number and Surface Curvature on the Stability of Gold Nanoparticles in Aqueous Solutions. *Langmuir* **2009,** *25* (18), 10604-10611.

53. Nikoobakht, B.; El-Sayed, M. A., Preparation and growth mechanism of gold nanorods (NRs) using seed-mediated growth method. *Chem Mater* **2003,** *15* (10), 1957-1962.

54. Orendorff, C. J.; Murphy, C. J., Quantitation of metal content in the silver-assisted growth of gold nanorods. *J Phys Chem B* **2006,** *110* (9), 3990-3994.

55. Haiss, W.; Thanh, N. T. K.; Aveyard, J.; Fernig, D. G., Determination of size and concentration of gold nanoparticles from UV-Vis spectra. *Anal Chem* **2007,** *79* (11), 4215-4221.

5.7 Supporting Information

Co-assemblies of **base** and OVA epitope-decorated peptide amphiphiles **1** and **2** were β-structured in nature:

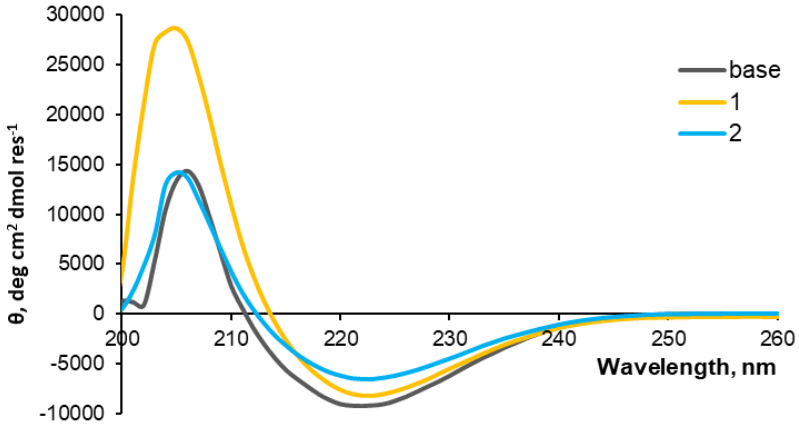

Figure S5.1. CD spectra showing that incorporation of 1 molar part of the active peptide amphiphile **1** or **2** does not affect the self-assembly behavior of the **base** peptide amphiphile: yellow line – 180 μM **base** + 20 μM **1**; blue line – 180 μM **base** + 20 μM **2**; gray line – 200 μM **base**. Samples were prepared in PBS (pH 7.2).

Size and surface charge of peptide amphiphile-coated GNPs and GNRs compared to citrate-stabilized GNPs and CTAB-stabilized GNRs:

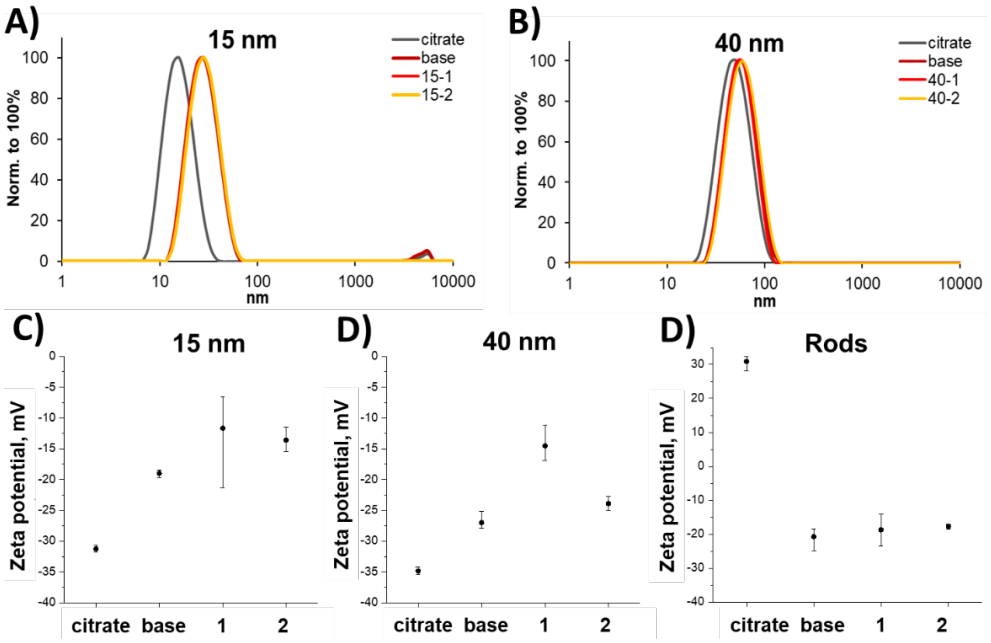

Figure S5.2. Sample characterization before and after modification obtained with DLS: (A) size distribution for 15 nm GNPs; (B) size distribution for 40 nm GNPs; (C) zeta potential values for 15 nm GNPs; (D) zeta potential values for 40 nm GNPs; (E) zeta potential values for GNRs. (A, B) samples were prepared in PBS (pH 7.2); (C-E) samples were prepared in PBS (pH 7.2) and diluted 10 times with MilliQ prior the measurement. Zeta potential is shown as a mean of three measurements with error bars indicating max and min values. Due to their shape, GNRs could not be analyzed for their hydrodynamic diameter.

GNP and GNR number concentrations were determined with ICP-MS:

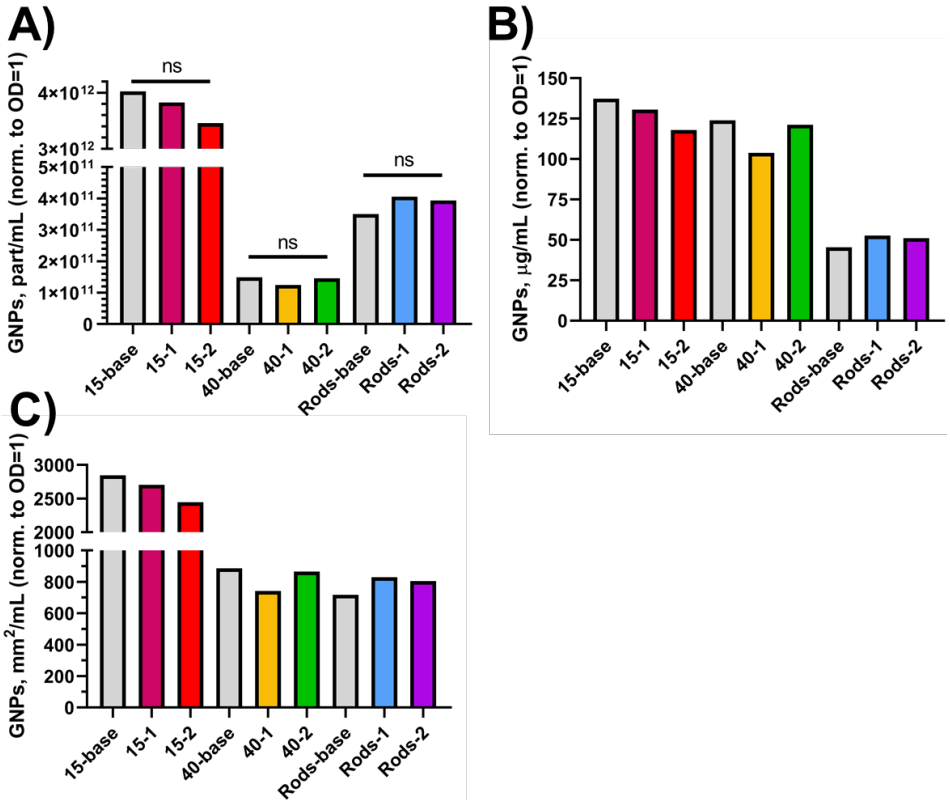

Figure S5.3. GNP and GNR chacteristics determined with ICP-MS and normalized to a suspension with an optical density of 1 (OD_{LSPR} = 1): (A) number concentration; (B) mass concentration; and (C) total gold surface available for contact as a function of volume. The mass concentration was measured once. To determine the significance of the difference between the concentrations of particles with the same gold core but different coating, a 10% deviation was introduced. According to a two-way ANOWA test performed in GraphPad Prism software, differences in metrics of nanoparticles comprising the same gold core, were found to be not significant (ns). Mass of one nanoparticle in ag: 15 nm GNPs = 34.1; 40 nm GNPs = 832.2; GNRs = 129.8. Surface area of one nanoparticle in nm^2: 15 nm GNPs = 706.86; 40 nm GNPs = 5944.7; GNRs = 2045.8.

Antigen loading was determined by UV-Vis with the help of a model peptide amphiphile **W**:

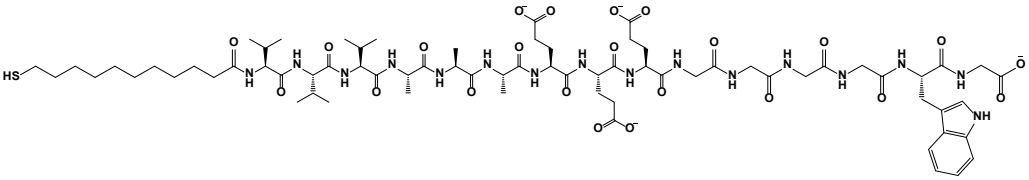

Scheme S5.1. Chemical structure of **W** used to determine coverage density and antigen loading onto different GNPs and GNRs.

Table S5.1. The ratio between optical density (OD) and GNP number concentration and epitope loading.

Gold core	Parameter	OD*	**base**	**1**	**2**
15 nm	Epitope μg/mL (OD=1)		n/a	2.52	4.2
	Epitope μg/mL (top conc.)	0.75	n/a	1.89	3.15
	Epitope ng in 50 μL** (top conc.)		n/a	94.5	157.5
	Number part/mL (OD=1)		4.03E+12	3.83E+12	3.46E+12
	Number part/mL (top conc.)	0.75	3.02E+12	2.87E+12	2.59E+12
	Particles in 50 μL (top conc.)		1.51E+11	1.44E+11	1.3E+11
40 nm	Epitope μg/mL (OD=1)		n/a	0.414	0.891
	Epitope μg/mL (top conc.)	1.00	n/a	0.414	0.891
	Epitope ng in 50 μL (top conc.)		n/a	20.7	44.5
	Number part/mL (OD=1)		1.49E+11	1.25E+11	1.46E+11
	Number part/mL (top conc.)	1.00	1.49E+11	1.25E+11	1.46E+11
	Particles in 50 μL (top conc.)		7.45E+09	6.24E+09	7.28E+09
GNRs	Epitope μg/mL (OD=1)		n/a	0.611	1.09
	Epitope μg/mL (top conc.)	1.94	n/a	1.19	2.12
	Epitope ng in 50 μL (top conc.)		n/a	59.3	105.8
	Number part/mL (OD=1)		3.50E+11	4.06E+11	3.93E+11
	Number part/mL (top conc.)	1.94	7.01E+11	7.87E+11	7.63E+11
	Particles in 50 μL (top conc.)		3.50E+10	3.93E+10	3.82E+10

*- Top conc. = top concentration used throughout this study. In the text this is also denoted as 1x dilution. **- 50 μL was the volume of a sample dose per well added to BMDCs during cell experiments. Total well volume was 200 μL. Cell number varied from $10^{*}10^{3}$ to $50^{*}10^{3}$ per well depending on the assay. For full details, see **5.5** Experimental section.

The GNP and GNR concentration range used in this study was as follows:

Table S5.2. GNP and GNR concentration range used for cell experiments.

Dilution	15-1	15-2	40-1	40-2	Rods-1	Rods-2
	Epitope dosage, ng in 50 µL*					
1x **	94.5	157.5	20.7	44.5	59.3	105.8
2x	47.3	78.7	10.3	22.3	29.6	52.9
4x	23.6	39.4	5.2	11.1	14.8	26.5
8x	11.8	19.7	2.6	5.6	7.4	13.2
16x	5.9	9.8	1.3	2.8	3.7	6.6
	Particle number in 50 µL					
1x	1.44E+11	1.30E+11	1.25E+11	1.46E+11	4.06E+11	3.93E+11
2x	7.18E+10	6.48E+10	6.24E+10	7.28E+10	2.03E+11	1.97E+11
4x	3.59E+10	3.24E+10	3.12E+10	3.64E+10	1.01E+11	9.83E+10
8x	1.79E+10	1.62E+10	1.56E+10	1.82E+10	5.07E+10	4.92E+10
16x	8.97E+09	8.11E+09	7.80E+09	9.10E+09	2.53E+10	2.46E+10

*- 50 µL was the volume of a sample dose per well added to BMDCs during cell experiments. Total well volume was 200 µL. Cell number varied from $10^{*}10^{3}$ to $50^{*}10^{3}$ per well depending on the assay. **- top concentration used throughout this study. In the text this is also denoted as 1x dilution. For detail, see **5.5** Experimental section.

Peptide amphiphile-coated GNPs and GNRs did not cause cytotoxicity:

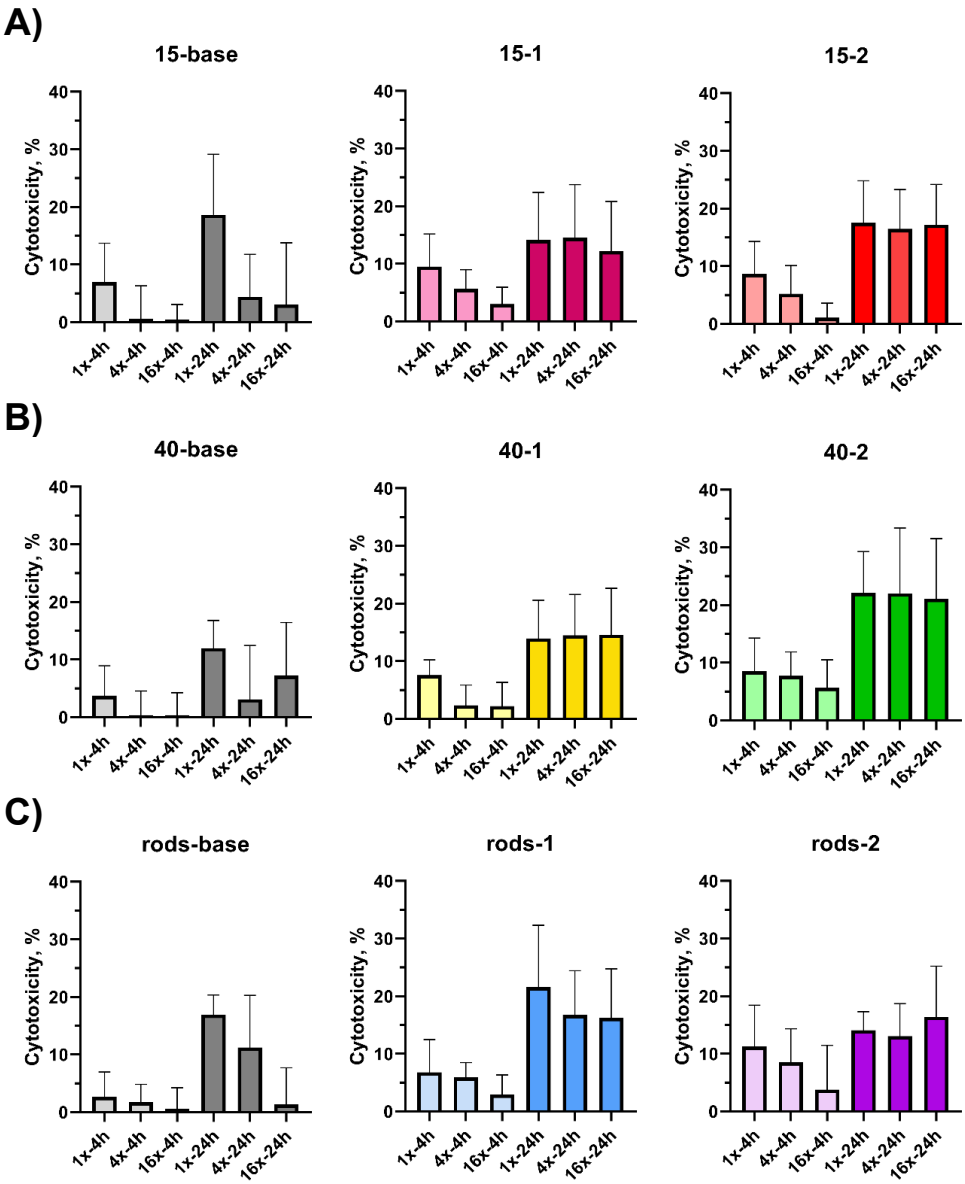

Figure S5.4. Cytotoxicity evaluated with an LDH release assay for: (panel A) 15 nm GNPs, (panel B) 40 nm GNPs, and (panel C) GNRs. GNP concentration range analyzed involved 1x, 4x, and 16x times diluted samples (**Table S5.2**). Lighter color shades indicate 4 h exposure time; darker shades – 24 h exposure time. Error bars indicate standard deviations and were calculated using GraphPad Prism software.

Subcellular localization of internalized GNPs and GNRs was assessed with TEM:

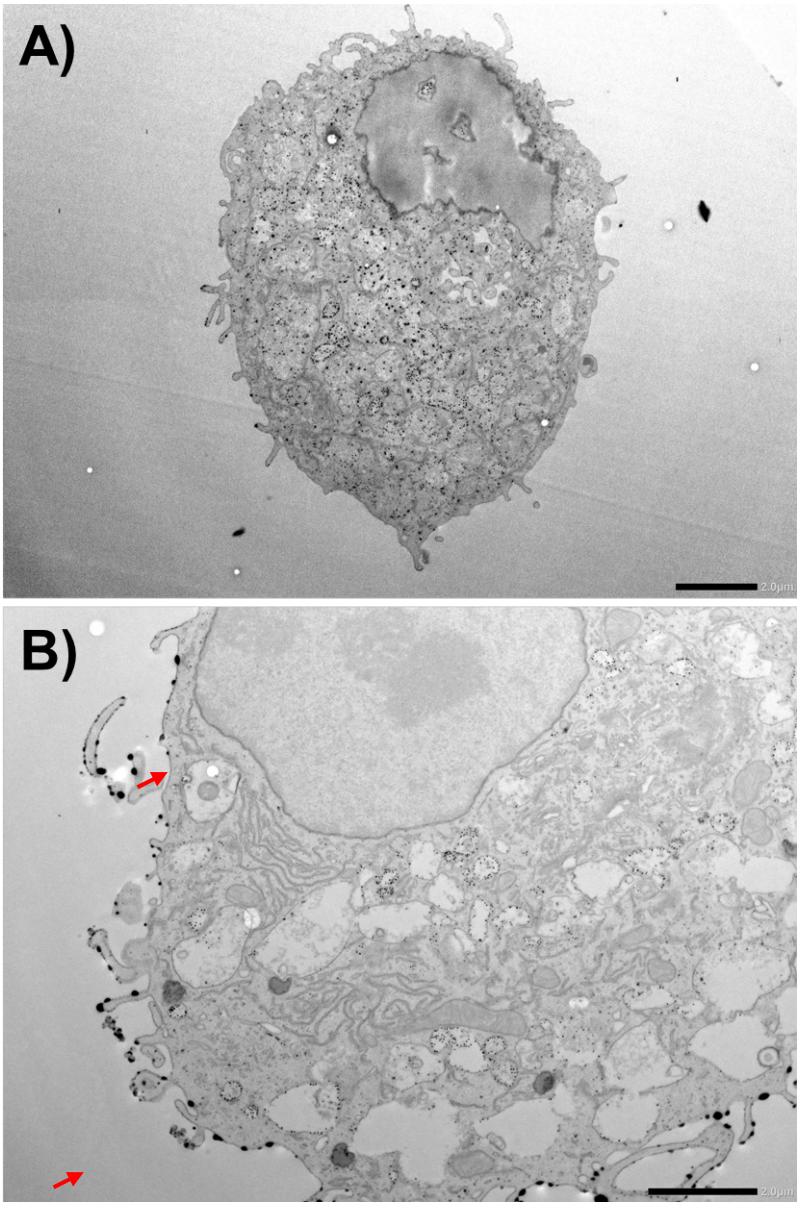

Figure S5.5A,B. TEM micrographs of cell sections: (A) BMDCs exposed to **15-1** and (B) BMDCs exposed to **15-2**. Scale bars = 2 µm. The round dark crystals on the outer side of the cell membrane are accumulations of the OsO_4 staining (indicated by arrows).

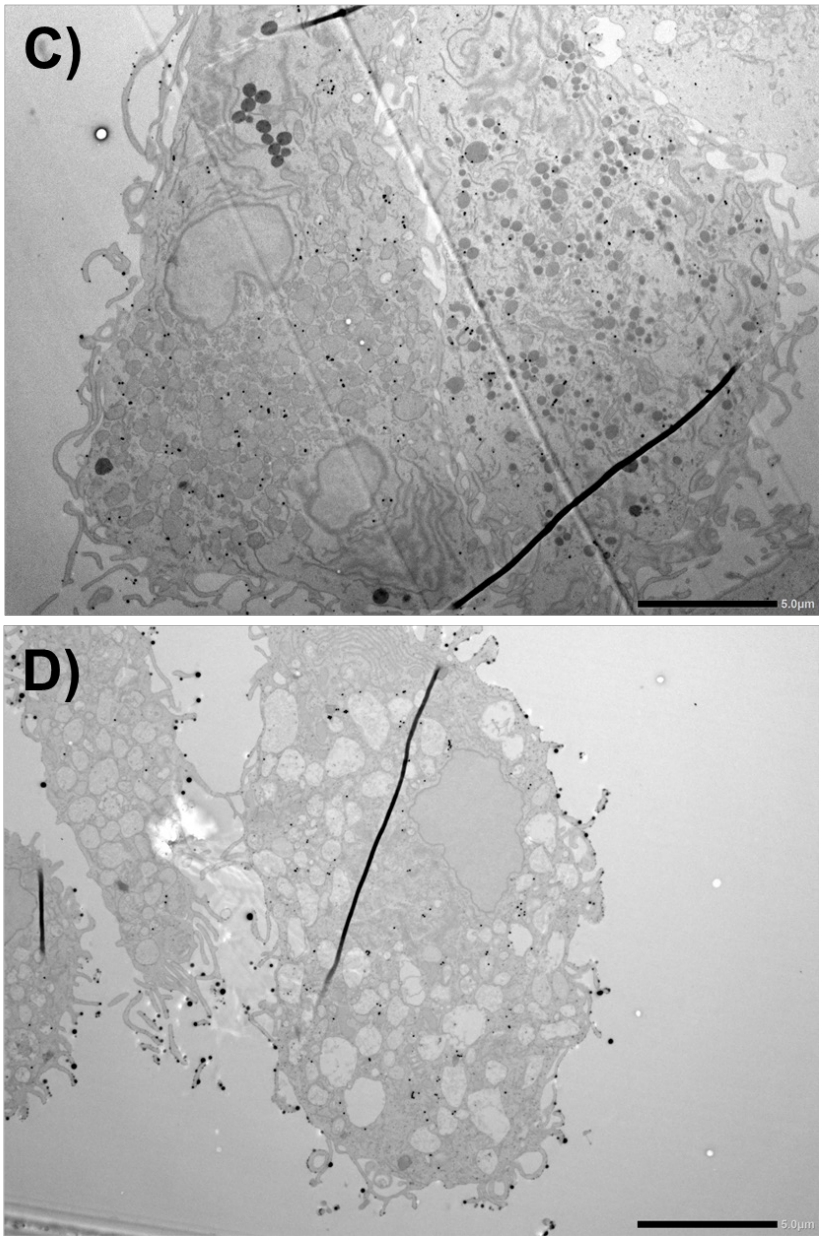

Figure S5.5C,D. TEM micrographs of cell sections: (C) BMDCs exposed to **40-1** and (D) BMDCs exposed to **40-2**. Scale bars = 5 µm. The round dark crystals on the outer side of the cell membrane are the accumulations of the OsO_4 staining.

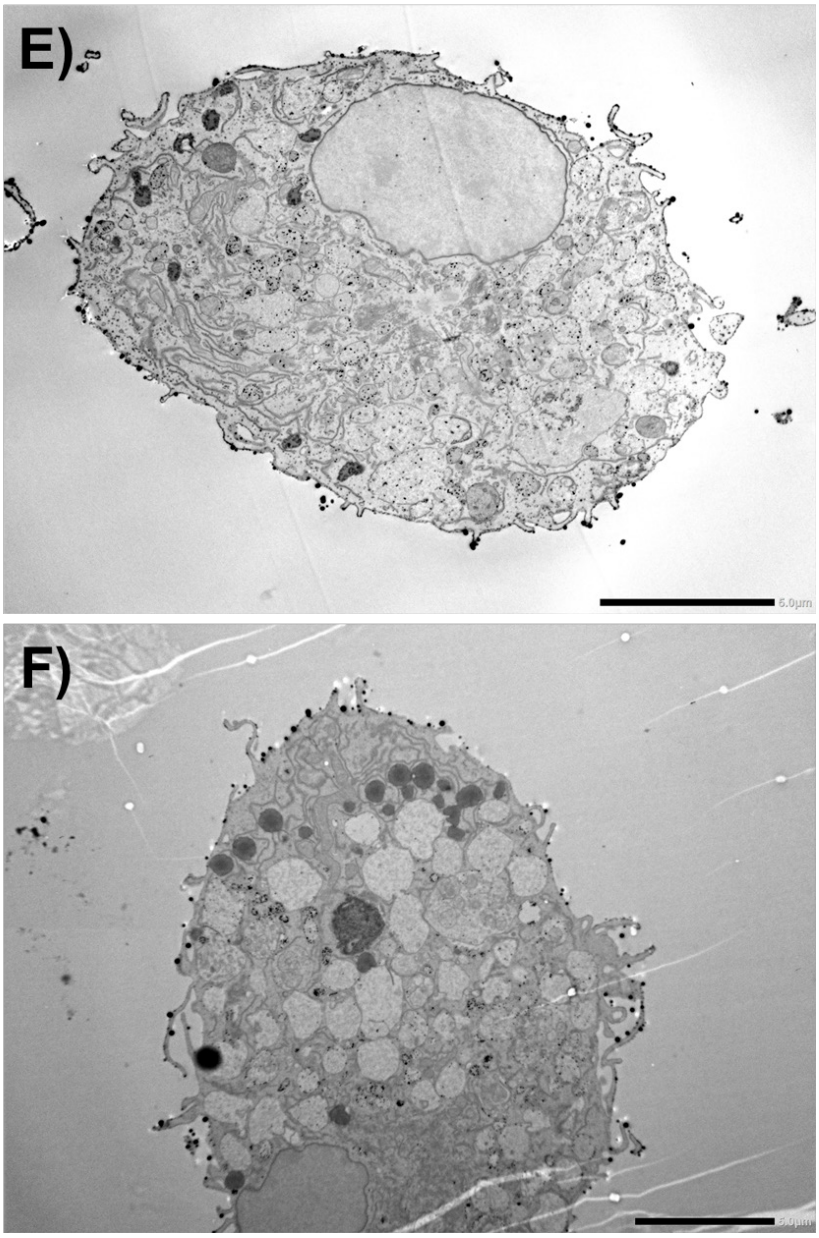

Figure S5.5E,F. TEM micrographs of cell sections: (E) BMDCs exposed to **Rods-1** and (F) DBMCs exposed to **Rods-2**. Scale bars = 5 μm. The round dark crystals on the outer side of the cell membrane are the accumulations of the OsO_4 staining.

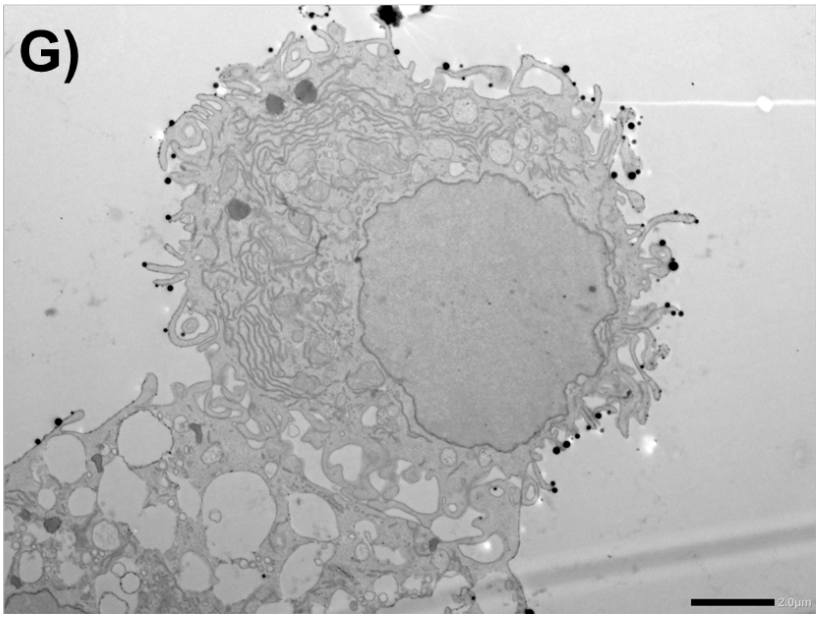

Figure S5.5G. TEM micrograph of a cell section: (G) BMDCs treated with PBS. Scale bars = 2 µm. The round dark crystals on the outer side of cell membrane are the accumulations of the OsO_4 staining.

TEM analysis of subcellular vesicles revealed differences between the uptake of GNPs of different shape and size by BMDCs:

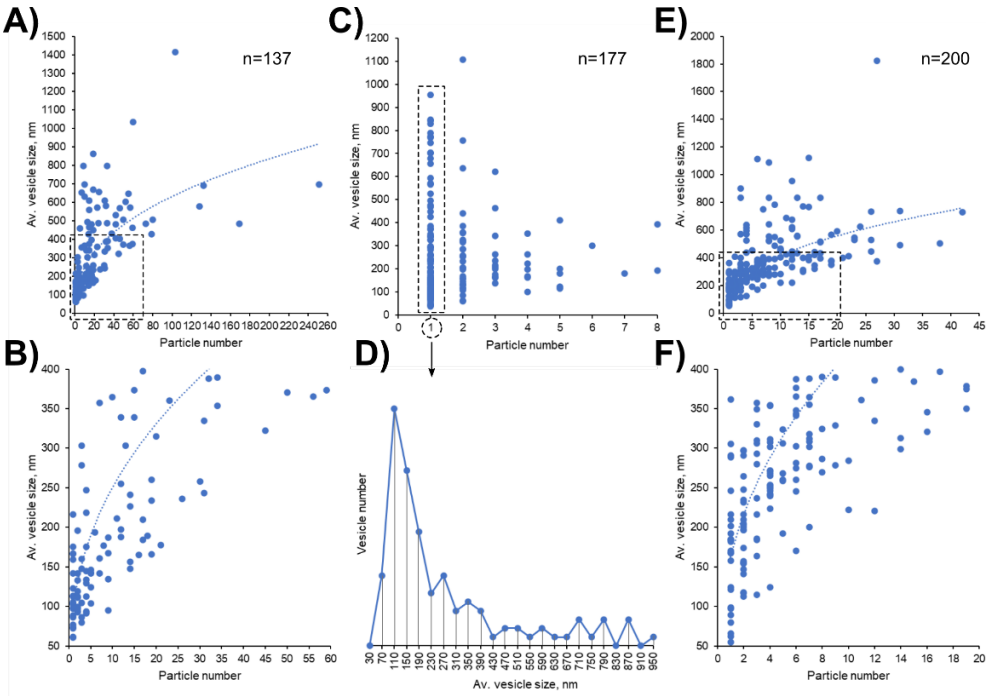

Figure S5.6. TEM analysis of BMDC sections based on average vesicle size and number of entrapped nanoparticles for: (A-B) **15-1**, (C-D) **40-1**, and (C) **Rods-1**. It was not possible to determine the vesicle type based solely on the TEM imaging. Vesicle types observed in this study were hypothesized to be different stages of endosomes, lysosomes, autophagosomes *etc*. (D) shows the size distribution of vesicles with 1 entrapped particle of **40-1**: it is suspected that endocytic vesicles have a size range of 40-120 nm.

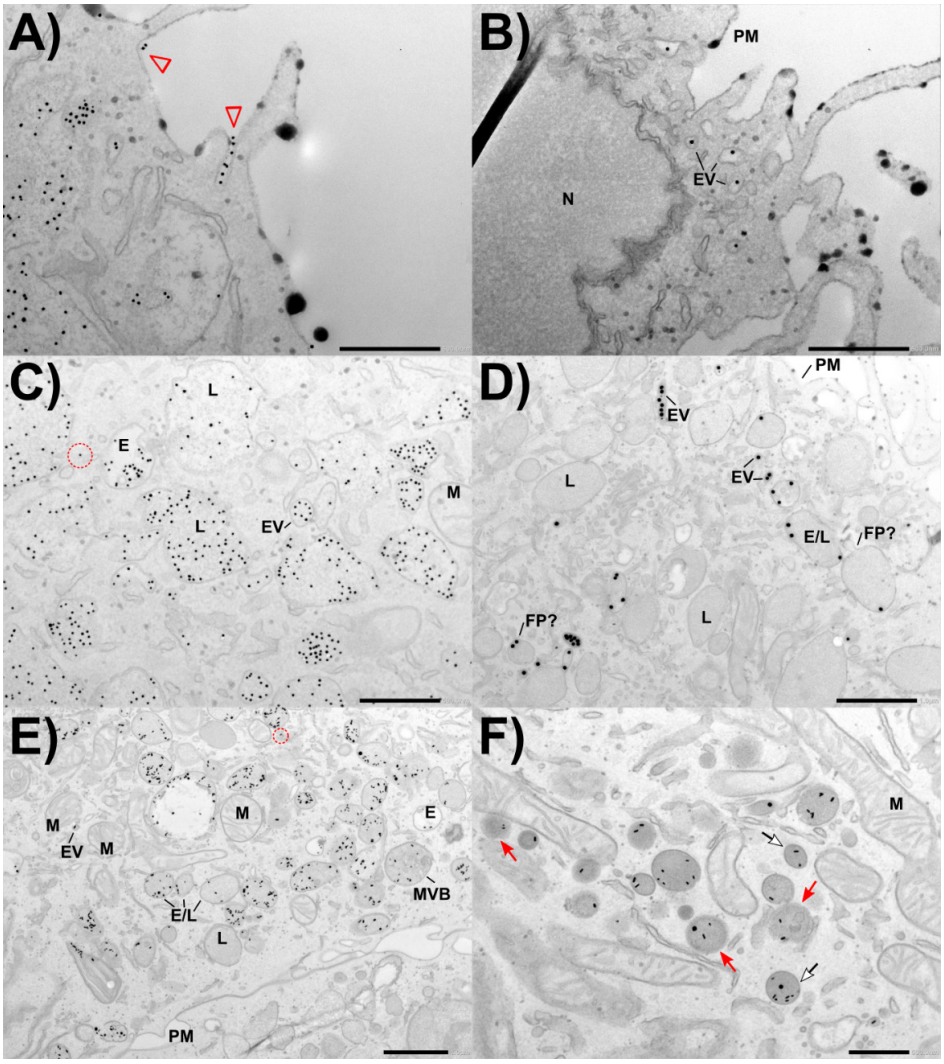

Figure S5.7. TEM images of a BMDC section: (A-C) DCs exposed to **15-1**; (D) DCs exposed to **40-1**; and (E,F) DCs exposed to **R-1**. These images show the subcellular localization of endocytosed GNPs and GNRs: EV = endocytic vesicle; E = endosome; L = lysosome; MVB = multivesicular body. Other cellular organelles present are: M = mitochondria; N = nucleus; PM = plasma membrane. It is possible that fusion pores (FP) formed by two vesicles were captured in (D). Red triangles indicate the potential entry of GNPs into the cells in panel (A). Red circles indicate GNPs and GNRs escaped into the cytosol in (C, E). Red arrows indicate vesicles with rough membranes and empty black arrows indicate vesicles with smooth membranes in panel (F). Scale bars = 1 μm (D,E) and 500 nm (A-C,F). The round dark crystals on the outer side of cell membrane are a result of the accumulation of stain (A,B).

Cellular uptake of epitope-coated GNPs and GNRs was quantified with ICP-MS:

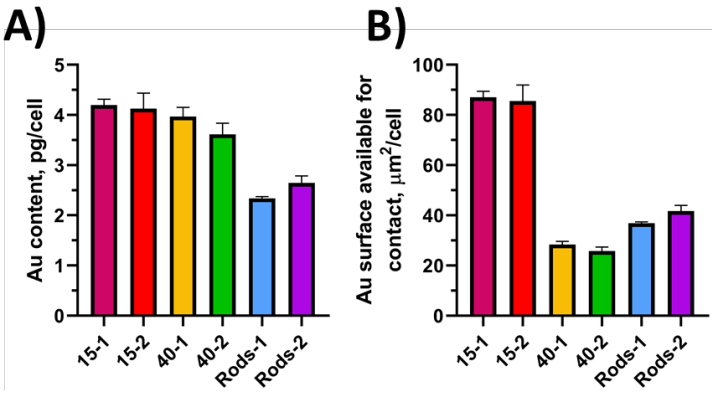

Figure S5.8. Quantification of cellular uptake visualized with TEM and shown in **Figure S5.4**. Quantification is based on ICP-MS data: (A) mean gold content in pg per cell; and (B) mean delivered gold surface available for contact in μm^2 per cell. Each column indicates a mean of three measurements; error bars indicate standard deviations and were calculated using GraphPad Prism software. More detail can be found in **Table S5.3**.

Activation of BMDCs by epitope-coated GNPs and GNRs through IL-12 and IL-1β secretion was tested with ELISA:

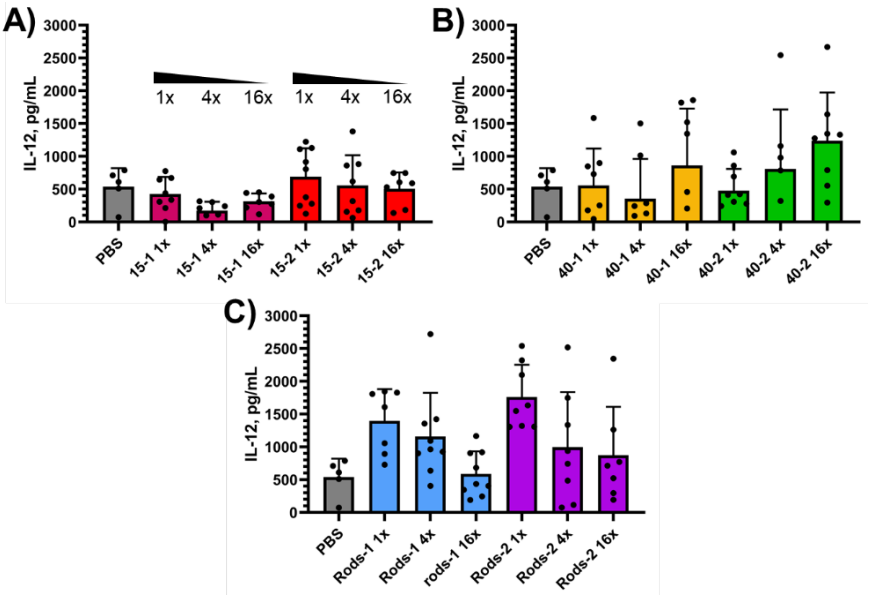

Figure S5.9. IL-12 levels in the cell culture supernatants of BMDCs after 24 h exposure to different GNPs: (A) GNPs with a 15 nm core; (B) GNPs with a 40 nm core; and (C) GNRs with a rod-like core of 45 by 15 nm in size. The BMDCs that were given PBS instead of GNPs or GNRs are present for comparison (gray color). The GNP concentration range analyzed included 1x, 4x, and 16x times diluted samples (**Table S5.2**).

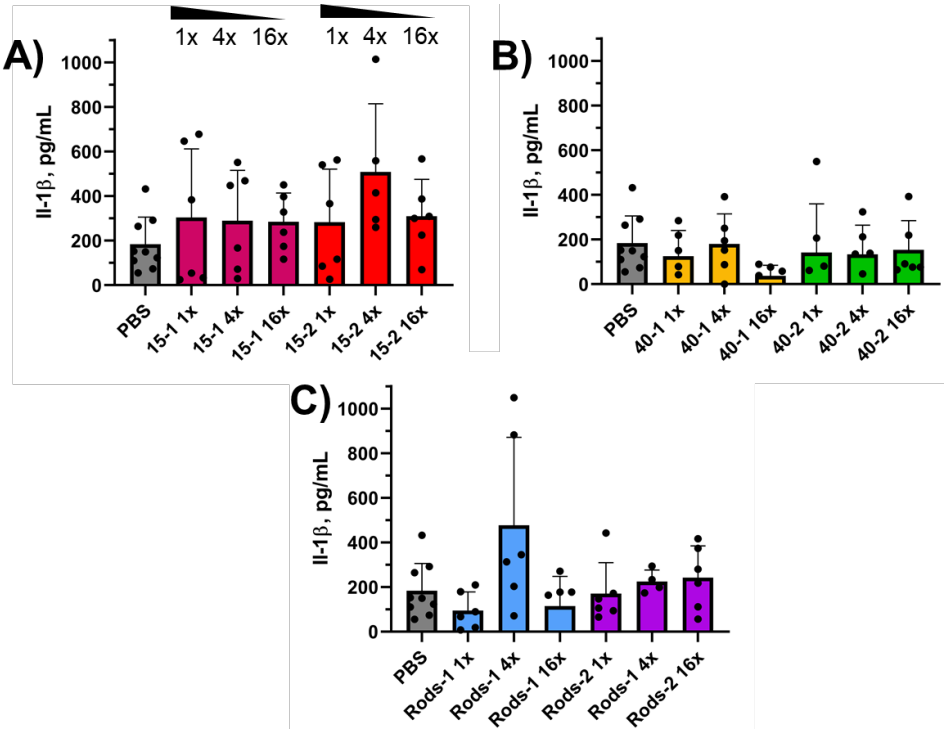

Figure S5.10. IL-1β levels in the cell culture supernatants of BMDCs after 24 h exposure to different GNPs: (A) GNPs with a 15 nm core; (B) GNPs with a 40 nm core; and (C) GNRs with a rod-like core of 45 by 15 nm in size. The BMDCs that were given PBS instead of GNPs or GNRs are present for comparison (gray color). GNP concentration range analyzed included 1x, 4x, and 16x times diluted samples (**Table S5.2**).

Activation of CD8+ and CD4+ T cells isolated from OT-I and OT-II mice by epitope-coated GNPs and GNRs was monitored with FACS according to the following gating strategy:

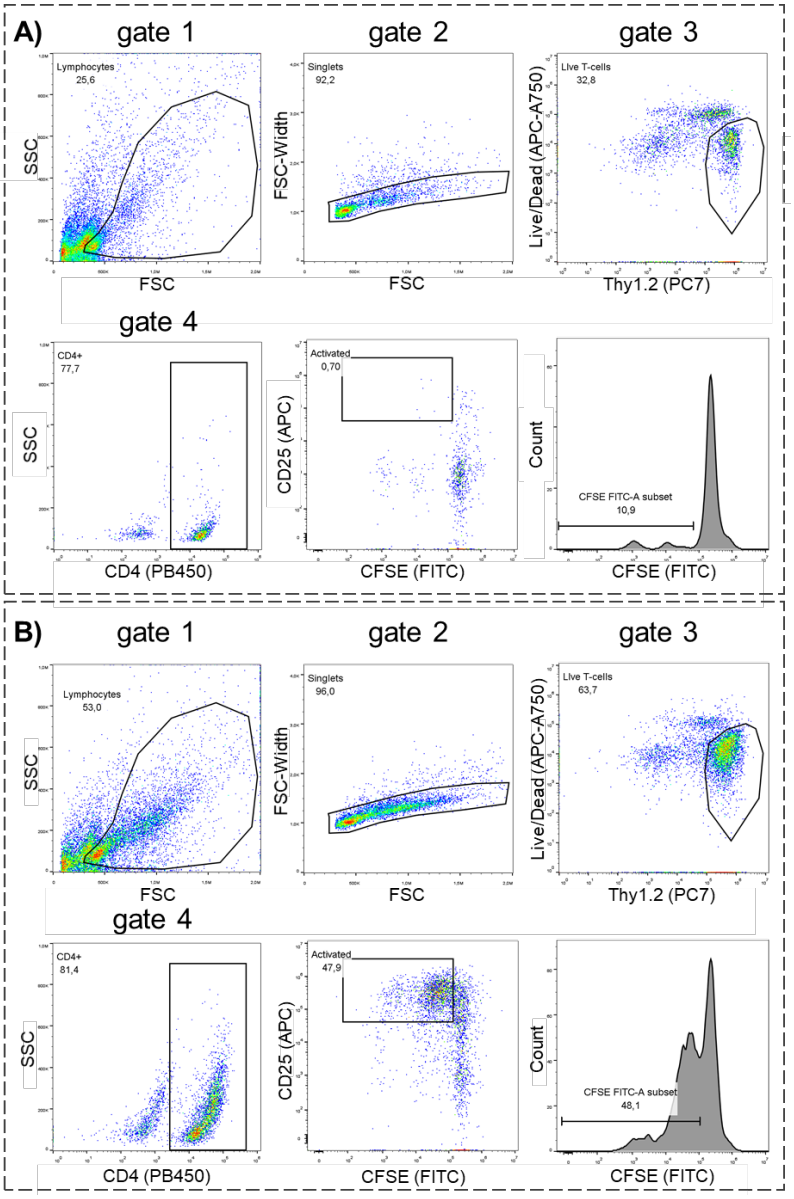

Figure S5.11. FACS gating strategy for OT-I and OT-II mice *ex vivo* experiments: (panel A) negative control – PBS and (panel B) positive control – 20 ng/well $OVA_{323-339}$. Data were analyzed on the area basis. Values for $CD25^{+}$ *versus* $CFSE^{low}$ are shown in **Figure 5.4, 5.5**.

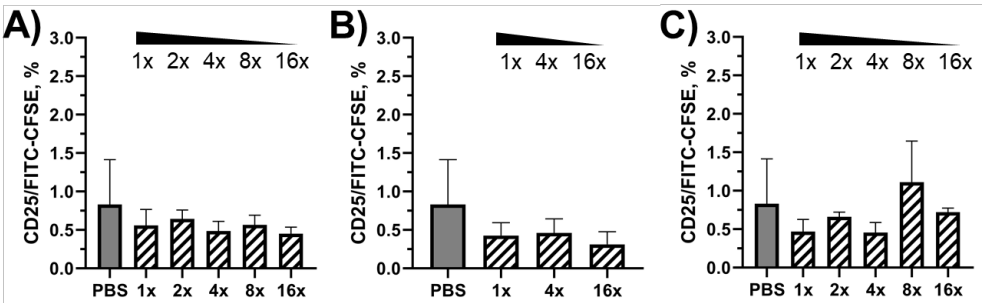

Figure S5.12. T-cell proliferation profiles of GNPs and GNRs coated with the **base** sequence (bearing no epitopes): (A) GNPs with a 15 nm core; (B) GNPs with a 40 nm core; and (C) GNRs with a rod-like core of 45 by 15 nm. Data represent a combined effect on both OT-I and OT-II derived T-cells. The BMDCs that were given PBS instead of GNPs or GNRs are present for comparison (gray color). GNP concentrations analyzed were 1x, 4x, and 16x (for 40 nm core) and 1x, 2x, 4x, 8x, and 16x (for 15 nm GNPs and GNRs) times diluted samples (**Table S5.2**).

Activation of BMDCs by epitope-decorated GNPs and GNRs through upregulation of cellular CD80, CD86, and MHC-I/$OVA_{257-264}$ markers:

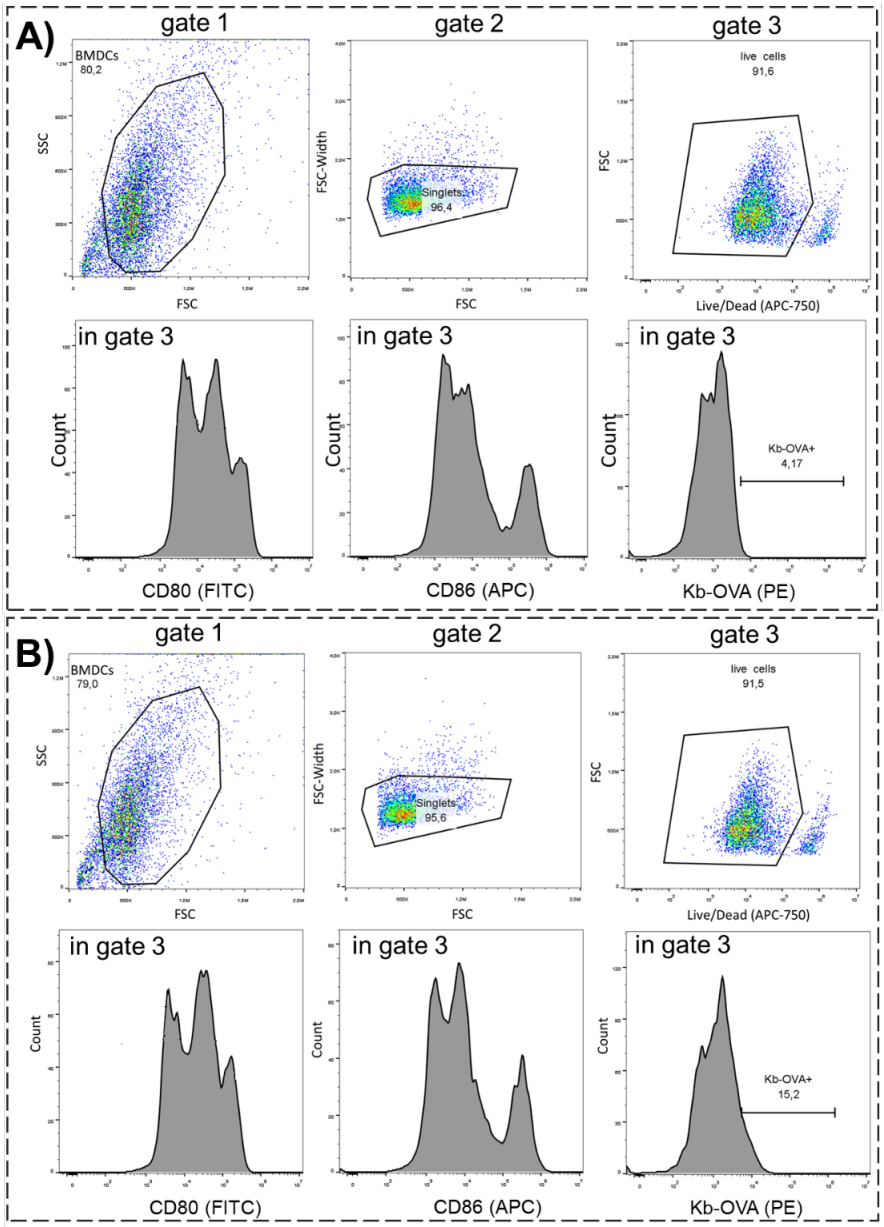

Figure S5.13. Gating strategy used in FACS analysis of BMDCs activation by epitope-decorated GNPs and GNRs. (panel A) negative control – DMEM medium and (panel B) positive control – 40 ng/well $OVA_{257-264}$. Data were analyzed on the basis of area.

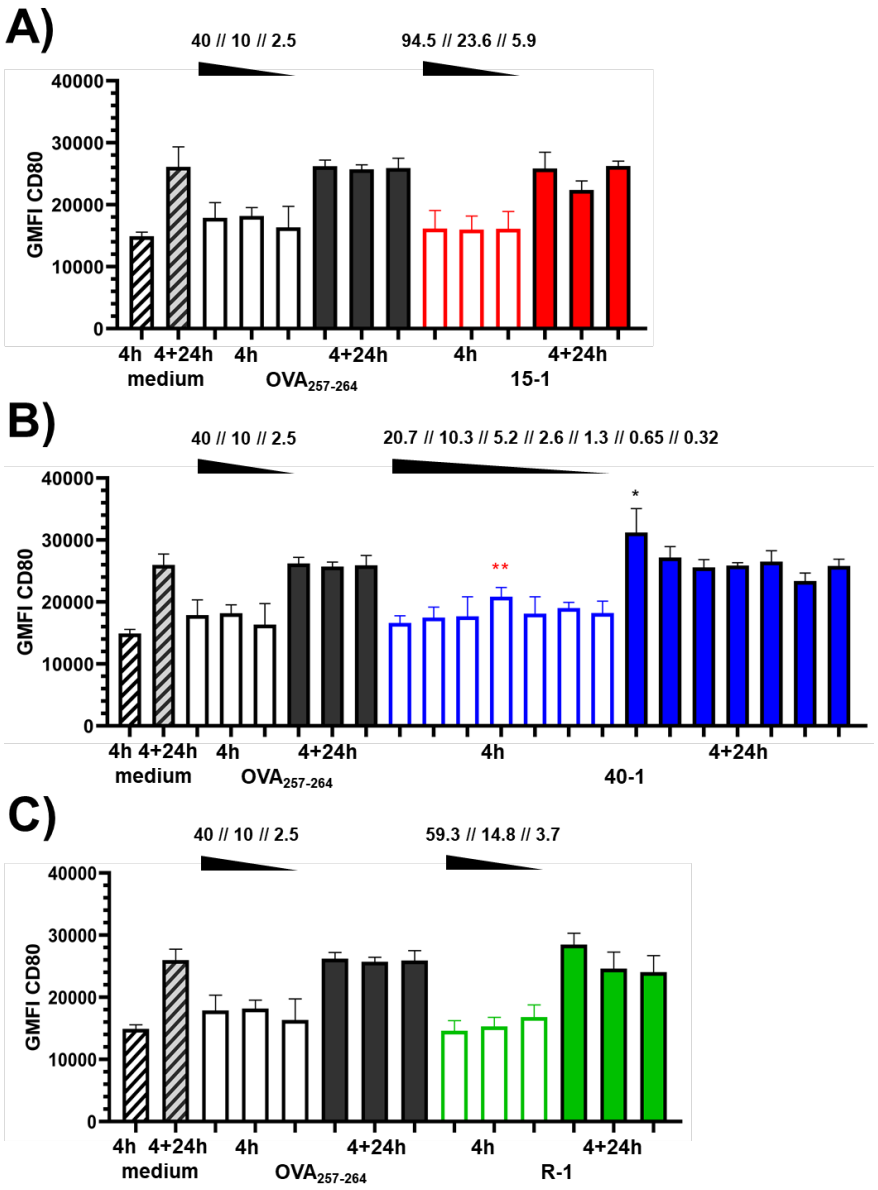

Figure S5.14. BMDCs activation was monitored through upregulation of CD80 cellular marker after a 4-hour incubation with GNPs and GNRs. Geometric mean fluorescence intensity (GMFI) gained for different samples was compared to the negative control (medium) and positive control ($OVA_{257-264}$): (A) **15-1**, (B) **40-1**, and (C) **R-1**. Empty columns show data right after the 4-hour incubation, and solid columns – after 24 hours after the incubation. Epitope dosage per well (in ng/well) is shown above the ◣ indicator.

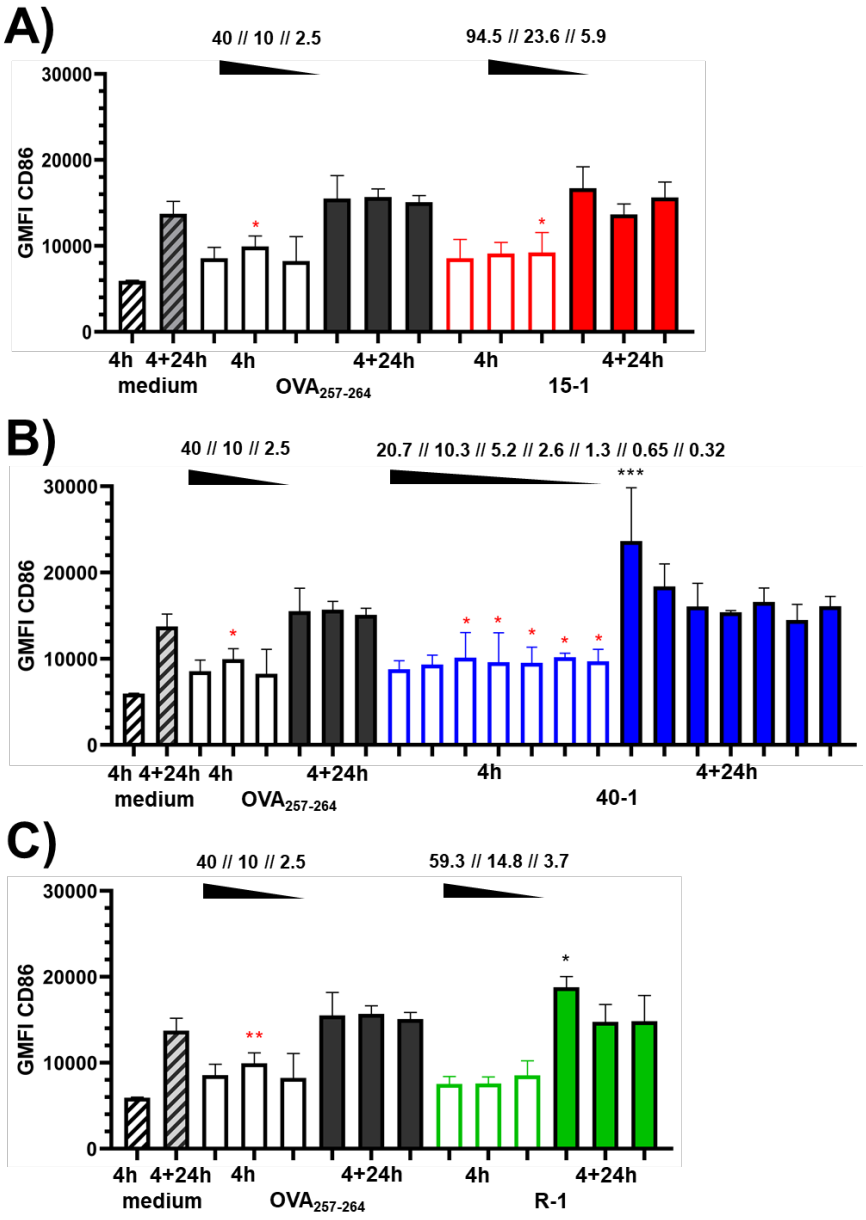

Figure S5.15. BMDCs activation was monitored through upregulation of CD86 cellular marker after a 4-hour incubation with GNPs and GNRs. Geometric mean fluorescence intensity (GMFI) gained for different samples was compared to the negative control (medium) and positive control ($OVA_{257-264}$): (A) **15-1**, (B) **40-1**, and (C) **R-1**. Empty columns show data right after the 4-hour incubation, and solid columns – after 24 hours after the incubation. Epitope dosage per well (in ng/well) is shown above the ◣ indicator.

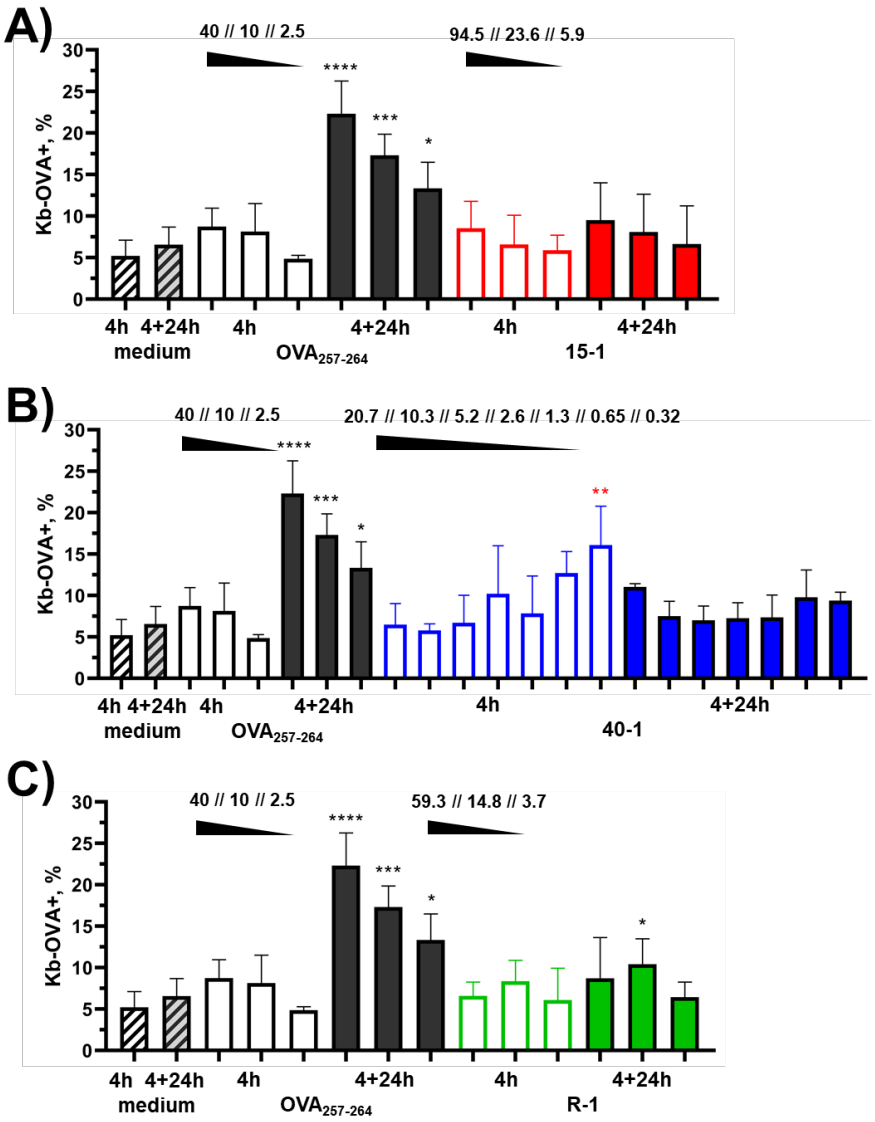

Figure S5.16. BMDCs activation was monitored through expression of MHC-I/$OVA_{257-264}$ complex on the cell surface after a 4-hour incubation with GNPs and GNRs. Geometric mean fluorescence intensity (GMFI) gained for different samples was compared to the negative control (medium) and positive control ($OVA_{257-264}$): (A) **15-1**, (B) **40-1**, and (C) **R-1**. Empty columns show data right after the 4-hour incubation, and solid columns – after 24 hours after the incubation. Epitope dosage per well (in ng/well) is shown above the ◣ indicator.

Purity of the peptide and peptide amphiphile compounds was determined by LC-MS:

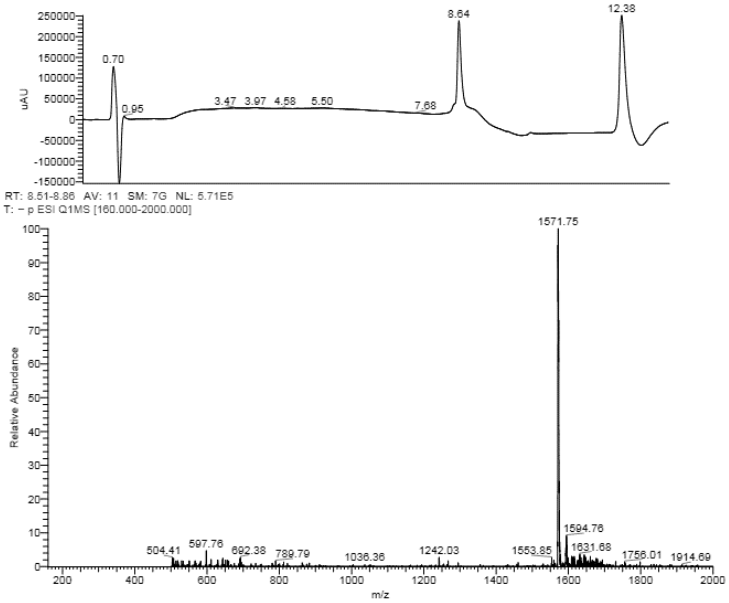

Figure S5.17. LC-MS spectrum for **base**. $[M-H]^{1-}_{theor}$ = 1571.83.

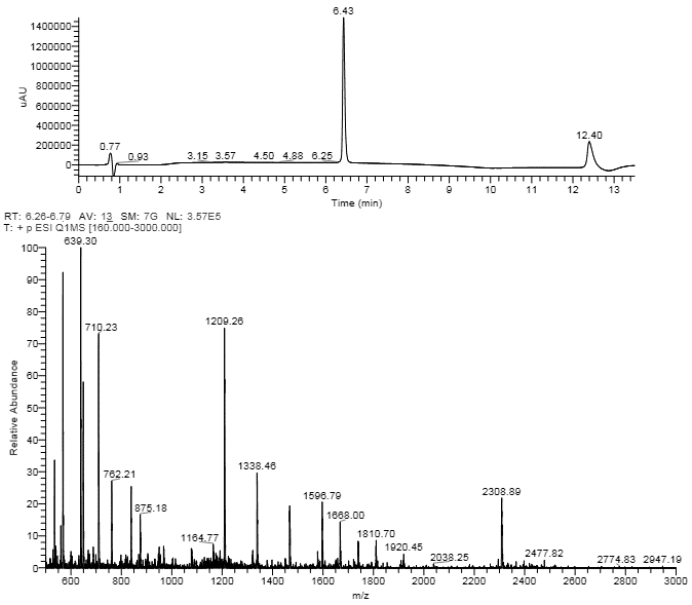

Figure S5.18. LC-MS spectrum for **1**. $[M+H]^{1+}_{theor}$ = 2309.26.

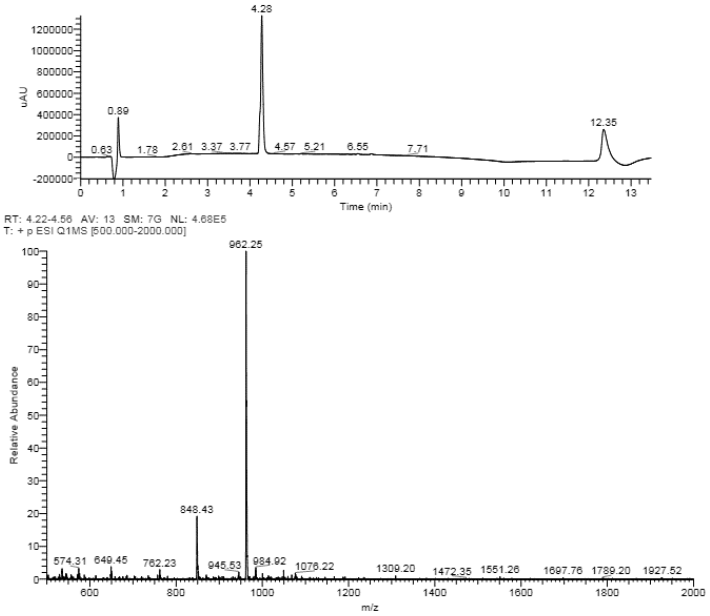

Figure S5.19. LC-MS spectrum for $OVA_{257-264}$. $[M+H]^{1+}_{theor}$ = 962.54. $[M+H]^{1+}$ = 848.43 belongs to $OVA_{257-264}$ with a deletion of one isoleucine (I, Ile).

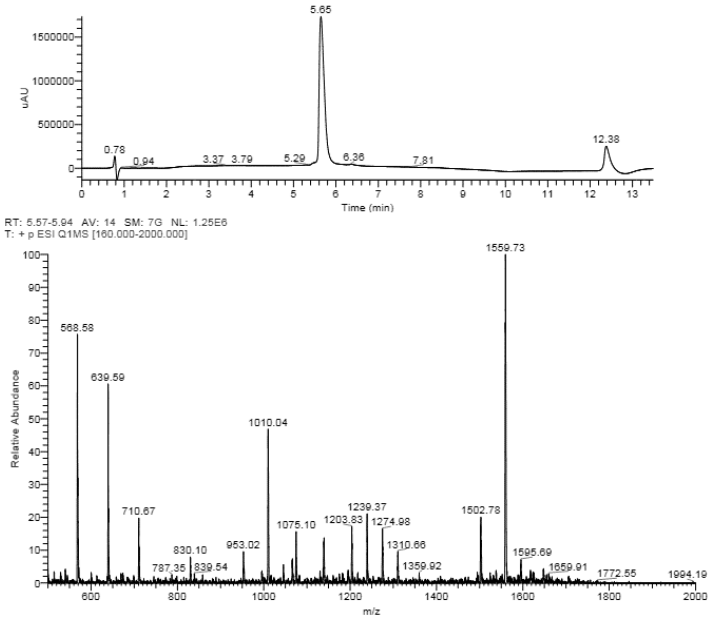

Figure S5.20. LC-MS spectrum for **2**. $[M+2H]^{2+}_{theor}$ = 1559.81.

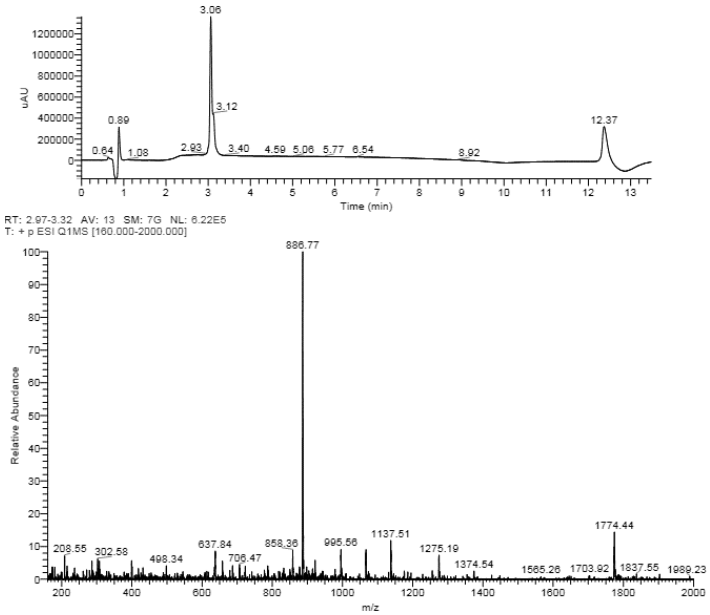

Figure S5.21. LC-MS spectrum for $OVA_{323-339}$. $[M+H]^{1+}_{theor}$ = 1773.90 and $[M+2H]^{2+}_{theor}$ = 887.45.

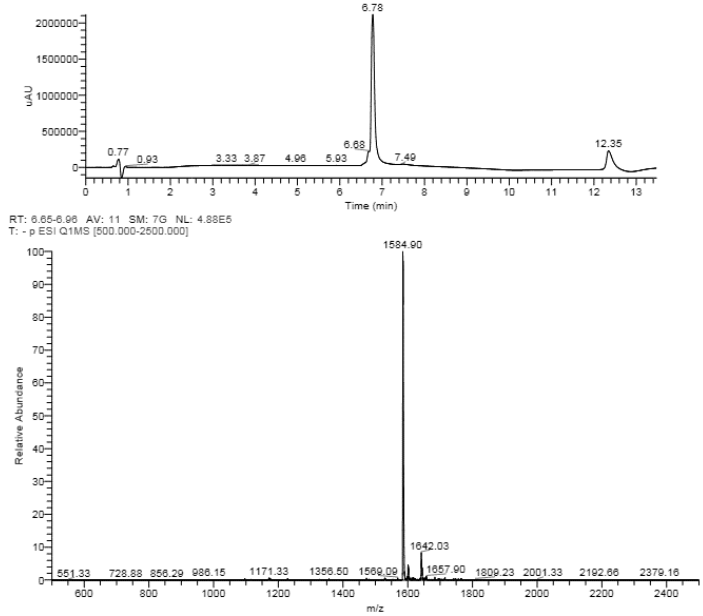

Figure S5.22. LC-MS spectrum for **W**. $[M-H]^{1-}_{theor}$ =1585.75.

CHAPTER 6

Summary and Perspectives

Gold nanoparticles (GNPs) are metallic nanoparticles that are facile to synthesize, have controllable shapes and sizes, are easy to functionalize, and possess extraordinary optical properties. Due to these characteristics, GNPs are extremely attractive tools for use in a multitude of applications spanning nanophotonics to sensing, to the treatment of autoimmune diseases. One major drawback is that their inherent instability under physiological conditions prevents their widespread use. It was previously shown that coating GNPs with biocompatible molecules can significantly reduce both their aggregation and cytotoxicity. However, commonly used silica or polymer coatings are not optimal due to the fact that surface functionalization, with therapeutic moieties for example, is not straightforward. Additionally, the thickness of these coatings is typically high, which is a disadvantage when GNPs are intended for use in sensing, for instance. A solution to this is to stabilize GNPs with peptides. A set of cysteine-containing oligopeptides has been developed to tackle this task. The cysteine side chain binds to the gold surface to form an Au-S bond, and the rest of the sequence self-assembles on the gold surface yielding β-sheet-like secondary structures. These oligopeptides possess a net negative charge, which induces electrostatic repulsion of individual GNPs, ensuring colloidal stability. Unfortunately, these oligopeptides have only been used to stabilize small (≤30 nm) spherical GNPs and reports of stabilization of larger GNPs, or other shapes, are not available. We have demonstrated this approach can be revised to create a peptide-based stabilizer suitable for a wide range of GNP shapes and size by using peptide amphiphiles. These molecules possess the features necessary for effective stabilization of gold surfaces: β-structured self-assembly behavior and a high net charge. Moreover, it was suggested that hydrophobic interactions between alkyl chains can contribute to the stabilizing effect of these peptide amphiphiles. This thesis has designed a series of peptide amphiphiles and characterized

their self-assembly properties, before exploring their suitability as coatings for GNPs of different shapes and sizes. Finally, the functionalization of the peptide amphiphiles was demonstrated to evaluate cellular immune responses to different GNPs.

To make peptide amphiphiles suitable for binding to a gold surface, the molecules had to be functionalized with a thiol group (HS-). A detailed study focusing on the effects that compositional changes (in both the alkyl chain and the peptide segment) impose on self-assembly is presented in **Chapter 2** of this thesis. To assess the effects of thiolation, a set of five peptide sequences (**V_3A_3**, **A_3V_3**, **A_6**, **$(VA)_3$**, and **$(AV)_3$**) and alkyl chains of two lengths (C16 and C11) were studied. Furthermore, dimeric species formed *via* thiol oxidation were compared to their monomeric counterparts. The self-assembly properties were compared to conventional palmitoylated peptide amphiphiles. As a general trend, thiolation lowered the amount of β-structure and the level of self-assembly was decreased, with the exception of those formed by one peptide segment, **$(AV)_3$**. Additionally, the fibers that formed were shorter in length. Dimerization of the C16 alkyl chain exhibited a pronounced effect on fiber appearance, in comparison to their monomeric counterparts, but not on the β-structure content. A change towards a shorter thiolated alkyl chain (C11) revealed a more complex nature of self-assembly: no common trends could be drawn for the five peptide segments, except for the fact that the content of α-structure increased in all cases. In general, dimerization of the C11 alkyl chain had a positive effect on both the fiber appearance and β-structure content. Interestingly, the **A_6** peptide amphiphiles demonstrated the highest α-content, which was reflected in the appearance of the fibers formed. The combined analysis of data obtained using circular dichroism (CD) spectroscopy, Fourier-transform infrared (FT-IR) spectroscopy, and transmission electron microscopy (TEM) allowed for the five peptide sequences to be divided into two groups: those with a

peptide-driven mode of self-assembly (**V_3A_3** and **A_3V_3**) or those where self-assembly is dependent on the alkyl chain composition (**A_6**, **$(VA)_3$**, and **$(AV)_3$**). The **V_3A_3** peptide domain exhibited minimal changes in terms of the self-assembly behavior in response to changes to the alkyl chain and so was presumed to be the most suitable candidate for stabilizing gold surfaces. This peptide amphiphile was subsequently employed in coating experiments, which are described in **Chapter 3**.

Chapter 3 of this thesis showcased the use of negatively charged, thiolated peptide amphiphiles as a stabilizer for spherical GNPs of 20, 40 and 100 nm diameter. These peptide amphiphiles were examined alongside well-known peptide stabilizers. The surface-curvature effect governed the stabilizing capacity of the peptidic stabilizers: higher net charge and more hydrophobic bulk were required for lower surface curvatures. Peptides with a lower net charge could only stabilize smaller GNPs (20 nm in diameter). An increased surface charge provided by the $CV_3A_3E_3$ peptide, was sufficient for effective stabilization of 40 nm GNPs, but failed to stabilize larger particles (100 nm in diameter). Thiolated peptide amphiphiles were capable of stabilizing all three GNP sizes, and maintained high colloidal stability due to formation of self-assembled monolayers (SAMs) on the gold surface. The surface-curvature effect was reflected in the SAM coverage density: it decreased from 3.72 to 2.17 peptide/nm^2 while the GNP size increased from 20 to 100 nm in diameter. The same trend was observed for the β-content: it decreased from 73.8% to 41.8%. It was proven that these SAMs are impermeable to competing thiols dissolved in water, this is because water is depleted from the gold surface due to the high density of the alkyl chains. Only the double chain variant (mercaptoundecanoyl)$_2$-$KV_3A_3E_4$ was capable of preserving the colloidal stability of all sizes of coated GNPs at high NaCl concentrations. The obtained results demonstrate that peptide amphiphile-coated GNPs are

stable under physiologically relevant conditions and suitable for biological and biomedical applications.

The same coating approach was used to explore the potential of thiolated peptide amphiphiles as stabilizers for gold nanorods (GNRs): **Chapter 4** of this thesis covers this study. GNRs are typically synthesized using a different chemical method called seed-mediated overgrowth, and the resulting surface chemistry is drastically different to that of spherical GNPs. GNRs are typically protected by a surfactant bilayer composed of cetyltrimethylammonium bromide (CTAB). In this chapter, this bilayer was shown to have limited permeability for peptides, whereas the three thiolated peptide amphiphiles that were tested effectively displaced CTAB, leading to a SAM formation at the GNR surface. The coating procedure was accompanied by more intense fiber formation in comparison with coated GNPs. This behavior was attributed to the charge of the original stabilizer: negatively charged citrate *versus* positively charged CTAB. The charge defined whether repulsive or attractive electrostatic interactions occurred upon addition of negatively charged thiolated peptide amphiphiles. Therefore, the coating procedure for GNRs was optimized to yield fiber-free samples. As in the case of peptide amphiphile-coated GNPs, SAM coverage densities and the β-content for GNRs were high (2.62-3.87 peptide/nm^2 and 51-58%, respectively depending on the peptide amphiphile composition). Interestingly, all three coatings were resistant to displacement by competing thiols, but only the double-chain (mercaptoundecanoyl)$_2$-K$V_3A_3E_4$ amphiphile was capable of preserving the GNR surface charge and colloidal stability at elevated NaCl concentrations. These observations help in determining how different thiolated peptide amphiphiles are displayed on a gold surface: due to the bidentate nature of (mercaptoundecanoyl)$_2$-K$V_3A_3E_4$, the coverage density is lower in comparison to the single chain counterparts, although this does not prevent effective hydrogen bonding as reflected in the high β-

content. On the other hand, the higher coverage density observed for the mercaptoundecanoyl-$V_3A_3E_3$ amphiphile resulted in packing defects as is evident from the lower β-content. However, extending the length of the alkyl chain, to obtain mercaptohexadecanoyl-$V_3A_3E_3$, allowed for an even higher coverage density and fewer packing defects, although the charge display on the gold surface was still obstructed, as it was rapidly screened upon addition of NaCl. A high negative charge and the presence of a hydrophobic segment make thiolated peptide amphiphiles superior GNR stabilizers in comparison with commonly used PEGs. SAMs formed by peptide amphiphiles exhibit similar stabilizing capacities to PEG, however peptide amphiphiles are up to 8 times shorter, meaning coating thicknesses are decreased. This feature is especially attractive for applications of GNRs in bio-sensing and nanophotonics where the coating thickness affects measurement accuracy.

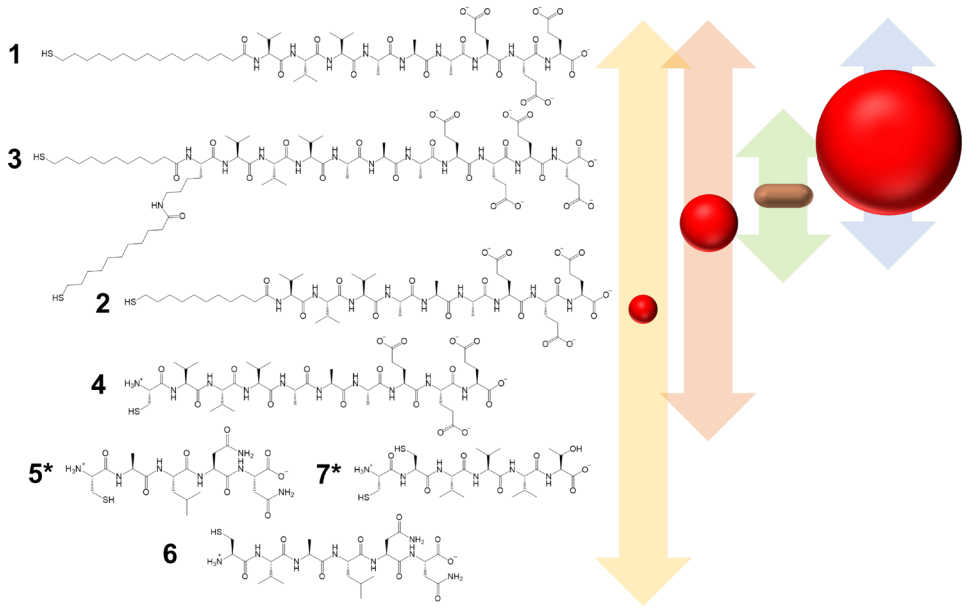

Scheme 6.1. Summary of peptides and peptide amphiphiles tested in this thesis as stabilizers for differently sized GNPs and GNRs. Arrows indicate the stabilizing capacity of different molecules with respect to GNP size and shape. GNPs and GNRs are shown to scale (from the left to right: 20 and 40 nm in diameter, 45 by 15 nm GNRs, 100 nm in diameter).

Since peptide chemistry offers a facile route to modification of a peptide sequence with various ligands, peptide amphiphile-coated GNPs and GNRs can be decorated with one or more functionalities. To demonstrate this, peptide amphiphile-coated GNPs of different sizes, and GNRs, were equipped with model epitopes derived from chicken ovalbumin ($OVA_{257-264}$ and $OVA_{323-339}$) and the evoked immune responses were studied *in vitro* and *ex vivo* using OT-I and OT-II mouse lines as described in **Chapter 5** of this thesis. The epitopes used stimulate either cytotoxic or helper T-epitopes and so it was possible to split the immune response into two components and draw conclusions regarding the impact of the shape and size of the epitope carrier particle. It was shown that peptide amphiphile-coated GNPs and GNRs do not cause cytotoxicity or induce inflammation through the IL-1β pathway. Furthermore, GNPs of 15 nm in diameter did not activate bone-marrow derived dendritic cells (BMDCs) and as a consequence did not evoke significant cytotoxic or helper T-cell responses. Although, at elevated concentrations 15 nm GNPs did show an increase in helper T-cell response but their effect was minimal in comparison to the performance of larger particles: GNPs of 40 nm in diameter and GNRs of 45 by 15 nm in size. Surprisingly, for GNPs of 40 nm in diameter, strong BMDCs activation through IL-12 secretion did not translate into 40 nm GNPs inducing superior cytotoxic and helper T-cell responses. Furthermore, GNRs delivered more antigen to the BMDC lysosomes than 40 nm GNPs. This is of importance since MHC-II is loaded with antigens inside lysosomes, thus GNRs elicited a stronger helper T-cell response. However, a different trend was observed when GNPs and GNRs were used to induce a cytotoxic T-cell response. 40 nm GNPs evoked a considerably stronger cytotoxic T-cell response than GNRs, indicating that the mass (or volume) of a delivery vehicle defines MHC-I antigen presentation. This can be explained by the fact that MHC-I and MHC-II utilize different pathways for presentation of the processed

antigens: MHC-I is loaded with epitopes present in the cytosol. Our findings indicate that shape and size of an antigen delivery vehicle do influence immune response and there are two key conclusions: (i) there is a size threshold below which delivery efficacy drops (~15 nm in diameter); (ii) there is a mass (or volume) threshold below which no effective MHC-I antigen presentation is possible (~40 nm in diameter). We believe these findings will have implications for vaccine development, and will help to form a better understanding of cellular uptake, as well as antigen egress from lysosomes into the cytosol.

In future, expanding the pool of displayed functionalities will accelerate the use of peptide amphiphile-coated GNPs and GNRs. For example, the thin, yet highly stable coatings are amenable to fulfilling GNPs potential in biosensing at the single molecule level and for target-specific imaging or biomarker detection assays. In addition, this system has demonstrated great potential as a model system to unravel the fundamental principles behind the behavior and function of biomacromolecules and cells.

CHAPTER 7

Nederlandse Samenvatting en Perspectieven

Goud nanodeeltjes (GNPs) zijn metallische nanodeeltjes die eenvoudig zijn te synthetiseren met controle over vorm en grootte. GNPs kunnen gemakkelijk worden gefunctionaliseerd en beschikken over bijzondere optische eigenschappen. Vanwege deze kenmerken zijn GNPs aantrekkelijk voor gebruik in een groot aantal toepassingen variërend van nanofotonica en sensoren, tot aan de behandeling van ziektes. Desondanks wordt het daadwerkelijke gebruik gehinderd door de inherente instabiliteit in fysiologische condities. Eerder werd aangetoond dat het modificeren van het oppervlak met biocompatibele moleculen resulteert in een significante vermindering van aggregatie en cytotoxiciteit. Het modificeren van GNPs met bijvoorbeeld silica of polymeren, is echter niet eenvoudig. Bovendien zijn deze coatings relatief dik, wat nadelig is voor bepaalde toepassingen. Een oplossing hiervoor is het stabiliseren van GNPs met peptiden. In dit proefschrift is een reeks cysteïne-bevattende oligopeptiden ontwikkelt waarin de thiol groep van cysteïne bindt aan het goud oppervlak via een Au-S binding. Dit resulteert in β-sheet-achtige secundaire peptide structuren op het goudoppervlak. Deze oligopeptiden beschikken over een netto negatieve lading die elektrostatische repulsie tussen individuele GNPs veroorzaakt resulterend in colloïdale stabiliteit. Tot dusver zijn peptiden alleen gebruikt voor het stabiliseren van kleine (≤30 nm), sferische GNPs en niet voor het stabiliseren van grotere GNPs of met een andere vorm. In dit proefschrift zijn nieuwe amfifiele peptiden ontwikkelt voor het stabiliseren van een breed scala aan GNPs met verschillende vorm en grootte. Deze moleculen beschikken over eigenschappen die zorgen voor een effectieve stabilisatie van GNPs: β-gestructureerd zelf-organiserend gedrag en een hoge netto lading. Bovendien bleek dat hydrofobe interacties tussen alkylketens kunnen bijdragen aan het stabiliserende effect van deze peptide-amfifielen. Wij hebben een reeks peptide-amfifielen ontworpen en hun zelf-organiserende eigenschappen gekarakteriseerd. De geschiktheid als coatings voor GNP's

van verschillende vormen en maten werd onderzocht. Ten slotte werd aangetoond dat functionalisatie van de peptide-amfifielen met specifieke epitopen de cellulaire immuunresponse kan beïnvloeden.

Om de peptide-amfifielen te binden aan een goudoppervlak, werd een thiol groep geïntroduceerd. Een gedetailleerde structuur-assemblage studie is beschreven in **Hoofdstuk 2** van dit proefschrift. Om de effecten van de thiol groep te evalueren, zijn vijf peptide sequenties (**V_3A_3**, **A_3V_3**, **A_6**, **$(VA)_3$**, en **$(AV)_3$**) en twee alkyl keten lengte (C16 en C11) bestudeerd. Bovendien is er een vergelijking gemaakt tussen monomeren en dimeren die gevormd worden door thiol-oxidatie. De zelf-organiserende eigenschappen zijn vergeleken met conventionele gepalmitoyleerde peptide-amfifielen. De introductie van een thiol groep leidde in het algemeen tot een vermindering van de hoeveelheid β-structuur en zelforganisatie, met uitzondering van één peptide segment, **$(AV)_3$**. Bovendien waren de gevormde assemblages korter. Dimerisatie van de C16-alkylketen had een duidelijk effect op de morfologie van de vezels in vergelijking met hun monomere tegenhangers, maar niet op de hoeveelheid aan β-structuur. Bij het gebruik van een kortere gethioleerde alkylketen (C11) konden er geen duidelijke trends worden ontdekt voor de vijf peptide-amfifielen assemblages, behalve dat het gehalte aan α-structuur in alle gevallen toenam. Dimerisatie van de C11-alkylketen had een positief effect op zowel de morfologie van de assemblages en de hoeveelheid aan β-structuur. Interessant genoeg vertoonden de **A_6**-peptide-amfifielen het hoogste α-gehalte, wat tot uiting kwam in de morfologie van de gevormde vezels. De gecombineerde analyse van gegevens verkregen met behulp van circulaire dichroïsme (CD) spectroscopie, Fourier-transformatie infrarood (FT-IR) spectroscopie en transmissie-elektronenmicroscopie (TEM) maakte het mogelijk dat de vijf peptidesequenties in twee groepen werden verdeeld: die met een peptide-gedreven modus van zelforganisatie (**V_3A_3** en **A_3V_3**) of die waarbij zelforganisatie afhankelijk is van de alkylketensamenstelling (**A_6**,

$(VA)_3$ en **$(AV)_3$**). Het **V_3A_3**-peptidedomein vertoonde minimale veranderingen in zelf-organiserend gedrag als reactie op veranderingen in de alkylketen en werd daarom verondersteld de meest geschikte kandidaat te zijn voor het stabiliseren van GNPs. Dit peptide-amfifiel werd vervolgens gebruikt in **Hoofdstuk 3**.

In **Hoofdstuk 3** van dit proefschrift werd het gebruik van negatief geladen, gethioleerde peptide-amfifielen als stabilisator voor sferische GNPs met een diameter van 20, 40 en 100 nm onderzocht. De kromming van het GNP oppervlak heeft een grote invloed op het stabiliserend vermogen van de peptidestabilisatoren: hogere netto lading en meer hydrofoob volume waren vereist voor lagere oppervlaktekrommingen. Peptiden met een lagere netto lading konden alleen kleinere GNPs (20 nm in diameter) stabiliseren. Een verhoogde oppervlaktelading ($CV_3A_3E_3$-peptide) was voldoende voor effectieve stabilisatie van 40 nm GNPs, maar niet voor grotere deeltjes (100 nm in diameter). Gethioleerde peptide-amfifielen waren in staat om GNP-groottes te stabiliseren resulterend in een hoge colloïdale stabiliteit door de vorming van zelf-geassembleerde monolagen (SAMs) op het goudoppervlak. Het oppervlakkrommingseffect werd weerspiegeld in de SAM-dichtheid: deze nam af van 3,72 tot 2,17 peptide / nm^2, terwijl de GNP-grootte toenam van 20 tot 100 nm in diameter. Dezelfde trend werd waargenomen voor het β-gehalte: deze nam af van 73,8% naar 41,8%. Deze SAMs bleken ondoordringbaar te zijn voor thiolen in oplossing van wege de hoge alkylketen-dichtheid. Eén variant ($(mercaptoundecanoyl)_2$-$KV_3A_3E_4$) was in staat om de colloïdale stabiliteit van alle GNPs bij hoge NaCl-concentraties te behouden. De verkregen resultaten tonen aan dat peptide-amfifiel gecoate GNPs stabiel zijn onder fysiologisch relevante omstandigheden en geschikt zijn voor biologische en biomedische toepassingen.

Hoofdstuk 4 van dit proefschrift beschrijft dezelfde gethioleerde peptide-amfifielen als stabilisatoren voor goud nanostaafjes (GNRs). GNRs worden meestal gesynthetiseerd met behulp van een andere procedure resulterend in een oppervlaktechemie die verschilt van sferische GNPs. GNRs worden doorgaans gestabiliseerd door een oppervlakteactieve dubbellaag van cetyltrimethylammoniumbromide (CTAB). In dit hoofdstuk werd aangetoond dat deze dubbellaag een beperkte permeabiliteit heeft voor peptiden, terwijl de drie gethioleerde peptide-amfifielen in staat waren tot een SAM-vorming op het GNR-oppervlak. De standaard coatingprocedure voor GNPs leidde tot significante vezelvorming. Dit werd toegeschreven aan de lading van de oorspronkelijke stabilisator: negatief geladen citraat versus positief geladen CTAB. Deze lading bepaalde de elektrostatische interacties optraden met de negatief geladen gethioleerde peptide-amfifielen. Daarom werd de coatingprocedure voor GNRs geoptimaliseerd. Net als in het geval van peptide-amfifiel gecoate GNPs, waren de SAM-dekkingsdichtheden en het β-gehalte voor GNRs hoog (respectievelijk 2,62-3,87 peptide/nm^2 en 51-58%). Alle geteste coatings waren resistent tegen concurrerende thiolen, maar alleen (mercaptoundecanoyl)$_2$-K$V_3A_3E_4$ was in staat om de colloïdale stabiliteit te behouden bij zeer hoge NaCl-concentraties. Vanwege de bidentate binding van (mercaptoundecanoyl)$_2$-K$V_3A_3E_4$ is de dekkingsdichtheid lager in vergelijking met de andere peptide-amfifielen. Desondanks bevatte deze SAM een hoog β-gehalte.

Het gebruik van langere alkylketens (mercaptohexadecanoyl-$V_3A_3E_3$) zorgde echter voor een nog hogere dekkingsdichtheid en minder pakkingsgebreken. Een hoge negatieve lading en de aanwezigheid van een hydrofoob segment maken gethioleerde peptide-amfifielen superieure GNR-stabilisatoren in vergelijking met veelgebruikte PEG-coatings. SAMs gevormd door peptide-amfifielen vertonen vergelijkbare stabiliserende capaciteiten als PEG, maar de peptide-amfifiele SAMs zijn tot 8 keer korter. Deze functie is vooral

aantrekkelijk voor toepassingen van GNRs in biosensing en nanofotonica, waarbij de laagdikte de meetnauwkeurigheid beïnvloedt.

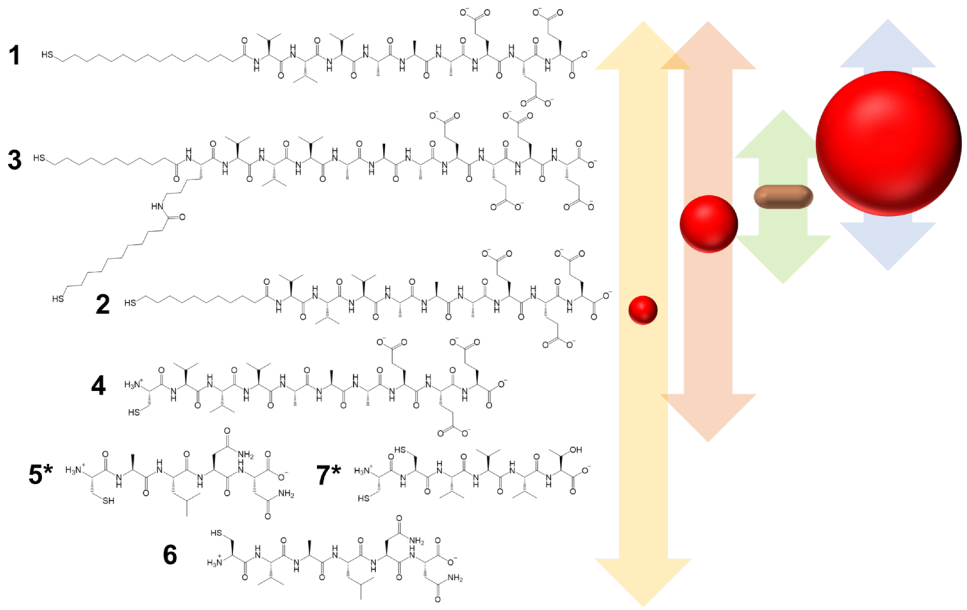

Schema 7.1. Samenvatting van peptiden en peptide-amfifielen die in dit proefschrift zijn getest als stabilisatoren voor GNPs en GNRs van verschillende grootte. Pijlen geven het stabiliserend vermogen van verschillende moleculen aan met betrekking tot de grootte en vorm van het GNP. GNPs en GNRs worden op schaal weergegeven (van links naar rechts: 20 en 40 nm in diameter, 45 bij 15 nm GNR, 100 nm in diameter).

Omdat modificatie van een peptidesequentie met verschillende liganden mogelijk is, kunnen peptide-amfifiel gecoate GNPs en GNRs gebruikt worden voor diverse toepassingen.

Als voorbeeld werden peptide-amfifiel gecoate GNPs van verschillende groottes en GNRs uitgerust met model-epitopen ($OVA_{257-264}$ en $OVA_{323-339}$). Vervolgens werden de opgewekte immuunresponsen *in vitro* en *ex vivo* bestudeerd met OT-I en OT-II muislijnen, zoals beschreven in **Hoofdstuk 5** van dit proefschrift. De gebruikte epitopen stimuleren óf cytotoxische óf helper-T-epitopen en in deze studie werd het mogelijk om de

immuunrespons op te splitsen in twee componenten en conclusies te trekken met betrekking tot de impact van de vorm en grootte van het epitoopdragerdeeltje. Aangetoond werd dat peptide-amfifiel gecoate GNPs en GNRs geen cytotoxiciteit of ontstekingen veroorzaken via de IL-1β-route. GNPs met een diameter van 15 nm induceerde geen activatie van beenmerg-afgeleide dendritische cellen (BMDCs) en wekten daardoor ook geen significante cytotoxische of helper-T-celreacties op. Hoewel bij verhoogde concentraties 15 nm GNPs een toename in helper T-celrespons vertoonden, was hun effect minimaal in vergelijking met grotere deeltjes (GNPs met een diameter van 40 nm en GNRs van 45 bij 15 nm). Verrassend genoeg vertaalde de sterke BMDC-activering door IL-12-secretie zich -voor GNP's met een diameter van 40 nm- niet in superieure cytotoxische en helper-T-celresponsen. Bovendien induceren GNRs meer antigeenproductie dan 40 nm GNPs. Dit is belangrijk omdat MHC-II is geladen met antigenen in lysosomen, waardoor GNRs een sterkere helper-T-celrespons opwekten. Er werd echter een andere trend waargenomen wanneer GNPs en GNRs werden gebruikt om een cytotoxische T-celrespons op te wekken. 40 nm GNPs wekten een aanzienlijk sterkere cytotoxische T-celrespons op dan GNRs, wat aangeeft dat de massa (of het volume) van het nanodeeltje de MHC-I-antigeenpresentatie bepaalt. Dit kan worden verklaard door het feit dat MHC-I en MHC-II verschillende routes gebruiken voor de presentatie van de verwerkte antigenen: MHC-I is geladen met epitopen die aanwezig zijn in het cytosol. Onze bevindingen wijzen uit, dat vorm en grootte van een antigeenafgiftedrager de immuunrespons beïnvloeden. Er zijn twee belangrijke conclusies: (i) er is een afmetingsdrempel waaronder de afgifte-efficiëntie daalt (~15 nm in diameter); (ii) er is een massa (of volume) drempel waaronder geen effectieve MHC-I-antigeenpresentatie mogelijk is (~40 nm in diameter). Deze bevindingen zullen naar verwachting een grote impact hebben voor de ontwikkeling van betere vaccins en zullen helpen om een

beter begrip te krijgen van de cellulaire opname, en antigentransport van lysosomen naar cytosol.

Er zijn verschillende toepassingen van peptide-amfifiel gecoate GNP/GNRs denkbaar. De dunne, maar zeer stabiele coatings zijn bijvoorbeeld geschikt voor biosensor toepassingen op het niveau van een enkel molecuul en voor doel-specifieke beeldvorming of biomarkerdetectie-assays. Bovendien kunnen deze nanodeeltjes gebruikt worden als modelsysteem om de fundamentele principes achter het gedrag en de functie van biomacromoleculen en cellen te ontrafelen.

Curriculum Vitae

Elena Aleksandrovna Egorova was born on May 28th 1989, in Serpukhov, Russia. She graduated from a high school in Serpukhov 2006 and entered Moscow State Academy of Fine Chemical Technology named after M.V. Lomonosov the same year. In 2010 Elena received a bachelor degree in chemistry. Two years later, she graduated from the Academy with a master degree in chemistry with specialization in polymer chemistry. Her master project was shared between the Academy and the Moscow State University, where Elena was conducting Reversible addition-fragmentation chain transfer (RAFT)-polymerization experiments under supervision of Prof. dr. Elena Chernikova. Her master's thesis was devoted to development of magneto-responsive hydrogels combining superparamagnetic properties of magnetite nanoparticles and biocompatible polymers. This work was reflected in two published papers.

From 2012 until 2016 Elena worked as a Junior Researcher at Institute of Biomedical Chemistry (IBMC), Moscow, Russia under supervision of Prof. dr. Ekaterina Kolesanova. There she was introduced to the field of peptide and protein chemistry, immunology and proteomics. Elena's main project focused on development of an epitope-based anti-hepatitis C virus (HCV) vaccine. The time at IBMC brought her two publications and a best poster prize at the International St. Petersburg Immunology Forum, 2015, Russia.

In 2016 Elena was granted a Global Education scholarship, a National Russian scholarship, which allowed Elena to start as a PhD candidate at the Supramolecular and Biomaterial Chemistry group of the Leiden Institute of Chemistry under supervision of Prof. dr. Alexander Kros in October of the same year. Her work was dedicated to expanding the use of gold

nanoparticles in biomedical applications *via* peptidic modification thereof. By virtue of collaborations with LACDR and CML (in the person of Bram Slütter, Gert Gooris, Joke Bouwstra, Redmar Vlieg, John van Noort and Fazel Abdolurphur Monikh) her thesis became a multi-disciplinary piece. Furthermore, four experimental chapters of this thesis were either published or submitted as scientific publications. During her stay at Leiden, she supervised five students and reported her work at several conferences:

Chains 2016

Dutch Polymer Days 2017

Ducth BioPhysics Days 2017

Chains 2017

Dutch Peptide Symposium 2018

European Peptide Symposium 2018

Chains 2018

GRC Meeting on Self-assembly and Supramolecular Chemistry 2019

Chains 2019

Chains 2020 (oral presentation)

List of Publications

1. Elena A. Egorova, Mark M. J. van Rijt, Nico Sommerdijk, Gert S. Gooris, Joke A. Bouwstra, Aimee L. Boyle, Alexander Kros, One peptide for them all: gold nanoparticles of different sizes are stabilized by a common peptide amphiphile. *ACS Nano*, **2020**, *14* (5), 5874-5886. doi.org/10.1021/acsnano.0c01021

2. Elena A. Egorova, Gert S. Gooris, Joke A. Bouwstra, Aimee L. Boyle, Alexander Kros, Self-assembly of conventional *versus* thiolated peptide amphiphiles, submitted

3. Elena A. Egorova, R. Vlieg, G. Arias Alpizar, J. van Noort, Gert S. Gooris, Joke A. Bouwstra, Aimee L. Boyle, Alexander Kros, Peptide amphiphile-stabilized gold nanorods for applications in two-photon microscopy, submitted

4. Elena A. Egorova, Gerda E. M. Lammers, Fazel A. Monikh, Bram A. Slütter, Aimee L. Boyle, Alexander Kros, Gold nanoparticles decorated with ovalbumin-derived epitopes: effect of shape and size on T-cell immune responses, in preparation

Publications issued before 2016:

5. E. Kolesanova, B. Sobolev, A. Moysa, E. Egorova, A. Archakov, Way to the peptide vaccine against hepatitis C. *Biochem Moscow Suppl. Ser. B*, **2015**, *61* (2), 254-264. doi.org/10.1134/S1990750815030026

6. V.F. Shalak, A.A. Vislovukh, O.V. Novosylna, A.I. Khoruzhenko, M.I. Kovalenko, E.F. Kolesanova, E.A. Egorova, A.A. Mishin, M.S. Krotevych, L.V. Skoroda, B.S. Negrutskii, Characterization of novel peptide-specific antibodies against the translation elongation factor eEF1A2 and their application for cancer research, *Biopolymers and Cell*, **2014**, *30*, 454-461. doi.org/10.7124/bc.0008C0

7. I. V. Bakeeva, E. A. Egorova, V. P. Zubov, N.S. Perov, I.V. Dementsova, E. V. Chernikova, Magnetosensitive organic-inorganic hybrid hydrogels. *Polymer Science Series B*, **2014**, *56* (3), 384-392. doi.org/10.1134/S1560090414030038

8. E. A. Egorova, V. P. Zubov, I. V. Bakeeva, E. V. Chernikova, E. A. Litmanovich, Controlled synthesis of oligomeric poly(acrylic acid) and its behavior in aqueous solutions. *Polymer Science Series A*, **2013**, *55* (9), 519-525. doi.org/10.1134/S0965545X13080026